

# **The Discrete Element Method in Archaeoseismological Research – Two Case Studies in Israel**

Inaugural-Dissertation

zur

Erlangung des Doktorgrades

der Mathematisch-Naturwissenschaftlichen Fakultät

der Universität zu Köln

vorgelegt von

**Gregor Schweppe**

aus Vreden

Köln 2019

Berichterstatter/Gutachter: Prof. Dr. K.-G. Hinzen

Prof. Dr. M. Melles

Tag der mündlichen Prüfung: 06.06.2019



Für meine Eltern

Christel und Hermann Schweppe

# TABLE OF CONTENTS

I.	Abstract.....	i
II.	Zusammenfassung .....	ii
III.	Acknowledgement .....	iv
1	Introduction .....	1
1.1	Archaeoseismology .....	3
1.2	Archaeoseismological Research in Israel.....	8
1.3	Two Case Sites in Israel .....	9
1.4	Guidelines of the Thesis .....	12
2	Region of Interest .....	13
2.1	Geographical Overview.....	13
2.2	Geological Overview.....	15
2.3	Tectonic.....	19
2.4	Seismicity .....	20
2.4.1	Intensity .....	20
2.4.2	Magnitude.....	22
2.4.3	Pre-Instrumental Earthquakes .....	23
2.4.4	Instrumental Earthquakes .....	25
3	Laser Scanning .....	27
4	Computer Models .....	31
4.1	Discrete Element Method.....	32
4.2	Model Verification .....	32
4.3	Collision detection.....	34
4.4	Units .....	35
4.5	Damping .....	36
4.6	Discrete Fracture Network .....	36
4.7	Software solutions .....	36
4.7.1	Universal Mechanism.....	37
4.7.2	Unity 3D.....	40
4.7.3	3 Dimensional Distinct Element Code .....	42

5	Roman Temple of Kedesh - Precariously Balanced Archaeological Structures.....	48
5.1	History of the Temple.....	48
5.2	Virtual 3D Model from Laser Scans .....	51
5.3	Creation of Discrete Element Models .....	52
5.3.1	Universal Mechanism.....	53
5.3.2	3 Dimensional Distinct Element Code .....	55
5.3.3	Unity 3D.....	56
5.4	Calculations .....	56
5.4.1	Analytic Ground Motion Signals.....	56
5.4.2	Earthquake Scenarios .....	57
5.5	Results .....	59
5.6	Discussion and Conclusion .....	66
5.7	Further Research.....	67
6	Crusader Fortress Ateret.....	68
6.1	History of the Site.....	69
6.2	Reconstruction of the Original State .....	73
6.3	Model Creation.....	77
6.4	Calculations .....	83
6.5	Results .....	85
6.5.1	First Scenario.....	87
6.5.2	Second Scenario .....	100
6.6	Discussion and Conclusion .....	106
6.7	Further Research.....	109
7	Discussion and Conclusion.....	111
8	Literature .....	112
9	Data and Resources .....	127
A.	<i>Appendix Crusader Fortress Ateret</i> .....	128
a.	<i>First Scenario</i> .....	128
b.	<i>Second Scenario</i> .....	150
	Erklärung.....	186

# I. ABSTRACT

Quantitative methods and particularly computer simulations have become increasingly important in the field of archaeoseismology in recent decades. In this work two approaches to investigate the ground motion history of two specific archaeological sites with computer models based on the discrete element method (DEM) are presented. During the model development, three different software codes are tried out to test which are suited best for these simulations.

Both sites that are in the focus of this work are located in Israel, a country rich on archaeological sites. At the ruin of the Roman Temple of Kedesh the concept of precariously balanced archaeological structures (PBAS) was introduced, in which the presence or absence of a certain ground motion in the past can be estimated. Since the destruction of the temple the ruin was exposed to numerous earthquakes. The goal here was to identify which ground motion would have destroyed the ruin. In 108 simulations with cycloidal pulses as ground motion with major frequencies ranging from 0.3 Hz to 2.0 Hz and PGAs from 1 m/s<sup>2</sup> to 9 m/s<sup>2</sup> the response of the ruin was calculated. Additionally, eight earthquake scenarios with two assumed, five historical and one recorded earthquake (ChiChi 1999) were used to test the stability of the ruin. The results of the simulations with the earthquakes show that only the record of the strong ChiChi earthquake would have destroyed the remains of the temple. The concept of PBAS does not only provide information about the current stability of the structure, which may be important in terms of the conservation of the cultural heritage, but also gives information about the parameters of the past earthquakes ground motions.

At the second site a different approach was followed. The ruin of the Crusader Fortress of Tell Ateret sits directly on the Dead Sea Transform Fault (DSTF); the fortification walls show a significant lateral offset that is related to movement along the fault line. At this point it is unknown whether the offset is the consequence of rapid movements during earthquakes or (at least in part) of slow creeping motion along the fault. In a discrete element (DE) model the original state of the northern fortification wall was reconstructed. The reconstruction formed the basis for 58 numerical simulations, in which the response of the model to ground motions were calculated. The simulations covered different movement directions and slip velocities along the fault line. The results show that a slow creeping movement could be ruled out as origin for the offset of the fortification walls. Furthermore, the results support the hypothesis that two coseismic movements displaced the fortification walls and also reveal that most of the slip occurred east of the fault line. Slip velocities of 3 m/s and 1 m/s could be estimated for the two movements. These can be assigned to two past earthquakes which occurred on May 20th 1202 and October 30th 1759.

## II. ZUSAMMENFASSUNG

In den letzten Jahrzehnten nahm die Bedeutung von quantitativen Methoden, besonders von Computer-Simulationen in archäoseismologischer Forschung zu. In dieser Arbeit werden für zwei ausgesuchte archäologische Stätte Ansätze zur Untersuchung der Bodenbewegungsgeschichte mit Computer Modellen vorgestellt, die auf der Diskrete-Elemente-Methode (DEM) basieren. Während der Modellentwicklung wurden drei Programmsysteme getestet, um festzustellen, welche am besten für unterschiedliche Fragestellungen geeignet sind.

Beide ausgewählten Stätte liegen in Israel, das reich an archäologischen Hinterlassenschaften ist. Das Konzept der prekär balancierten archäologischen Strukturen (PBAS) wird an der Ruine des Römischen Tempels von Kedesh eingeführt, mit dessen Modell das Vorhandensein oder Fehlen von Bodenbewegungen bestimmter Stärke in der Vergangenheit abgeschätzt werden kann. Seit der Zerstörung des Tempels war die Ruine mehreren Erdbeben ausgesetzt. Das Ziel war es, herauszufinden, welche Bodenbewegung die Ruine zerstört hätte. Dafür wurden 108 Simulationen durchgeführt, bei denen Cycloidal-Pulse mit Frequenzen von 0.3 Hz bis 2.0 Hz und Maximal-Beschleunigungen von  $1 \text{ m/s}^2$  bis  $9 \text{ m/s}^2$  als Bodenbewegungen verwendet wurden. In acht zusätzlichen Simulationen wurden synthetische Seismogramme von zwei angenommenen und fünf historisch belegten Erdbeben in der Levante sowie Messungen des ChiChi Erdbebens 1999 als Bodenbewegung verwendet, um die Stabilität der Ruine zu testen. Die Ergebnisse zeigen, dass nur Bodenbewegungen mit Amplituden ähnlich die des ChiChi Erdbebens die Ruine zerstört hätten, den Simulationen mit den historischen Erdbeben widerstand das Modell der Ruine. Der Ansatz der PBAS erlaubt es nicht nur Grenzen der Bodenbewegungsparameter der historischen Erdbeben anzugehen, sondern auch Aussagen über die momentane Stabilität der Struktur zu machen, welche wichtig für den Erhalt des Kulturerbes sein können.

An der zweiten Stätte wurde ein anderer Ansatz verfolgt. Die Kreuzritter Festung Ateret wurde direkt auf der Störungslinie der Toten Meer Transformstörung errichtet. Die Festungsmauern zeigen einen lateralen Versatz der zwischen 2.1 und 1.75 m variiert, der zuvor als Resultat von rein coseismischen Bewegungen an der Störungslinie interpretiert wurde. Bislang war jedoch unklar, ob nicht zumindest teilweise langsame (postseismische) Kriechbewegungen entlang der Störungslinie zum Gesamtversatz beigetragen haben, was einen deutlichen Einfluss auf die Magnitudenbestimmung der Beben hätte. In einem Diskrete-Elemente (DE) Modell wurde der ursprüngliche Zustand der Ruine vor dem Versatz rekonstruiert. Basierend hierauf wurden 58 numerische Simulationen durchgeführt, wobei unterschiedliche Versatzgeschwindigkeiten und unterschiedliche Versatzrichtungen auf beiden Störungsseiten berücksichtigt wurden. Die Ergebnisse zeigen, dass eine Kriechbewegung als Ursache für den Versatz unwahrscheinlich ist. Es wird die

Hypothese unterstützt, dass der Versatz durch zwei coseismische Bewegungen verursacht wurde. Es konnten Versatzgeschwindigkeiten von 3 m/s bzw. 1 m/s für die beiden Erdbeben vom 20. Mai 1202 und 30. Oktober 1759 zugeordnet werden.

### III. ACKNOWLEDGEMENT

I would like to thank the following people for their support during my Ph.D.:

First and foremost, I would like to thank Prof. Dr. Klaus-G. Hinzen for his comprehensive support and supervision.

I would also like to thank Prof. Dr. Shmulik Marco for the successful collaboration and the excellent guidance in Israel and Prof. Dr. Moshe Fischer for his archaeological expertise. A thank also goes to the team that supported us during the fieldwork in Israel.

I thank C. Fleischer for all the years of good discussions especially in the lunch breaks and Dr. Sharon K. Reamer for all the discussions and also the excellent advices for writing. In addition, my thanks go to all employees of the Seismological Station Bensberg of Cologne University, with whom I have been able to work constructively over the years.

I would like to thank Itasca Consultants Group who accepted me for the Itasca Education Program and not only provided the 3DEC Software Code, but also granted me a training course for the software. The thank applies especially to my mentor of the educational program Dr. Lothar te Kamp for the constructive discussions around discrete element models and particularly for the opportunity to run additional simulations when needed.

And finally, a special thank goes to my family who supported me unconditionally throughout my studies.

This work was partly funded by the German-Israeli Foundation for Scientific Research and Development (GIF 1165-161.8/2011).

# 1 INTRODUCTION

The aim of this thesis is to demonstrate the potential of computer models based on the Discrete Element Method (DEM) for archaeoseismological investigations. Two archaeological sites in the Levante were chosen which allow exploring the applicability of models based on the DEM under various archaeoseismological aspects and concluding on the nature of ground motions during ancient earthquakes.

In seismic active areas, particularly at plate boundaries, earthquakes are considered to be reoccurring events (Reid 1910, Bakun and McEvilly1984). The seismicity of a region is tightly connected to its tectonic environment. Strength of earthquakes can vary over many dimensions and their location is often bound to faults, either visible at the Earth surface or on blind faults within the crust (Wells and Coppersmith 1994). The recurrence time of large earthquakes can extend over long periods of time. It is essential to look at the earthquake history of the region in order to understand the seismicity of a certain area, particularly the probability of occurrence of earthquakes of a specific size is important (Marco *et al.* 1996, Begin *et al.* 2005). Any knowledge of a past earthquake, particularly a damaging one, is only a part of the puzzle but a substantial data point to improve the quantification of the seismic hazard of the region. It is therefore important to apply all techniques of modern seismology and where possible to refine the existing methods.

Three main branches of seismology investigate recent and past earthquakes: instrumental seismology, historical seismology, and paleoseismology. To clarify the approximate temporal relationships of the different branches, *Figure 1.1* from Galadini *et al.* (2006) shows the temporal classification of the different fields of expertise taking Italy as an example. As the time frames of the three disciplines overlap and geological sciences as well as historical sciences are involved, interdisciplinary work is essential for the study of past earthquakes.

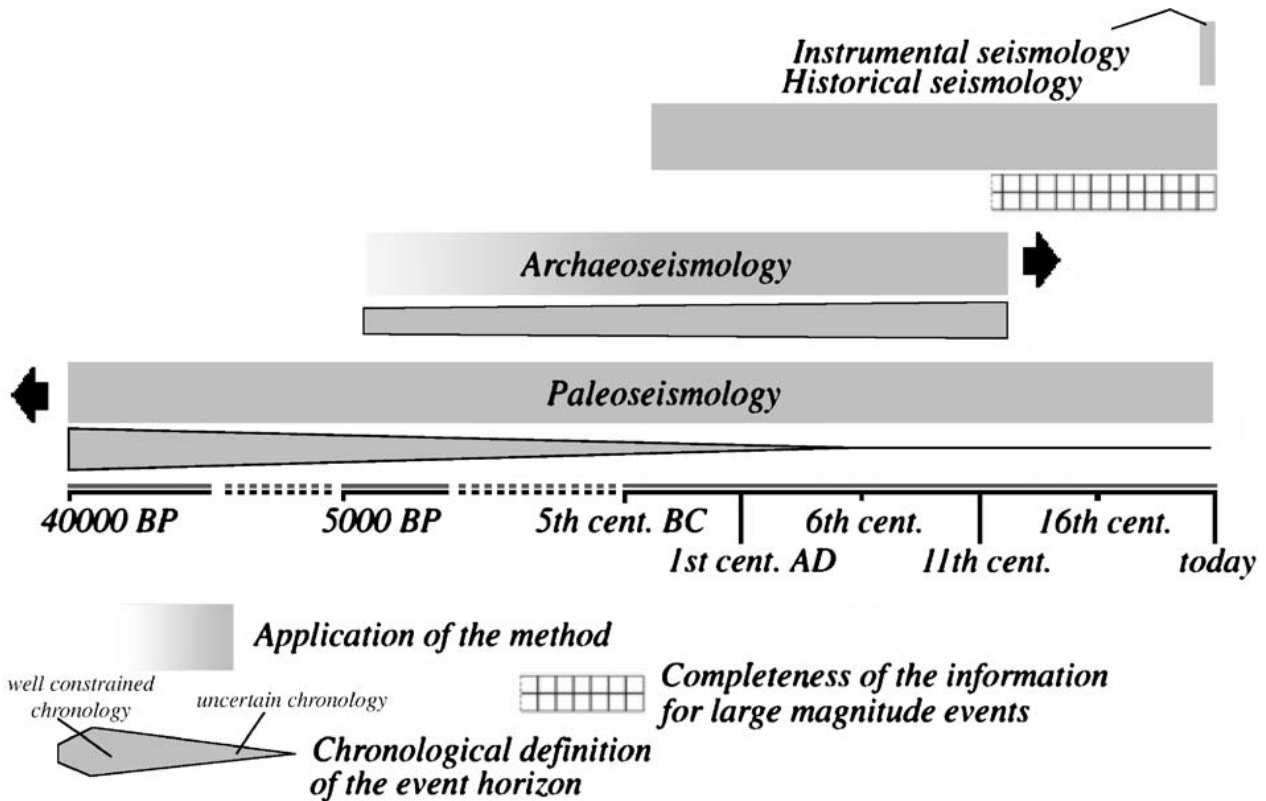


Figure 1.1: Chronological intervals of application of different researches on past earthquakes in Italy. (Galadini et al. 2006).

Instrumental seismology started at the end of the 19th century (Rebeur-Paschwitz 1895, Wiechert 1926) and modern digital seismology is only about five decades old (Adams and Allen 1961, Bogert 1961). It is based on the exact measurement of ground motions with seismometers and today capable to deliver precise localization of the seismic source and reveal details of the source mechanism and rupture process, particularly through the application of numerical models and the inversion of complete ground motion records. However, in relation to the interseismic cycle, the time between two large earthquakes at the same fault, the time span covered by modern seismological data is extremely short.

Historical seismology is based on historical *i.e.* written information. Naturally the time frame of this research is limited by the existence of a historical record, which can vary considerably from one cultural region to another; *e.g.* in North America few centuries are covered, in the Levante the written record extends several millennia (Ambraseys 1971). The interdisciplinary work with historians allows the reconstruction of how past earthquakes were perceived by the population and/or damaged constructions and infrastructure. Naturally the application is tied to populated area (Galadini et al. 2006).

Among the three disciplines paleoseismology covers the longest time span reaching back thousands or tens of thousands of years (McCalpin 1996). In paleoseismological research effects of earthquakes in the near surface lithology are investigated. If earthquakes of normal depth are strong enough, moment magnitude well above 6, they might leave persistent coseismic changes mainly in young sediments layers close to or at the activated fault line (McCalpin 1996). The stratigraphic record and precision of radiometric dating methods define the limit of the time frame for certain earthquakes (Ken-Tor *et al.* 2001). Paleoseismology is bound to locations close to active faults and is applicable only to earthquakes which are strong enough to change the structure of near surface deposits.

A new seismological discipline, often seen as a sub-discipline of paleoseismology (McCalpin 1996) is archaeoseismology, which focuses on archaeologically revealed information or traces which earthquakes left in persisting monuments. In the Encyclopedia of Solid Earth Geophysics archaeoseismology is defined as: “*The study of pre-instrumental earthquakes that, by affecting locations of human occupation and their environments, have left their mark in ancient structures uncovered by means of archaeological excavations or pertaining to the monumental heritage.*” by Hinzen (2011). Damaged buildings, rotated objects, collapse horizons and other archaeological evidence are the foundation for this kind of research. The time frame covered is shorter compared to paleoseismology, but can be significantly longer than the written record. The research is limited by the existence of the remains of man-made structures, but these do not need to be directly at the causative fault of an earthquake, because ground motions capable of damaging buildings can reach many tens of kilometers and damage can occur during earthquakes smaller in size than necessary to be detected in paleoseismology (Galadini *et al.* 2006).

### 1.1 Archaeoseismology

De Rossi (1874), Lanciani (1918), Evans (1928) and Agamennone (1935) pioneered using archaeological information to investigate past earthquakes. Increasing numbers of publications dealt with the topic of seismogenic damage on man-made structures found in archaeological investigations (*e.g.* Karcz and Kafri 1978; Zhang *et al.* 1986; Guidoboni 1996). However, the early archaeoseismological publications were often of descriptive nature. Damage observed in man-made structures during archaeological excavation has been documented, attributed to earthquakes and interpreted by means of common sense. In the last decades, quantitative methods gained popularity addressing archaeoseismological questions with analytical approaches and the use of modern engineering seismological methods (Galadini *et al.* 2006, Hinzen 2009a).

For these tasks computer simulations have been used in a wide range of application and have proven to be a useful tool in various ways. First models concentrated on investigating the dynamic response to ground motion of basic structures such as free standing columns (Papastamatiou and Psycharis 1993, 1996,

Psycharis *et al.* 2000, Konstandinidis and Makris 2005, Hinzen 2009a). These structures are naturally vulnerable to ground-motion and in the first approximation have simple geometries which is an advantage, because it keeps the computation time in reasonable bounds.

A large part of archaeoseismological research is the analysis of damaged or deformed masonry, as this method of construction has been widely used in the past. The masonry can be of various styles of different time-periods. For example, walls made of polygonal blocks are considered to be more earthquake-resistant than walls built with rectangular blocks. Hinzen and Montabert (2017) tested this hypothesis by comparing the dynamic behavior of walls with varying height and width ratio (h/w-ratio) and four different block geometries when excited with analytical ground motion and measured earthquake records. They confirmed that wall models with polygonal blocks have a higher earthquake resistance than the models with rectangular blocks. However, the authors made clear that the h/w-ratio is at least as important as the block geometry for the walls susceptibility to ground motion.

Not only the influence of the masonry style has been simulated in archaeoseismological research. Numerical models are as well capable to investigate the dynamic behavior of more complex structures. These simulations may also be linked with issues of cultural heritage preservation. Psycharis *et al.* (2003) analyzed the seismic behavior of the Parthenon Pronaos with discrete element models. In their study the multi drum columns of the temple were modeled with their existing imperfections to assess the vulnerability of the *in situ* state to ground motions. In addition, the effects of safety measures which are intended to increase the stability were simulated in terms of preservation of the architectural heritage. The simulations revealed that metal reinforcements support the drums of the columns against shear displacement, but are ineffective against uplift during stronger ground motions. In some cases, the reinforcements are counterproductive, suppressing the energy-dissipation of inter-drum movement. The authors could show that the imperfections have a severe influence to the stability of the columns and suggest eliminating those imperfections, to increase the stability.

Computer models are capable tools and it is therefore important to counter-check the validity of simulation results. Cakti *et al.* (2016) compared the results of a shake-table test with the results of a discrete element model. They constructed a 1/10 model of the Mustafa Pasha Mosque (Istanbul) on a shake-table and modeled the same on the computer. Both models were excited with scaled seismograms of the north-south component of the Montenegro earthquake (15.04.1979,  $M_w$  6.9). In total 26 tests were carried out with both models. The authors showed that the analytical and experimental results were in good agreement and concluded that the numerical simulation is also capable to calculate the realistic response for full scaled building. Galvez *et al.* (2018) analyzed the behavior of a two-story masonry with a discrete element model and a scaled model on a shake-table. The latter was excited with harmonic ground

motion in one horizontal direction with increasing frequencies. The response of the masonry was recorded by accelerometers. The same ground motion was used as boundary condition for the computer simulations. The simulated crack pattern and the point of collapse of both models are in good agreement. The validation of computer simulations is an essential step in the development process. Instead of using shake-table tests, models can also be verified by comparing the simulated results with analytical solutions of known problems, the verification process is described in detail in Section 4.2 (Model Verification).

In archaeoseismology numerical models are not only applied to investigate the response of man-made structures to ground motions. The wide application range of these models also allows considering alternative damage scenarios. *E.g.* in Pınara (Turkey) a severely damaged Roman mausoleum is located in close proximity to a steep cliff. To test whether the damage was caused by an earthquake or a rockfall, Hinzen *et al.* (2013a) reconstructed the Mausoleum in a discrete element model based on a detailed 3D laser scan and historical information. Next to synthetic seismograms and analytical ground motions as boundary conditions to test the behavior of the model, additionally rockfall scenarios were simulated. The results of the simulations were compared with the *in situ* measured state of the Roman mausoleum. The authors revealed that a rockfall was not likely to produce the observed damage, but a local earthquake with a moment magnitude of 6.3 is a possible cause. An example where anthropogenic influence is likely the source for the observed damage was presented by Hinzen *et al.* (2010). The Lycian sarcophagus of King Arttumpara in Pınara is damaged and deformed; it is rotated by  $6.37^\circ$  off its original position. Although parts of the damage pattern indicate an explosion, it was assumed that the coffin was rotated by an earthquake. A detailed discrete element model was developed based on a 3D laser scan of the Sarcophagus. Next to the response of the model to harmonic ground motions and recorded seismograms, also the effects of a blast on the Sarcophagus were simulated. The authors showed that a blast is likely the source of the observed rotation and could even reveal the amount of explosives used.

Computer models can also provide an opportunity to simulate secondary effects that are not related to damaged structures and still give valuable information about the ground motion history of a site. During archaeological excavation in Mycenaean Tiryns terracotta figures were found on the floor of a cult room and archaeologists hypothesized that the figures fell off a bench during an earthquake. Hinzen *et al.* (2014a) developed a computer model to simulate the movement of these figures due to ground motions to test the hypothesis that a damaging earthquake occurred in late Bronze Age. In the simulations many scenarios were covered with a large parameter space. In total 74,250 individual tests were calculated to cover all possible scenarios. The results revealed that in none of the simulated scenarios the outcome matched the archaeological findings. Therefore, the earthquake hypothesis was refuted.

*Figure 1.2* shows a general schematic workflow for a quantitative archaeoseismological investigation as it has been suggested by Hinzen *et al.* (2009). The model development relies mainly on two sections of input, first a reconstruction of the state of the investigated structure at the time when the potential earthquake occurred and second on boundary conditions such as earthquake ground motions and alternative causes. The latter are important, if it is not *a priori* clear that the observed structural damage is of coseismic nature.

For the reconstruction and quantification of damage of structural elements or complete buildings a precise documentation of the current state of the structure of interest is required (Schreiber and Hinzen 2010). Today 3D laser scanner and digital photography are common tools for documentation (*e.g.* Schreiber *et al.* 2009, Hinzen *et al.* 2010, Schreiber and Hinzen 2010, Schreiber *et al.* 2012, Hinzen *et al.* 2013a, Hinzen *et al.* 2013b, Hinzen *et al.* 2016a, Hinzen *et al.* 2018). Additional information from historical and archaeological records complete the dataset for the reconstruction. The boundary conditions are derived with geotechnical and seismological models based on geological, tectonic and geophysical information of the site. Also site effects may be taken into account (Hinzen and Weiner 2009, Hinzen *et al.* 2016b, Hinzen *et al.* 2018) for which explorative *in situ* measurements might be necessary (Hinojosa-Prieto and Hinzen 2015). With the complete geotechnical model synthetic seismograms for specific earthquake scenarios can be calculated and applied as input to models for the reconstructed structures.

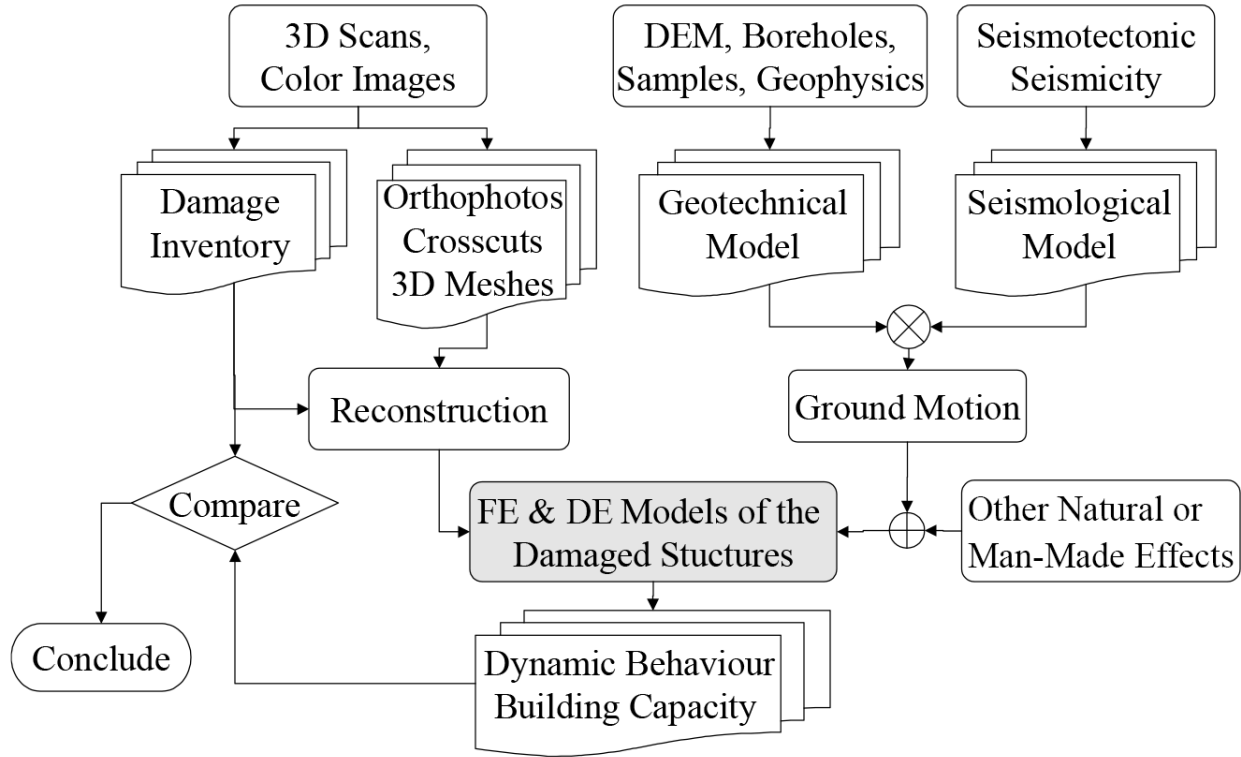


Figure 1.2.: Schematic flow chart of quantitative archaeoseismic modeling (after Hinzen et al. 2009).

The center of the work scheme in *Figure 1.2* is the model of the studied structure. Models based on the Finite Element Method (FEM) and DEM are established tools in engineering seismology to study the earthquake safety of contemporary buildings (Meskouris 1999, Meskouris *et al.* 2011); they can also be applied to study the behavior of (reconstructed) ancient structures. Their combination with the simulated earthquake scenarios and comparison with the (archaeologically) observed damage can help to find bounds for the parameters of the ground motion which once caused the damage (Stiros and Jones 1996, Galadini *et al.* 2006).

The reconstruction process heavily depends on the information that archaeologists and historians can provide about the man-made structures. The dates of creation, destruction and/or abandonment of a site define the time window for the damaging earthquake. Geologists and geophysicists provide information about the tectonic environment, the seismicity and local earthquake site effects. These data are vital to succeed with the quantitative approach to explore the potentially seismogenic damaging process. This illustrates the importance of interdisciplinary work in archaeoseismological research.

### 1.2 Archaeoseismological Research in Israel

The wealth of archaeological sites in Israel fascinated researchers for more than 150 years. The Palestine Exploration Fund, founded in 1865 (<https://www.pef.org.uk/history/>, last accessed 03.08.2018) initiated surveys for the exploration of the Levante. In “*The Survey of western Palestine.*” Conder and Kitchner (1882) reported about their expedition from 1871–1878. They describe several archaeological sites in detail, of which numerous show damage, now associated to seismic activity (Karcz *et al.* 1977, Karcz and Kafri 1978, 1981). Karcz *et al.* (1977) first used the term *archaeoseismic* to relate to damage on archaeological structures attributed to earthquakes. A wide range of archaeoseismological research has been carried out in Israel.

The ancient city of Jericho is located north of the Dead Sea in vicinity to the Dead Sea Transform Fault (DSTF). Alfonsi *et al.* (2012) were able to identify two Neolithic (7,500-6,000 BCE) earthquakes at Tell es-Sultan by analyzing archaeological reports of the excavations. They could reconcile the archaeological findings with paleoseismological evidence of past earthquakes.

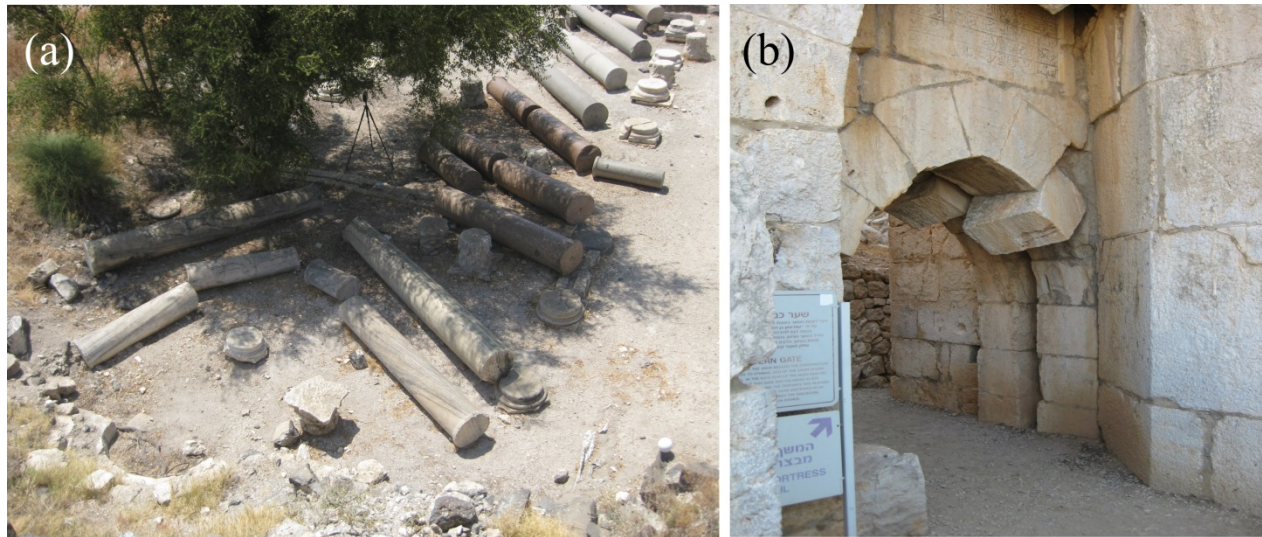


Figure 1.3: (a) Toppled columns of Hippos Sussita. (b) Dropped voussoir at the gate tower of Kalat Nimrod (Photos: K.-G. Hinzen).

An often mentioned prime example for earthquake damage are the perfectly aligned toppled columns of the so called Cathedral at Hippos Sussita at the Sea of Galilee (Figure 1.3 (a)) (e.g. Stiros and Jones 1996, Hinzen *et al.* 2011, Wechsler *et al.* 2018). This is located on a ridge about 2 km east of the Sea of Galilee. The perfect alignment of the columns was first misinterpreted as an indicator for the direction of ground motion. With a scenario based numerical analysis Hinzen (2010) showed that this hypothesis does not apply. The main earthquake that affected the site happened in 749 C.E. (Marco *et al.* 2003).

Wechsler *et al.* (2009) associated the same earthquake with the destruction of the synagogue of Umm-El-Qanatir. It is located about 10 km north-east of Hippos Sussita. The authors' main arguments are the abandonment of the close city Umm-El-Qanatir and a probable landslide, triggered by the earthquake. The synagogue was excavated by Kohl and Watzinger (1916) and is currently in the process of an elaborate anastylosis.

The 749 C.E. earthquake also impacted the western shore of the Sea of Galilee. In ancient Tiberias Marco *et al.* (2003) identified seismogenic damage at the Galei Kinneret excavation. The archaeological stratigraphy dates the damage in a time around the 749 C.E. earthquake. The authors showed that the findings are in good agreement with paleoseismic and historic evidence.

In northern Israel lies the Nimrod Fortress (or Kalat Nimrod). It was constructed in 1228 to control the valley between Mount Hermon and the rest of the Golan Heights, a former route from the Galilee to Damascus (Ellenblum 1989). The fortress was heavily damaged during the 1759 Lebanon earthquake. Many arches inside the ruin show damage, which are a strong indicator for a seismogenic origin. Keystones or *voussoirs* slipped from their original position (*Figure 1.4 (b)*). This is in particular evident in the so called "secret passage" of the gate tower, where the *voussoirs* slipped over a 20 m long section. Kamai and Hatzor (2008) tested the dynamic characteristics of the type of arches found in Nimrod with a discontinuous deformation analysis. They estimated a PGA of 0.4 g at 1 Hz to allow movement of the keystones or *voussoirs*. During a visit to the fortress one might get the impression that the grade of damage depends on the orientation of the according arches. Hinzen *et al.* (2016a) systematically examined the damage of 95 arches but could not confirm a dependency between the grade of damage and orientation of the arch.

### 1.3 Two Case Sites in Israel

In the course of this work two archaeological sites in Israel are studied in detail; both are located north of the Sea of Galilee and considered to show earthquake damage. The chosen sites are considered to be damaged by earthquakes (Fischer *et al.* 1984, Ellenblum *et al.* 1998). To document the current state of the sites they have been carefully surveyed with a 3D laser scanner, to get a detailed virtual 3D model of the damaged structures.

The first structure is the ruin of the Roman Temple of Kedesh, whose remains are currently in precarious stable condition (*Figure 5.2 (c)* and (*d*)). The temple was destroyed during an earthquake on May 19th 363 C.E. (Fischer *et al.* 1984). At this particular site information about the initial state of the Temple at the time of the earthquake is unclear and in addition the remains were heavily altered by anthropogenic influence (*i.e.* looting). A reconstruction of the process which caused the destruction is hardly possible.

## Introduction

For such sites with an unknown history of destruction the regular archaeoseismological approach described above with an elaborate reconstruction process is not feasible. *Figure 1.3* shows numerous examples of damaged archaeological sites in currently stable conditions.

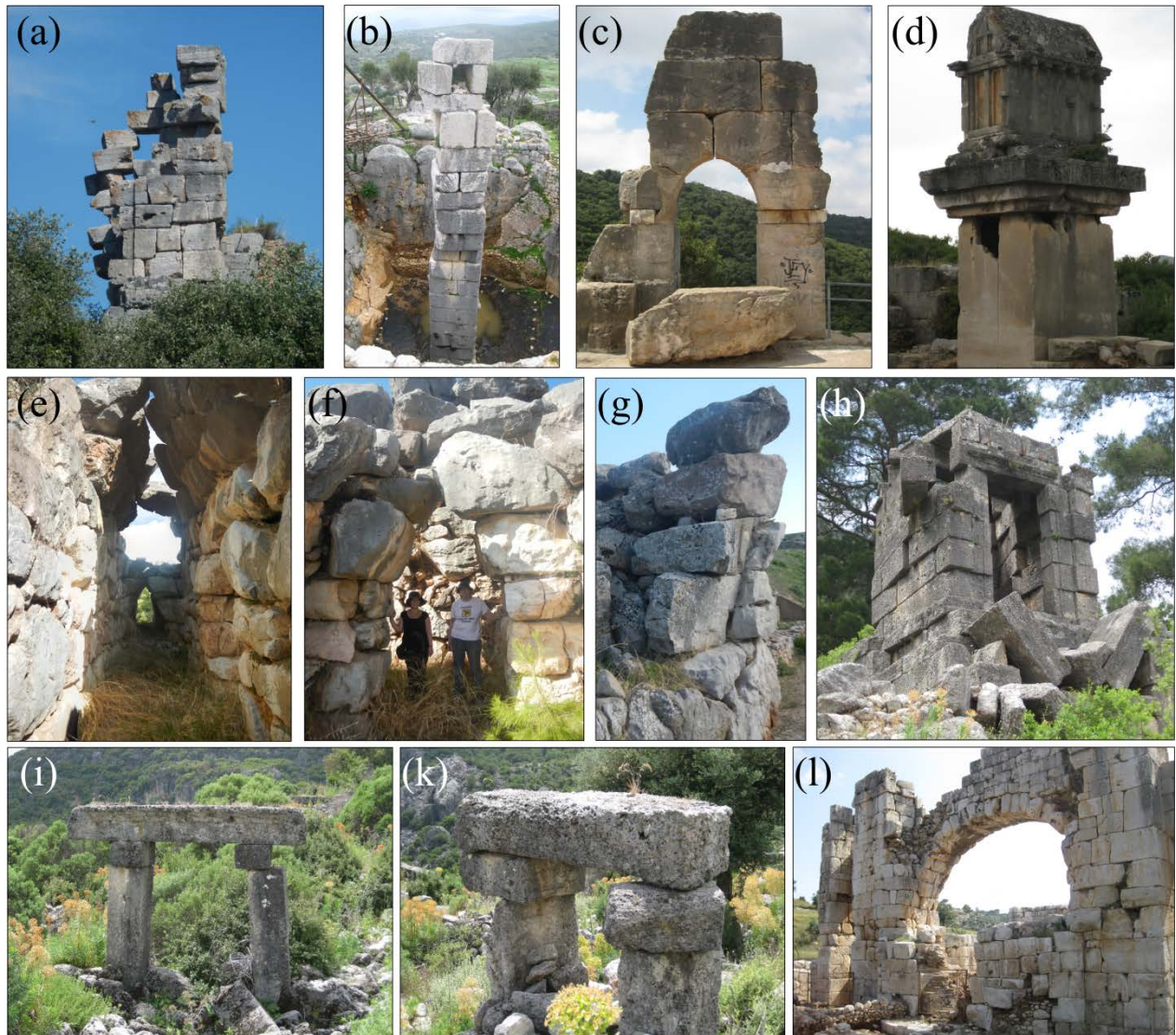


*Figure 1.4: Examples of precariously balanced archaeological structures: (a) ruin of the Roman harbor bath in Ephesus, Turkey; (b) pre-Roman rock cistern at Patara, Turkey; (c) ruin of Montfort Crusader castle, Israel; (d) Lycien sarcophagus Xanthos, Turkey; (e+f) Mycenaean corbeled vault, Tiryns, Greece; (g) ruin of Cyclopean wall of Tiryns, Greece; (h) Roman mausoleum Pınara, Turkey; (i+k) ruins of Roman bath Pınara, Turkey; (l) delicate Roman arch, Patara, Turkey (after Schweppe et al. 2017; Photos: K.-G. Hinzen)*

However, despite these problems it is still possible to derive information about the ground motion history from such sites. Not only archaeological remains can be in delicate stable states; under specific circumstances natural formations can also be in precarious condition. Precariously balanced rocks (PBR) are used as seismoscope to expand the knowledge of the ground motion history of a specific site (*e.g.*

Brune 1996, Anooshehpour 2004). In this work the concept of PBR is adapted for archaeological structures that are in a fragile condition.

Thus the ruin of the Roman Temple at Kedesh was considered a Precariously Balanced Archaeological Structure (PBAS) (Schweppe *et al.* 2017). The focus in this approach is not on the ground motion that destroyed the Roman Temple, but on the nature of the ground motions that did not topple the remains during the past 17 centuries. This method allows utilizing former not necessarily usable archaeological structures to gain information about the ground motion history of a site.

The second site is the ruin of the Crusader Fortress at Tell Ateret, a prominent archaeoseismological research site. Frankish Crusaders started the construction of a fortress directly on top of the DSTF fault line (Ellenblum *et al.* 1998). The fortress was still under construction when it was conquered by Muslim forces in 1179 and subsequently abandoned. Today the massive fortification walls are offset by tectonically caused movements along the fault. The fortification wall is 4.4 m wide and of double shell nature. The volume between the shells is filled with a mixture of basalt cobbles and mortar. While previous work concentrated on the sequence of earthquakes at Tell Ateret since Iron Age II (Marco *et al.* 1997, Ellenblum *et al.* 1998, 2015), details of the rupture process which deformed the northern fortification wall of the fortress is the core of this study. Therefore, a complex model has been developed, which is capable to simulate the movement of the walls, where the filling in between demanded special attention. With the final model, which is comprised by 52,864 individual blocks, various different scenarios were considered in the simulations. So far, exclusively two earthquakes have been assigned to the observed deformation of the fortification walls, based on the good agreement between the age of the archaeological structures at the site and the date of the known past earthquakes. The possibility of creeping motion has been disregarded, although creeping is known to exist along sections of the DSTF (Hamiel *et al.* 2016). Questions about the dislocation velocity at the fault and the amount of movement of each plate were addressed by the DEM model of the wall. Information about the dislocation velocity and the displacement of the fault are important parameters for inferring the magnitude of the past earthquakes.

In total three different software solutions were used for the model development of both sites. However, not all approaches proved functional. The development process for each model is described in the according chapters.

### 1.4 Guidelines of the Thesis

Following to this introduction Chapter 2 gives a geographical and geological overview of the study areas in Israel. It also includes an introduction to the tectonic setting and instrumental and pre-instrumental seismicity. The next two Chapters cover the methods used in this work. Chapter 3 describes the basic concept of Laser Scanning Technique and its applications. Chapter 4 gives a detailed overview of Computer Models based on the DEM and the development process for all software solutions used in the course of this work. Chapter 5 is split into two mayor sections, each dealing with one site. In the first section background information about the Roman Temple of Kedesh are given. Afterwards the surveying and the modeling process are described in depth and the results of the simulations are presented and discussed. The second section deals with the ruin of the Crusader Fortress of Tell Ateret. Here the same logical sequence as in the preceding section is followed. Lastly the discussion and conclusion, in which the results of both sites and the application of the DEM are considered in a wider angle of archaeoseismology is presented, closing with recommendations for further research.

The Thesis was partly funded by the German Israeli Foundation (GIF) Grant Number 1165. As part of the Itasca Education Program (IEP) Itasca provided the software licenses for 3DEC.

## 2 REGION OF INTEREST

This chapter gives an introduction to the area, where the selected archaeological sites are located. A short geographical and geological overview is followed by a description of the current tectonic setting and the pre-instrumental and instrumental seismicity.

### 2.1 Geographical Overview

Israel is located in the Middle East on the south-eastern shore of the Mediterranean Sea and the northern shore of the Red Sea. It has a surface area of 22,072 km<sup>2</sup> including the disputed territories ([www.cbs.gov.il](http://www.cbs.gov.il) last accessed 07.2017). The country has an elongated approximate triangular shape. From north to south the country is about 430 km long. The widest east-west extension is 115 km and the narrowest is 15 km.

The largest perennial river in Israel is the Jordan River. It is fed by three source flows: Hasbani, Dan and Banyas in the north and discharges into in the Dead Sea (Heimann and Sass 1989). On its way south the Jordan River crosses the Hula Basin (also Hula Valley), a former wetland which was drained for agricultural use in the 1950s. Prior the drainage the Hula Basin was the site of Lake Hula, the northernmost of originally three natural inland water bodies connected by the Jordan River (Hambright and Zohary 1998). The Hula Basin subsides along the DSTF and lies at an elevation of about 70 m. The flanks of the Golan Heights and the Upper Galilee (Naftali) mountains form the boundaries of the Hula Basin to the east and west respectively (Horowitz 1973). South, the basin is closed by a basalt block, which throttled the water flow downstream through the Jordan Gorge to the Sea of Galilee, which caused the historic wetlands (Hambright and Zohary 1998). The Jordan Gorge is a straight narrow gorge connecting the Hula Basin over approximately 10 km with the Sea of Galilee (*Figure 2.1 (b)*). Between the Sea of Galilee and the Dead Sea lies the Jordan Valley. The Dead Sea is a hyper-saline lake, the shore line is about 430 m (as of 2016 <https://isramar.ocean.org.il/> last accessed 10.2018) below sea-level (Quennell 1956a), which makes it the lowest point on land on Earth. South of the Dead Sea is the Araba Valley, another depression, that extends to the south to the Gulf of Aquaba, which opens into the Red Sea.

## Region of Interest

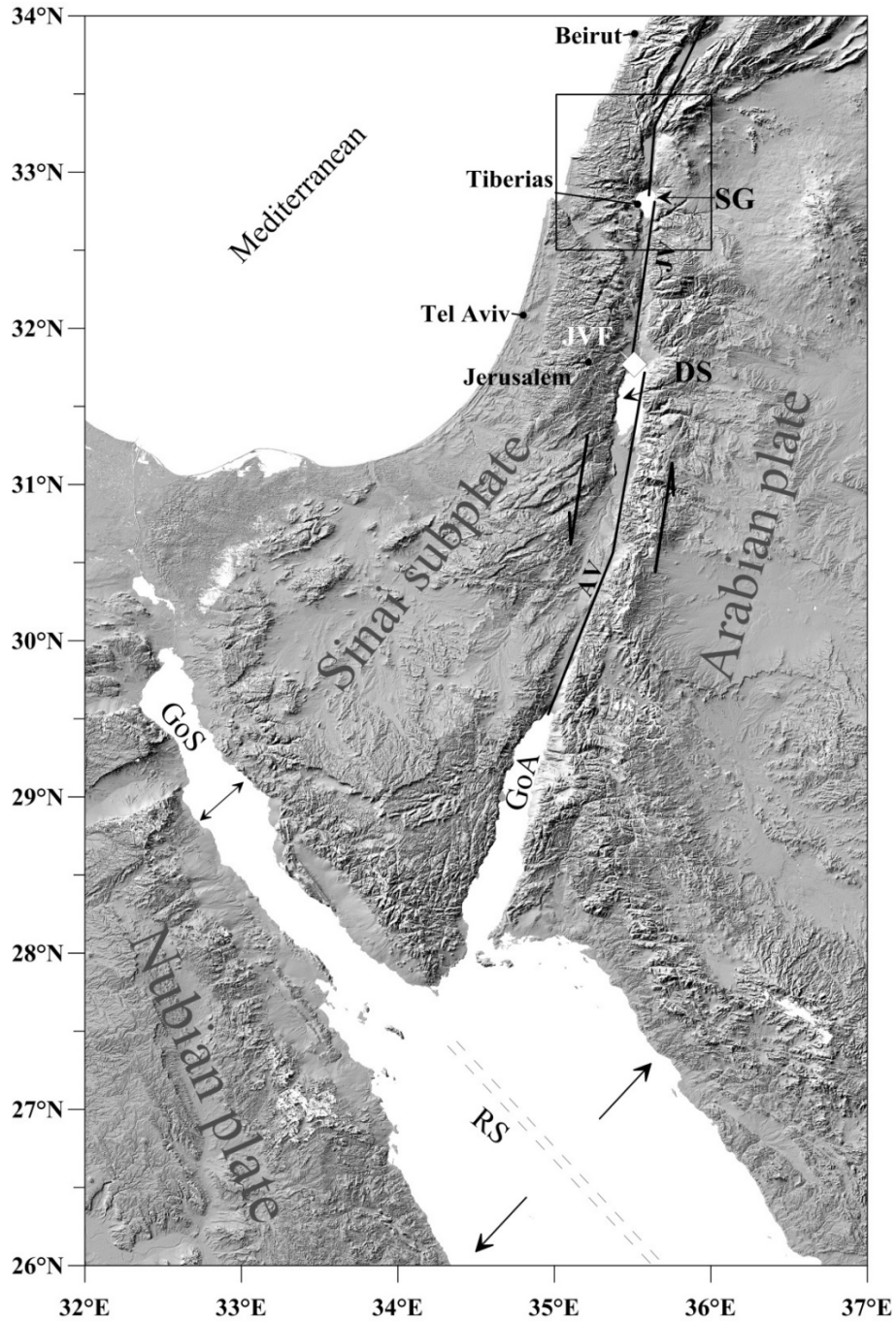


Figure 2.1: Digital terrain map of the DSTF (black lines), the single headed black arrows indicate the movement along the DSTF. The white rhombus marks the epicenter of the synthetic JVF earthquake (cf. Chapter 5); (RS = Red Sea, GoS = Gulf of Suez, GoA = Gulf of Aquaba, DS = Dead Sea, SG = Sea of Galilee, JVF = Jordan Valley Fault). The arrows indicate the rift movement of the GoS and RS rift, respectively. The dashed grey line marks the oceanic ridge. The black rectangle indicates the working area shown in (Figure 2.5) (after Schweppe et al. 2017).

## Region of Interest

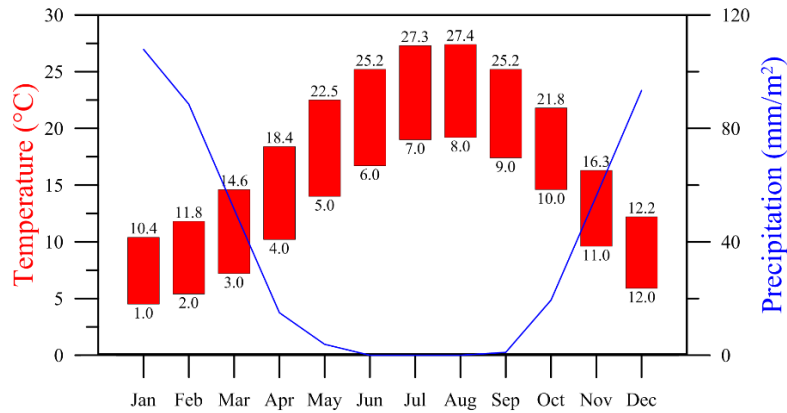


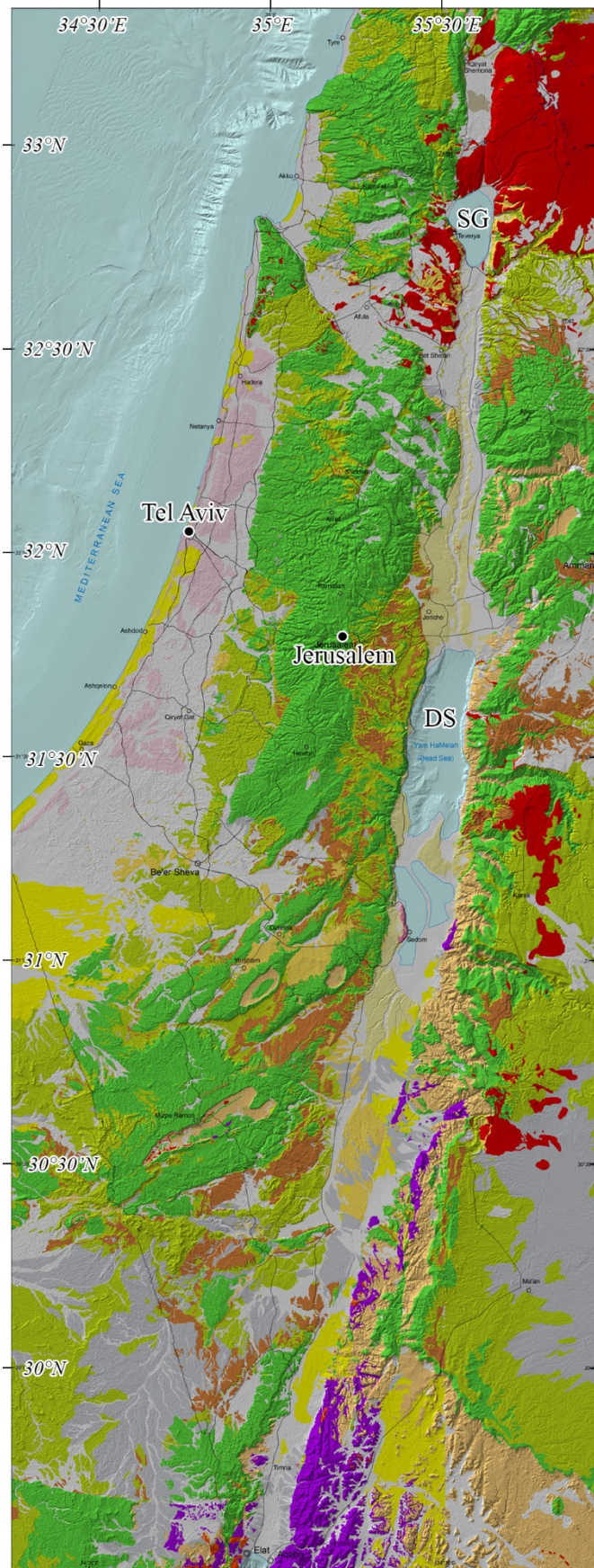
Figure 2.2: Multi-annual average of the temperature and precipitation in Israel. The blue line shows the monthly average precipitation ( $\text{mm}/\text{m}^2$ ) for the period 1981-2010. The red bars show the monthly average temperature ( $^{\circ}\text{C}$ ) of the years 1995 -2009 numbers on top and bottom are the minimum and maximum average temperatures measured in Israel (data from: [www.cbs.gov.il](http://www.cbs.gov.il) last accessed 07.2017).

The Mediterranean climate of the region is characterized by hot dry summers and mild wet winters. *Figure 2.2* shows average precipitation and temperatures of Israel by month. The annual average precipitation is  $437 \text{ mm}/\text{m}^2$ , for comparison the total average in Germany for the years 1961 to 1990 is  $848 \text{ mm}/\text{m}^2$  (<https://de.statista.com>, last accessed 05.2018). The seasonal temperature has a variance between minimum and maximum of about  $15^{\circ}\text{C}$  ([www.cbs.gov.il](http://www.cbs.gov.il) last accessed 07.2017).

## 2.2 Geological Overview

The geologic map shown in *Figure 2.3* gives an overview of the geology of Israel. The oldest rock formations are exposed in southern Israel and in northern direction the formation are getting younger. The oldest rocks are magmatic and metamorphic rocks of the Precambrian. Younger magmatic rocks are from Neogene and Pleistocene and are mostly exposed in the north, except of some locations in the east. The majority of the rocks are limestone from Mesozoic and Cenozoic times. In *Figure 2.3* it is evident, especially in the Precambrian formations, that pre-Miocene formations are offset. The formations in eastern Israel are shifted further north than west, which is the consequence of the left-lateral movement along the DSTF (Quennell 1959, Freund 1965, Freund *et al.* 1970, Bartov *et al.* 1980).

## Region of Interest



### Legend

- Alluvium - gravel, sand, silt, clay & rock debris; *Holocene*
- Sand (aeolian); *Holocene*
- Turf (*kavul*); *Holocene*
- Calcareous sandstone (*kurkar*), red sandstone & loam (*hamra*); *Pleistocene*
- Conglomerate; *Plio-istocene*
- 'Lisan Marl' - mostly aragonite; gypsum & clastic alternations; *Pleistocene*
- Rocksalt - evaporites (mostly halite); clastic alternations; *Pliocene*
- Sandstone, mudstone, marl & conglomerate; *Neogene*
- Chalk & chalky limestone; *Senonian - Pleistocene*
- Chert (including chalk alternations & phosphorites); *Senonian*
- Limestone, dolostone & marl; *Cambrian - Neogene*
- 'Nubian Sandstone'; *Cambrian - Cretaceous*
- Volcanic rocks - basalt & pyroclastics; mostly *Neogene & Pleistocene*
- Scoria cones
- Magmatic and metamorphic rocks; *Precambrian*

Figure 2.3: Geologic Map of Israel (1:500,000)  
 (from <http://www.gsi.gov.il>, last accessed 08.2018,  
 corrected stratigraphy).

Following Garfunkel (1988) the geologic evolution of Israel can be structured into three main parts.

1. Late Precambrian Pan African *orogenic stage*
2. Early Cambrian to End-Paleogene *platformal stage*
3. Early Neogene to Recent *rifting stage*

The *orogenic stage* contains the oldest rock formations, the rocks are exposed in southern Israel in the area of Elat and in the surrounding of the Red Sea (*cf. Figure 2.3*), they belong to the Arabo-Nubian Shield (Picard 1939). The rocks can be separated into two complexes, the *orogenic* and the *late-orogenic* complex. The first consists of metamorphic and plutonic rocks. The metamorphic rocks were heavily influenced by the events of the Pan-African orogeny (Matthews *et al.* 1989), the metamorphism reached high greenschist to middle amphibolite grade (Garfunkel 1988). With the ending of the main activity of the orogeny a widespread plutonic phase started, marking the main consolidation phase of the crust (Garfunkel 1988). The plutonic phase was followed by uplift and erosion. The *late-orogenic* complex is mainly composed of unmetamorphed sediments, high-level intrusions and volcanic rocks (Garfunkel 1988).

The *platformal stage* extends over a long time period from the end of the Pan-African Orogeny in early Cambrian to the onset of the rifting in Miocene, which includes the Paleozoic and Mesozoic eras in their entirety and the early Cenozoic era. The transition from the *orogenic* to the *platformal stage* began with an uplift followed by massive erosion, which formed a large peneplain. Only some resistant volcanic rock formations in southern Israel did not erode and formed hills of several hundred-meter height. After the initial erosion period the area was coined by vertical movement and global sea level changes (Garfunkel 1988). Periods of sedimentation were separated by phases of erosion; also phases with tectonic and magmatic activity occurred. In Israel Paleozoic sediments, mostly sandstones from continental and shallow marine environments are exposed in southern Israel, in the southern Negev, other deposits eroded (Garfunkel 1988). In Mesozoic time, between Later Permian and early Jurassic (Liassic) the tectonic setting changed with the breakup of Pangaea, which led to two major changes in Israel: from the Late Permian, the subsidence towards the Mediterranean continental margin increased and between Triassic and Liassic times there was differential movement, rifting and magmatism, which are associated with the formation of the Mediterranean passive continental margin (Garfunkel and Derin 1984, Garfunkel 1988). The tectonic-magmatic activity ended in Middle Jurassic, followed by subsidence, which usually increased towards the continental margin and led to sedimentation under both shallow and deep water conditions. In Latest Jurassic the sedimentation phase ended by the activity of an intra-plate hot-spot

causing widespread magmatism, regional uplift and erosion. This phase lasted until Early Cretaceous and eroded the older shallow-water deposits (Garfunkel 1988). In Cretaceous times the sea level rose and a phase of extensive sedimentation of mostly limestone and dolostone began (Sass and Bein 1982, Garfunkel 1988). In the Late Cretaceous and Paleogene, the sedimentation shifted and chalk and marl became the dominant sediments.

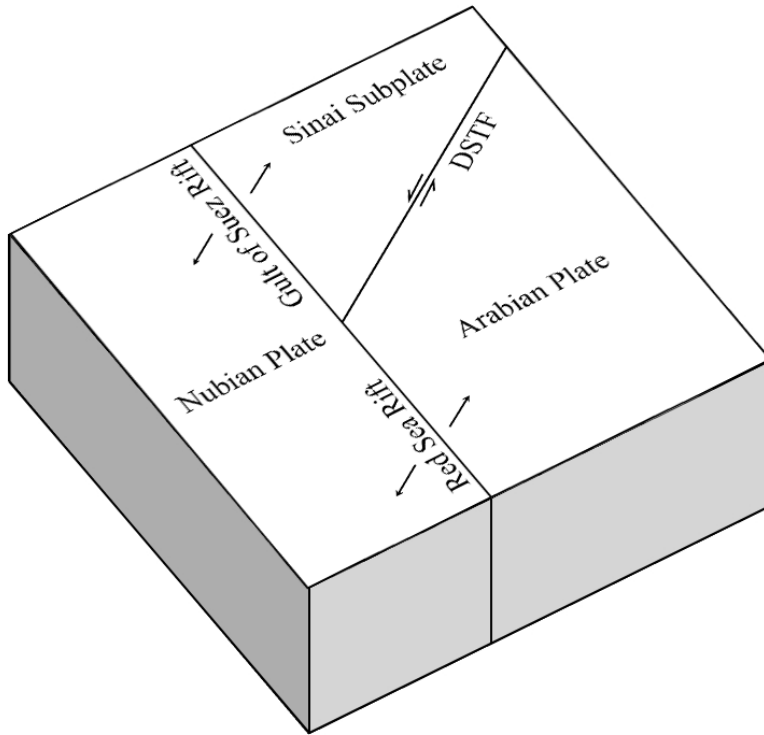


*Figure 2.4: Schematic block model of the initial tectonic setting at the beginning of the Mid-Cenozoic to Recent rifting stage. The movement along the DSTF allows the rifting systems to open (after Garfunkel 1988).*

The *rifting stage* was initialized by a significant change in the tectonic setting in the Neogene. The breakup of the Arabo-African continent with the onset of the rifting at the Red Sea and Gulf of Suez created new plate boundaries in the region, the movement along the DSTF started. A schematic representation of the initial tectonic setting and the movement directions of the plates has been given by Garfunkel (1988) (*cf. Figure 2.4*). The tectonic activity uplifted large areas above sea level and was accompanied by widespread magmatic activity,

particularly east of the DSTF. In Middle Miocene during an active volcanic phase the so called ‘Lower Basalt’ originated (Steinitz *et al.* 1978, Garfunkel 1988). In Pliocene another volcanic outburst covered a large area in southern Galilee and in the Golan heights with a basalt flow, this sequence is also called “Cover Basalt” (Steinitz *et al.* 1978, Garfunkel 1988). Between the volcanic events short phases of sedimentation are known. Today the pre-miocene formations from the pre-rifting stage are offset 105 km by the DSTF (Quennell 1959, Freund 1965, Freund *et al.* 1970, Bartov *et al.* 1980).

### 2.3 Tectonic

The tectonic system of Israel has been subject of geological research over 100 years (Suess 1891, Gregory 1921, Willis 1928). In the first publications the DSTF was also called “Dead Sea Rift”, because the depressions (such as the Dead Sea, Sea of Galilee, Hula Basin), located along the fault line, have been misinterpreted as a consequence of ramps or rifting (Willis 1928). However, the depressions are pull-apart basins and result from the movement along the DSTF (Ben-Avram and Schubert 2006).

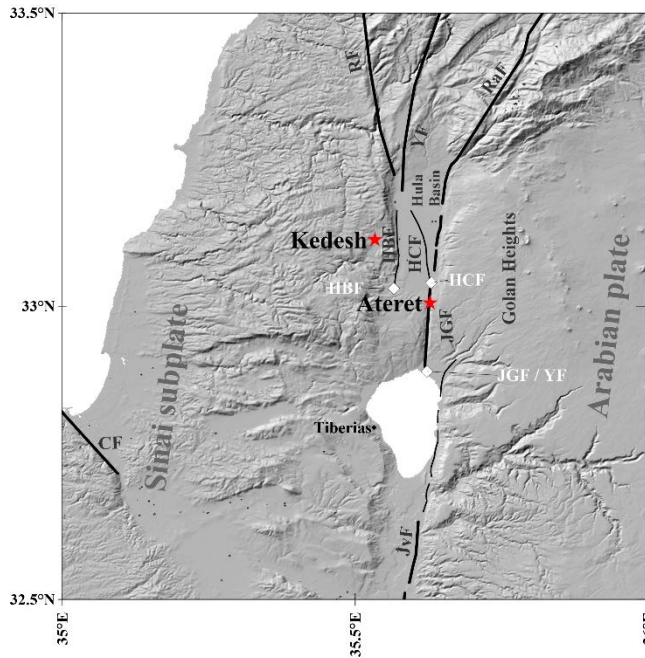


Figure 2.5: Working area; the red stars mark the location of the Roman Temple of Kedesh and the Ruin of the Crusader Fortress Ateret. Black lines show the local active strands of the DSTF (after Wechsler *et al.* 2014) (JGF = Jordan Gorge Fault, HCF = Hula Basin Central Fault, HBF = Hula Basin Border Fault, RaF = Rachaya Fault, RF = Roum Fault, YF = Yammouneh Fault, CF = Carmel Fault). The white rhombuses mark the epicenters of the sources used to calculate synthetic seismograms.

The DSTF is a left lateral transform plate boundary, which separates the Sinai subplate in its west from the Arabian plate in the east (Figure 2.1 and Figure 2.4). The fault line of the DSTF strikes north-south and connects the Red Sea in the south over a distance of 1000 km with the Anatolian Faulting System of the Bitlis-Zagros collision zone in the north (Quennell 1956b, Freund *et al.* 1968). GPS observations reveal that both plates are moving in northern direction separating from the Nubian Plate with different speeds (*e.g.* McClusky *et al.* 2003, Wdowinski *et al.*, 2004; Mahmoud *et al.* 2005, Reilinger *et al.* 2006, Vigny *et al.* 2006, Le Beon *et al.* 2008), the movement of the plates is connected with the extensional regime of the Red Sea and the Gulf of Suez. The opening speed of the Red Sea rift varies from  $14 \pm 1.0$  mm/yr at  $15^\circ\text{N}$  to  $5.6 \pm 1.0$  mm/yr at  $27^\circ\text{N}$  (McClusky *et al.*

2003). And the opening speed of the Gulf of Suez is  $1.5 \pm 0.4$  mm/yr (Mahmoud *et al.* 2005). The consequence of the different rifting speeds is the left-lateral strike slip movement observed at the DSTF (Figure 2.4). GPS measurements revealed an overall short term sinistral slip rate of 4-6 mm/yr (Wdowinski *et al.* 2004, Gomez *et al.* 2007a, Sadeh *et al.* 2012), which matches the long term geologic rates estimated by the 105 km offset of the geologic features (Quennell 1956b, Freund 1965, Bartov *et al.* 1980).

In Israel the DSTF is segmented into three main parts, named after the depressions; from south to north: the Araba Valley, the Jordan Valley and the Hula Basin (*Figure 2.1*). Between Araba Valley and Jordan Valley lies the Dead Sea; the Jordan Valley and the Hula Basin are separated by the Sea of Galilee and the Jordan Gorge, which connects the Sea of Galilee and the Hula Basin. In the Hula Basin the DSTF splays into several non-parallel faults. The most prominent branches from east to west are the Rachaya Fault (RaF), Yammounh Fault (YF) and the Roum Fault (RF) (*Figure 2.5*). In the so called Lebanese Restraining Bend (LRB) the deformation is partitioned between the strike-slip movement and crustal deformation (Gomez *et al.* 2007b). The slip rate along the sections of the DSTF is not constant (McClusky *et al.* 2003, Sadeh *et al.* 2012). Sadeh *et al.* (2012) analyzed the GPS data of 33 permanent and 145 survey GPS stations measured over 12 years. They were able to show that the slip rate and the locking depth of the DSTF tends to decrease from south to north. In the Araba Valley section they estimated a slip rate of 5.1 mm/yr and locking depth of 15.5 km. In the Dead Sea the slip rate decreased to 4.8 mm/yr and the locking depth was at 14.1 km. In the Jordan Valley segment itself the slip rate and locking depth was not uniform, the southern section had a slip rate of 4.9 mm/yr and a locking depth of 15.8 km was measured and in the northern part only a slip rate of 3.8 mm/yr and a locking depth of 12.4 km. In the Jordan Gorge Fault (JGF) they estimated a slip rate of 3.7 mm/yr at a locking depth of 8.7 km. In their study the authors also identified oblique motion at the Carmel Fault System (CFS) a fault system located west of the DSTF. A left-lateral motion of 0.7 mm/yr and extension rates of 0.6 mm/yr were measured. The authors concluded that lateral movement of the DSTF is inferred to the CFS, resulting the significant decrease of the slip-rate within the Jordan Valley. In their study Sadeh *et al.* (2012) found a good agreement between the geodetically estimated locking depth and the depth, above which 90% of the seismic moment has been released, which underpins the estimated locking depth. Hamiel *et al.* (2016) identified in their geodetic analysis of GPS data a shallow creep motion in the northern section of the Jordan Valley Fault (JVF), where Sadeh *et al.* (2012) measured the slower slip rate. They estimated creep movement in a depth up to  $1.5 \pm 1$  km with a creep rate of  $2.5 \pm 0.8$  mm/yr.

## 2.4 Seismicity

The seismicity of Israel is characterized by infrequent large earthquakes with periods of small to moderate earthquakes in between (Begin *et al.* 2005, Agnon 2014). This section first presents measures for the strength of earthquakes that are important for this work, followed by the description of the pre-instrumental and instrumental seismicity of Israel.

### 2.4.1 INTENSITY

The macroseismic intensity is a classification of the severity of earthquake ground motion in a certain area (*e.g.* Wood and Neumann 1931, Sieberg 1933, Medvedev *et al.* 1964, Grünthal 1998). It is based on

## Region of Interest

people's perception of the event and the effect that the ground motions have on man-made structures. Although the macroseismic maps based on these scales are biased by the proximity or lack of populated areas to the epicenter, construction types of the affected structures and local site effects, they are often the only measure able to estimate the strength of pre-instrumental earthquakes. Most intensity scales have twelve degrees, labeled with Roman numbers. The most prominent scales are the Modified-Mercalli scale (MM) introduced by Wood and Neumann (1931), the Medvedev-Sponheuer-Karnik scale (MSK) by Medvedev *et al.* (1964) and the European Macroseismic Scale (EMS-98) by Grünthal (1998). *Table 2.1* lists the short form of the twelve intensities of the European Macroseismic Scale (Grünthal 1998).

*Table 2.1: Short form of the European Macroseismic Scale EMS-98 (Grünthal, 1998).*

#	Definition	Description of typical observed effects
I	Not felt	Not felt
II	Scarcely felt	Felt only by very few individual people at rest in houses
III	Weak	Felt indoors by a few people. People at rest feel a swaying or light trembling.
IV	Largely observed	Felt indoors by many people, outdoors by very few. A few people are awakened. Windows, doors and dishes rattle.
V	Strong	Felt indoors by most, outdoors by few. Many sleeping people awake. A few are frightened. Buildings tremble throughout. Hanging objects swing considerably. Small objects are shifted. Doors and windows swing open or shut.
VI	Slightly damaging	Many people are frightened and run outdoors. Some objects fall. Many houses suffer slight non-structural damage like hair-line cracks and fall of small pieces of plaster.
VII	Damaging	Most people are frightened and run outdoors. Furniture is shifted and objects fall from shelves in large numbers. Many well built ordinary buildings suffer moderate damage: small cracks in walls, fall of plaster, parts of chimneys fall down; older buildings may show large cracks in walls and failure of fill-in walls.
VIII	Heavily damaging	Many people find it difficult to stand. Many houses have large cracks in walls. A few well-built ordinary buildings show serious failure of walls, while weak older structures may collapse.
IX	Destructive	General panic. Many weak constructions collapse. Even well-built ordinary buildings show very heavy damage: serious failure of walls and partial structural failure.
X	Very destructive	Many ordinary well-built buildings collapse.
XI	Devastating	Most ordinary well-built buildings collapse, even some with good earthquake resistant design are destroyed.
XII	Completely devastating	Almost all buildings are destroyed.

Another approach is the Environmental Seismic Intensity scale (ESI 2007) developed under the patronage of International Union for Quaternary Research (INQUA) (Michetti *et al.* 2007). Contrary to the above intensity scales, this is not based on the impact of an earthquake to human environment, but on the size and distribution of earthquake environmental effects, such as surface rupture, liquefaction or tree shaking. The ESI 2007 is intended to be a supplement to the other Intensity scales.

### 2.4.2 MAGNITUDE

In modern seismology the strength of instrumentally recorded earthquakes is quantified by magnitude. In 1935 Charles Richter published a magnitude which was based on instrumental measurements. His intention was to develop a measure “*freed from uncertainties of personal estimates or the accidental circumstances of reported effects*” (Richter 1935). He introduced the local magnitude ( $M_L$ ) which is based on the maximum amplitude of a seismogram measured with a Wood-Anderson-Seismometer and the epicentral distances.

The surface-wave magnitude ( $M_S$ ) was introduced by Gutenberg and Richter (1956). It is based on the measurement of the amplitudes of surface waves at certain periods. Empirical relations allow to estimate  $M_S$  from intensities derived from the historical record (*e.g.* Ambraseys and Melville 1988), which makes it valuable for the magnitude estimation of pre-instrumental earthquakes. However, it is important to point out that the empirical relationships are not globally valid, but refer to the specific regions for which they were developed.

Another important magnitude is the Moment Magnitude ( $M_w$ ) introduced by Hanks and Kanamori (1979). This measure is not based on the decline of the amplitude over distance, but on the seismic moment ( $M_0$ ) and is defined as:

$$M_w = (\log M_0/1.5) - 6.07 \quad (\text{Eq. 2.1})$$

where  $M_0$  is defined as (Aki, 1966):

$$M_0 = \mu AD \quad (\text{Eq. 2.2})$$

where  $\mu$  is the shear-modulus (Pa) of the involved rocks,  $A$  is the rupture area ( $\text{m}^2$ ) and  $D$  is the average displacement (m) on the rupture area.

### 2.4.3 PRE-INSTRUMENTAL EARTHQUAKES

The region around the DSTF is rich on information of pre-instrumental earthquakes (Agnon 2014). These are spread over three main archives; the historical, geological and archaeological archive. The historical record in Israel reaches back about 2000 years and provides comprehensive information about the seismic history of the area (Ambraseys 1971). Numerous research studies and historical earthquake catalogs are based on this record (*e.g.* Ambraseys *et al.* 1994, Guidoboni *et al.* 1994, Karcz 2004, Ambraseys 2005, Guidoboni and Comastri 2005, Sbeinati *et al.* 2005). The geological archive forms the basis of paleoseismological investigations. Both on-fault effects (*e.g.* Reches and Hoexter 1981, Marco *et al.* 2003, Meghraoui *et al.* 2003, Daëron *et al.* 2005, Wechsler 2014) and off-fault effects (*e.g.* Marco *et al.* 1996, Shaked *et al.* 2004, Agnon *et al.* 2006) are the subject of the research. The archaeological archive includes archaeological sites that have potential seismogenic damage. Karcz *et al.* (1977) compiled a list of sites that show evidence of seismic activity along the DSTF. In numerous further studies potential seismogenic damage on archaeological sites was investigated (*e.g.* Marco *et al.* 1997, Ellenblum *et al.* 1998, Marco *et al.* 2003, Shaked *et al.* 2004, Thomas *et al.* 2007, Wechsler *et al.* 2009, Sbeinati *et al.* 2010, Ferry *et al.* 2011, Hinzen *et al.* 2016a).

With this wealth of information from interdisciplinary and independent research it was possible to compile earthquake catalogs for the last 2000 years (*e.g.* Garfunkel 1981, Ambraseys and Barazangi 1989, Ben-Menahem 1991, Klinger *et al.* 2000a, Migowski *et al.* 2004, Wdowinski *et al.* 2004, Marco *et al.* 2005, Marco and Klinger 2014, Ellenblum *et al.* 2015). *Table 2.2* summarizes studies of 31 on-fault earthquakes for the DSTF over the last 2000 years validated by interdisciplinary studies.

*Table 2.2: List of on-fault palaeoseismic investigations at the DSTF system arranged by year of publications (after Marco and Klinger 2014). Bold letters indicate earthquakes used to simulate ground motions in this study. \* unless indicated different all dates are Common Era (CE).*

#	Reference	Segment	Achievement Earthquake*/Slip Rate (SR)/ Last Event (LE)/ Recurrence (Re)
1	Reches and Hoexter (1981)	S. Jordan Valley	31 BCE, 747
2	Marco and Agnon (1995)	Dead Sea	Re
3	Amit <i>et al.</i> (1996, 1999, 2002)	S. Araba Valley	Re
<b>4</b>	<b>Marco <i>et al.</i> (1997, 2005); Ellenblum <i>et al.</i> (1998)</b>	<b>Jordan Gorge</b>	<b>1202, 1759</b>
5	Galli (1999)	Araba-Jordan-Hula Valley	
6	Enzel <i>et al.</i> (2000)	Dead Sea	Re
7	Klinger <i>et al.</i> (2000a)	N. Araba Valley	1212

**Region of Interest**

#	Reference	Segment	Achievement Earthquake*/Slip Rate (SR)/ Last Event (LE)/ Recurrence (Re)
8	Klinger <i>et al.</i> (2000b)	N. Araba Valley	SR
9	Niemi <i>et al.</i> (2001)	N. Araba Valley	SR
10	Zilberman <i>et al.</i> (2000)	Hula Valley	
11	Gomez <i>et al.</i> (2001, 2003)	Serghaya Fault	1705 or 1759
12	Meghraoui <i>et al.</i> (2003)	Misyaf, Yammouneh	
<b>13</b>	<b>Marco <i>et al.</i> (2003)</b>	<b>Sea of Galilee</b>	<b>749</b>
14	Daëron <i>et al.</i> (2004, 2005, 2007)	South Yammouneh	1202
15	Zilberman <i>et al.</i> (2005)	S. Abara Valley	3/1068/
<b>16</b>	<b>Marco <i>et al.</i> (2005)</b>	<b>Jordan Gorge</b>	<b>1202, 1759/LE/SR</b>
17	Chorowicz <i>et al.</i> (2005)	Yammouneh	SE
18	Akyuz <i>et al.</i> (2006)	Northern Yammouneh	859, 1408, 1872
19	Nemer and Meghraoui (2006)	Roum Fault	1837, SR
20	Haynes <i>et al.</i> (2006)	N. Araba Valley	634 or 659/660, 873, 1068 and 1546
21	Elias <i>et al.</i> (2007)	Lebanon thrust	551
22	Thomas <i>et al.</i> (2007)	Aqaba	
23	Ferry <i>et al.</i> (2007)	Jordan Valley	SR
24	Le Beon <i>et al.</i> (2008)	Araba Valley	
<b>25</b>	<b>Nemer <i>et al.</i> (2008)</b>	<b>Rachaya and Serghaya faults</b>	<b>1759</b>
26	Makovsky <i>et al.</i> (2008)	Elat Fault	SR
27	Altunel <i>et al.</i> (2009)	S. Turkey	SR
28	Le Beon <i>et al.</i> (2010)	Araba Valley	SR
29	Karabacak <i>et al.</i> (2010)	Northern Yammouneh	SR
30	Ferry <i>et al.</i> (2011)	Jordan Valley	SR, Re, LE
31	Le Beon <i>et al.</i> (2012)	Araba Valley	SR

Table 2.3 continued.

### 2.4.4 INSTRUMENTAL EARTHQUAKES

The area of instrumental observation of the Levante began in 1898 with the installation of the first seismological station (Helwan HLW) in Cairo, Egypt. Until 1912 it was the station located closest to the study area. More remote stations were located in Istanbul and Athens. In 1912 the Observatory of Ksara started service in central-east Lebanon. The first station in Israel started operating in 1953, located at the Hebrew University of Jerusalem (JER) (Hofstetter *et al.* 2014). Over the time the number of operating stations increased. In 1983 two large seismic networks have been installed in the area. The Jordan Seismological Observatory (JSO) and the Israel Seismic Network (ISN) monitor the seismicity of the DSTF. Originally both networks contained 35 short period stations. In the course of time the networks have been updated and upgraded by several three component broadband seismometers and accelerometers. Additionally, temporary networks, operating 1-2 years, gathered additional important seismic information (Hofstetter *et al.* 2014).

In 2000 the catalogs of the large networks have been merged to one Dead Sea Transform catalog, which is continuously updated. It lists 6821 earthquakes above 2.0 in the years from 1900 to 2015 (<http://seis.gii.co.il/>, last accessed 09.2015). The seismicity along the DSTF is not equally distributed (*Figure 2.6*). Five spatial clusters can be distinguished; the first most northern cluster is located at the Hula Basin, the second at the Jordan Valley. The third cluster is located at the Dead Sea and has a wider spread of the epicenters. In the fourth cluster in the Araba Valley the epicenters are closer to the DSTF. The fifth, largest cluster is in the area of the Gulf of Aquaba in southern Israel and shows a wide distribution of earthquake activity. The strongest instrumentally recorded earthquake in 1995 occurred near Nuweiba (Baer *et al.* 1999, Klinger *et al.* 1999, Shamir *et al.* 2003) with  $M_w$  7.2 (*Figure 2.6*). The second strongest earthquake with  $M_s$  6.2 in 1927 has been located on the western shore of the Dead Sea (Shapira and Hofstetter 1993, Anvi *et al.* 2002, Zohar and Marco 2012, Hofstetter *et al.* 2014). In 1956 a  $M_s$  5.1 event occurred north the Sea of Galilee at the Mediterranean coastline near Beirut (Nemer and Meghraoui 2006).

## Region of Interest

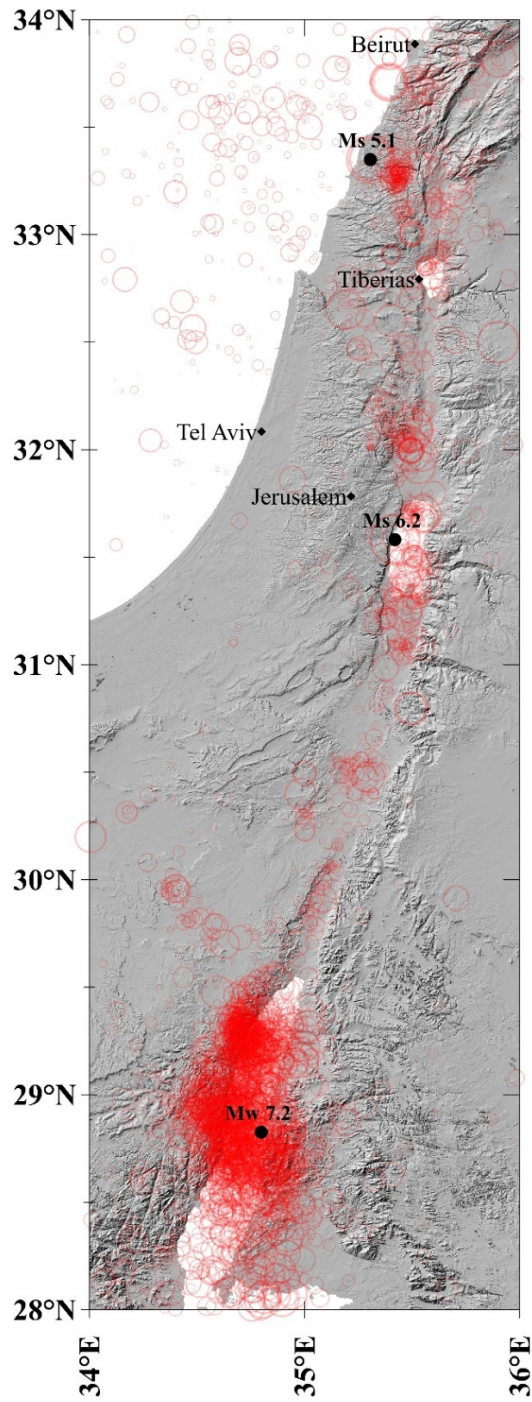


Figure 2.6: Seismicity of Israel and surrounding areas from 1900 to 2015 (<http://seis.gii.co.il/> last accessed 09.2015); the diameter of the red circles scales with the magnitude of the earthquakes. The solid black circles show the epicenters of the three strongest instrumentally recorded earthquakes:  $M_w$  7.2 Nuweiba 1996;  $M_s$  6.2 Jericho 1927;  $M_s$  5.1 Chim 1956.

### 3 LASER SCANNING

This chapter first gives a brief introduction to the laser scanning technology and how it is applied in archaeoseismological research. Afterwards the basic concepts of the post-processing workflow are introduced. Detailed information about the individual surveys for each site are presented in the according chapters.

LASER is an acronym and stands for **L**ight **A**mplification by the **S**timulated **E**mission of **R**adiation (Gould 1959) (in the following denoted as laser). The basic development was in the 1960, among others by Maiman (1960), who built the first functioning laser. The technique gained popularity and today lasers are ubiquitous not only in science, but also in medicine, industry and society. A laser is basically based on: a medium/amplifier and two resonators (a reflective mirror and a semi-reflective mirror) (Siegman 1986). The medium/amplifier is placed between the resonator and is excited, this process is called pumping (Siegman 1986). The atoms of the medium are pushed into a higher energy-level. When the atoms drop back into a lower energy level photons are emitted. The released photons oscillate between the resonators and are amplified in the medium, until the beam is released (Siegman 1986). A laser beam has specific physical properties: it is a polarized, spatially and temporally coherent light, directional and due to its defined frequency monochromatic (Siegman 1986). These properties allow accurate distance determination using laser technology.

Laser scanning is a surveying method where three-dimensional (3D) coordinates of a target's surface are recorded. It is a non-destructive, reflector- and contactless method. Unlike other conventional surveying methods (*e.g.* point and shoot techniques) the result of a laser scan is a 3D cloud of discrete points (also called point cloud) and not a single discrete point (Bryan 2004). The main difference between both methods is, that point and shoot surveys measure less, but carefully chosen points. The approach with 3D laser scanners is fundamentally different, where with each scan a large number of points is surveyed. The instrument systematically scans the target's surface; however, which points are hit by the laser-beam is somewhat arbitrary. If necessary, several separate scans of a target can be made from different perspectives. Through common reference points in the different scans, they can be combined to one large point cloud (this process is called *registration*). If there are additionally georeferenced points in the scans, the entire point cloud can be georeferenced.

The *iterative closest point* (ICP) algorithm is often used to register two point clouds based on the geometry of two clouds. Its main use is to register the output of two 3D laser scans against each other (Rusinkiewicz and Levoy 2001). The algorithm is based on four basic steps:

- (1) Estimation of the transform parameter
- (2) Transform of the point cloud
- (3) Calculate the root mean square (RMS) of the residual distances
- (4) Compare RMS with the previous one

These steps are iterated until an exit-criterion is matched. This can be for example a certain number of iterations or a threshold for the difference between the RMS of the previous and current cycle. The RMS of the last iteration is a measure of the quality of the fit. For the optimal result, preceding to the iteration the point clouds must be initially aligned. For the initial alignment different methods are available, for example by using corresponding reference points (as shown above) or user input, manually aligning (Rusinkiewicz and Levoy 2001).

In archaeoseismology 3D laser scanning is meanwhile an established method. Its application in archaeoseismological research has been introduced by numerous authors (*e.g.* Schreiber *et al.* 2009, 2010, Fleischer *et al.* 2010, Schreiber and Hinzen 2010, Hinzen *et al.* 2012). The non-invasive method allows rapid and precisely surveys of archaeological structures. The resulting 3D models enable exact measurement of distances, areas, angles and volumes with slight effort. Schreiber *et al.* (2012) showed the benefits of laser scanning survey of sites even during ongoing archaeological excavation. The resulting scans are a valuable source of information in archaeoseismological research, not only as foundation for reconstruction and documentation of damage, but also as a template for comparison of research results (*cf.* *Figure 1.2*).

Different types of laser scanners are based on different methods for distance determination. For archaeoseismological research two distance measuring methods are most relevant, time of flight (ToF) and phase difference. ToF scanners estimate the distance by measuring the travel time of a short pulse of laser light from the scanner to the target and back. This kind of instruments can cover large distances in order of kilometers. However, the huge measuring range comes at the cost of measuring speed. The scanner has a latency for each point to receive the pulse back. So called phase scanner use a modulated laser beam and determine the phase difference of the outgoing and incoming beam, which serves as precise measure of the distance. In comparison to the ToF scanner, phase scanners have only a measuring range of hundreds of meters. The acquisition speed is significantly higher than that achieved with ToF scanners. Both methods are used in archaeoseismology, the special needs of any survey determine which type of scanner to use (Yerli *et al.* 2010, Hinzen *et al.* 2013a).

The basic workflow from a survey to a finished point cloud can be separated into two parts: first the survey, where a structure is scanned onsite, second the so called post-processing, where the measured point clouds are digitally processed.

To survey a structure completely it is important to avoid shadowing effects (*Figure 3.1*). Each part of the object that is not hit by the laser beam will result in a gap in the point cloud. Before scanning a structure, it is important to prepare the site and plan the scanner positions. In archaeoseismological applications often the first step is to clean the scanning area mainly from vegetation between the scanner and the object to ensure an unhindered view particularly to the base of the structure, so that the connection of the structure to the ground is clearly visible in the scan.

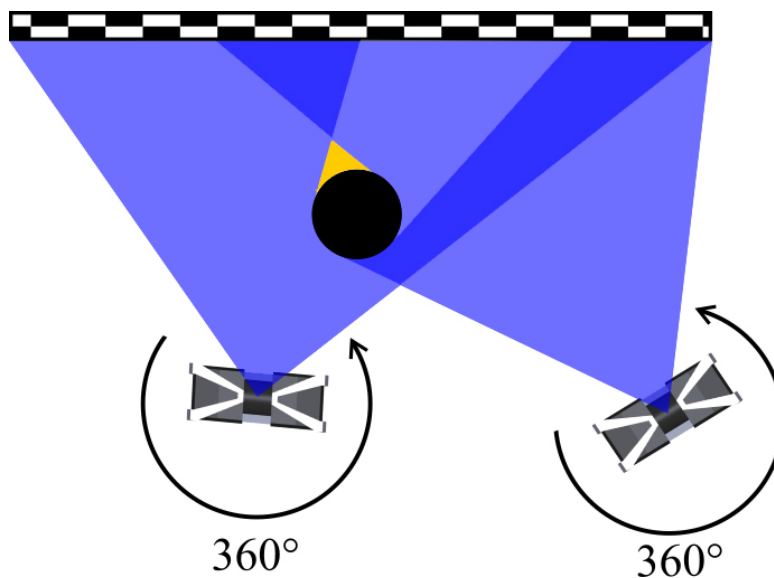


*Figure 3.1: Schematic representation of laser scanning positions and shadowing effects. The wall with the checkerboard pattern is the scan target. The solid black circle represents an object blocking the view to the wall. The blue areas indicate only the view from each the scanner position to the wall, but the scanner actually survey 360° of the surrounding. The heavy blue areas are covered from both scanner positions. The yellow highlighted area behind the black circle is a blind spot that will result in a data gap.*

The only shadowed area in the example of *Figure 3.1* is behind the round object blocking the clear view to the wall. In order to register scans from different positions, reference objects must either be placed between the view blocking object and the scanner or in the multiply covered sections (*Figure 3.1*). It is important to keep in mind that the shadowing effect also applies in the vertical direction. In optimal scenarios it is possible to also include laser scans from an elevated position or the top of the structure.

However, this turns out to be difficult most of the times and the resulting 3D point cloud shows walls with data gaps on the top. Unwanted items at the sites that cannot be removed, as fences, trees and such can be removed digitally.

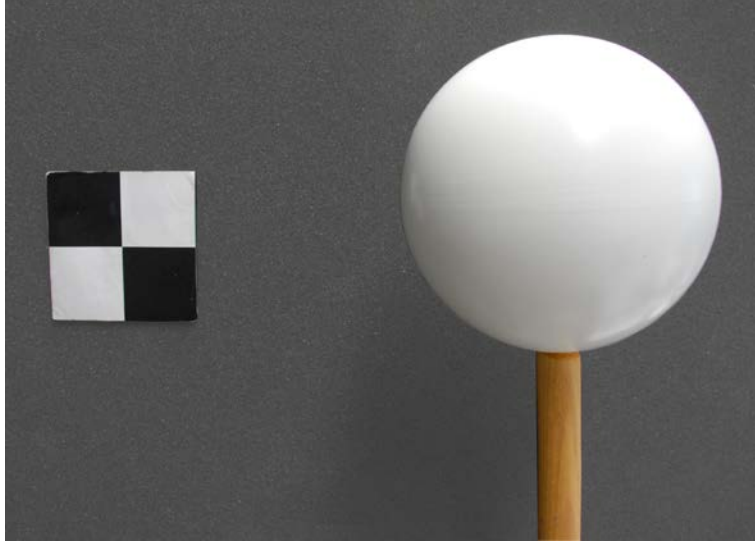


Figure 3.2: Example reference objects used in laser scanning to combine individual scans. Left: Checkerboard with an edge length of 10 cm. Right: White sphere with 25 cm diameter mounted on a support.

To register individual laser scans during post-processing to one point cloud neighboring scans must share at least three reference points; however, in practice usually much more points are used. Based on the reference points the separate point clouds of the scans are aligned in such a way that the reference points match. If the according reference points for all scans are brought together, a combined point cloud is the result. Figure 5.3 and Figure 6.4 (a) show the relative locations between the scanner positions for the two sites of this work. For these surveys a Faro Focus<sup>3D</sup>, a small size phase scanner was chosen. This scanner model has additional built in functions as an electronic compass, an altimeter and an electronic level. The metadata from these sensors are saved in the scans points and can be useful during post-processing *e.g.* for registering (Hinzen *et al.* 2013b). As reference points spheres with a diameter of 0.25 m and checkerboards with an edge length of 0.1 m were used (Figure 3.2). While 2D checkerboards allow the straight forward determination of a target point, the 3D spheres offer the advantage of a clear view from all directions. In an additional survey numerous scans were carried out in corporation with the Technion Israel Institute of Technology Haifa with a Leica P 16, a ToF laser scanner (Hinzen *et al.* 2017). In this survey reflectors placed in a special pattern were used as reference objects. The resulting 3D point clouds are vital for both, an accurate model development process and the comparison and if necessary as reference for the results of the calculated simulation. Details and the results of the laser scanning surveys of the two case sites are presented in the according sections.

To register individual laser scans during post-processing to one point cloud neighboring scans must share at least three reference points; however, in practice usually much more points are used. Based on the reference points the separate point clouds of the scans are aligned in such a way that the reference points match. If the according reference points for all scans are brought together, a combined point cloud is the result. Figure 5.3 and Figure 6.4 (a) show the relative locations between the scanner positions for the two sites of

## 4 COMPUTER MODELS

In this chapter the use of computer models is presented. After a brief historical context, basic terms are defined that are important for this work. This is followed by the introduction of the method which is the foundation of the models developed in the course of this work. Key concepts for the simulations are explained. Lastly each software solution that was used in this work is introduced and described how the concepts are implemented.

In the 1960s the evolving transistor technique ignited the success story of computer systems. This pioneered the path to the field of computer simulations in scientific research. Since then the usage of computer models in science is tightly connected to the evolution of computer system. First simulations were run on large mainframe computers. Since these large computer systems were expensive and maintenance intensive, it was common that several research groups shared a mainframe. The consequence was that each group only had a limited time access for simulations. The popularity of the personal computer with more and more increasing computation power in the 1980s further allowed scientists to advance in the field of computer simulations.

A *computer based model* (short: computer model or just model) is a digital representation of a system whose behavior should be simulated. A *computer simulation* (short: simulation) is the calculation of the behavior using the model, also called running a model. The *model time* is the time that is simulated. The *simulation time* is the time the calculation lasts until the *model time* is reached. The *time step* of a simulation is the time needed by the simulation for one computational step. A *step* is the process of calculating the systems next state.

A model, digital or analog, is always a simplification of the natural system. It is addressing a problem in the system. It is important to identify the essential components to describe the problem as accurate as possible, without adding unnecessary complexity. Each layer of complexity is a potential source for errors and increases the requirements for hardware and software.

Computer models allow scientists to simulate the behavior of complex systems that could hardly be examined with analog models. Additionally, simulations can be easily reproduced, or rerun with different boundary conditions. However, the results of computer simulations must be handled with care. It is essential to make sure that results of the simulation are correct. Therefore, it is important that the underlying software code used for the simulation is verified to calculate accurate results (*cf. 4.2 Model Verification*).

### 4.1 Discrete Element Method

Computer models can be categorized in different ways. This work focuses on models based on the discrete (also distinct) element method (DEM). The DEM is a numerical approach to simulate the mechanical behavior of discontinuous systems. The basic assumption is that each element of a model is an independent body in the system. It was established by Cundall (1988) to address molecular dynamic and rock mechanical problems. Models based on the DEM-concept can be composed of elements of arbitrary shape and size. After Cundall and Hart (1992) the term *discrete element* only applies to software or model that meet two requirements:

1. allows finite displacement and rotations of discrete bodies, including complete detachment;
2. recognizes new contacts automatically as the calculation progresses.

Different software solutions allow DEM simulations. For this work three different software solutions were tested for their application in archaeoseismological research.

### 4.2 Model Verification

To validate the results of the simulations the returned values must be verified. There are two common verification approaches. The first is to compare the results of a simulation with an analytical solution of a known problem. Motivated by slender vertically oriented objects, which did not fall during the great 1960 Chile earthquake Housner (1963) carried out an analysis of rocking motion of structures, which resemble an inverted pendulum. In his work he provides an analytical solution of the equation of motion of a rocking block.

*Figure 4.1 (a)* shows the geometry of a rocking block where the corners  $O$  and  $O'$  are the centers of rotation. The block properties are the height  $h$ , the width  $b$  and the weight  $W$ . The location of center of gravity  $cg$  is the distance  $h/2$  above the base and half the width  $b/2$  from the block's side.

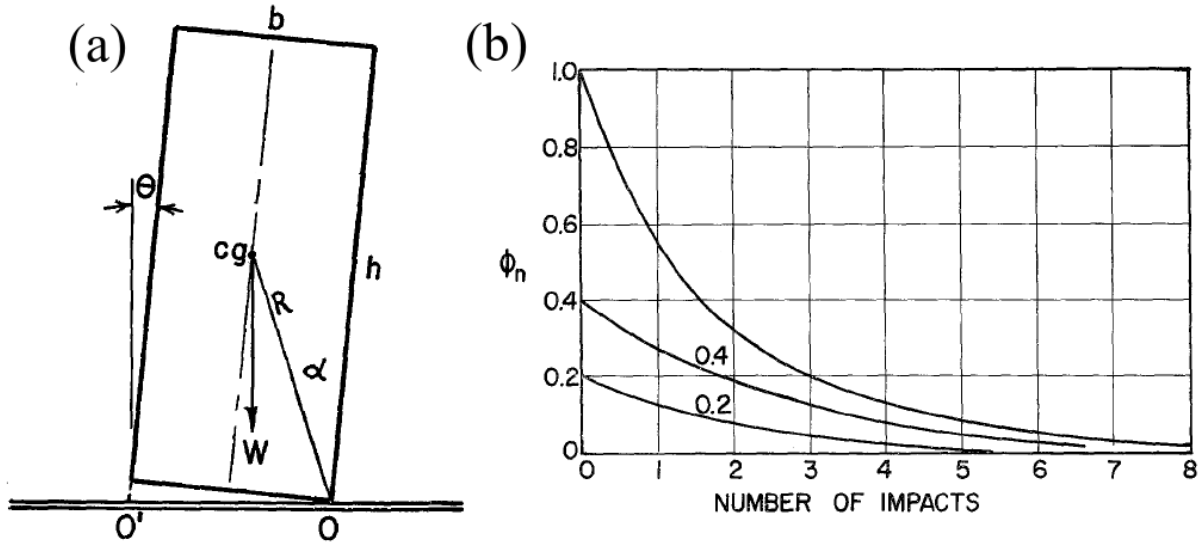


Figure 4.1: (a) Geometry of a rocking block. (b) Amplitude  $\Phi_n$  subsequent to  $n$ -th impact (after Housner 1963).

For this solution the longer edge of the block is always pointing up ( $h > b$ ). The radial distance from the center of rotation to  $cg$  is  $R = \sqrt{(h/2)^2 + (b/2)^2}$ . The angle between  $R$  and the block side is  $\alpha$ .  $\theta$  is the tilting angle of the block from the vertical (Housner 1963).  $\Phi = \theta/\alpha$  is the ratio between the angles. For  $\Phi = 1.0$  the block is in a tilted resting position and  $cg$  sits vertically above the rotation point: if  $\Phi > 1.0$  the block will tip over.

In the verification experiment to test the DEM software codes, the angle of deflection  $\theta$  is the changing boundary condition. The block is rotated by different  $\theta$  over a rotation point and then released. In a rocking motion the block will rock alternately at the rotation points  $O$  and  $O'$ . During rocking kinetic energy dissipates at each impact of the base of the block on the surface. Figure 4.1 (b) shows the calculated decay of amplitude against the number of consecutive impacts (Housner 1963). The larger the initial angle of deflection is the more impacts are necessary for the block to come to rest. The rocking period, as function of the angle, also decreases during the rocking process.

The other more elaborate approach to verify the software code is to run analog experiments. Afterwards, the same experiment is simulated with the software code. The results of the experiment and the simulation are compared to verify the simulation. The setup of the analog experiments can be relatively simple, such as the rocking block, described above (Hinzen 2009a). But they can also become very complex as described in the Introduction (Chapter 1).

Each of the three software codes used in this work has been verified by comparing simulated results either with Housner's analytical solution, measured values from analog experiments or both. These results are described in the according subsections in Software solutions (Chapter 4.7).

### 4.3 Collision detection

To analyze the dynamic behavior of multi-element systems in numerical computer models, the interaction of elements is an important part of the simulation. Therefore, it is crucial to correctly estimate the collision between elements. When two elements collide a new contact is created. The resulting forces acting on the involved elements must be calculated and included in the equations of motion (3DEC Manual 2016). The contact estimation for arbitrary complex shaped objects with many degrees of freedom is not trivial.

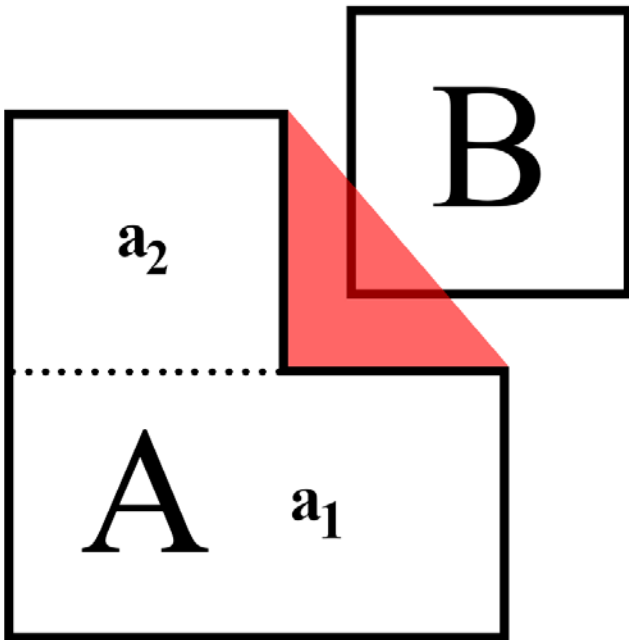


*Figure 4.2: Schematic representation of a concave block A with an colliding block B. In the red highlighted area detection collision is not possible in most software codes. The dotted line in block A marks a possible separation line to split the concave block into two convex blocks (a1 and a2).*

Concave objects are problematic for contact detection algorithms. *Figure 4.2* shows a schematic sketch of a two dimensional "L"-shaped block A and a block B in close proximity. The problematic area is highlighted in red. It is hardly distinguishable by geometric methods, whether block B touches block A or not (3DEC Manual 2016).

A common solution for this kind of problem is to separate the concave object into several convex shaped objects. These sub-objects are treated in the software code as one unit. The number of separations needed depends on the complexity of the concave blocks; in the example shown in *Figure 4.2* it would only be on a separation into two sub-objects. This procedure increases the total number of

convex objects in the model, which increases the calculation time. When forces are applied to one of the sub-objects, the forces are accordingly transferred to all combined elements (3DEC Manual 2016).

The automatic contact estimation in numerical simulations is computational intensive. In a first step the shape and relative position of both potentially colliding objects must be recognized correctly. Based on the object's shape the correct calculation steps must be estimated and executed. These calculation steps can get extremely complex. This procedure must be executed again for each potential contact scenario in the model (3DEC Manual 2016). Detailed information how the used software implement collision detection is given in the according sections in Software Solutions (Chapter 4.7).

## 4.4 Units

The software solutions do not dictate a unit system for a model, in principal imperial or metric systems both can be used. However, it is crucial to stay consistent within the units of one system and the factors of the units. *E.g.* when the length is given in *cm*, the velocity has to be *cm/s* and not *m/s*. *Table 4.1* lists measures for different unit systems and the according factors that can be used.

*Table 4.1: Units for important measures for different unit systems and factors. Highlighted units are used for in this work (after 3DEC Manual 2016).*

Measure	Metric System				Imperial System	
Time	<b>s</b>	S	s	s	s	s
Length	<b>m</b>	M	m	<i>cm</i>	<i>ft</i>	<i>in</i>
Velocity	<b>m/s</b>	m/s	m/s	<i>cm/s</i>	<i>ft/s</i>	<i>in/s</i>
Acceleration	<b>m/s<sup>2</sup></b>	m/s <sup>2</sup>	m/s <sup>2</sup>	<i>cm/s<sup>2</sup></i>	<i>ft/s<sup>2</sup></i>	<i>in/s<sup>2</sup></i>
Density	<b>kg/m<sup>3</sup></b>	10 <sup>3</sup> kg/m <sup>3</sup>	10 <sup>6</sup> kg/m <sup>3</sup>	10 <sup>6</sup> g/cm <sup>3</sup>	<i>slugs/ft<sup>3</sup></i>	<i>snails/in<sup>3</sup></i>
Force	<b>N</b>	<i>kN</i>	<i>MN</i>	<i>Mdynes</i>	<i>lb<sub>f</sub></i>	<i>lb<sub>f</sub></i>
Pressure/Stress	<b>Pa</b>	<i>kPa</i>	<i>MPa</i>	<i>bar</i>	<i>lib<sub>f</sub>/ft<sup>2</sup></i>	<i>psi</i>

There are multiple reasons to choose different unit systems. The first most obvious reason is a cultural background. An engineer in northern America will probably use the imperial system and an engineer in Europe will use the metric system. The scaling of units with factors is often done for convenience. For example, is it more pleasant working in small scaled models with *cm* and not *m*. Another more historic reason is to keep the values for the measures in a reasonable size. The program is very likely to fail if the values exceed the variable limits of the computer system (3DEC Manual 2016). However, this problem mostly relates to older computer systems and with modern 64bit computer this problem becomes less relevant. All models in this work are based on the metric system (*Table 4.1*).

### 4.5 Damping

Natural systems always contain some degree of damping, otherwise the system would oscillate permanent. Energy in a DEM model dissipates from the system by sliding, internal friction, collision or any kind of resistance elements encounter by enclosing materials like fluids and even air (3DEC Manual 2016). By applying correct damping, the system reaches over time the state of static equilibrium. Therefore, damping is an important part of computer simulations. The software codes used in this work implemented the damping in different ways, which is described in the according subsections.

### 4.6 Discrete Fracture Network

Fractures, faults and joints are natural features of rock masses. With different approaches fractured rock masses can be realized in DEM software codes: Cutting real fractures; during geologic mapping the location, dip and dip direction of the features are measured *in situ*. They can be reproduced in DEM models based on these measured values (3DEC Manual 2016). However, with a large number of unique faults with different orientations this approach will get labor intensive.

An alternative to the deterministic approach are stochastic methods to create fracture systems in a rock mass. One approach is to create a set of fractures based on statistical parameters describing orientation and number. The created fractures are not unique and will not reflect the real individual joints, as they do in the deterministic approach. Another statistical approach is the Discrete Fracture Network (DFN). DFNs have been initially developed in the 1970s for hydrogeological flow simulations in complex fractured rock masses. The fractures in a DFN are characterized by a stochastic description (3DEC Manual 2016) and the size, orientation and position of the fractures is unique. Therefore, they are a helpful tool to randomly separate a rock mass with fractures in a DE model.

### 4.7 Software solutions

In the course of this work three software codes were used and tested for different models. It turned out that none of the tested software code is perfectly suitable to address all archaeoseismological problems. So it is important to know advantages and disadvantages of the software codes for the application to specific problems.

### 4.7.1 UNIVERSAL MECHANISM

Universal Mechanism (UM) is a commercial software solution developed by the Laboratory of Computational Mechanics (Data and Resources). Its main focus lies on Multi Body Systems (MBS) mostly used for practical mechanical engineering problems including the kinematics and dynamics of railways or load analysis of trucks (*Figure 4.3*). The software resolves all requirements for the DEM. It is



*Figure 4.3: Examples of UM applications (from <http://www.universalmechanism.com> last accessed 02.2018).*

composed of two main programs called *UM Input* and *UM Simulation*. *UM Input* is used to describe the objects of the MBS, generating the equations of motion and compilation of equations by an external compiler. It is the part of the software where the model is created and all parameters are set. The program *UM Simulation* runs the actual simulation of

the model offering a wide range of equation solver and full control of the solving parameters. Depending on the solver, it is also possible that the time-step is adjusted during the simulation (UM Manual 2016). UM was developed to model mechanical problems. This is reflected in a wealth of built-in functions to apply boundary-conditions and monitor the model. It is convenient to track only specific parts or the entire model. Additionally, a wide range of functions and tools are available to analyze the results of a simulation inside UM without the need of third party software.

The software code was successful tested and used in archaeoseismological research and the simulation of seismoscopes (Hinzen 2009a, 2009b, Hinzen and Kovalev 2010, Hinzen *et al.* 2010, Hinzen *et al.* 2013a and Hinzen *et al.* 2014a). A useful feature for archaeoseismological applications is offered by so called scanning projects in which numerous simulations can easily be repeated with different boundary conditions.

However, if the number of interacting objects comprising the model increases, the simulation time is increasing drastically as well. Combined with the current lack of multi-processor support or Graphical Processor Unit (GPU) usage the calculation time exceeds practical limits for too complex models.

### 4.7.1.1 VERIFICATION

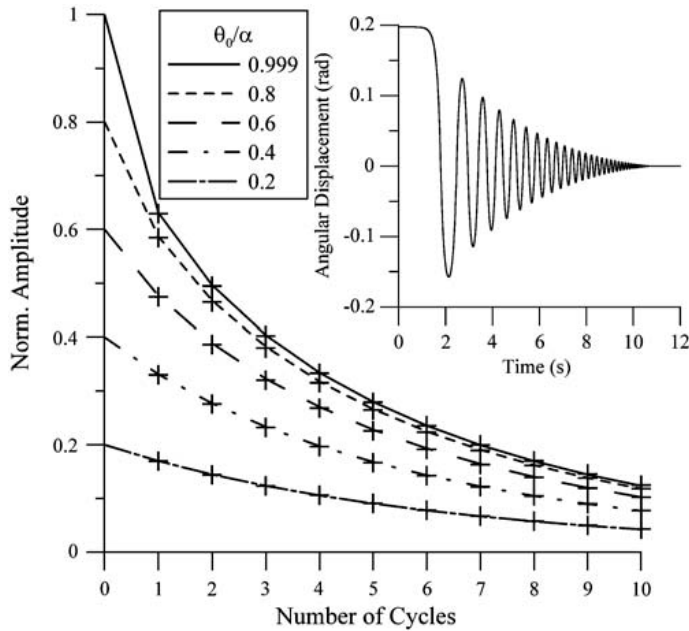


Figure 4.4: Lines show the decreases of the normalized rocking angle of a pure rocking motion of a slender block for different starting positions,  $\theta_0$ , with progressing number of cycles (after Housner 1963). The crosses show the amplitudes from corresponding experiments with the numeric model realized in UM. The inset in the upper right corner shows the time series of the angular displacement for the  $\phi_0/\alpha =$  ratio of 0.999 (Hinzen 2009a).

Hinzen (2009a) simulated the behavior of toppling columns with UM. In his work UM was verified by comparing the simulated decline of amplitude of a rocking block with the analytical formulation of Housner (1963). Figure 4.4 summarizes the results of five simulations with different rotation angle ( $\theta_0$ ) and the according analytical results. It is evident that both results are in good agreement with another.

### 4.7.1.2 COLLISION DETECTION

UM offers different approaches for collision detection. One approach is to manually set the contact forces between the objects in the model (UM Manual 2016). This mainly applies for simple models or models with clear contact relations between the bodies. It is mandatory to know which elements of the model will interact with each other before the simulation starts. UM

offers different kinds of contact types, the default type is a point-to-plane contact. Other contacts types are sphere-to-plane, circle-to-plane, sphere-to-sphere and sphere-to-z-surface (UM Manual 2016). During the simulation, only the previously defined contact forces are taken into account. Figure 4.5 shows an example of a simple model with two pilasters resting on the ground. With the assumption that the pilasters interact exclusively with the ground and not with each other during the simulations, only the contacts between each pilaster and the ground have to be pre-defined. The interaction between the pilasters will be ignored in the simulations. But to consider these interactions in the model, the contacts between the pilasters must additionally be set. This approach is effective as long as not too many elements (potentially) interact with each other. In models with complex geometries and unforeseen interactions between numerous bodies it is a tedious and error-prone task to pre-set all potential contacts by hand.

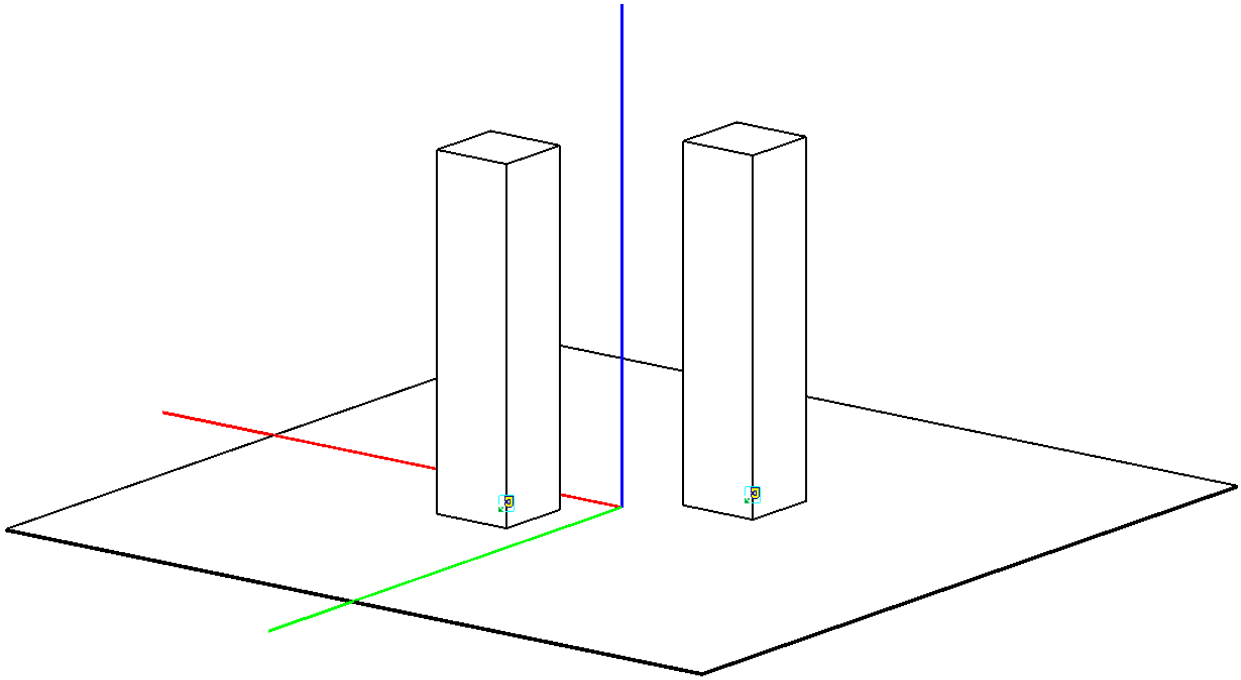


*Figure 4.5: A simple two pilaster model in UM. Both pilasters are resting on a ground plate. The joints between the pilasters and the base plate are marked with “J”-symbols. The axis of the base system are shown green, red and blue.*

UM can also automatically detect collision and calculate the appropriate contact forces using the *UM 3D Contact* module (UM Manual 2016). The implementation of which was actually triggered by the needs when first archaeoseismic models were realized with UM. The detection is done in two general steps, the so called far-field and near-field collision detection. The near-field detection is based on a three dimensional clipping algorithm by Cyrus and Beck (1978). This step is computational intensive and time-consuming. With each object added to the model the search time increases quadratically. To reduce the number of near-field detections the preceding step is the far-field collision detection. In this step imaginary spheres are wrapped around the objects and checked for intersections. Only objects with intersecting spheres are selected for the near-field collision detection. When two objects collide the contact forces are determined. For each contact point of an object the according contact point of the colliding object is obtained and the contact force is calculated (UM Manual 2016).

### 4.7.1.3 DAMPING

In UM damping coefficient  $\nu$  for 3D contacts is defined by the partial frequency  $k$  and the damping ratio  $\beta$  for each pair of bodies as follows:

$$\nu = 2\beta\sqrt{cm} \quad (\text{Eq. 4.1})$$

where the contact stiffness  $c$  is:

$$c = 4\pi^2 k^2 m \quad (\text{Eq. 4.2})$$

and  $m$  is the mass of the smaller body (UM Manual 2016).

### 4.7.2 UNITY 3D

Unity 3D (in the following referred as Unity) is a commercial game development platform based on the PhysX engine (Data and Resources). The PhysX engine is powerful and fulfills all requirements for DEM calculations. The biggest difference between Unity and the other software codes used in this work, is the object-orientated programming concept. Each element of the model is an object with its own functions and variables. Custom functionality can be added in Unity with the programming language C#. Simple geometries can be created inside Unity. Extensions can enhance the modelling capabilities, such as Archimatix (<http://archimatix.com/>, last accessed 05.2018) that is focused on creating node-based parametric models. For other complex geometries 3rd party software such as Blender (Data and Resources) is used for modelling. When the basic geometry is created all objects need to be prepared for simulation. To apply correct physical properties to all elements a so called rigid body element is applied. For contact estimation numerous collider types are available, in this work mesh collider are applied to each element. As game development software Unity was never intended to be used for numerical simulations. Therefore, custom C# functions must be written in order to apply boundary conditions such as ground motion to the model. Unity supports multiple processors and additionally computations are done on the GPU which allows simulation speeds of moderate size models in close to real-time (Unity Manual 2017). Although Unity is a very powerful tool, it is not suitable for all kinds of archaeoseismological research. The focus on gaming and speed results in a lack of physical settings and there is no support for rock mechanical properties. For the same reason there is also no monitoring for the response of the discrete elements of the model provided and must be custom written.

### 4.7.2.1 VERIFICATION

Unity is not yet widely used in archaeoseismology. A first study introduced a tool based on Unity to investigate the dynamic behavior of medieval architectural structures to ground motion (<https://www.sas.upenn.edu/ancient/masons/abstracts/Agudo/R-ONeill.html>, last accessed 05.2018). This work was the origin of the Archimatix extension. Furthermore, Hinzen and Montabert (2017) analyzed the response of different wall types to ground motion. To verify Unity, they compared the simulated values with the analytical solution of Housner (1963) for the tipping block.

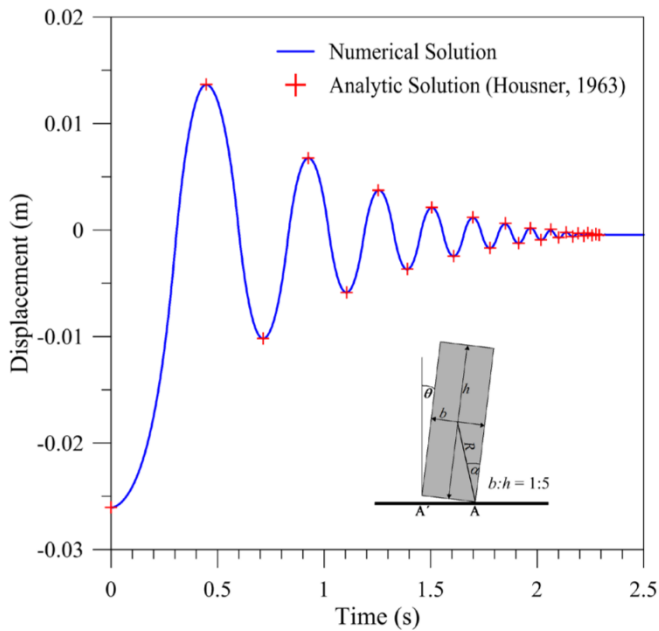


Figure 4.6: Verification tests for the PhysX engine. On the left the blue line shows the horizontal displacement of the center of gravity of a rectangular block rocking over the rotation points A and A' (O and O' in Figure 4.1) with a height to width ratio of 5 as indicated in the insert. The red crosses give the amplitudes predicted by analytic solution of Housner (1963) (after Hinzen and Montabert 2017).

Figure 4.6 shows the comparison between the simulation and the analytical solution. Different time-steps for the simulation have been tested and for a time-step of 0.001 s the results are in good agreement with the analytical solution.

### 4.7.2.2 COLLISION DETECTION

In Unity colliders are used for collision detection, which is a more object orientated approach compared to the other presented solutions. A collider is assigned to each object and when a contact occurs the collider of the objects recognize the collision and the appropriate physical law is applied (Unity Manual 2017). Compared to the above described methods this seems simple. But it is worth to mention that this method cannot be applied in most software codes by design. The software code must follow the object-orientated programming style and not be process orientated.

### 4.7.2.3 DAMPING

As a gaming engine Unity does not distinguish between static and dynamic problems. The damping depends on different parameters. The friction follows a Mohr-Coulomb friction model. During collision the energy dissipation is defined by a coefficient of restitution (Unity Manual 2017).

### 4.7.3 3 DIMENSIONAL DISTINCT ELEMENT CODE

3 Dimensional Distinct Element Code in short 3DEC (Cundall 1988, Hart *et al.* 1988) is a commercial software code developed by Itasca (Data and Resources). It is based on the 2D formulation for DEM modeling Universal Distinct Element Code (UDEC). 3DEC and UDEC are numerical software codes based on the DEM concept. The included FISH scripting language allows creating versatile and custom build solutions. 3DEC has been introduced for three-dimensional simulations of advanced geotechnical and civil engineering problems including the simulation of discontinuous rock masses, rock mechanical engineering and ground water flow. Its application range goes from slope stability of open pit mines, dynamic analysis of dams (Lemos *et al.* 2006) and examining tunnels (Konietzky *et al.* 2004), examples of which are shown in *Figure 4.7*.

3DEC was used in numerous archaeoseismological studies of the dynamic behavior of complex structures. Psycharis *et al.* (2003) provided a numerical study investigating the dynamic behavior of a proposed restoration of the Parthenon Pronaos in Greece. Oliveira *et al.* (2012) investigated the seismic safety of the Roman temple of Evora. The discrete element model was calibrated with accelerometer measurements of the dynamic properties of the existing temple. Alexandris *et al.* (2004) investigated the collapse mechanisms of traditional Cypriot architecture. In the study UDEC was used for the 2D and 3DEC for the 3D analysis. Lemos *et al.* (2015) analyzed the non-linear behavior of the obelisk in Lorca during the earthquake on the 11th May 2011.

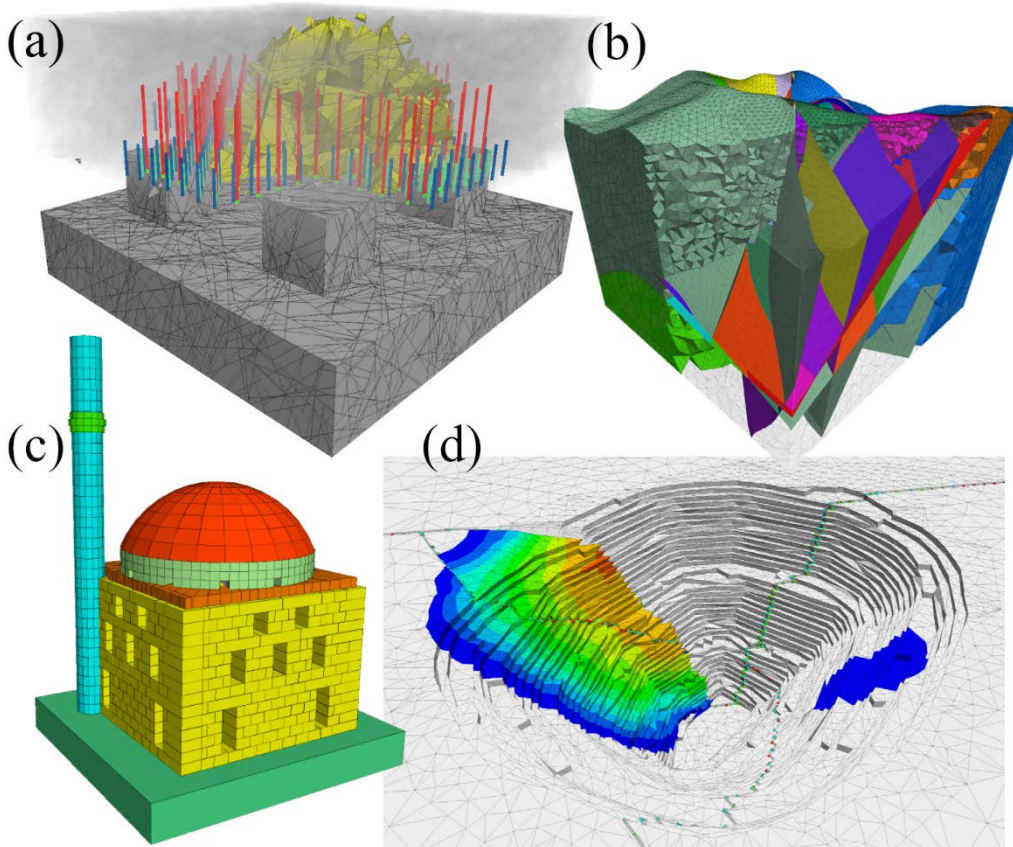


Figure 4.7: Example application of 3DEC. (a) Pillars in jointed rock with rockbolts supporting the span in between. The yellow material is ground between the pillars that has mobilized. (b) Cut-away view of a geological model defined by nine intersecting faults. (c) A scale model of the 15th century Mustafa Pasha Mosque in Skopje, which underwent a comprehensive shake table program, is modeled by the discrete element approach (Cakti et al. 2016). (d) Large open-pit mine intersected by three major faults showing slope movement on the west wall. (modified from <https://www.itascacg.com/sites/itascacg.com/files/ICG16-BRO-3DEC-520-01.pdf>, last accessed 10.2018)

3DEC is an explicit time-stepping algorithm. The dynamic response is calculated for each time-step. The size of the time-step is estimated by the mass of the blocks, stiffness and damping at the joints (Papantonopoulos *et al.* 2002). During one time-step acceleration and velocity of the elements are constant.

The discontinuous medium is separated into polyhedral blocks by joints or contacts. In 3DEC blocks can either be rigid or deformable. In each step of the calculation the forces and motion of the blocks are estimated. Analytic expressions and synthetic or recorded seismograms can be used as boundary conditions.

### 4.7.3.1 VERIFICATION

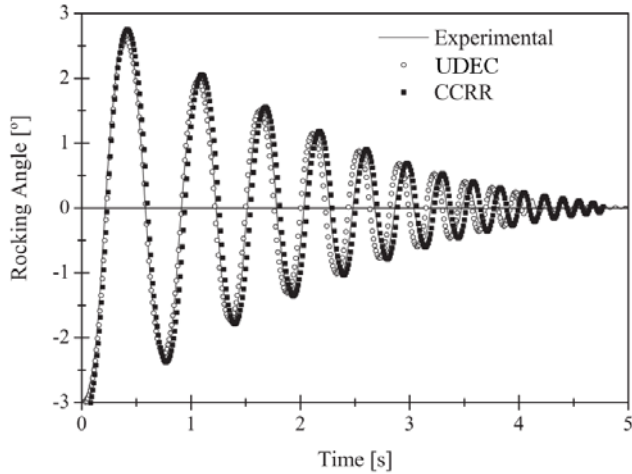


Figure 4.8: Comparison of a free rocking motion response of a free standing block: experimental estimated (black line), simulations DEM model UDEC (open circle) and CCRR (black squares) (from Peña et al. 2007).

For verification the experimental estimated rocking response of four granite blocks have been compared to the simulated results of UDEC Peña *et al.* (2007). In the work the authors also compared the measurements and the results of the DEM model with *complex coupled rocking rotations* (CCRR), another mathematical formulation of rocking behavior of rigid objects by Prieto and Lourenco (2005). Figure 4.8 shows the results of the analog experiment and the simulations with according parameters. It is shown that the experimental results and the simulated results are in a good agreement even in the last cycles (Peña *et al.* 2007).

### 4.7.3.2 COLLISION DETECTION

In 3DEC the collision detection is automated. As described earlier the calculation effort would be very high for models with numerous elements that possibly contact, without advanced detection methods. With each element added to the model the search time would increase quadratically. In 3DEC cell mapping is used to reduce the search time. By identifying the nearest neighbor, the number of elements that need to be checked for contact are reduced. To identify blocks in close approximation a three dimensional mesh of rectangular cells is placed above the void that contains all model elements. The space that is occupied by a block is represented by a block envelope. The block envelope is the smallest three dimensional box which sides are parallel to the coordinate system of the mesh. If the block envelopes of two or more blocks touch the same cell, these elements will be checked for contact (3DEC Manual 2016).

In Figure 4.9 the concept of cell mapping is shown in a 2D scheme. Three arbitrary shaped blocks (A, B and C) and their block envelope are mapped into the cells. Block A and C are most distant to each other and have no common cells. Even though block A and B are in close proximity to each other, they do not share a cell and therefore are not checked for contact. The blocks B and C do share two cells, are identified as neighbors and are checked for contact.

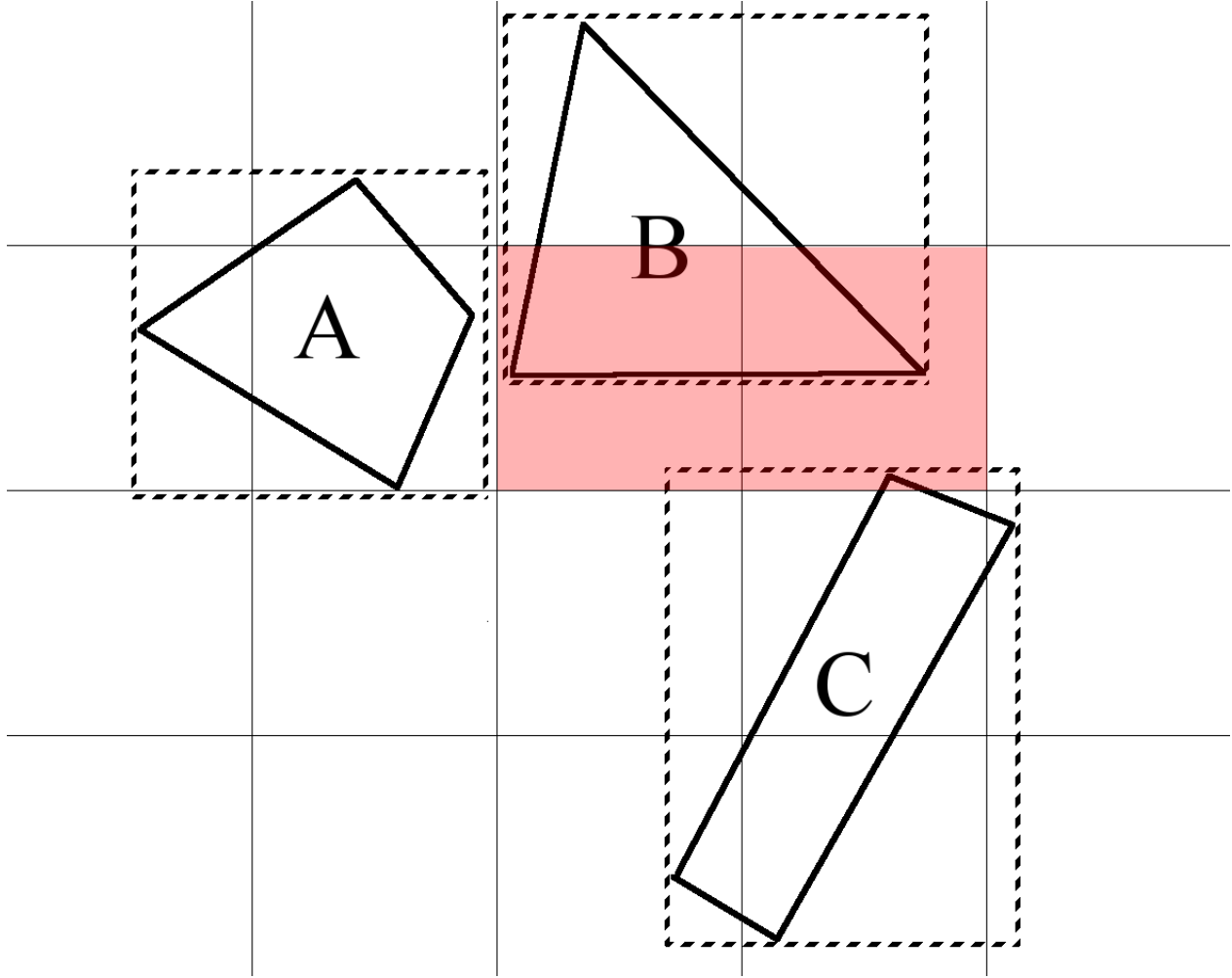


Figure 4.9: Schematic representation of a cell mapping mesh. The common cells of two blocks are highlighted in red. The block envelope is shown with dashed lines. Blocks A, B, C have solid black outlines.

After positive contact detection different contact types must be considered and the appropriate physical laws applied. In three dimensional space arbitrary shaped blocks can contact in many different ways. Figure 4.10 visualizes the possible contact types of the collision of two simple blocks: vertex to vertex, vertex to face, vertex to edge, edge to edge, edge to face and face to face. Often it is not an easy task to estimate the type of contact. The number of possible contacts  $n$  can be estimated as shown in Eq. 4.3 where  $v_A, e_A, f_A$  and  $v_B, e_B, f_B$  are the number of vertices, edges and faces for two blocks A and B.

$$n = (v_A + e_A + f_A) * (v_B + e_B + f_B) \quad (\text{Eq. 4.3})$$

If two simple blocks as the columns in Figure 4.1 with each eight vertices, 12 edges and six faces collide there are 676 possible contact types. To check all possibilities takes a significant calculation time, however utilizing similarities between contact types can reduce the calculation time.

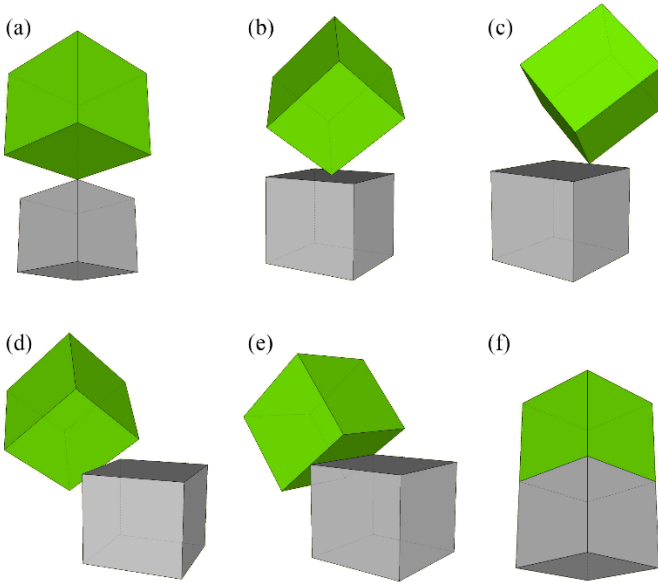


Figure 4.10: Contact types: (a) vertex to vertex; (b) vertex to face; (c) vertex to edge; (d) edge to edge; (e) edge to face; (f) face to face

The number of possible contact types can be reduced by substituting contacts. Some contact types can be identified by multiple contemporaneous vertex to face contacts. A vertex to vertex contact can as well be classified when three or more vertices to face contacts exists in the same location. When a vertex collides with an edge it can be expressed by two vertices to face contacts. Other contact types can be estimated by edge to edge contacts. Two edge to edge contacts are the same as one edge to face contact. A face to face contact can be expressed as three or more edge to edge or three or more vertices to face contacts (3DEC Manual 2016). With this substitution the number of possible contact types decreases to:

$$n = v_A * f_B + v_B * f_A + e_B * f_A \tag{Eq. 4.4}$$

This would reduce  $n$  in the above example to 240. Still the estimation of contact type is not trivial and therefore a time consuming task. To optimize the process and simplify the calculation the concept of a virtual common plane, introduced by Cundall (1988), can be used. The common plane is placed in the space between the two blocks. It is much easier to check the contact of each block with a plane separately, than checking the two blocks against each other. The plane has to be equidistant to both blocks if the blocks rotate relative to each other the plane is rotated as well. To estimate if a block is touching a plane only vertex to plane contacts need to be checked. This reduces the number of contacts to:

$$n = v_A + v_B \tag{Eq. 4.5}$$

In our example this further reduces the number of contacts to 16.

### 4.7.3.3 DAMPING

In DEM generally two classes of problems are addressed: static (or quasi-static) and dynamic problems. 3DEC provides different forms of damping for both problems. The approach to solve static problems is similar to the concept of dynamic relaxation described by Otter *et al.* (1966). The movement is damped to reach a force equilibrium under the applied boundary conditions as fast as possible.

For dynamic problem solving 3DEC offers different damping options. The mass-proportional damping applies a force in the opposite direction of the velocity and is proportional to velocity and mass. This kind of damping is used for solving quasi-static problems with a finite difference scheme (Otter *et al.* 1966). The stiffness-proportional damping is proportional to the incremental stiffness matrix multiplied by relative velocities or strain rates on contacts or stress in zones. To solve dynamic problems either stiffness-proportional or mass-proportional or a combination of both, called Rayleigh damping, can be used (3DEC Manual 2016). Rayleigh damping is frequency dependent and combines mass- and stiffness-proportional damping.

In Bui *et al.* (2017) local damping is recommended for dynamic analysis of a dry-joint masonry wall construction. This local damping is suitable for failure of structures or falling blocks in caves (3DEC Manual 2016). In Psycharis *et al.* (2003) Rayleigh Damping with a small mass-proportional damping is recommended for dynamic analysis to avoid too small time-steps. However, in models with many blocks mass-proportional damping is the only practical option in 3DEC. The damping parameters are set to small values between 1-5% applied to the critical frequency of the system (personal communication M. Christianson, Itasca).

In 3DEC density scaling is used to improve the calculation speed by scaling the density of the solid material. In a quasi-static problem inertial forces are not important. The grid points masses can be scaled for optimal numerical convergence without affecting the solution. However, for dynamic analysis inertial forces are important. Therefore, density scaling is not suitable for this kind of problems.

## 5 ROMAN TEMPLE OF KEDESH - PRECARIOUSLY BALANCED ARCHAEOLOGICAL STRUCTURES

Some of the presented results for the Roman Temple of Kedesh have already been published in Schweppe *et al.* (2017).

### 5.1 History of the Temple

Ancient Kedesh was a flourishing city in northern Israel during the 2nd and 3rd century C.E. (Fischer *et al.* 1984). One of the first written mentions of the city is found in the Bible in the book of Joshua (20:7) as a city of refuge. In a long lasting project the Roman Temple was constructed on a small ridge east of the ancient city of Kedesh (*Figure 1 (c)*), about 25 km north of the Sea of Galilee on the east side of the DSTF above the Hula Basin. The religious purpose has been widely discussed. At this point it is clear, that different deities were worshiped in the temple (Fischer *et al.* 1984, Magness 1990, Ovadiah *et al.* 1993).

A *peribolos* is the structural boundary of the *temenos*, the sacred temple area. The *peribolos* of the Roman Temple of Kedesh had a roughly rectangular shape and measured 55 m x 80 m (Fischer *et al.* 1984). The temple included a *portico* and a *cella*; the complete structure measured 31.25 m x 20.66 m (*Figure 5.1*). The *portico* in front of the *cella* had the dimension 8.62 m x 20.66 m. During archaeological excavation in 1981 and 1983-1984 foundations of six columns were found, this makes the *portico* a *hexastylus* (Fischer *et al.* 1984). The *cella*, the inner chamber, was 23.63 m x 20.66 m in size. For the construction well-worked limestone and dolomite ashlar were used, without mortar. The east facing entrance of the *cella* had a large ceremonial gate and two smaller doors and was opposing the entrance of the *peribolos* to the *temenos*. The doorway of the gate lay 1.46 m above the floor level. Therefore, the two smaller doorways flanking the gate were meant to access the temple and the large gateway only served as *sacred* or *manifestation doorway* (Ovadiah *et al.* 1993).

The current archaeological doctrine is that on May 19th 363 C.E. an earthquake destroyed the temple. Unearthed ceramics and coins indicate that the temple was abandoned after the earthquake (Fischer *et al.* 1984). First archaeological investigation has been done by Renan (1864), Condor and Kitchner (1882).

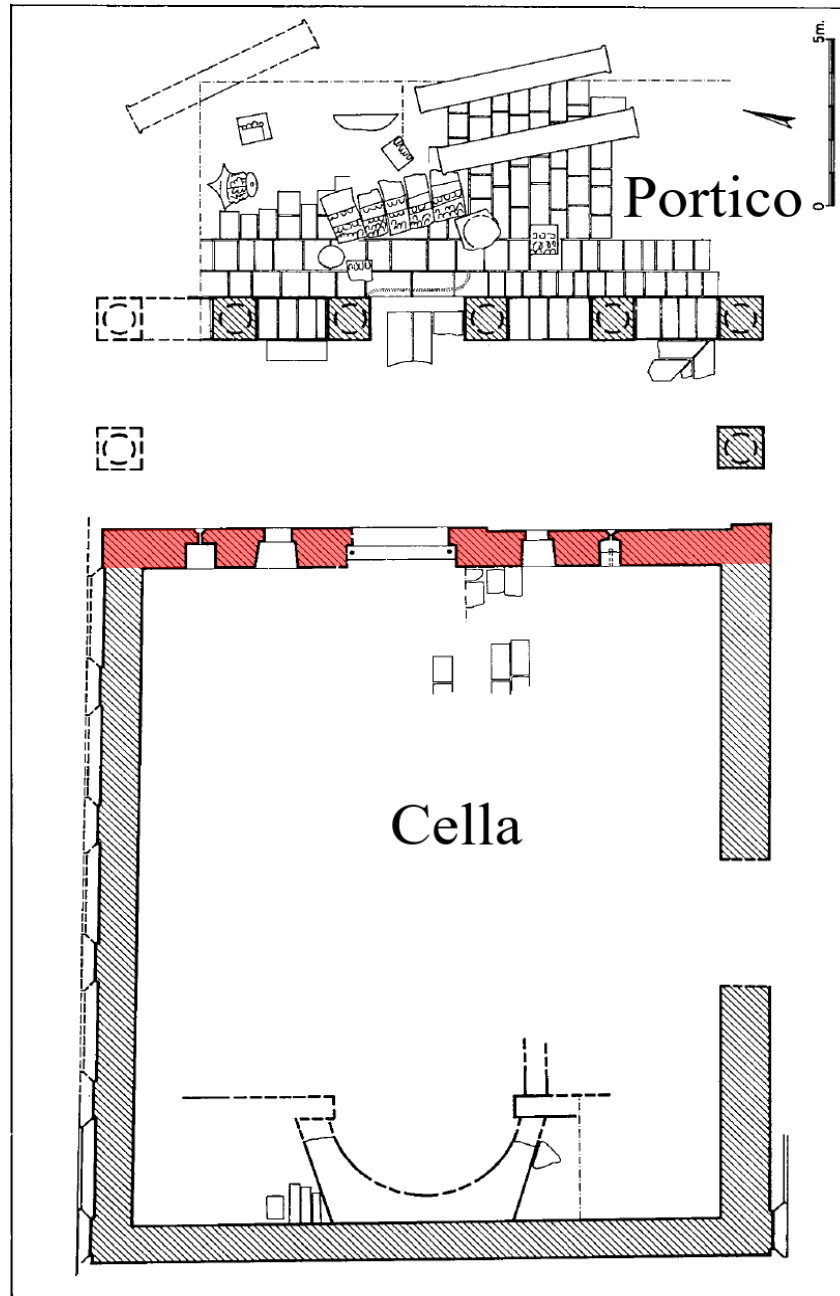


Figure 5.1: Reconstruction of the floor-plan of the Roman Temple of Kedesh. The front of the temple that is still persisting is highlighted in red (after Fischer et al. 1984).

Today only two sections of the temple front are persistent (Figure 5.1 and Figure 5.2 (a)). While the foundation of the *cella* walls is still visible, any rising parts are missing; the same applies to the *portico*. During excavations archaeologists did not find any indications for a roof on the *cella*. It was discussed whether the *cella* was roofed with wooden beams; temples with similar roofing methods were known from Syria (Ovadiah et al. 1993). However, it is likely that the porch had a roof since fragments of terracotta tiles were found in the *portico*.

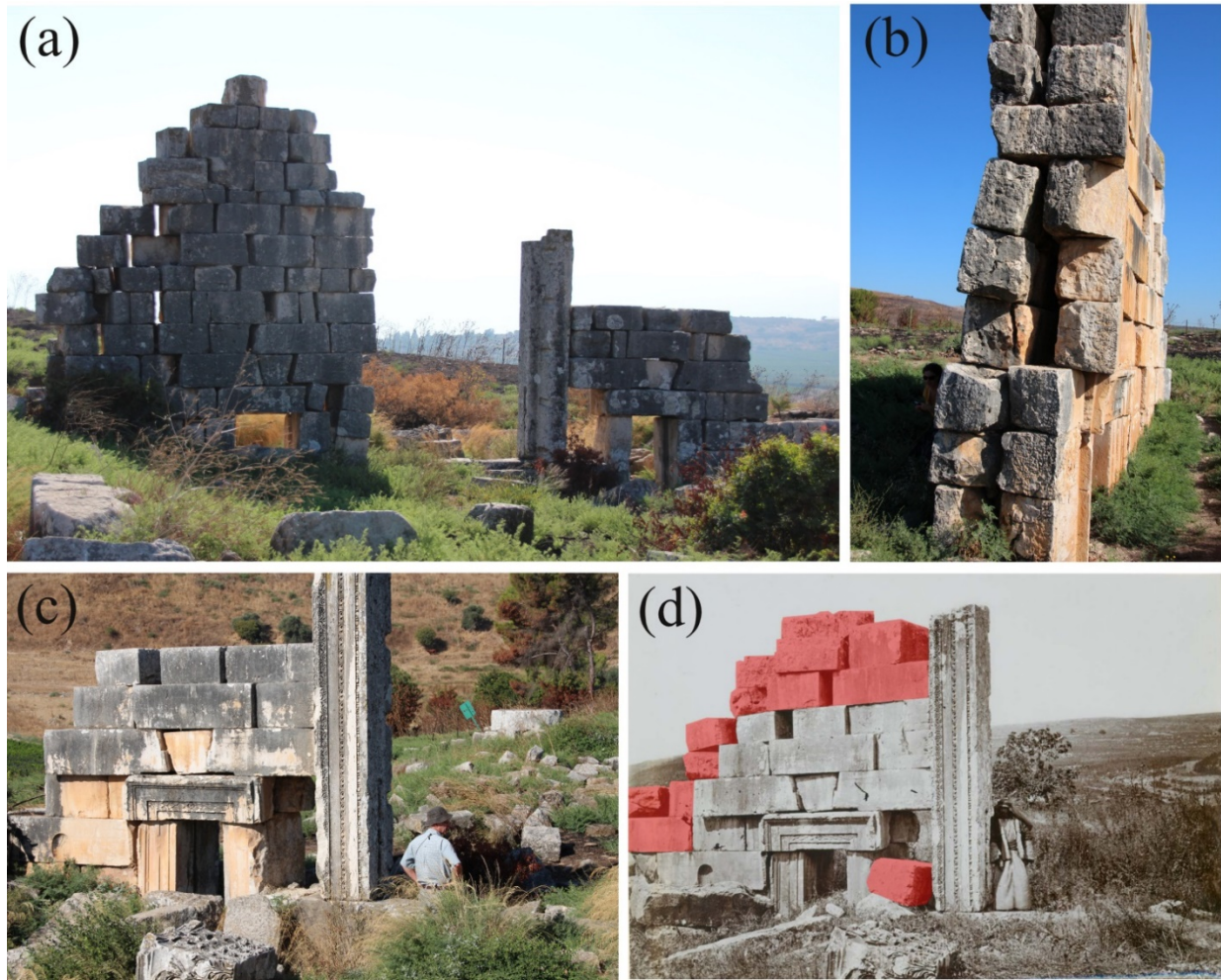


Figure 5.2: (a) View from west towards the remains of the Roman Temple of Kedesh. The northern and southern sections have heights of 7.26 m and 3.59 m, respectively. The door-jamb at the southern section is 4.4 m high. (b) View from the south to the northern section showing the gap between the two shells. (c) Photo showing the current state of the southern section of the ruin (Photos: Schweppe). (d) Photo by Kitchener from 'The Survey of Western Palestine' (Conder and Kitchener 1882). The red highlighted ashlar are missing today (after Schweppe et al. 2017).

As mentioned above, only the two sections of the front wall are partially preserved (Figure 5.2 (a), (b) and (c)). The remains are structured in two sections separated by a 3.33 m gap of the former gate. The southern doorjamb of the gate has a height of 4.5 m and is still *in situ*; however, the northern doorjamb and the lintel are missing. The northern and southern sections have remaining heights of 7.26 m and 3.59 m, respectively. From north to south sediments form a slope that buried some blocks of the northern section (Figure 5.2 (a)). The masonry consists of double shell ashlar for both wall-sections. To increase the stability of the masonry some ashlar are oriented orthogonal to the wall trend and connect both shells. The wall is *pseudoisodomic*, i.e. within rows all ashlar are of equal height, but among rows the heights differ (Schweppe et al. 2017). The northern wall has a concave bend to the east, gaps between the ashlar (Figure 5.2 (a)) and the opening between the two shells (Figure 5.2 (b)) indicate that the persisting sections have been affected by earthquake ground motions.

Archaeological sources provide only limited information about the original state of the Roman Temple when the earthquake occurred. The archaeological investigation gives reliable information about the temporal classification of the temple and when it was abandoned. But apart from the basic geometry and dimension, there is a lack of important structural information such as the roof structure or whether the *portico* was structurally connected to the *cella*. Therefore, a reconstruction of the temple for an archaeoseismic investigation of the ground motion, by which it was destroyed, would be rather speculative.

Another issue is that the state of the temple was altered after the collapse occurred 1655 years ago, partially even in its recent history. Kitchner and Condor documented during their Western Palestine Survey (1871-1878) that the *portico* and most parts of the *cella* were missing. *Figure 5.2 (d)* shows a photo (Conder and Kichtner 1882) taken during that survey of the southern section of the front wall. Hinzen *et al.* (2018) showed the value of rephotography of archaeological sites to identify in detail how the site was altered over time. During a field campaign in 2013 a photo of the southern section was taken from a similar perspective (*Figure 5.2 (c)*). Comparing the state shown *Figure 5.2 (d)* with the current state shown in *Figure 5.2 (c)* it is evident that the highlighted ashlar are missing. These ashlar cannot be located in close vicinity to the ruin and it can be assumed that they were looted from the site. Archaeologists believe that settlers used the well-shaped blocks of the temple particularly from the *cella* as building material. In addition, Fenner (1905) reported that locals tried to overthrow parts of the remaining wall during a field campaign to annoy the scientists. With this background it is not possible to distinguish natural from anthropogenic damage.

### 5.2 Virtual 3D Model from Laser Scans

During the field campaign in 2013, the remains of the temple were surveyed by 24 3D laser scans. To avoid shadowing effects and to get an undistorted view the base of both walls, the vegetation close to the structure had to be removed. Checkerboards and spheres with a diameter of 0.25 m were used as target markers for referencing. The resulting model has a mean target tension of 0.0026 m and contains more than 80 million points. *Figure 5.3* shows the scanner positions around the site. Most scans are in close vicinity to the ruin and even on top of the southern section. Some scans were carried out from distance positions to complete the point cloud.

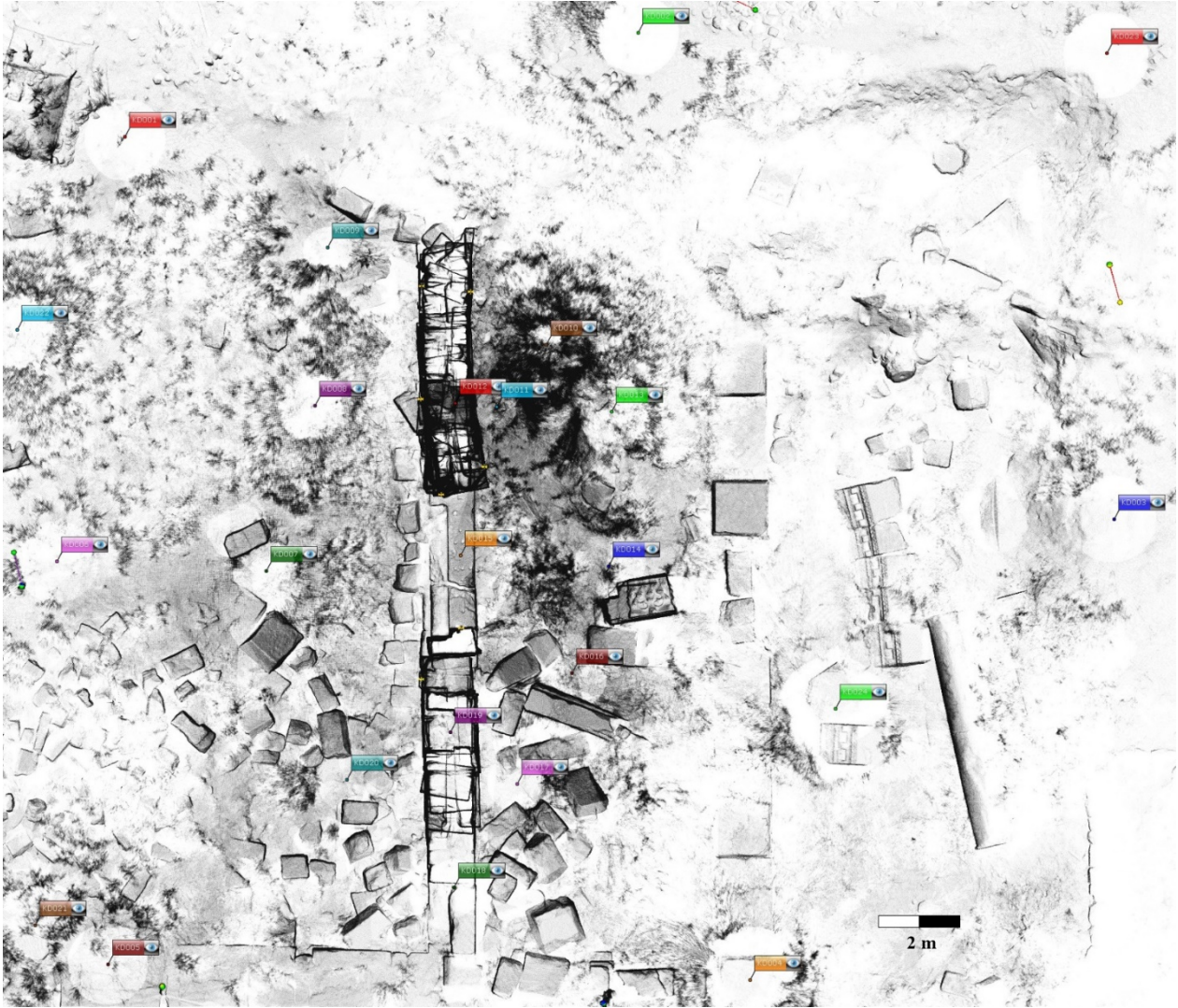


Figure 5.3: Correspondence view of the laser scanning project of Kedesh. The points with the colored labels mark the laser scanner positions of the 24 scans.

### 5.3 Creation of Discrete Element Models

Though a reconstruction of the temple was not possible this structure offered the possibility for another approach. The goal of this model was to determine the current stability of the ruin. The concept is well-known for Precariously Balanced Rocks (PBRs) (Brune 1996). Therefore, in Schweppe *et al.* (2017) the ruin was used as a seismoscope and introduced the concept of Precariously Balanced Archaeological Structures (PBASs). Therefore, a model of the current state of the ruin was created. All models created for the Ruin of the Roman Temple were based on the 3D point cloud. The first challenge was to find a way to transfer the geometry of the ruin from the 3D point cloud to a discrete element model. Three software codes were used to test the feasibility of this transfer and to compare the effectiveness of the resulting models; as discussed in the following subsections.

A seismoscope is an instrument that indicates the occurrence of an earthquake, but does not record a seismogram (Richter 1958). The earliest known seismoscope was invented by Chang Hêng in 132 C.E. (Dewey and Byerly 1969). In an effort to increase the number of P-wave first motion observations for the development of fault plane solutions, Wilhelm Hiller, a German seismologist, attempted to use seismoscopes in the 1930s. A simple instrument was developed to measure the direction of impact. Hinzen and Kovalev (2010) related in their study to this simple instrument as “Hiller’s seismoscope”. They analyzed the ability of the seismoscope to measure the P-wave polarity with a computer model. The authors concluded that the instrument is not capable to provide the information necessary to construct a fault plane solution. However, the instrument is capable to indicate the presence or absence of certain ground motion. The same concept to conclude to a certain ground motion at a specific site is used by Precariously Balanced Rocks (PBR) (Brune 1996). This method uses natural geologic formation that are in a static delicate shape. By estimating the ground motion that would topple the formation it is possible to conclude the absence of ground motion of certain strength, since the formation is still *in situ*.

### 5.3.1 UNIVERSAL MECHANISM

The first attempt was a UM model of the northern section of the temple wall, where each ashlar was represented by a cuboid. For each cuboid the average length and depth of the according ashlar was estimated in the 3D point cloud. As it is characteristic of pseudoisodomic walls, all cuboids in a row had the same height. The cuboids at the foundation of the ruin were fixed to the baseplate to represent the buried ashlars at the site. A comparison of the model with photos of the ruin showed discrepancies due to the simplifications inherent in the modeling approach (*cf. Figure 5.2 (a), (b) and Figure 5.4 (a), (b)*). Important details, like the opening between two shells were not sufficiently represented. The estimation of the ashlar dimension was not sufficient to correctly reflect the rotation of the cuboid. Furthermore, the ashlars were partially eroded and not perfect rectangular cuboids any more. Lastly, more complex shapes *e.g.* the keystones above the small doorways were not well represented in the model. Psycharis *et al.* (2003) pointed out how important the current imperfections are to correctly estimate the stability of a structure; therefore, this approach was not feasible.

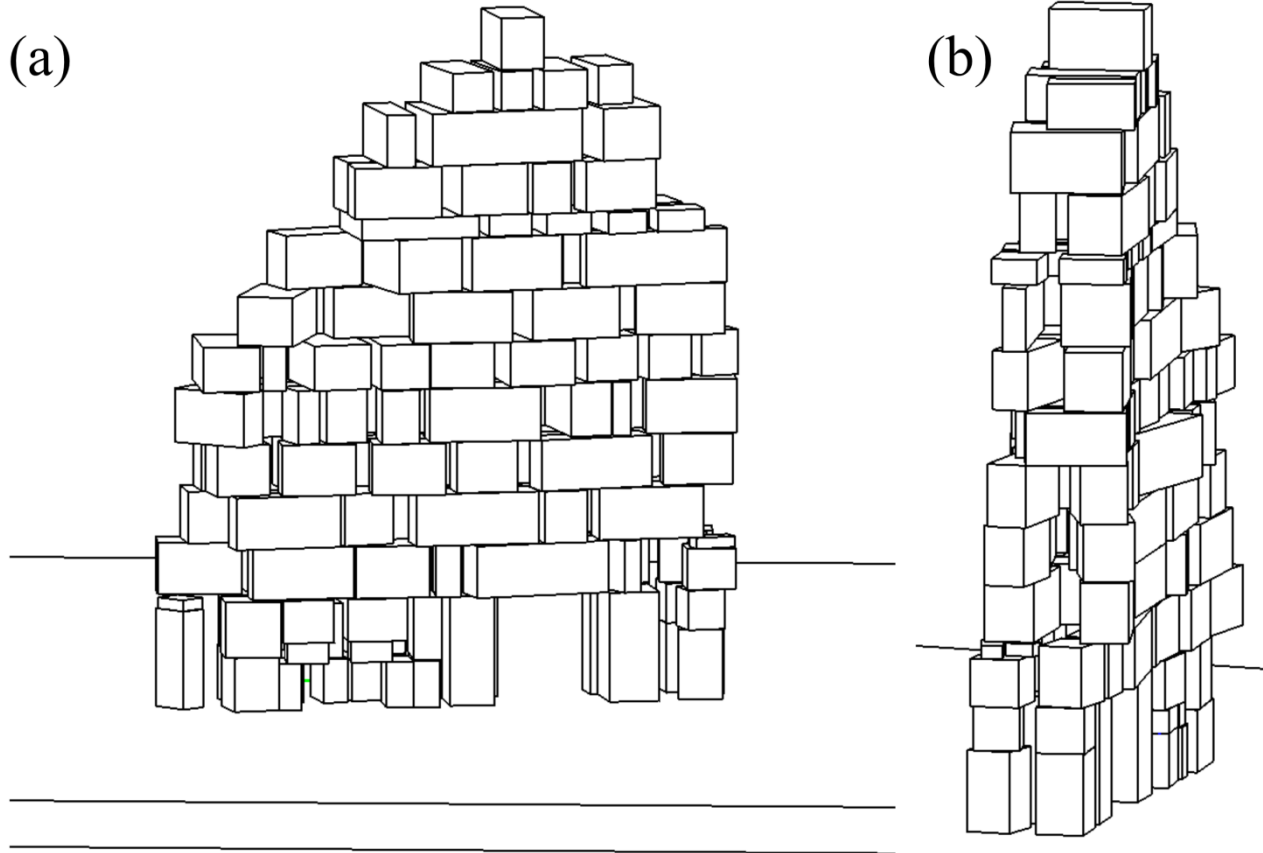


Figure 5.4: UM model with cuboids: (a) View from the east to the wall. (b) view from north to south to the opening of the southern section.

To overcome the shortcomings in geometry of the cuboid model the ashlar had to be modeled in more detail. To better represent the non-uniform shape of the ashlar each block was modeled by a polyhedron. Each face of a polyhedron was defined by tetrahedrons, based on the corner vertices of the according ashlar. The coordinates of the vertices were estimated from the 3D point cloud. With custom written programs the coordinates were converted to UM input files. This method allowed preserving the position and orientation of each block in the model (cf. Figure 5.2 (a), (b) and Figure 5.5 (a), (b)).

Preliminary tests with simple models showed that the calculation time for a simple model with cuboids is half as long as those for model with polyhedrons. Therefore, despite the geometric deficiencies of the cuboid model, further tests were carried out with both models. It turned out, that the calculation time for the northern section already exceeded practical time spans. And although both models were stable under static load, when ground motion was introduced sometimes numerical errors occurred in the calculation of the mass matrix.

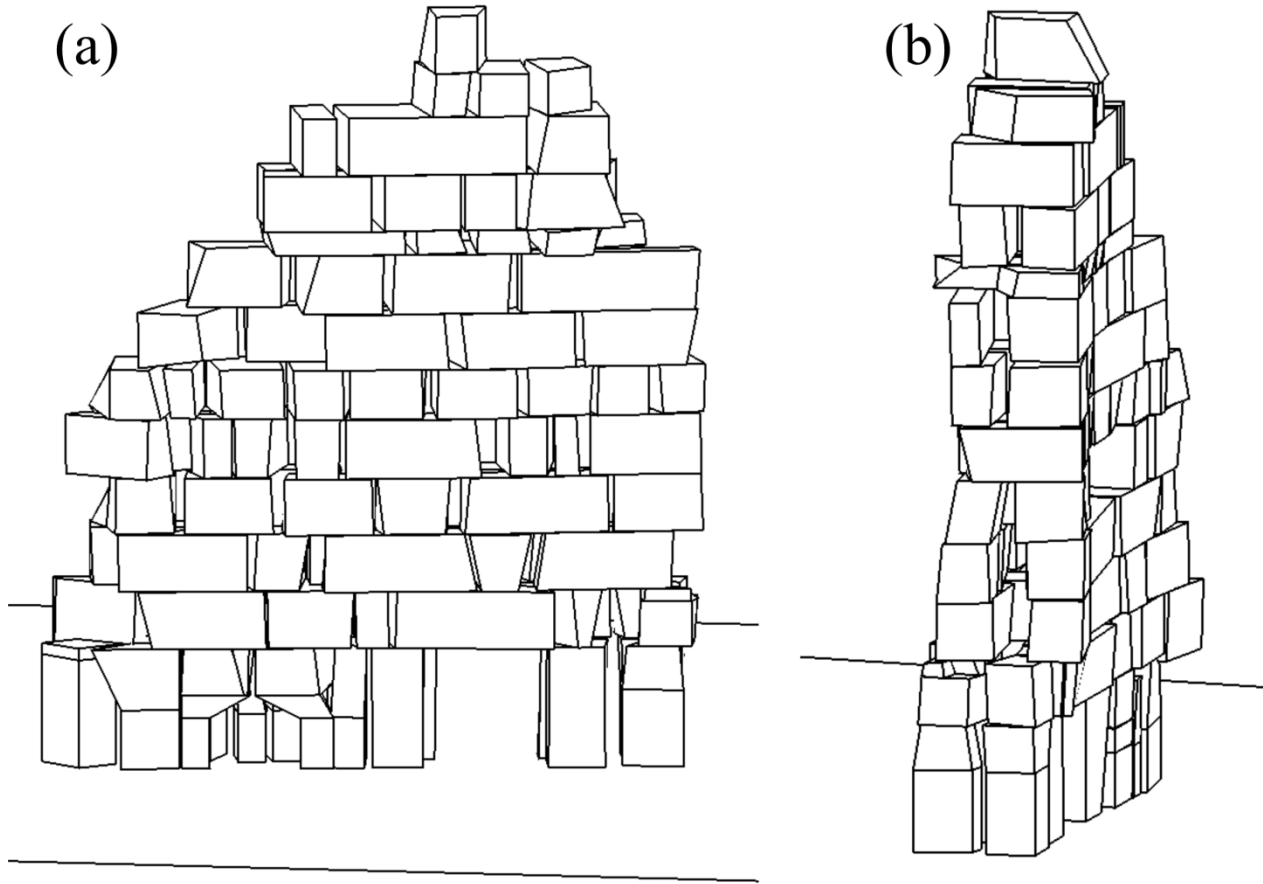


Figure 5.5: UM model with polyhedron: (a) View from east to the southern section. (b) View from north to south to the opening of the southern section.

### 5.3.2 3 DIMENSIONAL DISTINCT ELEMENT CODE

In 3DEC the calculation time is not changing with the block geometry. Therefore, the more accurate definition of the ashlar based on the vertices was used for the 3DEC models presented in the following. With custom written *FISH* routines, the irregular shaped blocks were created. Again the blocks at the foundation were joined with the baseplate.

First tests with the model showed that the basic geometry was stable. With a mass-proportional damping of 3% at a critical frequency of 1 Hz the calculation time was suitable. However, the consequence of the low damping values was a bounciness of the blocks, when the walls collapsed due to ground motion the blocks started bouncing off the baseplate. Sometimes, when ground motion was applied to the baseplate a rattling motion was introduced into both sections; leading to an uncontrolled collapse of both sections.

### 5.3.3 UNITY 3D

3DEC allowed exporting the model in a Unity readable format. During the migration from 3DEC to Unity rounding errors of the vertex coordinates occurred. Therefore, fine-tuning in Blender (Data and Resources) was necessary to precisely align corners of adjacent blocks to avoid unrealistic penetration of one block into another. This would introduce internal stresses into the model, which can cause unwanted movements and eventually lead to uncontrolled collapse of the model. The damping coefficient for the simulations was set to 0.86 and first tests showed that the model was stable under static and dynamic conditions. The final, stable model was composed of 142 discrete objects, 141 blocks and the baseplate. With this model numerous calculations were carried out, the results of which are given in the following section.

## 5.4 Calculations

### 5.4.1 ANALYTIC GROUND MOTION SIGNALS

For the first simulations an analytic ground motion signal, the cycloidal pulse, was used. Cycloidal pulses (Zhang and Makris 2001) fulfill the boundary conditions of zero acceleration, velocity and displacement at the start of the signal and of zero acceleration and velocity at the end of the signal (*i.e. Figure 5.6 (a)*). The displacement history is comparable with a simple version of a horizontal ground motion close to a strike slip fault (Hinzen and Montabert 2017). This signal type was previously successfully applied in archaeoseismological research (Hinzen 2009b, Hinzen and Montabert 2017). Major frequencies ranged from 0.3 Hz to 2.0 Hz and the PGAs from  $1 \text{ m/s}^2$  to  $9 \text{ m/s}^2$ . In total 54 impulses were applied in parallel and orthogonal direction to the wall trend. The response spectra for the signals are illustrated in *Figure 5.6 (b)*.

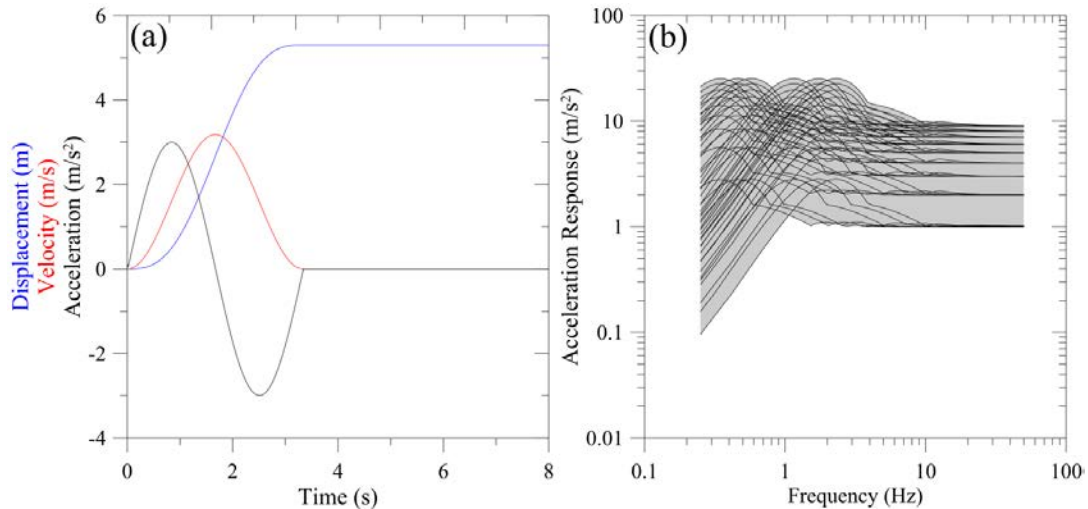


Figure 5.6: (a) Time-series of a cycloidal pulse with a frequency of 0.3 Hz @ PGA of 3 m/s<sup>2</sup>. (b) Acceleration response spectra of 54 cycloidal impulses used to test the dynamic behavior of the model of the Roman Temple of Kedesh.(Schweppe et al. 2017)

#### 5.4.2 EARTHQUAKE SCENARIOS

In total eight earthquake scenarios were used to test the stability of the ruin. Two of which were local speculative events without historical context. The assumption was based on the close proximity of the Hula Basin Fault (HBF) and Hula Central Fault (HCF) in the Hula Basin. Five scenarios resembled historical earthquakes along the DSTF (*cf.* Chapter 2.4.3). The eighth earthquake was the M 7.7 Chi Chi earthquake in Taiwan. The latter was chosen, because records are available that were recorded in close vicinity to the activated fault, an earthquake of this magnitude is possible in the study area and the large observed PGA provided a chance to double-check, if the model could correctly simulate the failure of the ruin. The parameters of the all earthquakes are listed in *Table 5.1*.

Schwellenbach (2015) reconstructed the ground motion from the 1759 Lebanon Earthquake. In the course of that work Green's Functions were calculated, based on the current velocity model of Israel provided by Geophysical Institute of Israel, GII (2013). With this set of Green's function synthetic seismograms were calculated for the earthquake scenarios listed in *Table 5.1*; for the Chi Chi earthquake a measured strong motion record was used. The earthquake source in the calculation was represented by an arbitrary number of rectangular dislocation planes (Wang 1999), the distribution of sub-sources follows the Gutenberg Richter law. The seismograms of the earthquakes were calculated for one to three activated fault segments whose geometries have been simplified from *Figure 2.5*. The second segment of the JVF earthquake had a dip of 70°; all other segments dip with 90°. The seismic moment estimated by the relation by Wells and Coppersmith (1994) is based on the surface rupture length. A left-lateral movement was assumed for each segment. The displacement and acceleration seismograms for each earthquake scenario are shown in *Figure 5.7*.

## Roman Temple of Kedesh - Precariously Balanced Archaeological Structures

Table 5.1: Parameters of two assumed earthquakes ( $\dagger$ ), five historic earthquakes along the DSTF and in addition a strong motion record (\*) from the 1999 Taiwan earthquake (Tai).  $D_{min}$  is the minimum distance to the surface trace of the faults from the Roman Temple of Kedesh. (HBF = Hula Basin Fault, HCF = Hula Central Fault, JVF = Jordan Valley Fault, YF = Yammouneh Fault, JGF = Jordan Gorge Fault, RaF = Rachaya Fault, RoF = Roum Fault).

ID	Year	M	Latitude	Longitude	Epicentral Distance (km)	$D_{min}$ Distance (km)	Comp.	PGA (m/s <sup>2</sup> )	
1	HBF $\dagger$	-	5.8	33.03	35.566	12.6	4.2	Z	1.57
								N	1.08
								E	1.87
2	HCF $\dagger$	-	5.9	33.04	35.63	9.9	7.9	Z	0.60
								N	1.10
								E	1.22
3	JVF	749	7.4	31.76	35.50	149.2	32.5	Z	0.29
								N	2.49
								E	0.46
4	YF	1202	7.6	32.88	35.62	26.5	6.4	Z	1.75
								N	2.48
								E	5.00
5	JGF	1759	6.1	32.88	35.62	26.5	13.6	Z	0.20
								N	0.66
								E	0.33
6	RaF	1759	7.1	33.25	35.68	21.5	21.7	Z	0.25
								N	0.92
								E	0.81
7	RoF	1837	6.8	33.18	35.55	8.7	9.0	Z	0.53
								N	3.42
								E	0.72
8	Tai*	20.09.1999	7.7	23.85	120.82	31.7	-	Z	7.13
								N	8.37
								E	7.93

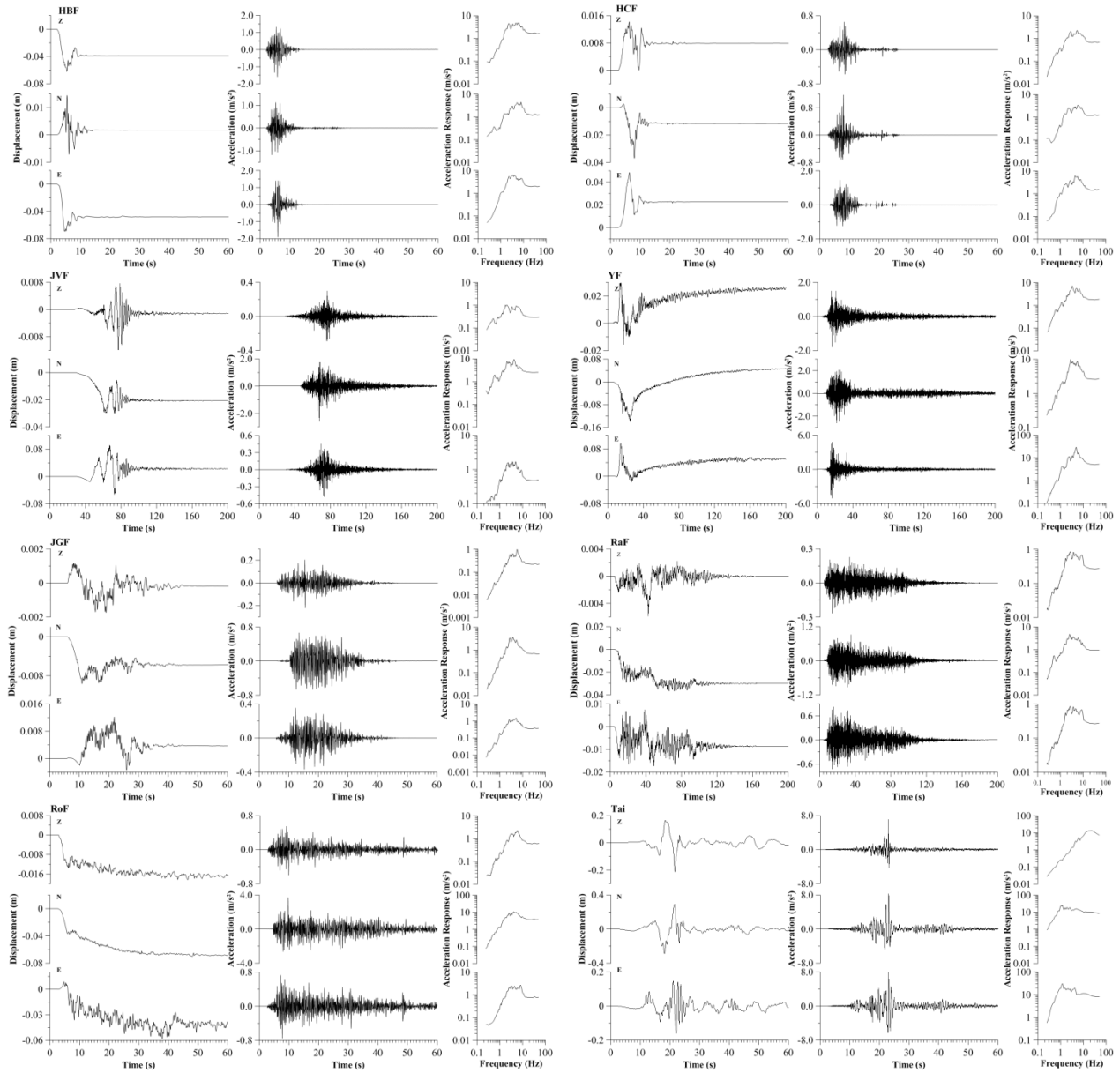
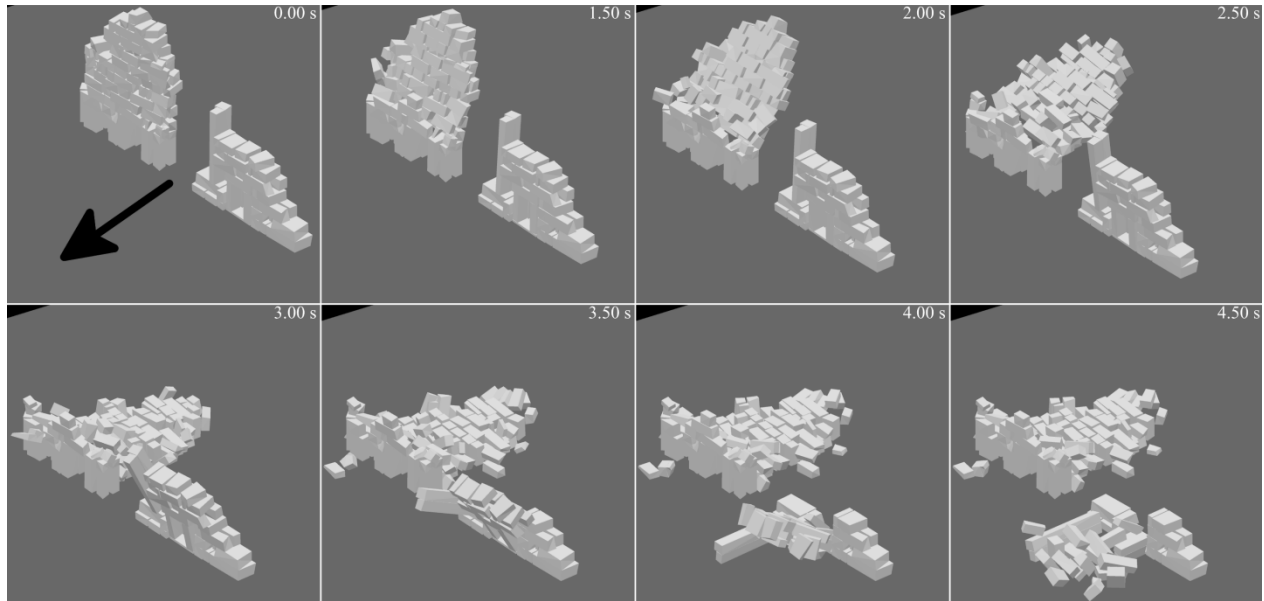


Figure 5.7: Displacement and acceleration time series and acceleration response spectra of the earthquake ground motions used in the calculations. The earthquake source code given in the upper left of each figure corresponds to the list in Table 5.1 (Schweppe et al. 2017).

## 5.5 Results

The simulations with cycloidal pulses revealed two distinct failure mechanisms. In the specific case when a cycloidal pulse with a frequency of 0.3 Hz and a PGA of  $3 \text{ m/s}^2$  was applied to the baseplate orthogonal to the wall trend, both failure mechanisms occurred. Figure 5.8 illustrates the outcome of the simulation. The southern (smaller) wall was falling during the stopping phase in direction of the ground motion (denoted as first failure mechanism). The northern wall topples, due to the inertial forces during starting phase of the pulse, in the direction opposite to the ground movement (second failure mechanism).



*Figure 5.8: Snapshots of the collapsing walls of the Roman Temple of Kedesh during a horizontal ground motion in form of a cycloidal pulse with a frequency of 0.3 Hz @ PGA of 3 m/s<sup>2</sup> at consecutive times. The black arrow in the first snapshot indicates the direction of the impulse from east to west; the time of each snapshot is given in the upper right corner (Schweppe et al. 2017).*

In order to assess the effects of ground motion to the model, the displacement of each block was tracked at its center of geometry during the entire simulation time. The model time for the simulations with the analytic impulse lasted 7 s. The model time for the earthquake scenarios ran 10 s longer than the earthquake records in order to track the full response of the model. As measure for displacement of the blocks the modulus of displacement vector (MDV) was selected (Hinzen 2009b, Hinzen and Montabert 2017). The MDV is the length of the vector that connects the starting position and resting position of a block. *Figure 5.9* shows an example of the results for the simulation with an impulse with 0.3 Hz frequency and 3 m/s<sup>2</sup> PGA, which is shown in *Figure 5.8*. The results for 54 tests are summarized in a matrix of six frequencies and nine PGAs for the ground motion applied orthogonal and parallel to the wall trend in *Figure 5.10* and *Figure 5.11*, respectively. The results revealed that larger ground motion accelerations were needed to topple the walls when the frequency of the impulse increases. In both matrices the cases in which the walls were damaged are divided by a diagonal from the undamaged cases.

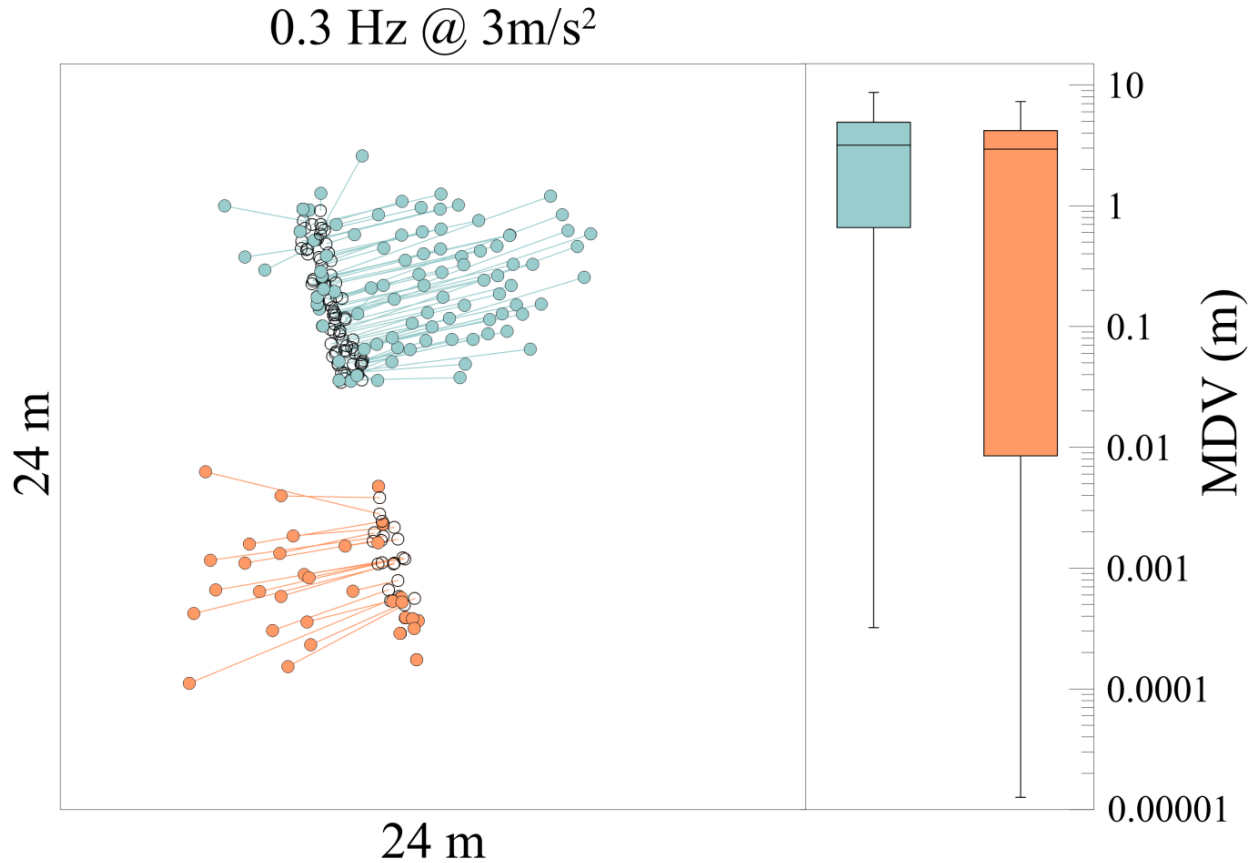


Figure 5.9: Final resting positions of building ashlars at the end of the application of cycloidal pulses. It shows the result of the horizontal ground motion orthogonal to the wall for a cycloidal pulse with  $0.3 \text{ Hz @ } 3 \text{ m/s}^2$ . The plot on the left is a bird eyes view (map  $24 \times 24 \text{ m}$ ) of the model. The colored lines connect the starting (open circles) and end positions of the block's center of gravity; blue and orange for the northern and southern section of the wall, respectively. The length of the lines corresponds to the horizontal component of the modulus of the final displacement vector (MDV). The graphs on the right side of the map show box plots with the distribution of the MDVs in a logarithmic scale from  $0.00001$  to  $15 \text{ m}$ . The colored sections indicate the range from the first to the third quartile of MDVs, the horizontal line indicates the median and the lines with the whiskers give the minimum and maximum MDV values for each experiment (Schweppe et al. 2017).

The tests with the ground motion applied orthogonal to the wall trend showed that the northern (taller) section was less stable than the southern section during ground motion with low frequencies. At a small PGA of  $1 \text{ m/s}^2$ , no toppling occurred at frequencies ranging from  $0.3$  to  $2 \text{ Hz}$ ; at  $2 \text{ m/s}^2$ , the northern wall collapsed with the first failure mechanism while the southern section survived the test. At a PGA of  $3 \text{ m/s}^2$  the northern section showed a changeover in the toppling direction. It toppled opposite of the direction of the ground motion, *i.e.* with the second failure mechanism. The southern section underwent the second failure mechanism at frequencies above  $0.3 \text{ Hz}$  and PGAs above  $3 \text{ m/s}^2$ . The changeover point from the first to the second failure mechanism for the southern section was at a frequency of  $0.5 \text{ Hz}$  with PGAs from  $5$  to  $7 \text{ m/s}^2$ ; the blocks of the southern section fell in both directions. The simulations at  $1 \text{ Hz}$  showed that the southern section failed with the first mechanism at a PGA of  $4 \text{ m/s}^2$ , the northern section collapsed

## **Roman Temple of Kedesh - Precariously Balanced Archaeological Structures**

---

only at PGAs above  $6 \text{ m/s}^2$  with the second failure mechanism. Sometimes blocks dropped out of the sections (*e.g.*  $5 \text{ m/s}^2 @ 1 \text{ Hz}$ ), indicating that the edges of the sections were more vulnerable. Most of these cases were close to the diagonal of the matrix between the unstable and stable state of the sections. Both sections were mostly stable in the tests with 1.5 Hz and 2 Hz, only a few ashlar from the edges fell down at the largest PGAs. However, a clear increase of the internal deformation with increasing PGAs is shown by the median values of the MDVs.

## Roman Temple of Kedesh - Precariously Balanced Archaeological Structures



Figure 5.10: The results of horizontal ground motions orthogonal (from right to left) to the wall trend. Rows and columns give the PGA and main frequency of the pulses, respectively, as indicated at the left and top border. Each individual graph has the same scaling as the graphs in Figure 5.9 (Schweppe et al. 2017).

## Roman Temple of Kedesh - Precariously Balanced Archaeological Structures

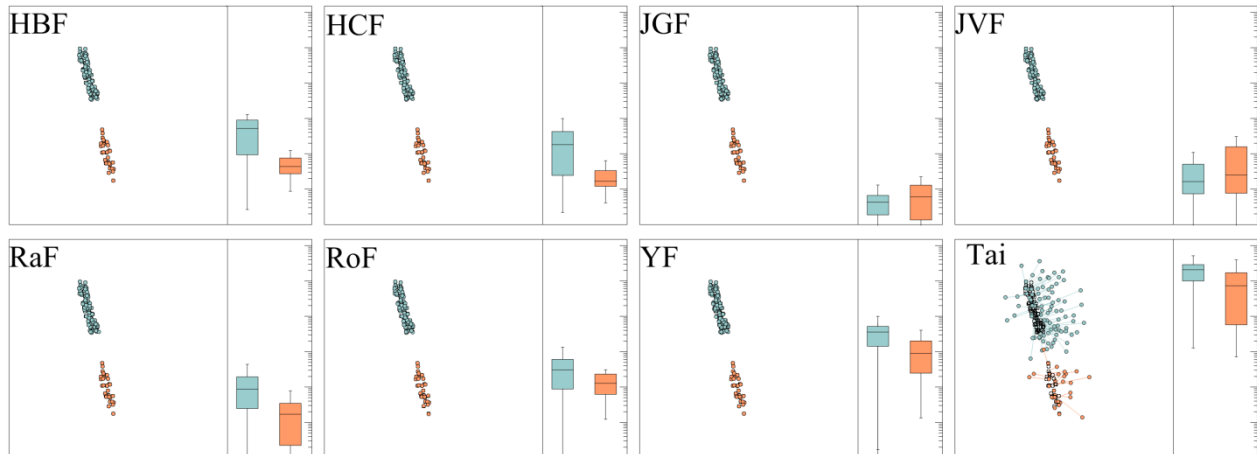


Figure 5.11: The results of horizontal ground motions parallel (top to bottom) to the wall trend. Rows and columns give the PGA and main frequency of the pulses, respectively, as indicated at the left and top border. Each individual graph has the same scaling as the graphs in Figure 5.9 (Schweppe et al. 2017).

## Roman Temple of Kedesh - Precariously Balanced Archaeological Structures

The tests, in which the ground motion was applied parallel to the wall trend, show that both sections were much less vulnerable to ground motion in this direction (*Figure 5.11*). At PGAs of  $4 \text{ m/s}^2$  and  $5 \text{ m/s}^2$  blocks fell out the southern section, while the northern section only showed internal deformation. Just PGAs of  $6 \text{ m/s}^2$  and above lead to mayor collapse of ashlars. For the southern section no major toppling direction was evident. However, most ashlars of the northern section fell in direction of the ground motion, indicating the first failure mechanism.

*Figure 5.12* shows the final resting position of the ashlars after the simulations for the eight earthquake scenarios. It stands out that only the recorded strong motion record lead to a collapse of the structure. None of the synthetic seismograms harmed the sections, only internal deformation occurred. *Table 5.1* shows that the largest PGA for the historical earthquakes JVF, JGF, RaF and RoF consistently are in north-south direction, the direction in which the sections are least vulnerable. With  $5 \text{ m/s}^2$  in east west direction the largest historical earthquake (YF) is the only historical event that exceeded a PGA of  $4 \text{ m/s}^2$ . The response spectrum of this event has the acceleration response peaks between 3 Hz to 6 Hz; at lower frequencies the acceleration response is below  $1 \text{ m/s}^2$  (*Figure 5.7*). The recorded strong motion of the Chi Chi earthquake that collapsed both sections in comparison exceeds PGAs of  $7 \text{ m/s}^2$  on both horizontal components (*Table 5.1*). The acceleration response at 0.5 Hz is above  $5 \text{ m/s}^2$  in the horizontal directions and peaks at values above  $10 \text{ m/s}^2$ .



*Figure 5.12: Final resting positions of building ashlars at the end of the application of the earthquakes. Each individual graph shows the results for one earthquake ground motion. The codes in the upper left corner indicate the earthquakes, which are listed in *Table 5.1*. See caption of *Figure 5.9* for scale and details (Schweppe et al. 2017).*

### 5.6 Discussion and Conclusion

The study of precariously balanced rocks is a well-established method to investigate the vibration history of a specific site and to draw conclusions about the past seismicity of a region (Brune 1996). Here the same concept was applied to the Roman Temple of Kedesh, a Precariously Balanced Archaeological Structure. With 24 laser scans the site was surveyed. Based on the resulting 3D point cloud a DEM model was developed, to study the stability of the Temple during ground motion. A total of 54 analytical signals (cycloidal pulses) with frequencies from 0.3 Hz to 2 Hz and PGAs from  $1 \text{ m/s}^2$  to  $9 \text{ m/s}^2$  were applied as ground motion to the model (each orthogonal and parallel to the wall trend). Additionally, seismograms of eight earthquake scenarios were used as ground motion in the model. Two of these are hypothetically in close proximity to the temple's location. Five scenarios relate to historical events that have already been studied in archaeo- and paleoseismological research. The eighth ground motion is a strong motion record from the 1999 Taiwan Chi Chi earthquake.

The simulations with the analytical signals reveal two failure mechanisms. The first occurs during the stopping phase of the input signal, when the wall collapses in direction of the ground motion. In the second failure mechanism the wall topples in opposite direction of the ground motion, due to high inertial forces during the starting phase of the signal. The tests with different direction of the ground movement have shown that the resistance of the wall against ground movement strongly depends on the azimuth. The height to width ratio (h/w-ratio) is an important factor for the performance of the wall (Hinzen and Montabert 2017). This is also reflected in the stability differences between the two sections. The northern (taller) section with a larger h/w-ratio is more vulnerable to lower frequencies than the southern (smaller) section.

It must be emphasized that none of the simulated historic earthquake scenarios toppled the ruin. The ground motion that occurred during the earthquakes at the site may differ somewhat from this forward model, but if the ground motion would have been significantly stronger than in the model, the ruin would have suffered further damage.

The stability of the ruin of the Roman Temple of Kedesh is at the first sight surprising. Hinzen and Montabert (2017) pointed out in their work that a low h/w-ratio is important for the dynamic stability of free-standing walls. However, it is difficult to give an exact measure for the h/w-ratio for both sections, since they have varying width at the base and different heights. The current h/w-ratio for the southern section can be estimated to 3.2. It should be noted, that the height was altered since 1882. However, the height of the southern section did not exceed the height of the doorjamb. Therefore, the h/w-ratio was still smaller for the southern section than for the northern. But the northern section reaches a height of 7.26 m only at its center, the first complete row of ashlar however is at a height of about 5 m. When taking the

full height into account the h/w-ratio is 6.5. However, the effective h/w-ratio for the northern section with a height of 5 m might be as small as 4.5. For comparison some of the Inca walls described as earthquake resistant had h/w-ratios below 3 (Torres 2014, Hinzen and Montabert 2017). In conclusion the remains of the Kedesh Temple achieve their relative low vulnerability to ground motion from the small h/w-ratios of both wall sections.

This approach leaves no conclusion for the dynamic response of the original temple and it must be assumed that it was substantially different from that of the current remains. It can also not be postulated with certainty that the earthquake on May 19th 363 C.E. transformed the temple from an intact state to the current configuration. Next to weathering it is evident that the state of the ruin was altered by looting, some of it rather recent and it can be assumed that many more human alterations occurred in the preceding 1655 years. However, the front wall of the temple proved to be the most earthquake resistant part of the temple. The h/w-ratio, the double shell nature and its north-south orientation contributed to the survival of historic earthquakes of the region. Based on the simulation we cannot exclude that local earthquakes in the Hula Basin (HBF and HCF *Table 5.1*) occurred during the live time of the ruin. The record of the Taiwan Earthquake showed that both sections collapse, when exposed to strong loads. The vulnerability of the Ruin of the Roman Temple of Kedesh to earthquakes depends on the prevailing direction and the amplitude of the ground motion. According to the simulations the sections of the ruin fail to withstand low frequencies of 1 Hz with PGAs of  $6 \text{ m/s}^2$  and above in east-west direction. So in conclusion, in premise that the ruin came to its current appearance during the destruction of the temple on May 19th 363 C.E. a PGA of  $6 \text{ m/s}^2$  has probably not been reached at the site during any earthquake in the past 1656 years.

### 5.7 Further Research

At this point site effects are not considered in this model. For further research the impact of site effects would be interesting to take into account. This would require more field work and additionally seismic on site measurements.

In the presented simulations it could be shown that none of the historic earthquakes by itself toppled the remains of the temple. Another interesting approach would be to apply a sequence of earthquake ground motion to the model, to investigate the cumulative impact of the earthquake sequence.

As shown in *Figure 1.4* the Ruin of the Roman Temple is not the only archaeological structure in delicate shape. The application of the presented approach to other PBASs would help to improve the method and gain more information about the vibration history of archaeological sites where the destruction history may be uncertain.

## 6 CRUSADER FORTRESS ATERET

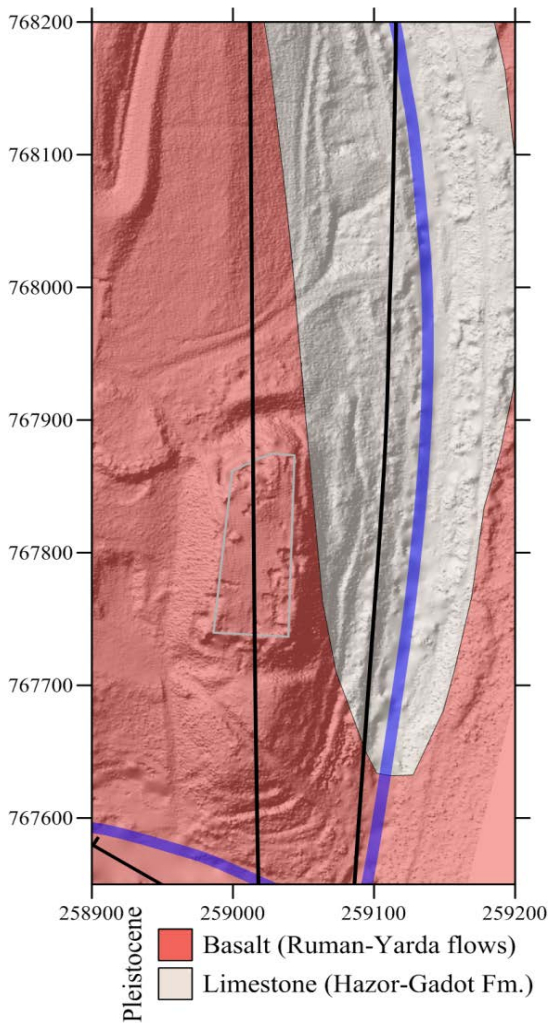


Figure 6.1: Geologic overview of the area around Tell Ateret. The outline of the fortress is marked in grey and the Jordan River in blue. The black lines show the course of the local faults (after Sneh and Weinberg 2006).

The ruin of the Crusader Fortress at Tell Ateret is an interesting site for archaeoseismological research, because it was constructed directly on top of the DSTF. The remains of the fortress are located about 15 km north of the Sea of Galilee (*cf. Figure 2.5*) on a small basalt ridge on the western bank of the Jordan River. The massive fortification walls of the fortress show an offset that is related to the left-lateral movement along the fault (Marco *et al.* 1997, Ellenblum *et al.* 2015). The deformation of the crusader fortress is associated with two earthquakes (Marco *et al.* 1997, Ellenblum *et al.* 2015): the first occurred on May 20th 1202 with an estimated magnitude of  $M_S = 7.6$  (Ambrasyes and Melville 1988) and the second on October 30th 1759 with  $M_S = 6.6$  (Ambrasyes and Barazangi 1989) (*cf. Chapter 2.4.3*). In all previous studies, the dislocation of the wall has been interpreted as a direct effect of the two earthquakes. However, the question has to be asked, whether the full amount of dislocation is of coseismic nature or if for example post-seismic creep contributed to the total observed dislocation. This question is particularly important as creep motion at the DSTF has been documented (Ben-Menahem 1981) and also recent GPS measurements (Hamiel *et al.* 2016) reveal some creep motion at the JVF south of the Sea of Galilee.

Although the measurements do not show recent creep motion at the JGF, it cannot be ruled out a priori for the last 834 years. Theoretically a total offset of 3.42 m since the construction of the fortress would be possible, assuming the current estimates of long term displacement rates of 4-6 mm/yr (Wdowinski *et al.* 2004, Gomez *et al.* 2007a, Sadeh *et al.* 2012). The consequence of a slow motion component in the deformation process would make a difference in the magnitude estimate of the earthquakes, because the latter depends among other parameters on the observed coseismic surface dislocation.

At this point numerous questions regarding the seismic history of the site can be raised. It is certain that during the last 834 years two major earthquakes occurred in close vicinity of the site. However, it is uncertain in which way the ground motion of the earthquakes affected the ruin of the crusader fortress. To find out more about the ground motion history of the site, a DEM model of the northern fortification wall has been developed in the course of this work to investigate the dislocation velocity that has offset the fortification wall of the ruin of the crusader fortress.

The key questions to be answered with the model are:

1. Does the dislocation velocity affect the deformation pattern of the fortification walls?
2. Is it possible to decide, based on the deformation pattern of the wall, whether the total offset is the result of a rapid coseismic movement or slow creep movement has to be considered as well? Can new insights be gained on the dislocation velocity of the individual events?
3. Is it possible to discern the amount of slip by which the two sides of the fault contributed to the total displacement? And in case of a coseismic displacement, a follow up question is: Is it possible to distinguish between the effects of the two earthquakes?
4. How do the results compare to preceding research?

In the following sections the steps towards the development of the final DE model are described including the site history and the reconstruction of the original state prior to the 1202 earthquake. Then the results of the simulations addressed to answer the above mentioned questions are presented.

### 6.1 History of the Site

After the victory of the battle of Montgisard in 1177 the crusaders wanted to consolidate their power in the Muslim frontier area in northern Israel (Ellenblum 2007). Frankish crusaders started therefore the construction of the fortress at Tell Ateret in October 1178 (Braber 1998, Ellenblum *et al.* 1998, Ellenblum 2007), which would have enabled the crusaders to control the only crossing of the Jordan River between its source in the north and the Sea of Galilee, a crucial part of the connection between Acre and Damascus (Ellenblum *et al.* 2007). According to historical records the former King of the Muslims Salah Al-Din tried to prevent the construction multiple times by offering compensation payments to the Christian King Baldwin IV (Braber 1998). When Baldwin declined all offers and the construction continued, Salah Al-Din resorted to a military solution. The first attack of the Muslims in June 1179 was defended by the Franks (Barber 1998). But in a second attack the Muslims defeated the Crusaders and conquered the unfinished fortress (Barber 1998, Ellenblum *et al.* 1998, Ellenblum 1998, 2007). The historical record reports that this second attack was carried out in a hurry, as the Muslims feared reinforcement troops for the crusaders. Chroniclers of Salah Al-Din documented that Tell Ateret was conquered with a common siege technique of that time. To bring down the massive fortification walls sappers excavated a gallery

beneath the walls. Brushwood was brought into the gallery and lit to destroy the wooden support structures. The first attempt failed and the fire was extinguished. The sappers extended the gallery and when the supporting structures were burned again the gallery with the walls above collapsed. Without the protective fortification walls the Crusaders were not able to withstand the Muslim forces and lost the battle. After the victory Muslims demolished the fortress within a year (Barber 1998, Ellenblum *et al.* 1998, Ellenblum 2007).

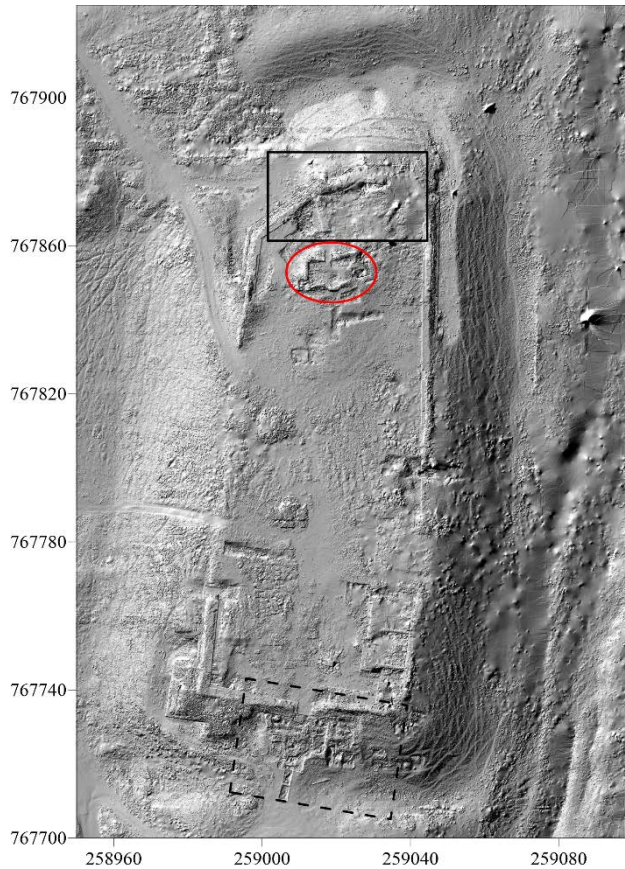


Figure 6.2: Digital terrain model of Ateret in Israeli Transverse Mercator (ITM) coordinate system. The area of interest for this work is marked with a black rectangle. The remains of the mosque are encircled by a red ellipse. The main focus area of Ellenblum *et al.* (1998) is marked with a dashed rectangle (DTM by Hinzen *et al.* 2017).

Archaeological excavation (*cf.* Figure 6.2) revealed that the location has a long record of human settlement (Ellenblum *et al.* 2015). From oldest to youngest the following structures were found: Fortification walls from the Iron Age IIA (980-830 BCE); remains from the Hellenistic period (333-63 BCE); the Crusader Fortress of Ateret (1178-1179); and a Mosque from the Ottoman period (1517-1917). All these structures are offset, which is related to the left-lateral movement along the DSTF. Due to missing parts, the offset of the Iron Age IIA remains cannot be estimated. Walls of the Hellenistic structures are dislocated 6 m (Ellenblum *et al.* 2015). At the southern wall of the crusader fortress the excavators measured a total offset of 2.1 m. The youngest structure the Ottoman Mosque is offset by 0.5 m (Marco *et al.* 1997, Ellenblum *et al.* 2015). It is evident that the offset increases with the age of the affected structures. Ellenblum *et al.* (2015) interpreted the offset as coseismic effect of several earthquakes that accumulated in the structures. In Figure 6.3 the sequence of events that shifted the structures at Tell Ateret are summarized.

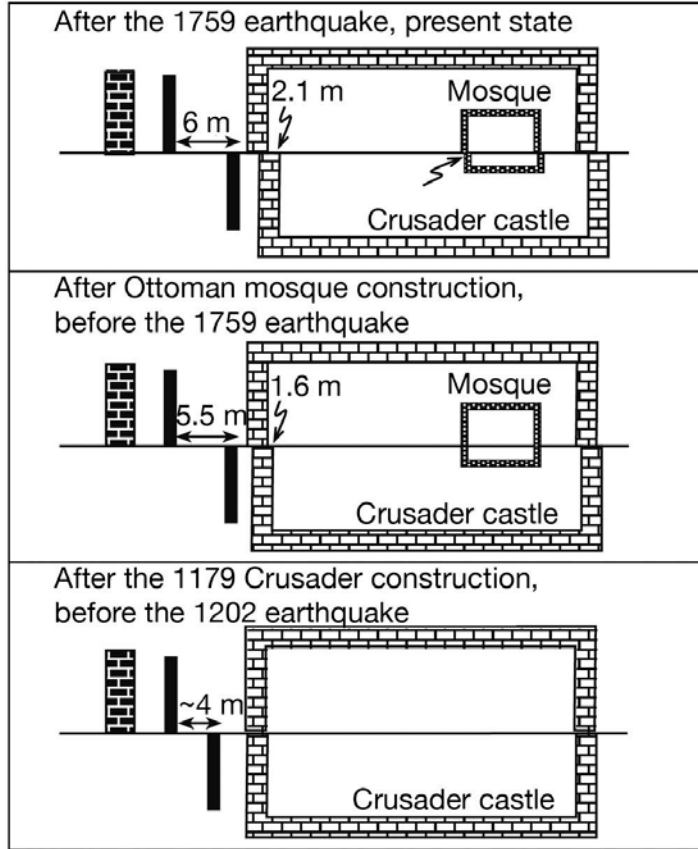


Figure 6.3: Schematic illustration of the stages of accumulated slip (values are rounded) in the Ateret structures since 1179, timeline from bottom to top (after Ellenblum *et al.* 2015).

Christian writers. Due to misleading records and confusion in calendar conversion the earthquake was first listed with multiple entries in numerous catalogs. In their work, Ambraseys and Melville (1988) reviewed primary sources, such as original reports of witnesses and include “*local histories and documentary material, general chronicles, diaries, private correspondence and travel narratives*”, to clarify the correct date, location and scale of the event. The sources reported intensities from VIII to IX in a wide area, ranging from Nabulus (south of the Sea of Galilee) to Arqa (Libanon) (Ambraseys and Melville 1988). The magnitude estimation was based on intensity attenuation relationship, based on the earthquake catalog for the Baltic region by Shebalin *et al.* (1974) (Eq. 6.1 ):

$$M_S = 0.40 + 0.45(I_i) + 2.8 \times 10^{-4}(R_i + 1.8 \log(R_i)) \quad (\text{Eq. 6.1})$$

Where  $I_i$  is the intensity and  $R_i$  is the radius of the isoseismal of  $I_i$ . Due to the widespread area of effect of the earthquake the authors were not able to determine the exact location and the extent of the epicentral region. However, they pointed out that the area between the upper Jordan and the area around Baalbek (Libanon) experienced the strongest impact from the earthquake.

After 1179 two earthquakes occurred that are potentially accountable for the offset of the crusader fortress (Marco *et al.* 1997, Ellenblum *et al.* 1998). A strong, widely felt earthquake at May 20th 1202 and a smaller event on October 30th 1759. First macroseismic information of these events were mentioned by Sieberg (1933) and are objects of research since then.

Ambrasyes and Melville (1988) estimated an  $M_S$  7.6 for the event on May 20th 1202 by analyzing available historic macroseismic information. The earthquake was felt in a large area with an averaged radius of 1200 km and is associated with a tsunami event between the Syrian and Lebanese coast and Cyprus (Salamon *et al.* 2007). The shaking was documented in numerous historical records by Muslim and

The second earthquake which affected the remains of the fortress occurred on October 30th 1759. Ambraseys and Barazangi (1989) estimated an  $M_S$  6.6 again based on the intensity and the radius of the isoseismal of the area in which the earthquake was felt. Following Ambraseys and Finkel (1987) the felt magnitude  $M_F$  (Eq. 6.2) is equivalent to  $M_S$ .

$$M_F = -0.53 + 0.58(I_i) + 1.96 \times 10^{-3}(R_i + 1.83 \log(R_i)) \quad (\text{Eq. 6.2})$$

With this a magnitude of  $M_S$  6.6 has been estimated. Sbeinati *et al.* (2005) derived intensities up to VIII from numerous historical records. In Safed about 15 km west of Tell Ateret an intensity of VII has been reported. This event is considered to be a strong “foreshock” of the  $M_S$  7.4 earthquake on November 25th 1759 (Ambraseys and Barazangi 1989).

The exact sources of the May 1202 and both 1759 events are controversial, because the macroseismic information cannot resolve exactly on which fault the earthquakes originated. Daëron *et al.* (2005) narrowed down the sources of these events based on paleoseismological on fault evidence. They concluded that the 1202 earthquake ruptured along the YF and afterwards the fault remained locked. The estimated potential fault length ranges from Tell Ateret, south of the Hula Basin about 200 km north into the Lebanon. They located the sources of the events on October and November 1759 on the RaF and Serghaya Fault (SF) respectively. The SF extends the RaF in north-eastern direction. The RaF section has a potential rupture length of about 50 km and is associated with the “foreshock” in October 1759. The “mainshock” in November originated on the SF section with a potential rupture length of about 140 km.

Marco *et al.* (1997) have been the first who associated the 2.1 m offset observed at the southern fortification wall of the Crusader Fortress at Tell Ateret as a coseismic effect. In their work they estimated a potential  $M_S$  7.4 earthquake with an average slip of 2 m. In the following research at Tell Ateret findings of Ellenblum *et al.* (1998, 2015) supported these assumptions. The researchers assigned the smaller offset of 0.5 m of the Ottoman Mosque to the October 1759 earthquake and the remaining 1.6 m offset of the fortress walls to the May 20th 1202 earthquake. Independent studies support these assumptions, Marco *et al.* (2005) found about 15 km south of Tell Ateret in 2 m depth four paleo channels in a paleoseismic survey, of which the older two were offset 2.7 m and the younger 0.5 m. The minor shift was attributed to the October 1759 earthquake based on radiocarbon dating. The researchers assigned the remaining 2.2 m offset to the May 20th 1202 earthquake. These offset corresponds well with the archaeological findings at Tell Ateret.

## 6.2 Reconstruction of the Original State

First an initial model had to be created, which comprised the starting point for all simulations. This required a conscientious reconstruction of the northern fortification wall. The process was based on information derived from 3D laser scans of the deformed wall, a digital terrain model (DTM), archaeological data and historical information. The current state of the excavated wall was precisely surveyed with 17 individual 3D laser scans. To capture a complete image of the deformed wall, the scanner was placed at locations outside the fortress, beneath the canopy, built over the ruptured section of the wall as protection against weathering and inside the fortress. Scanner positions are shown in *Figure 6.4 (a)*. Additionally, a DTM of the surroundings of the ruin of the Crusader fortress (*Figure 6.2*) was made by Hinzen *et al.* (2017) with a terrestrial laser survey, which had a grid spacing of 0.05 m.

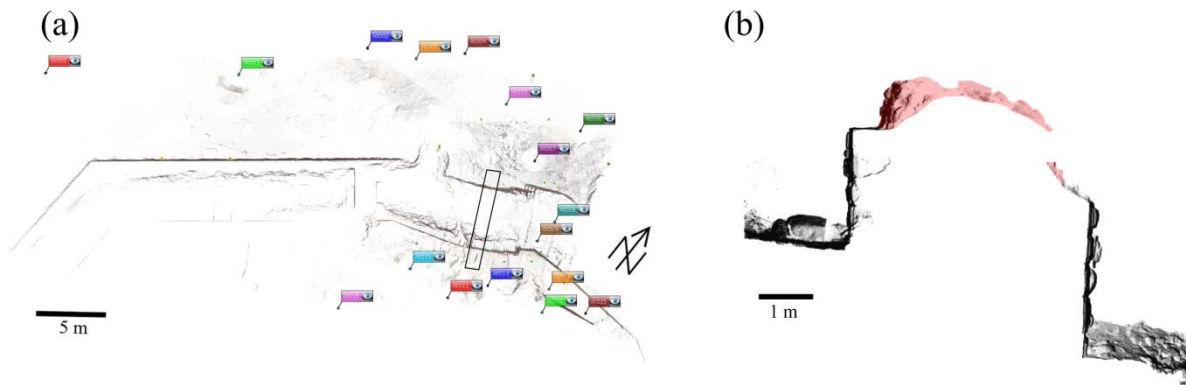


*Figure 6.4: (a) Correspondence view of the section of the fortress which is marked with the black rectangle in Figure 6.2. The colored labels mark the scanner positions. The black rectangle in (a) marks the cross-section of the wall shown in (b) The outer(northern) shell of the fortification wall is on the right and the inner on the left side. The top of the filling between the two walls is highlighted in red.*

The double-shell masonry of the fortress is comparable to the Roman *opus implectum*. The outer and inner shells were made of well-worked ashlar and the interspace was filled with a mixture of basalt cobbles and mortar highlighted in the cross-section *Figure 6.4 (b)*. Because large parts of the wall west of the deformation were not excavated the wall line of the inner wall is not fully visible in *Figure 6.4 (a)*, the same applies to the course of the outer shell east of the deformation, where the remains were still buried.

In *Figure 6.5* the current state (2013) of the northern wall was documented; (a) and (c) show the offset of the eastern part of the northern wall. Left and right of the offset the material of construction ramps was still *in situ*. The western part of the northern wall (*Figure 6.5 (b) and (c)*) was excavated on the outside of the fortress and did not show any deformation. This is also evident in the top view of the point cloud in *Figure 6.5 (d)*. The top view in *Figure 6.5 (e)* clearly shows the deformation. In order to address the key

questions stated above, the actual displacement at the fault had to be determined. The displacement at the fault could only be deduced from the observed dislocation of the wall. However, measuring the actual displacement of the walls was hampered by the not trivial reconstruction of its original position. From the laser scan model an offset of 1.75 m was estimated, the crack in the wall had an offset of about 0.5 m.

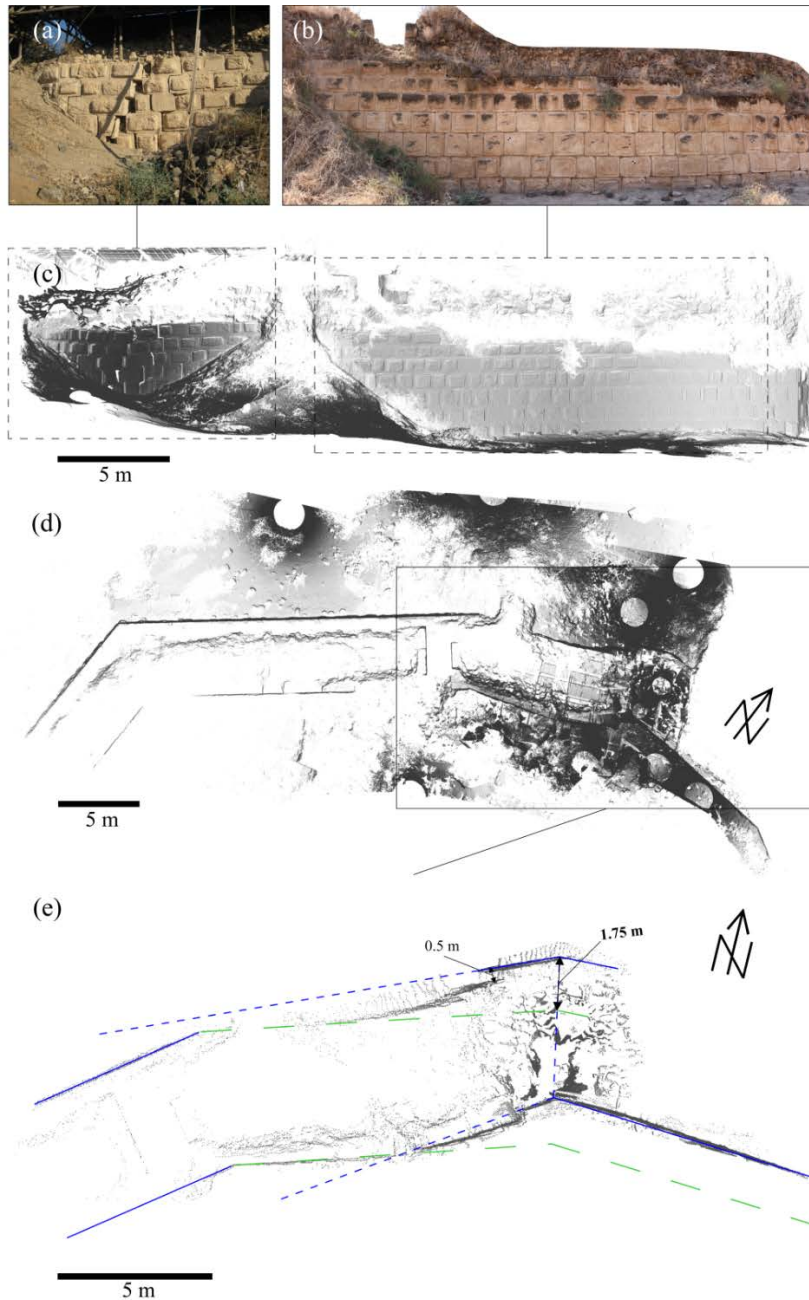


Figure 6.5: (a) Photo of the offset wall from outside of the fortress (view from north to south). (b) Photo of the wall west of the offset from outside of the fortress. (c) 3D laserscan model of the northern wall seen from the outside of the fortress. The sections covered by the photos from (a) and (b) are marked with dashed rectangles. (d) Top view of the scan model of the northern fortification wall. The section inside the rectangle is magnified in: (e) Laser scanning points are shown in grey. The blue solid lines mark the current position of the ruptured wall. Blue dashed lines are the extrapolation of the current wall position while the dashed green lines show the inferred original position.

In the DTM and the laser scans the course of the current fortification walls (*cf. Figure 6.1, Figure 6.2, Figure 6.4 and Figure 6.5 (d)*) is visible, which provides important information about the basic geometry of the original structure. As mentioned above the forces of Salah Al-Din demolished the fortress after the victory, but obviously the lower parts of the fortification wall survived the grinding. When researchers started excavating the remains of the fortress were still covered. They assumed that when the fortress was abandoned, the inside and outside of the walls were partly covered by the construction ramps, except of the upper three block rows (*Figure 6.6 and personal communication S. Marco*). In *Figure 6.6* it is noticeable that layers of the ramp match the heights of the remaining block rows of the wall. As shown in *Figure 6.5* parts of the ramps were untouched by the excavation. It is a valid assumption that most parts of the walls were covered by soil during the last 834 years. During the excavation the researchers also found that the inner shell was based on a higher ground-level than the outer shell due to a slope in the natural terrain (*cf. Figure 6.4*). The height difference between the foundations basis was about 1.5 m (*personal communication S. Marco*), which is also evident in the 3D laser scans (*cf. Figure 6.4 b*).



*Figure 6.6: Photo of the northern wall from outside the fortress during the excavation. On the right the well worked blocks are already excavated. On the left-hand side the structure of the construction ramps is clearly visible. Black lines mark features inside the ramps that align with the rows of the wall (Photo by Marco in 1995).*

In the 3D point cloud the absolute offset of the northern fortification wall was measured to be 1.75 m (cf. *Figure 6.5 (e)*). For the reconstruction process the position of the course of all structures located east of the fault line were shifted 1.75 m in southern direction, the position of the structures west of the fault line remained in their position. It is worth mentioning that this does not imply the reversal of the actual ground motion, but it was a workable solution to reconstruct the original geometry of the northern fortification wall. For the reconstruction some general assumptions were made: the fortification wall had equal width of 4.4 m around the fortress; corner angles of the inner and outer shell were equal.

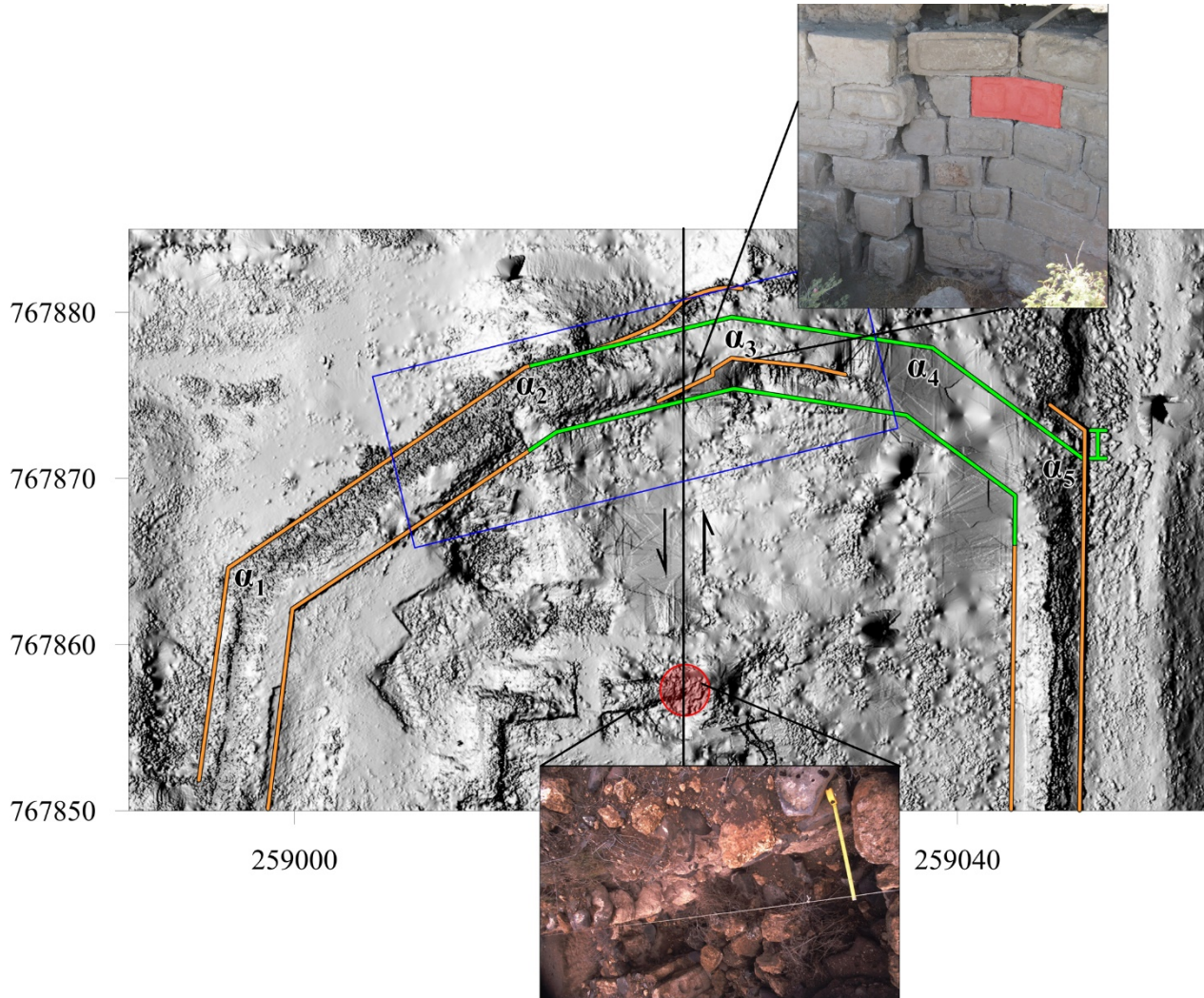


*Figure 6.7: Reconstruction of the original wall course. The orange lines mark the current course of the inner and outer shell. The green lines mark the reconstructed course of the inner and outer shell. The green marker on the north-eastern corner indicates a 1.75 m shift between the current wall line and the assumed original position. The red circle highlights the offset of the Ottoman Mosque, which is also shown in the lower photo (by Marco in 1995). The upper photo shows the offset of the inner shell. The red highlighted block was fitted by the stonemason to extend over the corner. The angles of the corners are marked by  $\alpha_1$  to  $\alpha_5$ . The blue rectangle marks the section of the fortification wall which is part of the DE model. The black line indicates the course of the DSTF, the arrows indicate the relative direction of movement (DTM by Hinzen et al. 2017).*

Angles of the corners  $\alpha_1$ ,  $\alpha_2$  and  $\alpha_5$  (*Figure 6.7*) could be measured in the DTM, the assumption was that the bending of the corners was not significantly deformed from their original shape.  $\alpha_3$  could not be measured directly in the DTM because the corner was heavily deformed. However, some blocks were fitted by the stonemason to extend over the corner (*Figure 6.7* upper image) and the angle of  $22.5^\circ$  could be measured in the detailed 3D point cloud on an intact angled block. There was no information about  $\alpha_4$ , because this section of the fortification wall was still covered, therefore, this was completely constructed. Based on the estimate of an offset of 1.75 m at the fault, the corner  $\alpha_5$  was shifted by this amount in southern direction to reconstruct the original position. From this point the reconstructed wall line was plotted with the angle  $\alpha_5$ . From east the course of the fortification wall was well recognizable. From the corner  $\alpha_2$  the angle of the outer shell is visible in the DTM. The measured angle of  $20^\circ$  was confirmed in the detailed 3D point cloud (*cf. Figure 6.5 (e)*). When applying the  $22.5^\circ$  angle to the corner  $\alpha_3$  the wall course from the eastern and the western, coming from  $\alpha_5$ , match well.

In summary the initial model had to represent a 4.4 m wide fortification wall of *opus implectum* style, which was angled at two points with  $20^\circ$  and  $22.5^\circ$  respectively. The exact course of the wall lines is shown in *Figure 6.7* (inside the blue rectangle). The shells were built by well worked ashlar with mortared joints, the inner shell was based on a foundation 1.5 m higher than the outer shell, while both shells ended at the same height. The space between the shells was filled with a mixture of mortar and basalt up to the top of the shells. The inner and outer shell were mostly covered with a construction ramp made of densified soil, only the three uppermost ashlar rows were exposed.

### 6.3 Model Creation

The development of the initial model was separated into four steps to avoid errors that might be introduced due to the complexity of the model. Each step focused on certain structural elements of the model:

1. the inner and outer shells, composed of discrete limestone blocks of mainly rectangular shape;
2. a baseplate with different height levels capable of following the chosen boundary conditions representing the slip along the fault line;
3. the fill between the shells, a mixture of basalt cobbles and mortar;
4. the ramps covering both sides of the wall composed of densified soil.

Not only the implementation of the basic geometry was important. The model also had to reflect properly the response of all structural elements to the applied boundary conditions. Therefore, the correct functionality of the model and the software code was constantly controlled during the development process. This required often the development of smaller ‘proof of concept’ models, which only simulated specific aspects of the larger final model.

Different software solutions were tested to realize this challenging model. In UM a preliminary simple model was developed, composed by one shell with both flanks angled by  $30^\circ$  on a two-part ground plate. However, for different reasons the development did not exceed this basic status. One problem was that numerical artifacts lead to ‘random explosions’ without apparent reasons. But the major problem was that the simulation of the displacement with only one shell caused large computation times and it was foreseeable that the simulation times of the complete model would not be viable. Further challenges were the realization of the filling between the walls and of the construction ramps. Another modeling approach was started with Blender (which could ultimately be exported to Unity). This attempt was discontinued, because apart from some minor problems the missing possibility to model all geotechnical features and material properties were a major obstacle.

The modeling of the northern section in 3DEC was started with the program Version 5.0. After successfully testing the software code with preliminary models containing a simple wall on a fault, a more complex model had to be developed. *Figure 6.8* shows the basic model geometry. It included the first three structural elements listed above. The first effort was to create a functional model with these units that was stable under static load. The fourth structural element, the ramps, was added later to the model. This separation during the model development is important to avoid errors in the final model.

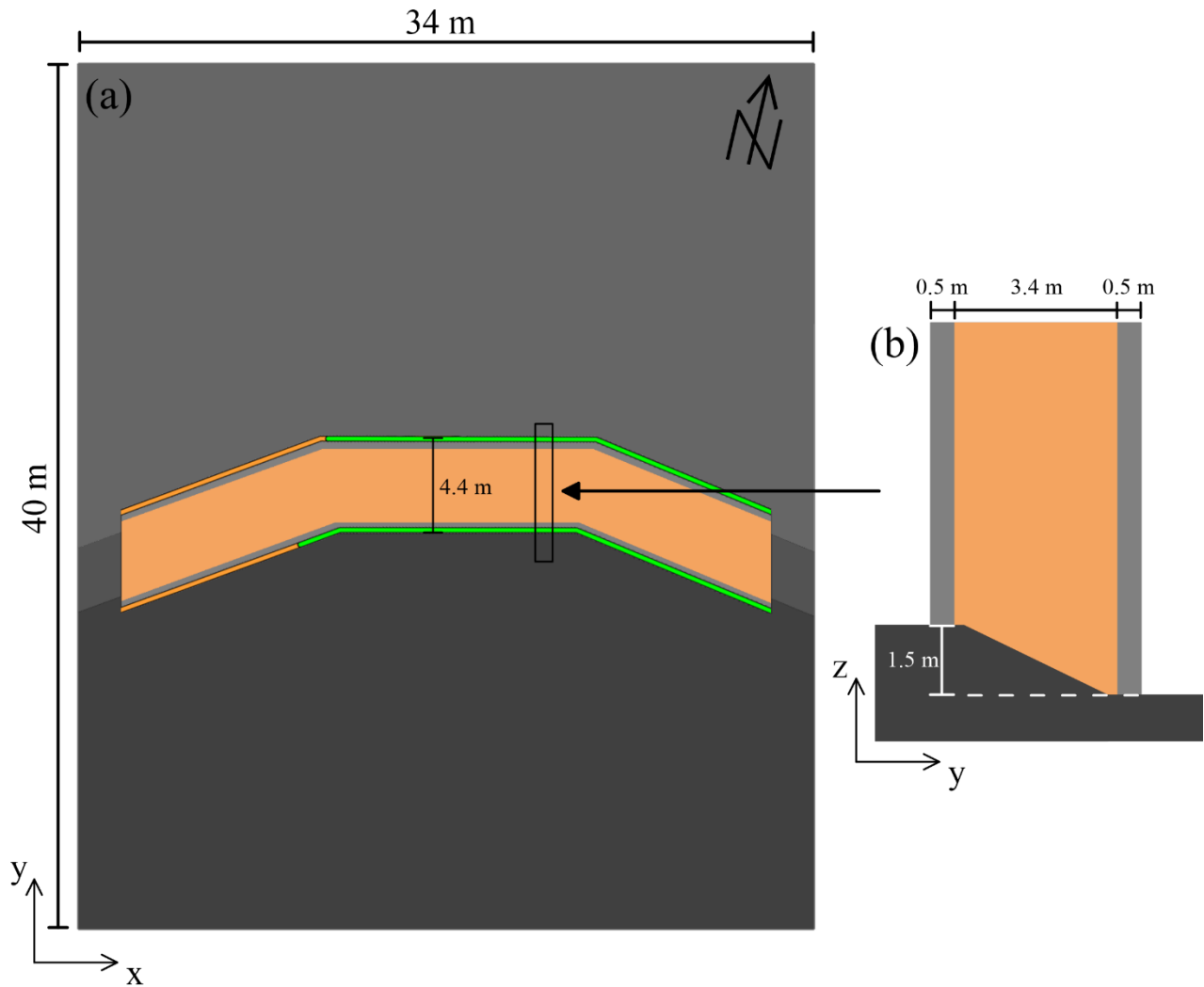


Figure 6.8: Composition of the 3DEC basic block model for Ateret. (a) Top view to the baseplate shown in dark grey. The lower part is slightly lighter in color than the higher part. The light grey blocks represent the inner and outer shell. The reconstructed wall course line is shown in orange and green (cf. Figure 6.7). The block for the filling is shown in orange. The black rectangle marks the part which is shown in (b). Side view to the cross-section. The axes show the direction of the model coordinate system.

3DEC allows to easily separate larger volumes into smaller discrete elements. Therefore, the basic model geometry was represented by eight simple blocks, which were cut later. Each structural unit was composed by one or more blocks. The baseplate with the dimensions 34 m x 40 m was composed of three joined parts, a left, a central and a right block. The cross-section (Figure 6.4 (b)) shows that the inner and the outer shell were founded on different elevation levels, due to the conditions of the natural terrain. Therefore, the baseplate incorporated the two different ground-levels with a height difference of 1.5 m as shown in Figure 6.8 (b). The inner and outer shells were each one block with flanks angled by  $22^\circ$  and  $22.5^\circ$  respectively. Both shells had a width of 0.5 m. The outer (northern) shell had a height of 8 m and the inner (southern) of 6.5 m, respectively. The 3.4 m wide filling between both sections were composed of

three joined blocks and fit between the sections. Joined blocks in 3DEC are handled as one unit. From this basic geometry the blocks could be split into more complex structures.

The block model reflected the reconstructed basic geometry of the northern fortification wall, but was lacking functionality such as applying movements to the baseplate and movement of the shells or inside the filling. To add the functionality to the model the blocks had to be separated into discrete elements. The baseplate was separated into two sections with the fault line striking with  $13^\circ$  from the y-axis. Different boundary conditions, such as a movement, could be applied to both sections independently. The simple blocks representing the shells were split by horizontal cuts into twelve rows. With vertical cuts the rows were separated into distinct blocks representing the well worked ashlars. Each block was a discrete unit and could move in each direction. During the development process adding proper functionality to the filling turned out to be not straight forward. The challenge was to transform the block representing the filling so that it mechanically behaved in a way as a mixture of basalt cobbles and mortar. 3DEC in general provides in general two different approaches which could be applied to this problem: rigid and deformable blocks. A solution with deformable blocks was omitted. On the one hand the inhomogeneous nature of the filling could hardly be represented by one deformable block and on the other would deformable blocks add a computational overhead to the model (3DEC Manual 2016). Therefore, the filling was realized with rigid blocks. The general idea was to separate the filling into numerous smaller blocks to ensure the mobility inside the filling. Different cutting geometries were tried out, ranging from regular parallel cuts to irregular cutting geometries using DFN (*cf.* Section 4.6). When a ground motion was applied to the base plate the individual blocks of the filling interacted in such a way with each other that additional unwanted artificial movement was implied to the model.

With 3DEC version 5.2, Itasca released an upgrade of the software including new features. The key feature important for this work was the implementation of the Bonded Block Model (BBM), which allows automatically separate continuums into numerous polyhedral elements (3DEC Manual 2016). With this method a 4 m wide section of the filling located above the fault line was separated into numerous tetrahedral blocks with an edge length of 0.5 m. The intention was to reduce the overall number of blocks in the model and the results of tests were promising. But the close confinement hampered the movement in the filling and therefore the complete filling between the walls was cut into tetrahedral blocks with an edge length of 0.5 m. In this approach the tetrahedrons represented the basalt and the joints the mortar between the basalt cobbles.

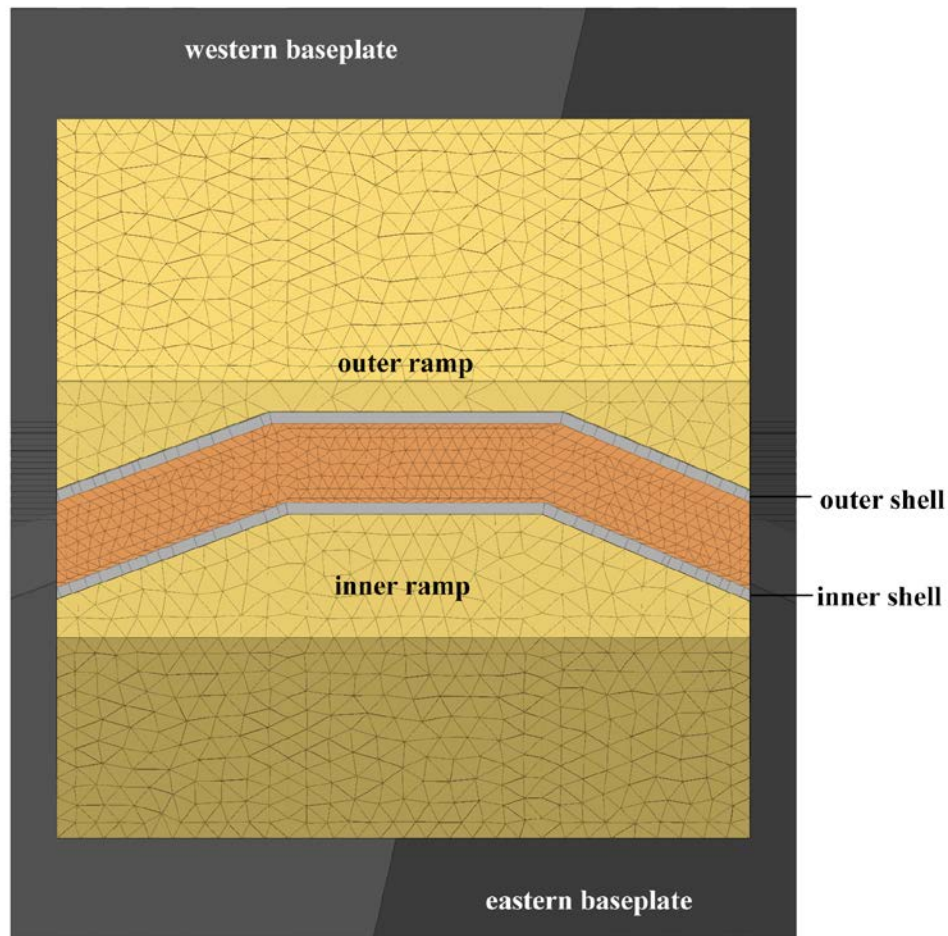


*Figure 6.9: Discrete element model of Ateret walls top view. In sandy-yellow are the ramps inside and outside the castle. The inner and outer shell are shown in light grey color. The filling is colored in orange. The eastern baseplate is in a basaltic dark grey and the western in a medium grey.*

After the promising tests using BBM to enable the movement in the filling this technique was also applied to model the ramps. Each ramp was represented by one unit of three joined blocks, which was then separated into numerous tetrahedral blocks with an edge length of 1 m. The geometry of the construction ramps was built in such a way that most parts of the shells were covered with an assumed horizontal working area close to the wall and an outward slope of  $30^\circ$ . To stabilize the boundaries of the model confining walls prevented blocks from dropping to the side. Tests showed that these retaining walls were far away enough to prevent influence on the fracture zone. The finished model was composed in total by 52,864 rigid blocks (*Figure 6.9*). For the simulation appropriate material properties had to be applied to each structural element. The exact material properties of the different elements were not known and some approximations from the literature had to be taken. The source material of the limestone was comparable with the limestone of the Hazera Formation (personal communication Marco), whose material properties

were published by Kamai and Hatzor (2008). The material parameters of the mortar were taken from Krausz (2002). The density for the basalt is in range of the values published by Bourbie *et al.* (1987). The material properties of the ramps represent densified soil following Bowles (1996). *Table 6.1* summarizes the chosen material properties:

*Table 6.1: Material properties for the blocks in the DE model of the northern wall of Ateret fortress: Limestone, Hazera Formation (after Kamai and Hatzor 2008), Basalt (Bourbie et al. 1987) and Mortar (Krausz, 2002), Densified soil ( from Bowles, 1996). Fields marked with \* are not necessary for the model*

	Density	Young's modulus	Poisson ratio
Limestone	1890 kg/m <sup>3</sup>	17 GPa	0.37
Basalt	3000 kg/m <sup>3</sup>	_*	_*
Mortar	_*	2.5 GPa	0.17
Densified Soil	2600 kg/m <sup>3</sup>	80.0 MPa	0.3

The normal ( $k_n$ ) and shear-stiffness ( $k_s$ ) of the wall joints were estimated following Bui *et al.* (2017) after Lourenco *et al.* (2005).

$$k_n = \frac{1}{\left(\frac{1}{E_m} - \frac{1}{E_b}\right) * h_b} = \frac{E_b * E_m}{(E_b - E_m) * h_b} \quad (\text{Eq. 6.3})$$

and

$$k_s = \frac{k_n}{2 * (1 + \nu)} \quad (\text{Eq. 6.4})$$

where  $E_m$  and  $E_b$  is the Young's modulus of the mortar and blocks respectively.  $\nu$  is the Poisson ratio of the wall blocks and  $h_b$  is the block height, which is 0.67 m for the outer and 0.54 m for the inner shell.

In order to create a stable start model for dynamic simulations the completed model was set under static load for a model time of 5 s. This completed the development process and the model could be used to address the questions stated above.

## 6.4 Calculations

In total 58 model calculations, which covered different ground motion scenarios, were carried out. As shown in Section 2.3, despite both plates moving north, at the DSTF a sinistral movement between the eastern (Arabian) and western (Sinai) plate is observed, due to different velocities of movement. However, while the differential motion between the two plates is well documented and explored (*e.g.* Freund 1968, Bartov 1980, Garfunkel 1988, McClusky *et al.* 2003, Wdowinski *et al.*, 2004; Mahmoud *et al.* 2005, Reilinger *et al.* 2006, Vigny *et al.* 2006, Le Beon *et al.* 2008), there was no information about the absolute displacement of either side during a single earthquake. In two scenarios different movement combinations that were potentially possible by the tectonic environment were considered. As analytical signal for the ground motion the cycloidal pulse was used in all simulations (*cf.* Chapter 5.4.1). As pointed out by Hinzen and Montabert (2017) the displacement history of a cycloidal pulse is comparable with a simple version of the movement along a strike-slip fault. The model time of the simulations depended on the frequency of the cycloidal pulse and was varied from 2 s to 34 s. One second model time required on average 26 hours of simulation time.

The first scenario focused on combinations of displacement directions (*cf.* Figure 6.10) with various speeds of the plates. Only a single movement at the fault was assumed to be the cause of the dislocation of the fortification wall. Overall the scenario included 22 simulations, in which the total displacement of 1.75 m was applied to the baseplate with different directions and varying velocities ranging from 0.1 m/s to 5 m/s. In nine simulations it was assumed that the western plate was locked and only the eastern plate shifted north (Figure 6.10 (a)). In another six simulations the eastern and western moved with half the total displacement in opposite directions (Figure 6.10 (b)). And in five further simulations the eastern plate was locked and only the western plate was offset south the total displacement (Figure 6.10 (c)). In the last two simulations both plates shifted north with different velocities (Figure 6.10 (d)). As described earlier, both, the Sinai plate and the Arabian plate are moving in northern direction. GPS survey in close vicinity to the JGF revealed that horizontal velocities east of the fault line were about twice as fast as west (Sadeh *et al.* 2012). Therefore, in the model the eastern and western plate were displaced in the same direction with the according velocities maintaining the left sinistral character of the movement. The simulations of this scenario aimed to investigate the effect of different dislocation velocities and movement directions on the model.

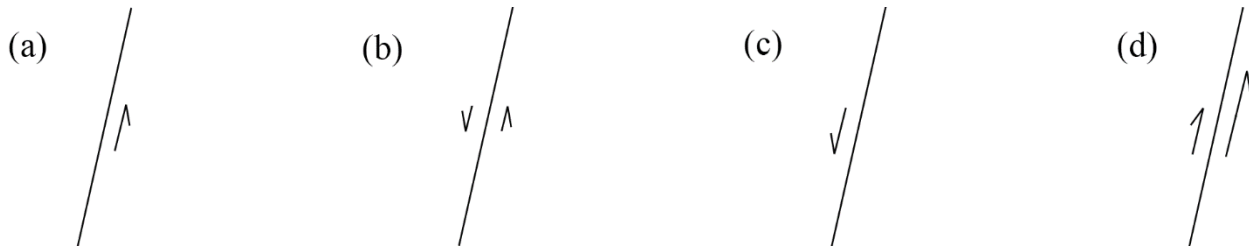


Figure 6.10: Overview of the displacement directions of the first scenario. The fault line indicates the north-south direction, where up is north. (a) the eastern plate is moved north and western plate is locked; (b) eastern plate is moved north and western is moved in opposite direction south; (c) eastern plate is locked and the western plate is moved in southern direction; (d) both plates are moved in northern direction.

The second scenario covered the current hypothesis that two earthquakes dislocated the fortress wall. As shown above the offset of the younger event was estimated to be 0.5 m (Ellenblum *et al.* 2015). Based on the measurement of a total 1.75 m displacement, the preceding earthquake caused a displacement of 1.25 m. Therefore, in six simulations an offset of 1.25 m with different dislocation velocities was assumed. These are in the following denoted as the first stage of the scenario and represent the 1202 earthquake. In a second stage each end status of the first stage was again displaced again by another 0.5 m in five different simulations with ground motion velocities ranging from 1 m/s to 5 m/s. Overall the second stage included 30 simulations representing the 1759 earthquake.

Due to the lack of fix points between the original and current state of the northern fortification wall, the ICP technique (*cf.* Chapter 3) was used as an objective method to estimate the fit between the end state of the simulation and the observation at the site. In 3DEC the coordinates of the vertices of each block at its end position and the displacement vectors were recorded. A dataset of the points located on the outside of the shells was exported and used as the target point cloud for the ICP, in the following this is denoted as ‘calculated points’. The measured points from the 3D laser scanning survey were denoted as ‘measured points’ were used as source point cloud in the ICP algorithm. For the initial alignment the calculated and measured point clouds were placed close to each other manually. As exit criterion a RMS threshold of 0.0001 m was used.

For the interpretation of the results from the numerical tests, two aspects are important: (1) the fit of the deformed structure with the current situation and (2) the situations of currently missing blocks, mainly from the top rows of the inner and outer shells. The first is in the following referred to as deformation of the wall and the latter will be referred to as destruction. The deformation of the fortification wall was a direct effect of ground movement, parameters of which are in the focus of this section. In *Figure 6.5 (a), (b) and (c)* it is evident that currently the filling overtops the shells, *i.e.* ashlars are missing. The history of the missing blocks is uncertain. It is possible that some of the blocks protruding above the construction

ramps have been removed during the demolition by the Muslim forces, or that blocks dropped out of the wall as a coseismic effect during the earthquake(s) or that locals used the remains of the fortress as a quarry during the last 834 years. (Even since our field campaign in 2013 larger blocks have been stolen from the southern part of the wall).

### 6.5 Results

For each simulation a summary, as shown in *Figure 6.11*, is available and gives an overview of the results. In *Figure 6.11 (a)* the relative displacement of the blocks to the displacement of the underlying baseplate is shown. A short vector means the block shifted with the baseplate, but no further movement occurred. A long vector means that the block moved independently from the baseplate which is particularly evident when a block dropped out of the shell. The visualization of the relative displacement helps to track additional movement introduced to the model *e.g.* by inertial forces acting on the wall. In *Figure 6.11 (b)* the absolute displacement vectors of the blocks together with the current state surveyed by the laser scanner is shown. The vector plots give a good impression about the horizontal movement of the model and how good the results match with the measured point cloud. To estimate differences in the movement in respect to the row level of the ashlar, boxplots in *Figure 6.11 (c)* and *(d)* show the distribution of the length of the displacement vectors relative to the baseplate for each block row. The box shows the range first and third quartile of displacement values and the whiskers mark the minimum and maximum displacement that occurs within a row. The median is a good measure how strong individual rows are affected. The boxplots illustrate the differences in the displacement from the bottom to the top row.

Despite giving an overview of the results, these plots are not efficient to compare the results of the various simulations. Therefore, only selected plots are shown in the following which are used to discuss certain aspects, however, all summary plots are listed in the appendix A.

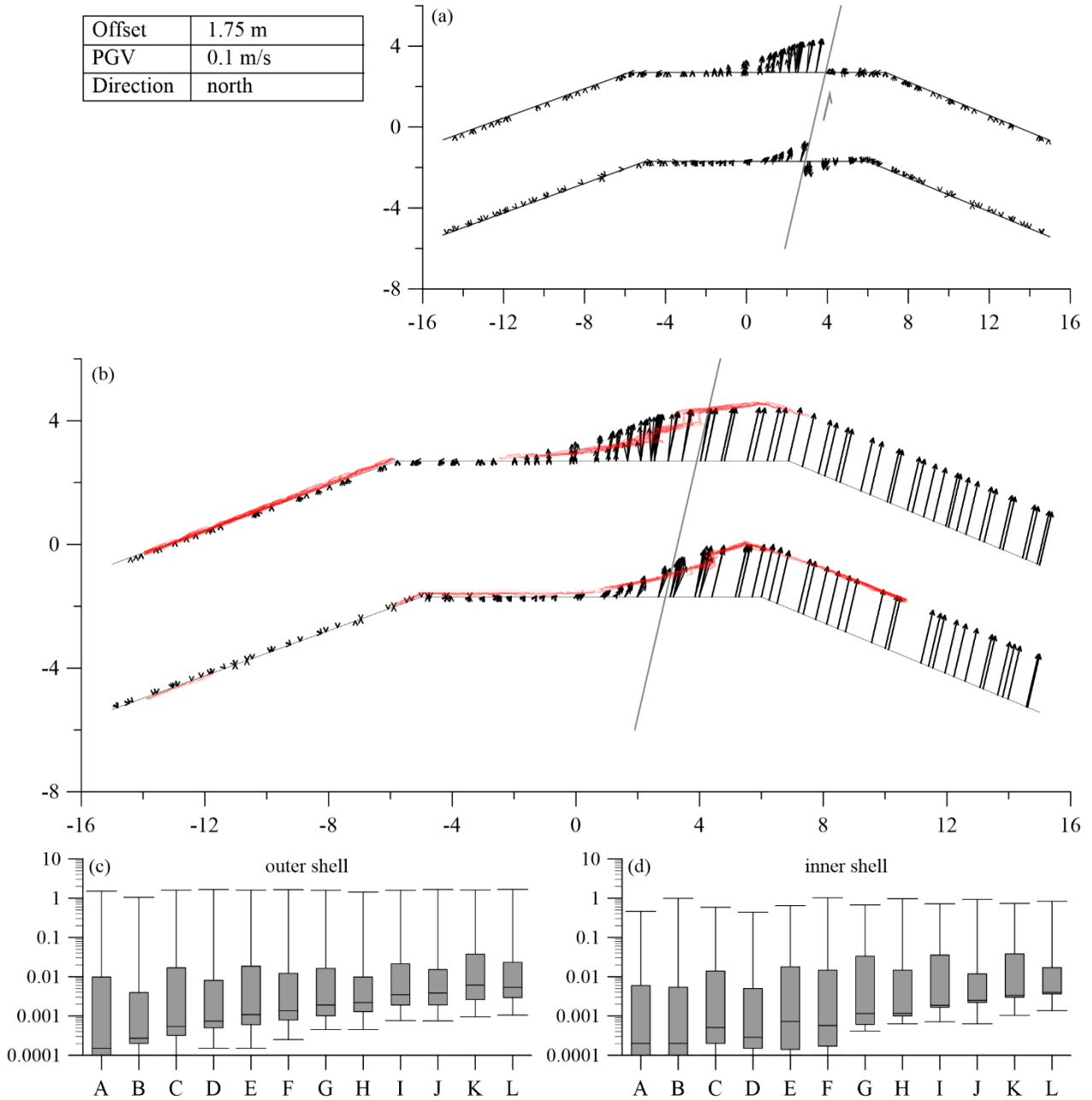
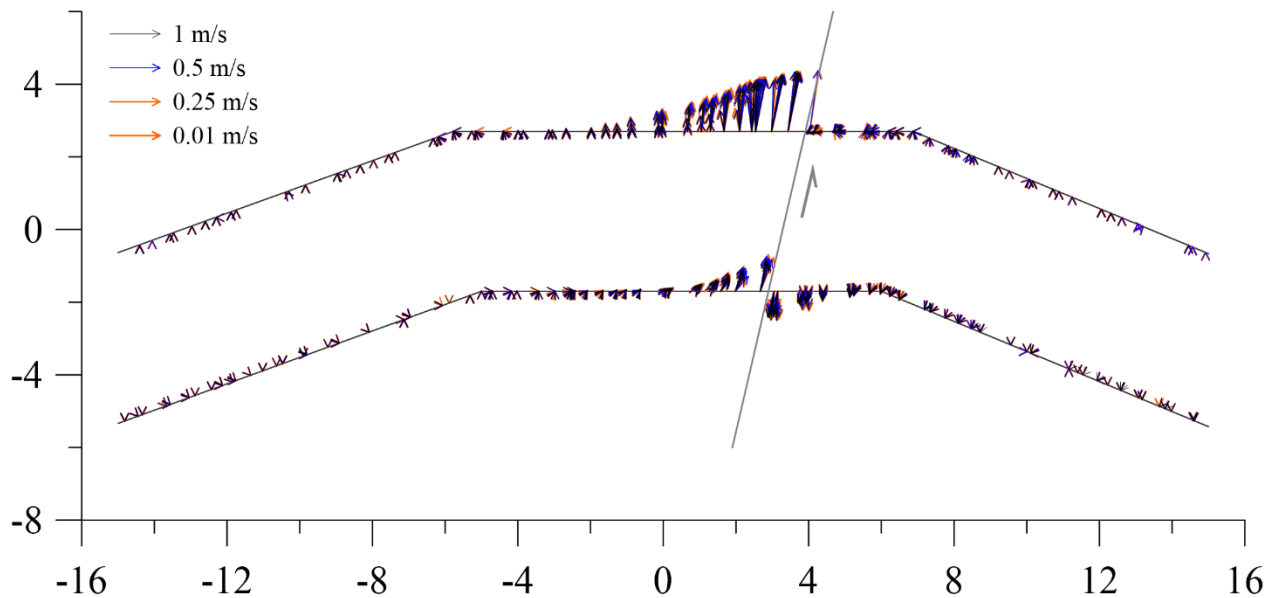


Figure 6.11: Results of the simulation with a cycloidal pulse for a displacement of 1.75 m and a PGV of 0.1 m/s. (a) Displacement vectors of the blocks relative to the displacement of the baseplate beneath the blocks from a top view perspective. The light grey line marks the course of the fault line in the model. The light grey arrows point in direction of the ground motion. The dark grey lines mark the course of the initial wall line. (b) Vector plot of the absolute displacement (m) of all blocks from a top view perspective. The grey line marks the course of the fault line in the model and strikes in north-south direction. The superposed red points are the measured points from the 3D laser scanning survey. (c) Boxplot of the vector length relative to the displacement of the baseplate for all blocks in individual rows with row A: bottom and row L: top of the outer shell. (d) the same as (c) for the inner shell.

### 6.5.1 FIRST SCENARIO

In the first nine simulations of this scenario the eastern plate was shifted by 1.75 m in one motion with slip velocities of 0.1 m/s, 0.25 m/s, 0.5 m/s, 1 m/s, 2 m/s, 2.5 m/s, 3 m/s, 4 m/s and 5 m/s. The results for the simulation with the slowest velocity of 0.1 m/s are summarized in *Figure 6.11*: (a) it is evident that most of the blocks placed on the eastern plate shifted with the baseplate. The only relative displacement was observed close to the fault line and declined rapidly with increasing distance to the fault line. East of the fault line just blocks of the inner shell were shifted in opposite direction of the ground motion. In contrast, the blocks west of the fault line which rested on the locked plate showed large relative displacements. During the movement the fortification wall, enclosed by the ramps, was pulled apart and the blocks on the western plate were pulled along with the moved part of the fortification wall on the eastern plate. The outer shell of the eastern part could not move in opposite direction of the ground motion, because it was pushed by the filling, which in turn was supported by the slope of the two ground levels. The inner shell was only backed by the ramp, which was softer than the filling and could give way. Except for the pull-apart movement no additional displacement occurred, which means that no significant inertial forces acted on the wall. This interpretation is supported by the absolute displacements in *Figure 6.11* (b). All blocks resting on the eastern plate were shifted with the underground and the displacement decreased to the west, where the baseplate was locked. In *Figure 6.11* (c) and (d) it is noticeable that the blocks of the upper rows of both shells were displaced further than the lower rows. The overall median of the relative displacement to the baseplate did not exceed 0.01 m within all rows.



*Figure 6.12: Displacement vectors of the displacement relative to the baseplate of the four simulations with the lowest slip velocities plotted on top of each other. The grey line marks the course of the fault and the grey arrow points in direction of the ground motion. Velocities are indicated by the vector color as shown in the legend, scales are in (m).*

In *Figure 6.12* the relative displacement of the blocks from simulations with the slip velocities between 0.01 m/s and 1 m/s are shown in combination. Most displacement vectors overlap indicating only minor differences between the results of the two tests. Most differences exist at the outer shell close to the fault line. The displacement that occurred in the simulations is due to a pull-apart effect, which was the direct consequence of the ground motion. It can be concluded that in simulations with slip velocities of 1 m/s or less no significant inertial forces contribute to the deformation of the fortification wall.

In simulations with higher slip velocities inertial forces increasingly contributed to the overall deformation. Large parts of the shells were contained between the filling and a ramp, which prevented the covered blocks from tipping over. Two major effects can be observed as response to inertial forces: one is that blocks dropped out of the upper rows, which were not covered by the ramps and second the shells were tilting in or against the direction of the ground motion depending on the failure mechanism. To illustrate these effects of fast ground motion, the results for the simulation with 5 m/s, the highest slip velocity assumed in the tests, are presented in *Figure 6.13*. Blocks dropped out of the outer and inner shell in opposing directions (*cf. Figure 6.13 (a) and (b)*). The blocks dropping out of the inner shell were falling in opposite direction of the ground motion due to the second failure mechanism the blocks of the outer shell, however, fell in direction of the ground motion, following the first failure mechanism. The outer shell was backed by the filling why the blocks could not move in opposite direction of the ground motion, therefore they dropped only during the stopping phase. As a consequence, the pull-apart effect was different on the inner and outer shell. The part of the inner shell east of the fault line was displaced, while on the western side the displacement was negligible. On the outer shell the effect was the other way round, the section west of the fault line was displaced but not the one east of it. It is also evident that some tilting occurred, particularly the inner shell east of the fault line significantly tilted in opposite direction of the ground motion. In contrast blocks of the outer shell moved in this direction at the border of the model. The rest of the blocks were displaced in the direction of the ground motion. Here again the inner shell tilted due to the second failure mechanism, but the outer shell, backed by the filling could only move in the ground motion's direction during the stopping phase. The filling, supported by the slope, hampering the outer shell moving in opposite direction is the main reason for the difference in the response of both shells to the ground motion. Comparing the boxplots for the test with the highest slip velocity in *Figure 6.13 (c) and (d)* to the results of the slowest movement *Figure 6.11 (c) and (d)* it is clear that all rows of both shells were stronger displaced and the upper rows again were more affected than the lower ones.

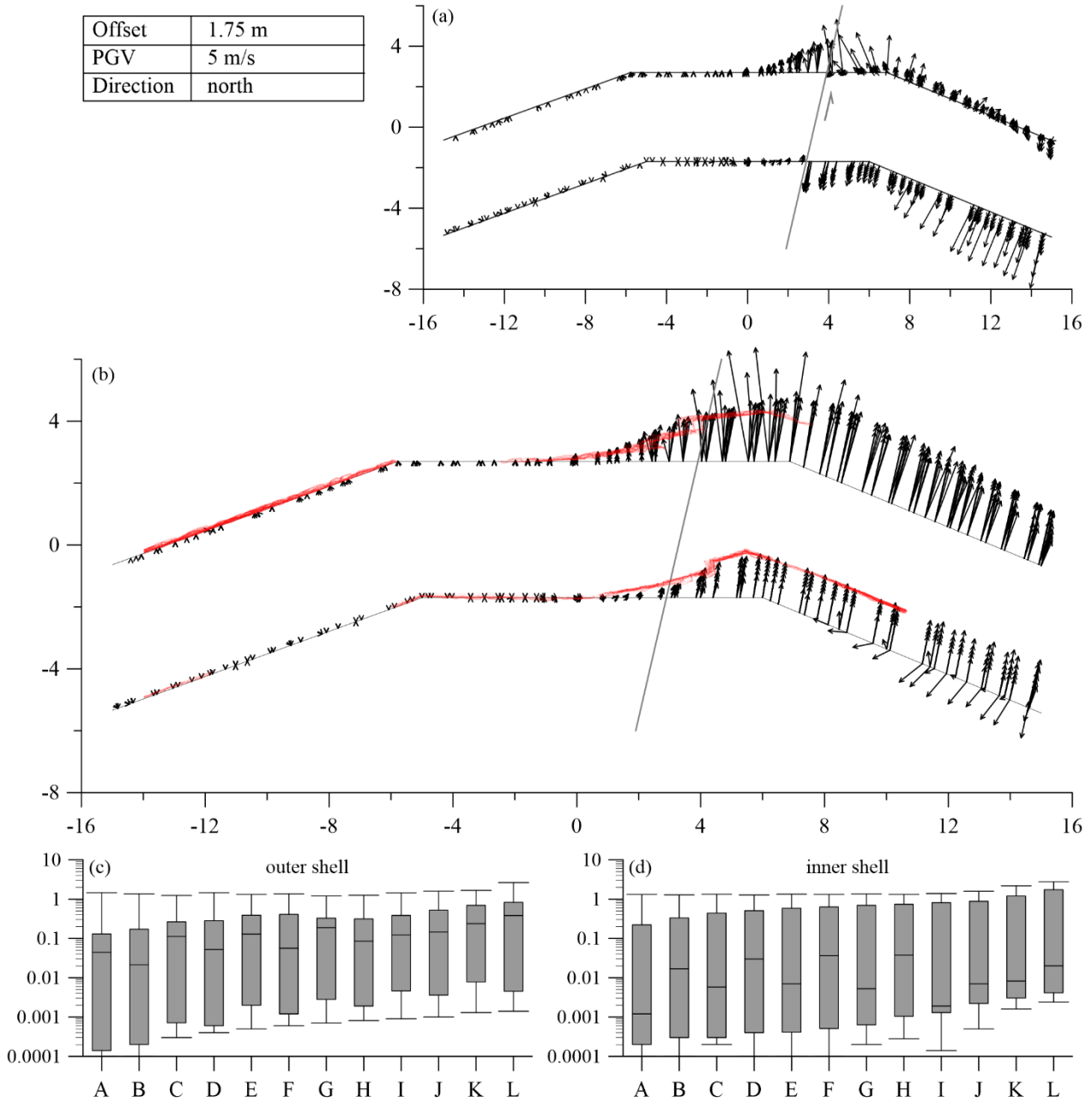
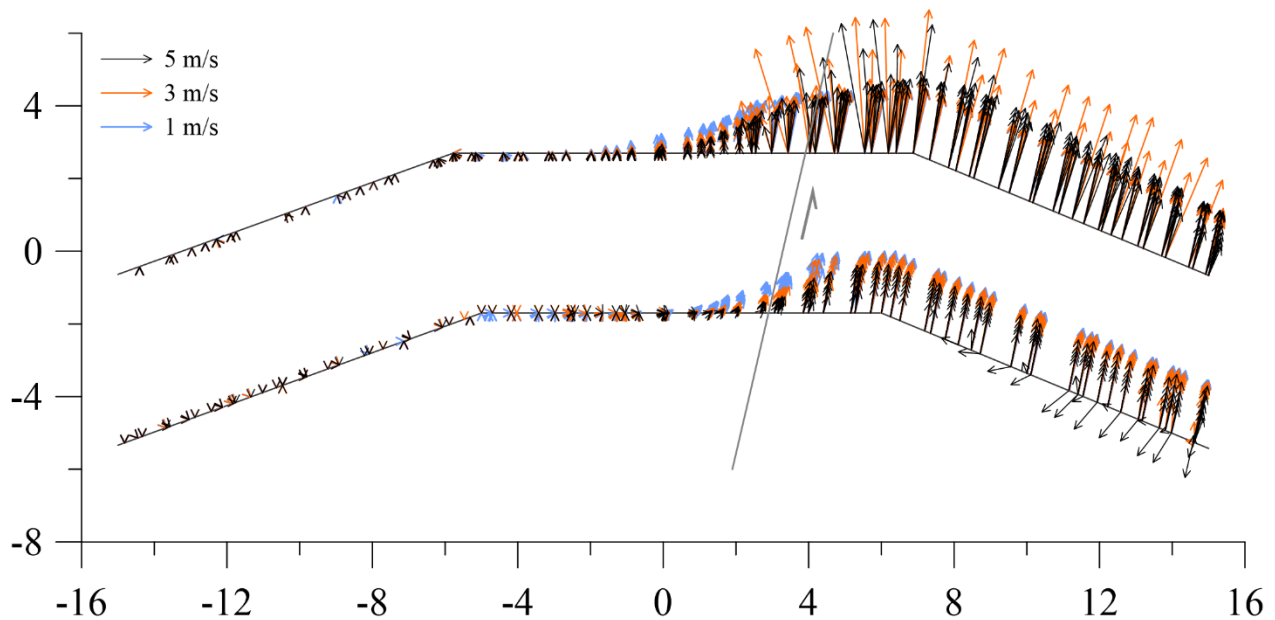


Figure 6.13: Results of the simulation with a cycloidal pulse for a displacement of 1.75 m and a PGV of 5 m/s. (a) Displacement vectors of the blocks relative to the displacement of the baseplate beneath the blocks from a top view perspective. The light grey line marks the course of the fault line in the model. The light grey arrows point in direction of the ground motion. The dark grey lines mark the course of the initial wall line. (b) Vector plot of the absolute displacement (m) of all blocks from a top view perspective. The grey line marks the course of the fault line in the model and strikes in north-south direction. The superposed red points are the measured points from the 3D laser scanning survey. (c) Boxplot of the vector length relative to the displacement of the baseplate for all blocks in individual rows with row A: bottom and row L: top of the outer shell. (d) the same as (c) for the inner shell.

So the slip velocity had significant influence to the outcome of the calculations. In particular, the presence or absence of inertial forces capable of influencing the deformation was decisive for the results of the simulations. The strength of the inertial forces acting on the wall depends on the acceleration, which increased with higher slip velocity, visible in *Figure 6.14* showing the difference in the absolute displacement vectors for 1 m/s, 3 m/s and 5 m/s. Also the pull-apart at low slip velocities deformed the shells at larger distance from the fault line more, than at higher slip velocities, where the deformation was confined closer to the fault-line. At a slip velocity of 3 m/s more blocks dropped out of the outer shell in direction of the ground motion than in the simulation with the higher velocity of 5 m/s, where the tilting effect was more prominent. The strong tilting of the 5 m/s experiment indicated a strong second failure mechanism. The outer shell tilted in the direction of the ground motion during the stopping phase. The minor tilting and numerous falling blocks of the outer shell during the 3 m/s ground motion velocity indicated the first failure mechanism, where the blocks fell during the stopping phase. As shown in Section 5 free standing walls fail due to high inertial forces. Therefore, the strong tilting lets conclude that it is likely that without the construction ramps the fortification wall would have suffered total destruction, which supports the hypothesis that the fortification walls were buried since the demolition by the forces of Saladin.



*Figure 6.14: Displacement vectors showing the absolute displacement of ashlars during simulations with the displacement velocities ranging from 1 m/s, 3 m/s and 5 m/s plotted on top of each other. The grey line marks the course of the fault and the grey arrow points in direction of the ground motion. Velocities are indicated by vector color as shown in the legend, scales are in (m).*

This first nine simulations provide vital information of the model behavior under increasing slip velocities. As shown in *Figure 6.12* when no inertial forces influence the deformation, further reducing the slip velocity does not change the outcome of the simulations. So the experiment with the lowest velocity of 0.01 m/s can be seen as a proxy for a creeping ground motion. True creep movement along the fault line with velocities in the range of mm/yr cannot be modeled with the current capabilities of 3DEC due to unrealistic long calculation times.

On the other hand, when the slip velocity exceeds 1 m/s the displacement vectors in *Figure 6.14* indicate that the part of the fortification wall resting on the moving plate is more prone to destruction than the one on the locked plate, where inertial forces are lacking. Furthermore, blocks of the outer shell drop in direction of the ground motion more often than blocks of the inner shell, which only fall at velocities of 3 m/s and higher. The deformation is also affected by the slip velocity; at slow velocities the pull-apart affects both shells at large distance from the fault line. With increasing velocities, the pull-apart just affects the closer vicinity of the fault line (*cf. Figure 6.14*). Additionally, due to the tilting of the shell at higher ground motion velocities the relative displacement of the shells is reduced, which is especially the case for the inner shell.

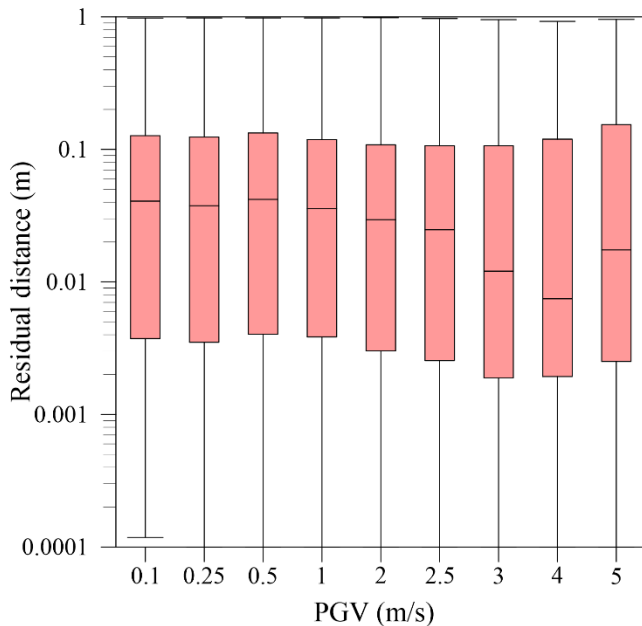


*Figure 6.15* summarizes residual distances of the above presented nine simulations. The residual distance is the distance between the calculated and measured points, after they are matched by the ICP. For the first four simulations, the residual distances are rather similar, which is expected due to the small differences in the results of the simulations (*cf. Figure 6.12*). With increasing velocities above 1 m/s the median of the distances starts to decrease up to a slip velocity of 4 m/s, for the simulation with 5 m/s the median is again at a higher level. Overall the median ranges from 0.008 m to 0.04 m.

*Figure 6.15: Boxplot of the residual distances between the calculated result and the nearest neighbor of the measured points.*

In further six simulations of the first scenario both plates were moved in opposite directions with velocities of 0.5 m/s, 1 m/s, 2 m/s, 3 m/s, 4 m/s and 5 m/s. *Figure 6.16 (a)* and *(b)* show that the results of the simulations can be classified into those with absence or presence of inertial effects. The results for the simulations with the three slowest slip velocities were similar. Both shells were pulled apart, but no

inertial forces contributed to the deformation of the fortification wall. A comparison of *Figure 6.16 (a)* with the relative displacement of the preceding simulations in *Figure 6.12* shows that there are only minor differences, although the absolute direction of movement is rather different.

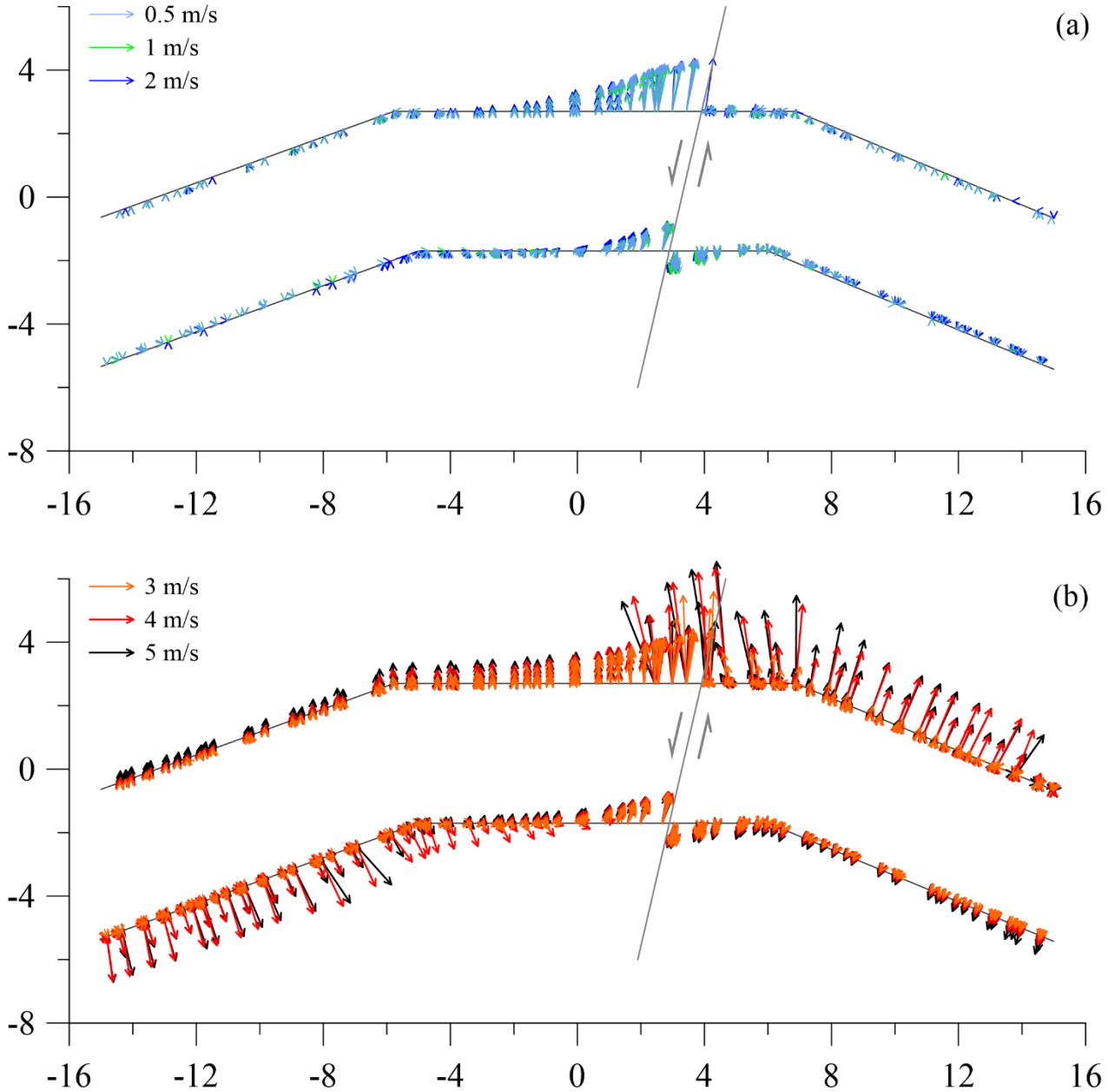
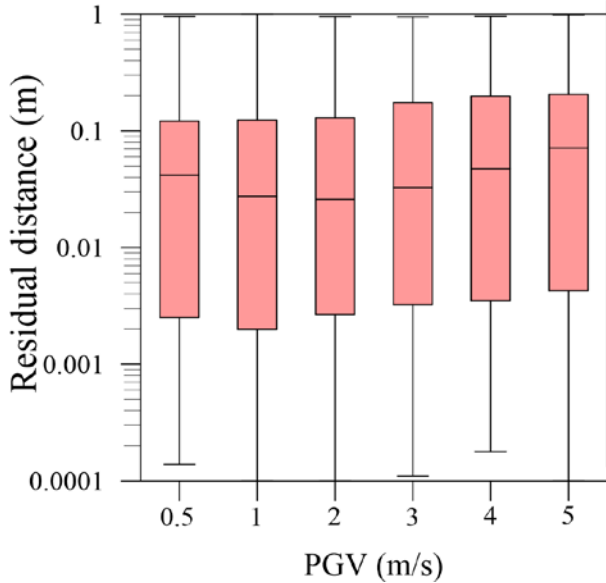


*Figure 6.16: Relative displacement from the simulations with the baseplates moved in opposite direction. (a) simulations with low slip velocities; (b) simulations with high slip velocities. Velocities are indicated by vector color as shown in the legend, scales are in (m).*

In the three simulations with higher slip velocities inertial forces influence the deformation and destruction. *Figure 6.16 (b)* shows blocks dropping out of the shells in the direction of the ground motion on both sides of the fault line. Additionally, blocks drop out of the outer shell in the opposite direction of movement close to the fault line, where the pull-apart effect is strongest. At the highest velocities the wall



is tilting in direction opposite to the ground motion. Comparing these relative displacements with those of the preceding simulations the most striking difference is that here the destruction occurs on both sides of the fault line. It is also evident that the deformation caused by the pull-apart is not shifting in this simulations. As a result, the effect of the higher slip velocities is not as strong as before. This is backed by *Figure 6.17*, in which the range of the residual displacement does not vary significantly, but is overall increasing with higher velocities. The median of the simulation ranges from about 0.026 m to 0.071 m, where the simulations with 1 m/s and 2 m/s have the lowest median.

*Figure 6.17: Boxplots summarizing the residual distances between the calculated points and the nearest neighbor of the measured points for simulations where the plates are moved in opposite directions.*

Based on the results of the previous simulations, no slip velocities below 1 m/s were used in the following simulations due to the missing effect of the inertial forces. In the next five simulations the western plate was shifted southwards with 1 m/s, 2 m/s, 3 m/s, 4 m/s and 5 m/s. The results were significantly different from those of the preceding simulations with the moving eastern plate. *Figure 6.18* representatively shows the results for 3 m/s slip velocity. Part (a) of *Figure 6.18* shows that only blocks, which rested on the western plate, were affected by the ground motion, blocks dropped out of the inner and outer shell. The deformation was mostly limited to the western side of the fault line, which is obvious in the pattern of the absolute displacements (*Figure 6.18 (b)*). In the plots it is obvious that the calculated results do not match the measured values, a clear indication against a locked eastern plate.

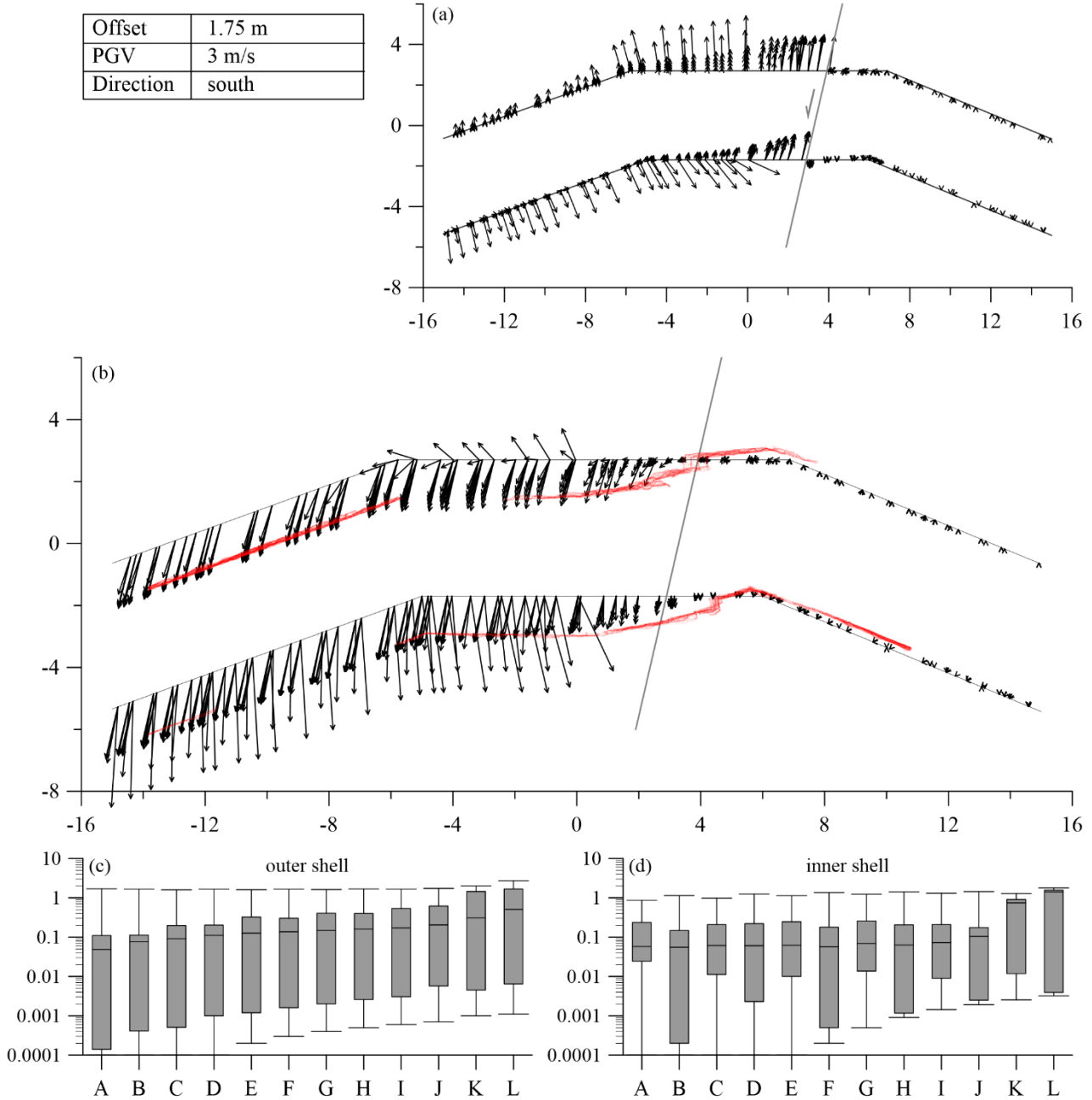


Figure 6.18: Results of the simulation with a cycloidal pulse for a displacement of 1.75 m and a PGV of 3 m/s. (a) Displacement vectors of the blocks relative to the displacement of the baseplate beneath the blocks from a top view perspective. The light grey line marks the course of the fault line in the model. The light grey arrows point in direction of the ground motion. The dark grey lines mark the course of the initial wall line. (b) Vector plot of the absolute displacement (m) of all blocks from a top view perspective. The grey line marks the course of the fault line in the model and strikes in north-south direction. The superposed red points are the measured points from the 3D laser scanning survey. (c) Boxplot of the vector length relative to the displacement of the baseplate for all blocks in individual rows with row A: bottom and row L: top of the outer shell. (d) the same as (c) for the inner shell.

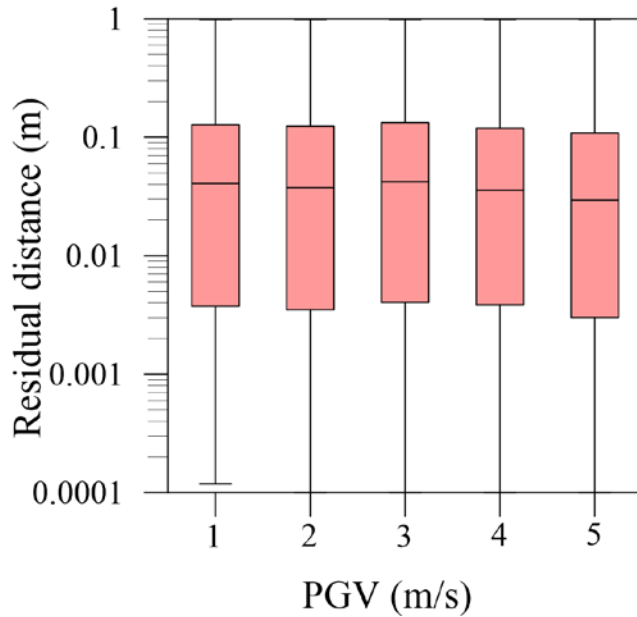


Figure 6.19: Boxplots summarizing the residual distances between the calculated points and the nearest neighbor of the measured points for simulations where the western plate is moved in southern direction.

The main reason for the model's different responses to the ground motion in southern direction compared to a locked western plate is due to the interaction of the effect of the filling with the slope beneath and the ramp. When the western plate is moved south the filling, backed by the slope and the ramp, hampers the movement of the blocks located east of the fault line in direction of the ground motion. Therefore, a section of the fortification wall in larger distance west of the fault line is pulled apart by the ground movement. The residual distances between measured and calculated points show that there are no significant differences between the results for different slip velocities, the median of the distances for all tests are close to 0.04 m (Figure 6.19).

In the last two simulations of this scenario both plates were moved northward with different displacements and slip velocities. These were the most extreme simulations of this scenario, because the eastern plate was shifted by 3.5 m and the western plate by 1.75 m. Therefore, only two simulations were carried out to get an impression of the model behavior. In one calculation with low slip velocities the western plate was moved with 1 m/s and the eastern plate accordingly with 2 m/s, in a second calculation the western plate was shifted with 2.5 m/s and the eastern plate with 5 m/s, respectively. The results for the simulation with the higher ground motion are summarized in Figure 6.20. The vector plots (Figure 6.20 (a) and (b)) show that both sections east and west of the fault line were affected by the ground motion. Blocks dropped out of the outer shell in direction of the ground motion. East of the fault line blocks fell also out of the inner shell in opposite direction of the ground motion. The boxplots in Figure 6.20 (c) and (d) show that all blocks were displaced relatively to the baseplate. Again the upper rows were displaced stronger than the lower. Comparing the results of the simulation with the measured values again reveals large differences (cf. Figure 6.20 (b))

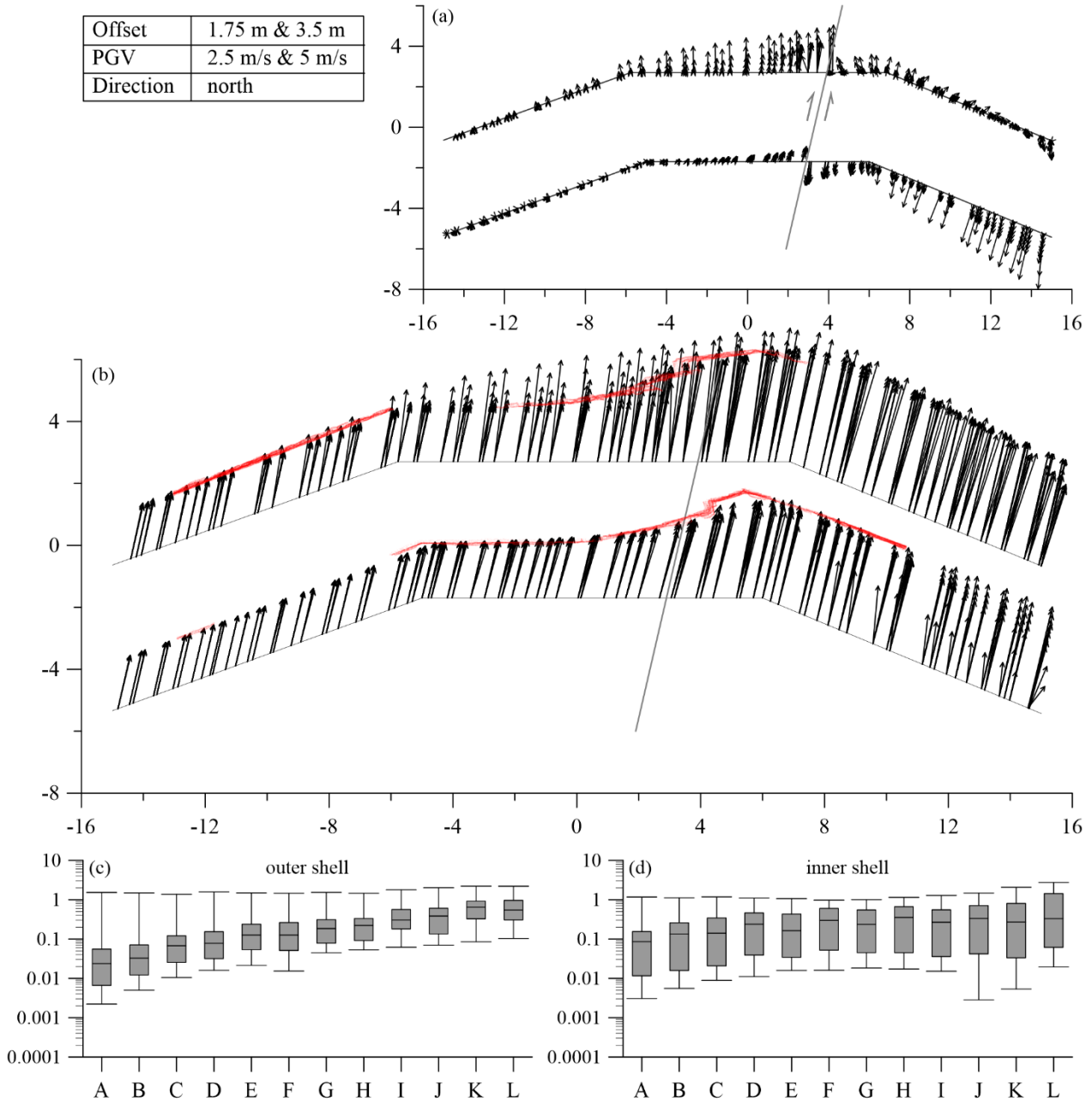


Figure 6.20: Results of the simulation with a cycloidal pulse for displacements of 1.75 m and 3.5 m and PGVs of 2.5 m/s and 5 m/s respectively. (a) Displacement vectors of the blocks relative to the displacement of the baseplate beneath the blocks from a top view perspective. The light grey line marks the course of the fault line in the model. The light grey arrows point in direction of the ground motion. The dark grey lines mark the course of the initial wall line. (b) Vector plot of the absolute displacement (m) of all blocks from a top view perspective. The grey line marks the course of the fault line in the model and strikes in north-south direction. The superposed red points are the measured points from the 3D laser scanning survey. (c) Boxplot of the vector length relative to the displacement of the baseplate for all blocks in individual rows with row A: bottom and row L: top of the outer shell. (d) the same as (c) for the inner shell.

The 22 simulations of the first scenario provide vital information about the response of the model to different boundary conditions. It could be shown that both the direction of movement and the slip velocity have large impact on the model's response. Independent of the direction of movement in all simulations the fortification wall is deformed by a pull-apart effect of the ashlar in both shells. This effect has different characteristics depending on the combination of direction of movement and the slip velocity. It can also be shown that the inertial forces acted at the fortification wall at slip velocities above a threshold of 1 m/s. Further, there is a significant difference in the outcome for changes in the movement direction.

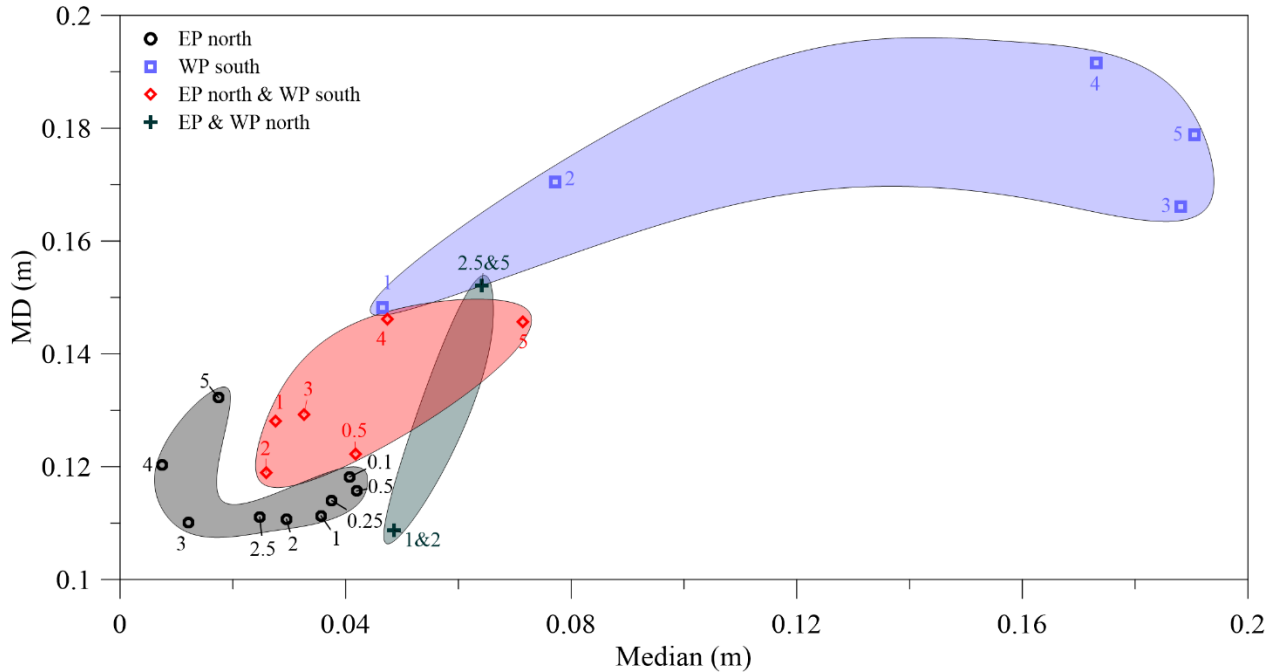


Figure 6.21: Mean deviation from the median (MD) plotted versus the median of the residual distances of all simulations of the first scenario. Results with the same direction of ground motion are outlined by polygonal splines with the same color. The labels show the velocity (m/s) of the according simulation; (EP = Eastern Plate and WP = Western Plate).

To estimate which simulation matches best to the observed deformation the residual distances between the measured and calculated points were used as a quantitative measure. The median of the residual distances and the mean deviation from the median (MD) are key values to resolve differences between the simulations. The lower the median, the smaller is the residual distance between half of the measured and calculated block positions. However, the median does not provide information about the upper boundary of the range of residual distances. The MD shows the mean dispersion of the residual distances around the median. A low MD means that overall the residual distances are close to the median and a large MD, in contrast, means that the distances in average differ largely from the median. In combination these values allow to evaluate the correspondence between the calculated and measured values.

*Figure 6.21* shows the MD and median of the residual distances from the point cloud fitting. The overall largest difference between simulations and measurement are observed in case of the southward movement of the western plate. The simulations where the western plate is locked and only the eastern plate is moved north show much better fits. A transition from the lower slip velocities to the higher values is well visible for this set of simulations. The best matching result is achieved with a slip velocity of 3 m/s northward shift of the eastern plate of 1.75 m. The results of the simulation are summarized in *Figure 6.22*. Blocks dropped out of both sections of the wall east and west of the fault line. The inertial forces acted on the wall and the inner shell moved against the direction of ground motion, which indicates the second failure mechanism. Most parts of the fortification wall west of the fault line were not affected by the ground motion. Only close to the fault line the outer section was deformed by the pull-apart effect.

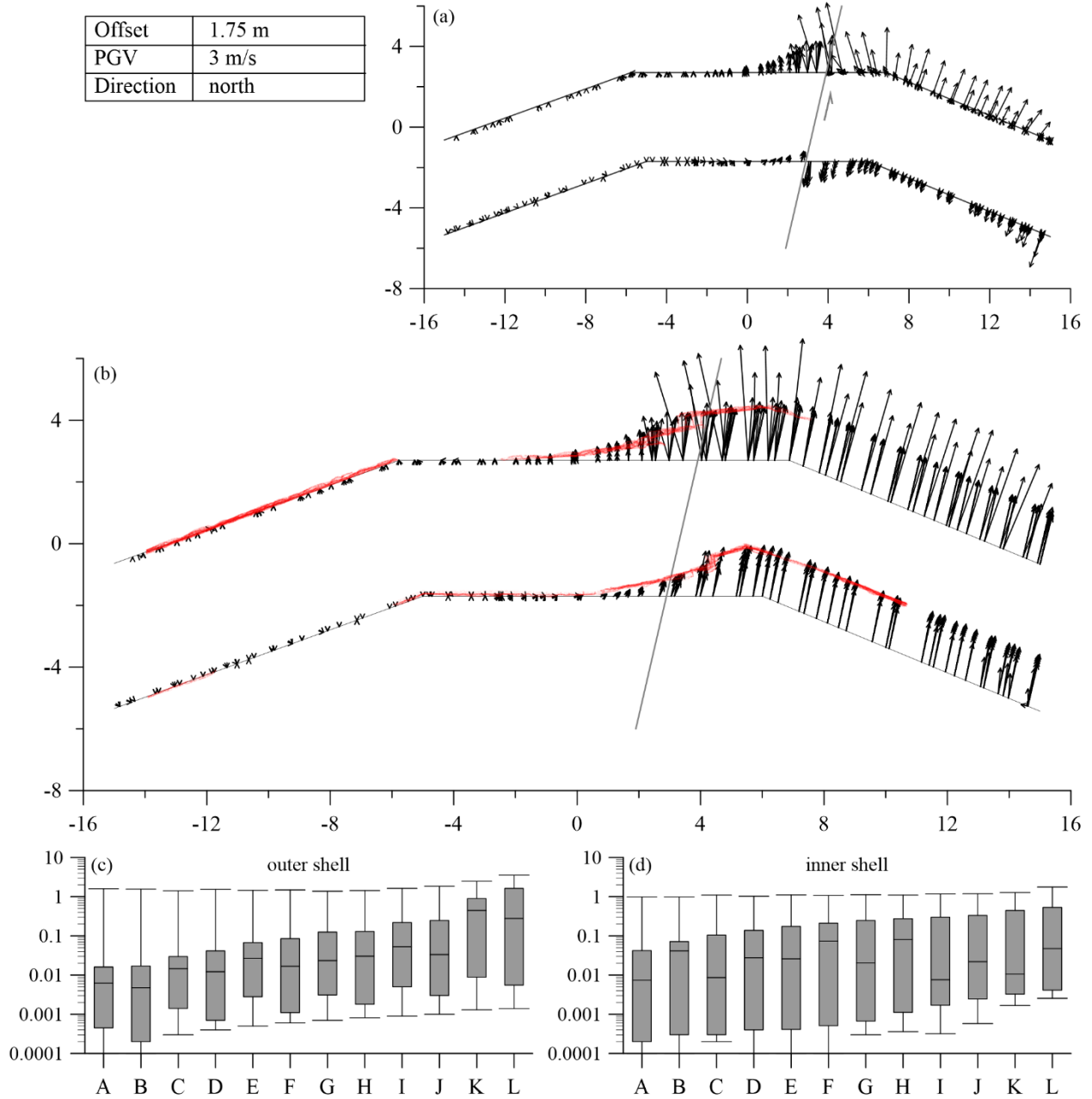


Figure 6.22: Results of the simulation with a cycloidal pulse for a displacement of 1.75 m and a PGV of 3 m/s. (a) Displacement vectors of the blocks relative to the displacement of the baseplate beneath the blocks from a top view perspective. The light grey line marks the course of the fault line in the model. The light grey arrows point in direction of the ground motion. The dark grey lines mark the course of the initial wall line. (b) Vector plot of the absolute displacement (m) of all blocks from a top view perspective. The grey line marks the course of the fault line in the model and strikes in north-south direction. The superposed red points are the measured points from the 3D laser scanning survey. (c) Boxplot of the vector length relative to the displacement of the baseplate for all blocks in individual rows with row A: bottom and row L: top of the outer shell. (d) the same as (c) for the inner shell.

### 6.5.2 SECOND SCENARIO

In the second scenario, the current hypothesis assuming that two earthquakes shifted the fortress wall is adopted. Based on the results of the first scenario the western plate was kept locked and only the eastern plate was moved northward in the second scenario. In the first stage the eastern plate was shifted in six simulations 1.25 m north with 1 m/s, 2 m/s, 2.5 m/s, 3 m/s, 4 m/s and 5 m/s slip velocity. Besides the somewhat smaller dislocations the results of these tests were similar to the results of the first scenario with the same slip velocities (*cf. Figure 6.23*).

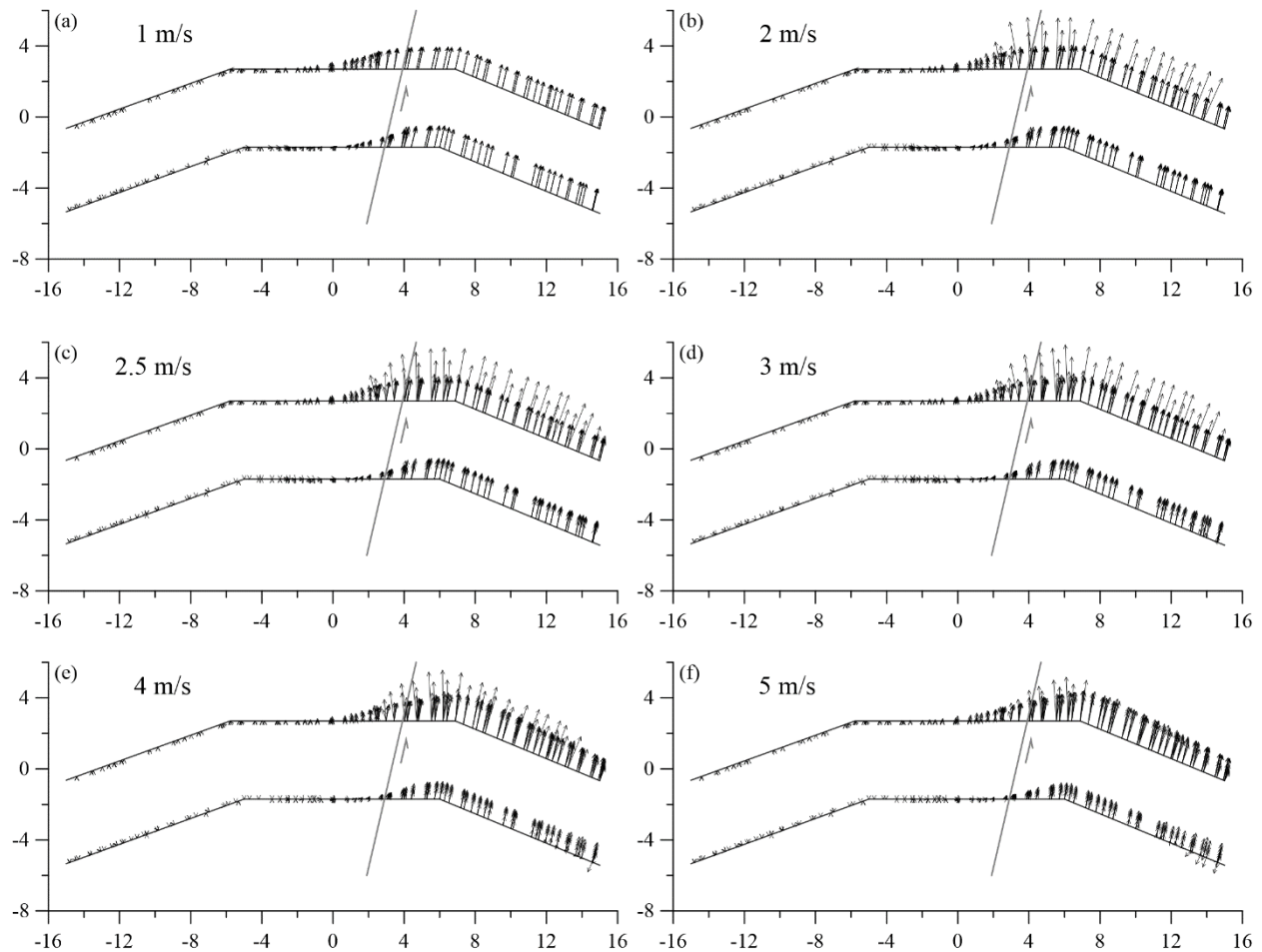


Figure 6.23: Absolute displacement vectors for the first stage simulations of the second scenario. The grey line marks the fault line and the grey arrow points in direction of the ground motion: (a) 1 m/s; (b) 2 m/s; (c) 2.5 m/s; (d) 3 m/s; (e) 4 m/s; (f) 5 m/s. All scales are in (m).

At 1 m/s no inertial forces influenced the deformation, the induced movement was due to the pull-apart effect. First inertial effects were observed at slip velocities of 2 m/s. In the section east of the fault line blocks dropped out of the outer shell's upper rows; however, the shells were not tilted. First signs of tilting

occurred at velocities of 2.5 m/s and above. With increasing velocity, also the deformation of the shells increased, but less blocks dropped out of the shells. At velocities of 3 m/s and above blocks of the inner shell showed movement in opposite direction of the ground motion at the eastern border of the model.

In the second calculation each end state of the simulation of the first stage was offset by another 0.5 m with ground motion velocities of 1 m/s, 2 m/s, 3 m/s, 4 m/s to 5 m/s, which resulted in a total of 30 simulations. To estimate the effect of the second slip velocity to the already offset model, the results based on the first stage simulation with no inertial effects can be reviewed.

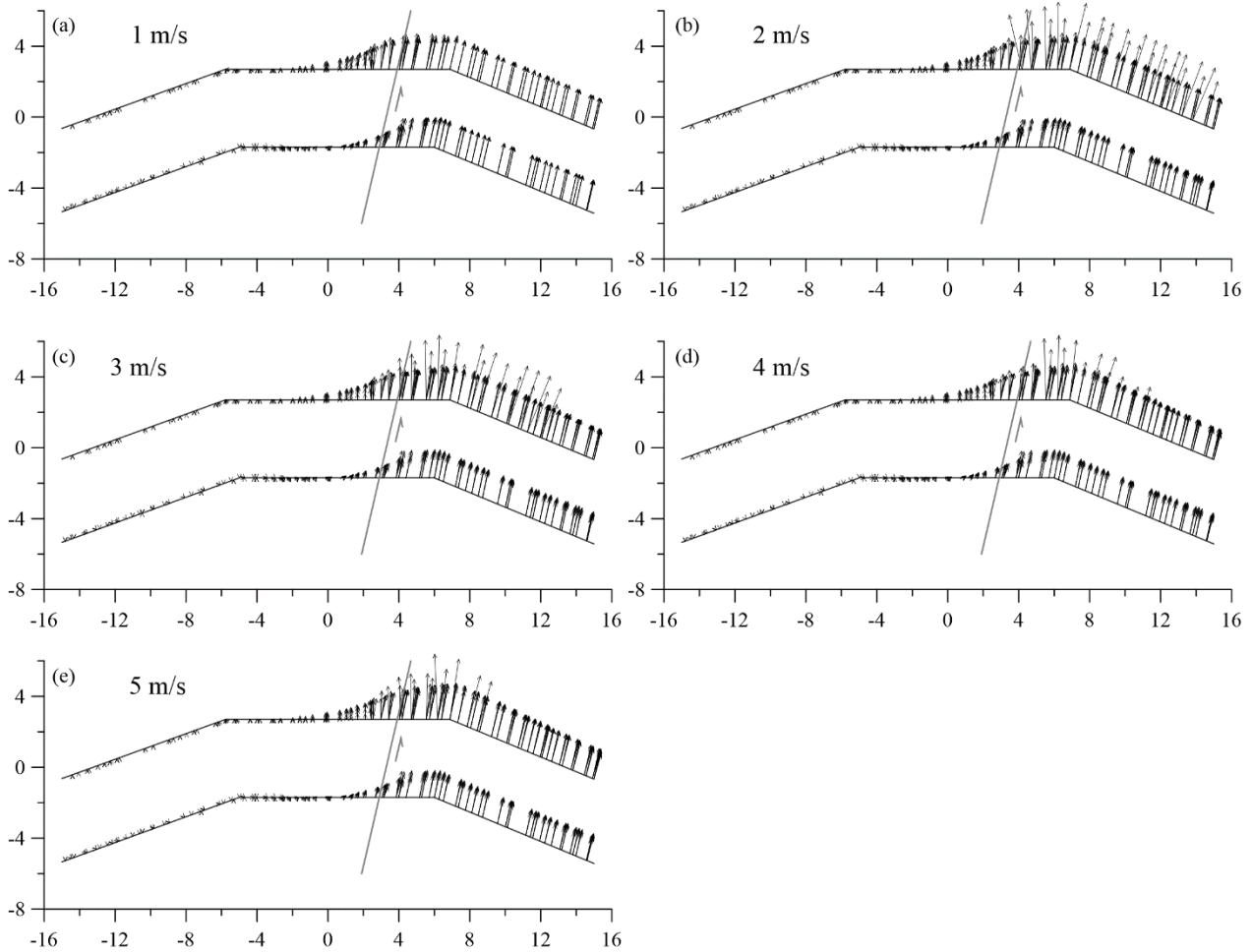
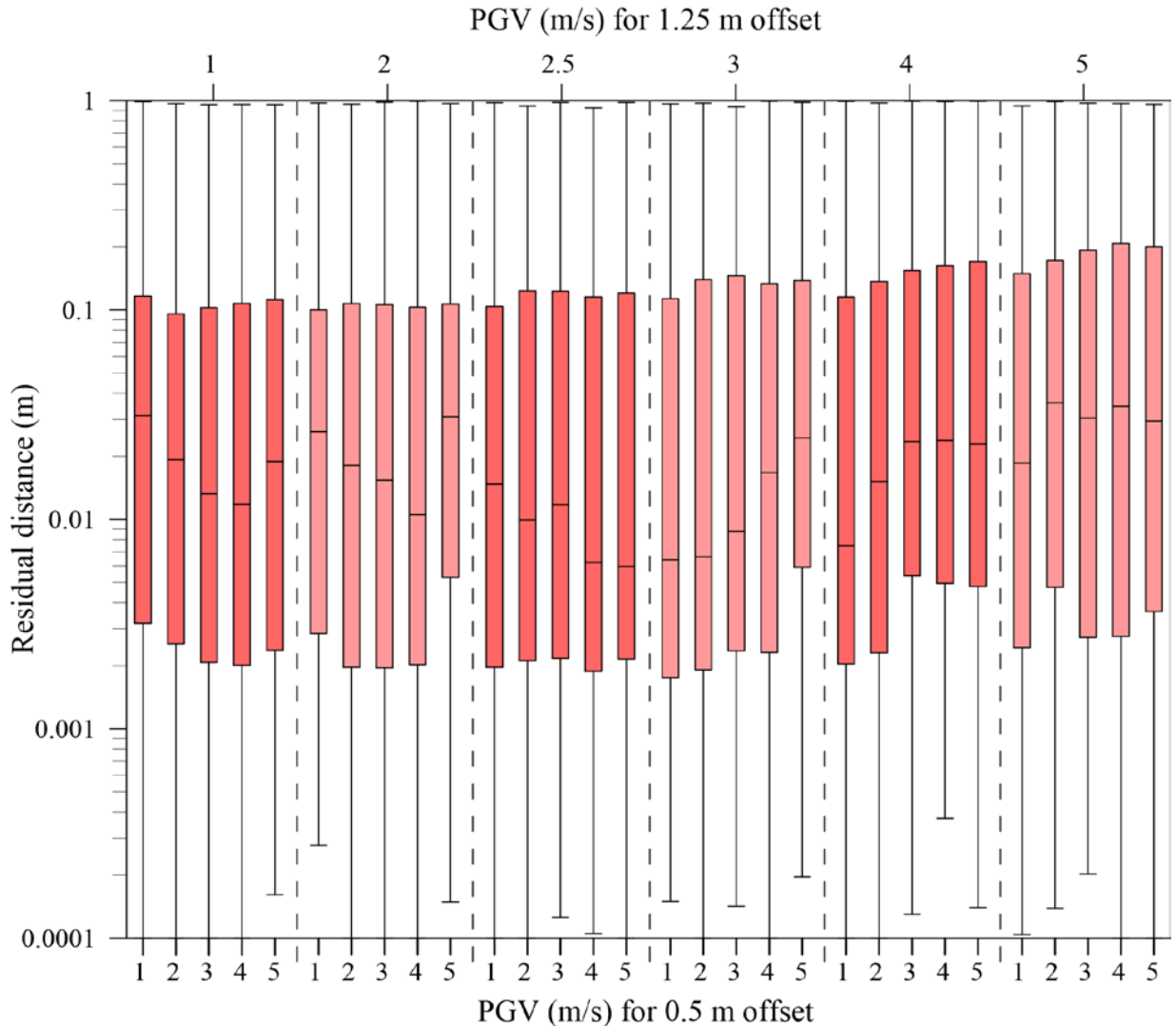


Figure 6.24: Absolute displacement vectors of the second stage which are based on the slowest first stage simulations with 1 m/s where: (a) 1 m/s; (b) 2 m/s; (c) 3 m/s; (d) 4 m/s; (e) 5 m/s. All scales are in (m).

In the simulation with the combination of the slowest slip velocities (*Figure 6.24 (a)*) no blocks dropped out of the inner or outer shell and no tilting occurred. At slip velocities of 2 m/s and above (*Figure 6.24 (b)-(e)*) blocks dropped out of the outer shell in direction of the ground motion during the simulation of the second earthquake. In *Figure 6.24 (c-e)* it is clear that with increasing slip velocities, less blocks dropped out of the shell, but the tilting increased, which led to a decrease in the length of the absolute displacement vectors.

As shown in *Figure 6.23* and *Figure 6.24* the ground motion velocity of both stages had significant influence on the deformation and destruction of the fortification wall. At velocities of 2 m/s and above both movements were strong enough that inertial forces influenced the deformation of the fortification wall. The overview of the distances between the measured and calculated points is given in *Figure 6.25*.



*Figure 6.25: Boxplots summarizing the residual distances between the calculated points and the nearest neighbor of the measured points grouped by the first stage. The velocities of the first stage are listed at the top x-axis. The according velocities of the second stage are listed at the bottom x-axis.*

Again the median of the residual distances indicate how well the calculated results match the observation. The simulations based on the lowest slip velocity of 1 m/s in the first stage show a decrease of the median with increasing velocities of the second stage from 1 m/s to 4 m/s. At slip velocities of 5 m/s the median starts to increase again. The same applies to the simulations based on the first stage with 2 m/s slip velocity. The median decreases for these simulations from 1 m/s and reaches its minimum at the calculation with 4 m/s, then it is increasing again. The observed pattern changes in the calculations based on the simulations with 2.5 m/s of the first stage, where first tilting occurs. The median of the three slowest simulations does not decrease as it did before, it varies between 0.01 m and 0.015 m. In contrast

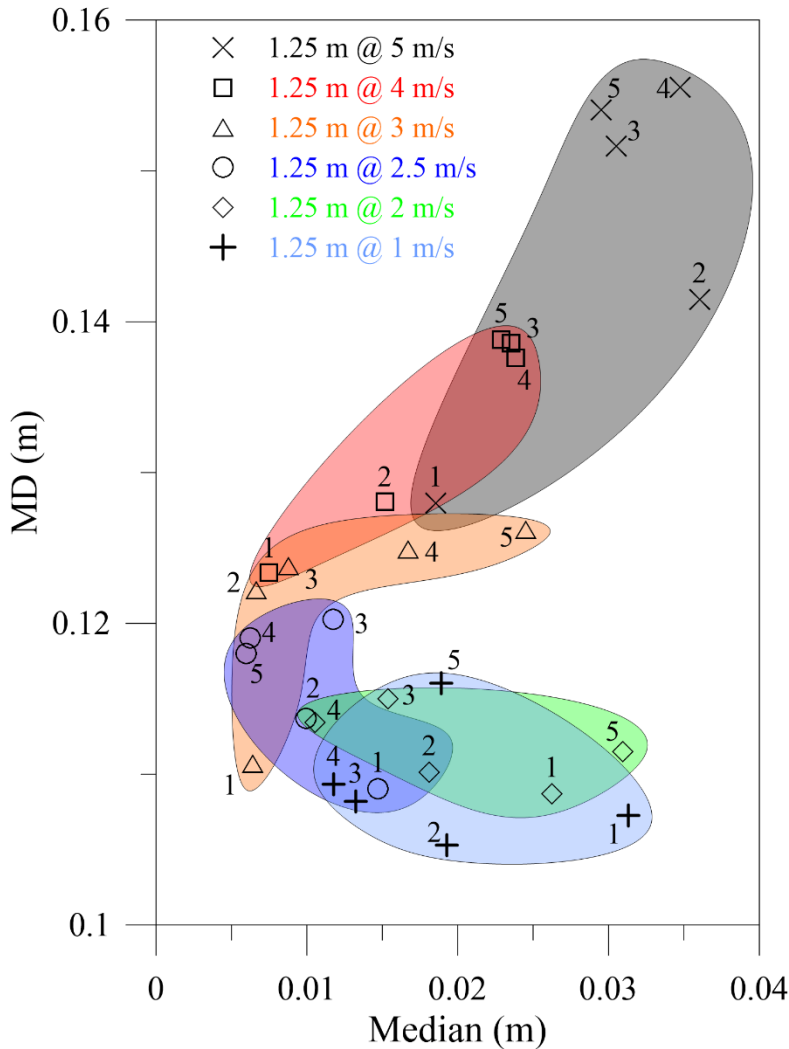


Figure 6.26: Mean deviation from the median (MD) plotted versus the median of the residual distance of all simulations of the second scenario. Simulations with the same first stage are highlighted with the same color. The labels show the velocity (m/s) of the according simulation.

the median of the two fastest simulations lies around 0.006 m. For all these simulations of the second stage the lowest median is observed in case of a fast second movement. This changes in the simulations which are based on simulations with a slip velocity of 3 m/s in the first stage. Here the lowest median is the result of the slowest movement of the second stage simulations and increasing for higher slip velocities. The same effect also applies to the first two simulations, based on the first stage simulations with 4 m/s. At velocities above 3 m/s for the second earthquake the median does not change significantly. The same is observed in the simulations based on the first stage with the highest slip velocity of 5 m/s. The median is the lowest with 1 m/s slip velocity in the second stage. With higher slip velocities the median reaches values between 0.03 m to 0.035 m.

In *Figure 6.26* the MD is plotted against the median, it is obvious that the slip velocity of the first stage has a strong influence on the result. The simulation with a slip velocity of 3 m/s in the first stage and 1 m/s in the second stage fits best with the observed deformation at the northern fortification wall of Tell Ateret. It is shown that the results of the simulations based on the first stage calculation with 1 m/s, 2 m/s and 2.5 m/s converge towards the best fit with increasing velocities. All fits of simulations based on higher first stage slip velocities divert more and more from the best fit. *Figure 6.27* summarizes the results of the best fit of the second scenario calculations. The vector plots *Figure 6.27 (a)* and *(b)* show, that in addition to the pull-apart effect inertial forces influenced the deformation and destruction. Blocks dropped out of the inner and outer shell and the inner shell was tilting in opposite direction of the ground motion. In the boxplots it is again visible that the upper rows of the ashlar were more affected than the lower ones, but it is also evident that most blocks of all rows experienced some effect. By comparing the results with the point cloud *Figure 6.27 (b)* it turns out that both deformed shells do not match the point cloud equally well. At the outer shells the end positions of the vectors tend to overextend the measured values, this is particularly the case east of the fault line close to the bend. The inner shell shows an overall better fit with the measured values. It has to be pointed out that even the crack of the inner shell was reproduced in these simulations. Comparing the best fits of the first and second scenario (*Figure 6.21* and *Figure 6.26*) shows that the simulation of the second stage has the overall best match to the measured point cloud. This strongly supports the two earthquake hypothesis.

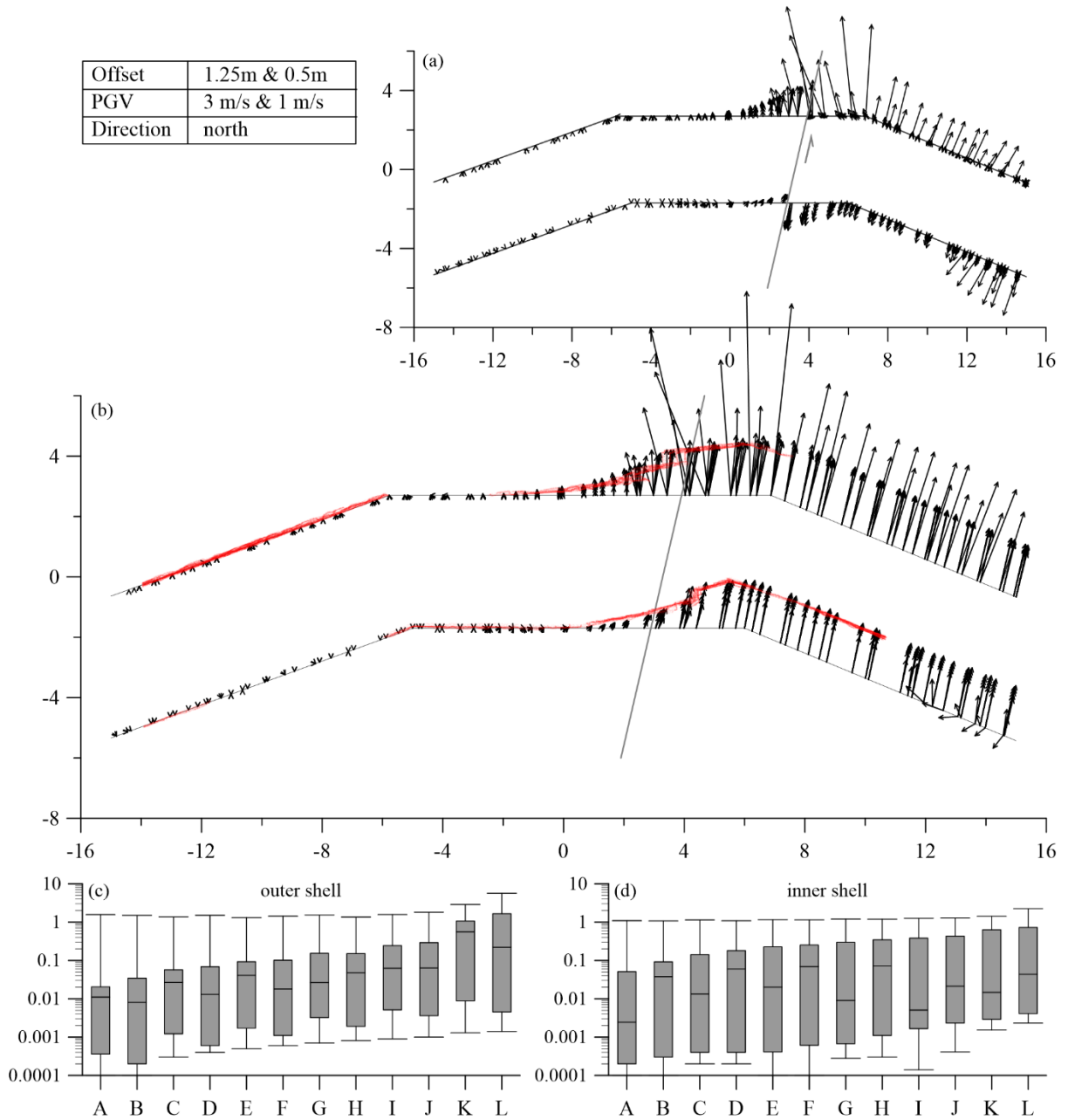


Figure 6.27: Results of the simulation with a cycloidal pulse for a displacement of 1.25 m @ 3 m/s and 0.5 m @ 1 m/s. (a) Displacement vectors of the blocks relative to the displacement of the baseplate beneath the blocks from a top view perspective. The light grey line marks the course of the fault line in the model. The light grey arrows point in direction of the ground motion. The dark grey lines mark the course of the initial wall line. (b) Vector plot of the absolute displacement (m) of all blocks from a top view perspective. The grey line marks the course of the fault line in the model and strikes in north-south direction. The superposed red points are the measured points from the 3D laser scanning survey. (c) Boxplot of the vector length relative to the displacement of the baseplate for all blocks in individual rows with row A: bottom and row L: top of the outer shell. (d) the same as (c) for the inner shell.

## 6.6 Discussion and Conclusion

The Crusader Fortress of Tell Ateret has been constructed on top of the DSTF and the remains of the massive fortification wall are offset. Based on paleoseismological, archaeological and historical information, it was concluded in numerous studies (Marco *et al.* 1997, Ellenblum *et al.* 1998, Ellenblum *et al.* 2015, Marco *et al.* 2005) that the observed offset has been caused by two earthquakes, the first on May 20th 1202 and the second on October 30th 1759. In this section the question was examined of whether the offset could also be (at least in part) due to creep movement along the DSTF and what can be learned about slip velocities and locked plates. Therefore, a Discrete Element Model of the northern fortification wall was developed to address this question and to find out more about the ground motion history of the site. The reconstruction of the original state of the northern fortification wall for the model development was based on 3D laser scan point clouds. With 17 scans the deformation of the northern fortification wall was surveyed and additionally the surroundings were covered in a terrestrial laser survey (Hinzen *et al.* 2017). In the resulting 3D point cloud, a total displacement of 1.75 m could be estimated for the northern fortification wall, which is less than the 2.1 m estimate deduced from the excavation at the southern wall. In 58 simulations combinations of different slip velocities and movement direction were applied as boundary condition to the model. The simulations were separated in two scenarios, the first of which involved 22 simulations that focused on different movement directions along the DSTF with different slip velocities. The second scenario focused on the current hypothesis that two earthquakes of different size offset the fortification wall. With 36 simulations combinations of coseismic displacement of two earthquakes were covered. The results of the calculations were systematically compared with the observed deformation of the northern wall based on a *ICP* algorithm.

The simulations of the first scenario revealed that most of the deformation is the effect of pulling the wall apart during the ground movement. The direction of the movement had strong impact on the deformation. All simulations had a relative displacement representing a left-lateral shift of 1.75 m, but the amount of absolute displacement east and west of the fault line varied. It was shown that the results of the simulation matched best the observed damage, where the western side of the fault (Sinai plate) was locked and all movement occurred in northern direction on the western side of the fault (Arabian plate). Simulations with the opposite movement characteristic, where the Sinai plate was moving south and the Arabian plate was locked or where both plates moved north did not match the observed damage that well. Simulations where both the Sinai and Arabian plate moved in opposite direction with the same amount of slip only minor changes in the resulting deformation occurred at increasing slip velocities. The main reason for the various outcome of different movement direction was the effect of the interaction of the mortar-basalt filling with the underlying slope on the shells of the wall. The filling, backed by the slope, hampered the movement in southern direction and promoted movement in northern direction.

Not only the direction of movement, but also the slip velocity influenced the resulting deformation and destruction. At high velocities inertial forces acted on the wall, resulting in blocks dropping out and tilting of the wall in direction or in opposite direction of the ground motion, which is denoted as first and second failure mechanism, respectively. It is important to emphasize that further reducing the slip velocity below the threshold of inertial effects has no significant influence on the resulting deformation as the simulations showed. This allows to conclude that extremely slow creep movements in the range of mm/yr do not explain the observed deformation. The best matching simulation of the first scenario had a slip velocity of 3 m/s with a locked Sinai plate and full displacement of the Arabian plate.

In the second scenario the model was displaced in two steps to simulate two earthquakes. Based on the results of the first scenario here only the Arabian plate was moved north and the Sinai plate was kept locked. The first displacement of 1.25 m was applied with slip velocities of 1 m/s to 5 m/s, representing the May 20th 1202 earthquake. And in a second movement the end state from the first test was further displaced by 0.5 m, simulating the October 1759 earthquake. Observations were best matched in the simulations with a higher slip velocity of 3 m/s for the 1202 earthquake and a slip velocity of 1 m/s for the 1759 earthquake. The simulation of the second scenario better fits the observations than the best result for the first scenario.

With the presented results the key questions stated above can be answered:

*(1) Does the slip velocity affect the deformation pattern of the fortification wall?*

The dislocation velocity affects the deformation of the fortification wall particularly, when a level of ground motion severity is reached, where inertial forces influence the deformation and destruction.

*(2) Is it possible to decide, based on the deformation pattern of the wall, whether the total offset is the result of a rapid coseismic movement or slow creeping movement has to be considered as well? Can new insights be gained on the slip velocity of the individual events?*

Based on the results creeping movement as cause of the observed deformation is unlikely. Although it is not possible in the numerical experiments to displace the plates with extremely low slip velocities mm/yr, which matches observed creep velocity at the DSTF (Wdowinski *et al.* 2004, Gomez *et al.* 2007a, Sadeh *et al.* 2012), it could be shown that reducing the slip velocity, when no inertial forces are acting on the fortification wall, has no further effect on the outcome of the simulation and produces no good fit with the observation. Therefore, the calculations where no inertial forces act can be assumed as representative for a creeping motion. The deformation caused by a slow dislocation velocity is a gentle pull-apart and does not match the sharp offset, which is observed close to the fault line. The best fitting simulation is based on

rapid movements with slip velocities of 3 m/s and 1 m/s for the May 20th 1202 and October 30th 1750 earthquake, respectively.

(3) *Is it possible to discern the amount of slip by which the two sides of the fault contributed to the total displacement?*

According to the simulation of the first and second scenario the Sinai plate has been locked during the earthquakes and the full displacement has happened on the Arabian plate.

(4) *How good fit the results to the preceding research?*

*Table 6.2: Peak ground acceleration for MM Intensities (after Wald et al. 1999).*

PGA ( m/s <sup>2</sup> )	Intensity
< 0.017	I
0.017-0.14	II-III
0.14-0.38	IV
0.38-0.90	V
0.90-1.77	VI
1.77-3.34	VII
3.34-6.38	VIII
6.38-12.16	IX
>12.16	X+

The results of the simulations support the current hypothesis that two earthquakes since 1178 shifted the fortification wall. Wald *et al.* (1999) developed a relationship between MM Intensity and PGA in California, which is summarized in *Table 6.2*. The cycloidal pulse with a displacement of 1.25 m and a velocity of 3 m/s has a PGA of 11.3 m/s<sup>2</sup> and according to the relationship of Wald *et al.* (1999) corresponds to an intensity of IX. This matches the estimation of Ambraseys and Melville (1988) which is based on historical information. The cycloidal pulse with a displacement of 0.5 m and a velocity of 1 m/s has a PGA of 3.14 m/s<sup>2</sup>. This translates for the October 30th 1759 event to an intensity of VII, which is in range of the intensities estimated by Sbeinati *et al.* (2005) for this event.

To estimate the magnitude of the earthquakes that are used in the simulations a relationship for earthquakes in the Middle East from Ambrasyes and Melville (1988) can be used:

$$M_S = 1.1 + 0.4 \log(L^{1.58} D^2) \tag{Eq. 6.5}$$

where  $L$  is the rupture length and  $D$  is the relative displacement in centimeters. Based on the potential rupture length of 200 km and 50 km provided by Daëron *et al.* (2005) and the estimated offset of 1.25 m and 0.5 m magnitudes of  $M_S = 7.4$  for the May 20th 1202 event and  $M_S = 6.7$  for the October 30th 1759 event can be estimated, which is within the range of preceding magnitude estimations mentioned above (*cf.* Ambrasyes and Melville 1988, Ambrasyes and Barazangi 1989, Marco *et al.* 1997).

It is interesting that the crack of the inner shell could be reproduced in the simulations. Particularly, because it is not visible in the results of simulation reflecting the 1202 earthquake, but only after the second movement. It can be argued that the 0.5 m crack observed at the inner and outer shell (*cf. Figure 6.5*) was mainly caused by the 1759 earthquake, which offset the already deformed and broken fortification wall, the second earthquake had an easy going compared to the first.

In this approach the destruction of the fortification wall is mainly limited to the section that is founded on the moving plate, because only here inertial effects topple the ashlar, which is in contrast to the observation. However, it is uncertain to which amount the current destruction (missing blocks) is of anthropogenic origin. Further uncertainties are given by the fact that the model is an approximation to the real geometry and not an exact copy and only simple ground motion model (cycloidal pulse) was used. However, it could be shown that a model based on DEM is capable of bracketing the ground motion parameters of the events that caused the deformation. Not only could a creeping motion been excluded as the main reason for the offset, but it could also be shown that two rapid movements of the Arabian plate are more likely as cause of the deformation than a southward slip of the Sinai plate. For the best fitting simulation result the first earthquake caused an offset of 1.25 m at a slip velocity of 3 m/s and the second an offset of 0.5 m at a slip velocity of 1 m/s. In context of the historical record these values agree well with the investigations of the earthquakes on May 20th 1202 and October 30th 1759, respectively.

### 6.7 Further Research

Despite the careful reconstruction of the original course of the wall lines the process could be elaborated. Currently the material properties are only approximations from the literature. With laboratory test the properties of the material of the archaeological site could be evaluated. Since it has been shown in this work that it is possible to simulate the response of the northern fortification wall, an exact block by block reconstruction of the fortification wall would be feasible to potentially improve the accuracy. However, this would require further excavation at the site, which would be particularly necessary on the north-eastern corner. Also with more on site investigation the exact course of the fault line could be examined, to improve the current approximation.

Currently there are different offset estimations at the remains of the fortress. At the southern fortification wall the Marco *et al.* (1997) estimated an offset of 2.1 m, the offset measured at the northern wall is 1.75 m. To evaluate the discrepancies in the offset further research is needed. A renewed excavation at the southern wall would provide valuable information to compare the offset of the northern and southern fortification wall. As shown in the simulation with the model of the northern fortification wall it is evident, that the model geometry and the direction of ground movement have significant influence on the outcome of the simulation. An additional DE model would provide important information about the

response of the southern fortification wall. It is feasible that the differences between the estimated offsets can be resolved with the combination of a 3D laser scan and DE models of the northern and southern fortification wall, additionally it would be possible to validate the estimated results in this work.

# 7 DISCUSSION AND CONCLUSION

In the course of this work the investigation of the ground motion history of two archaeological sites in northern Israel is presented. With computer models based on the DEM numerous simulations were carried out to gain information about the stability of the archaeological structures and the ground motion history of the sites. Based on the historical information and the current state of the structures, different approaches were chosen for each site.

At the ruin of the Roman Temple of Kedesh it was shown that the concept of precariously balanced archaeological structures is capable to determine the vibration history of a site and allows reasonable conclusion about the seismic activity of the region. This method in particular allows to gain information from archaeological sites with uncertain destruction history and a reconstruction is not feasible.

With the DE model of the remains of the fortification walls of the crusader fortress at Tell Ateret the slip velocity of two past earthquakes could be estimated. The model illustrates the potential of the application of DEM in archaeoseismological research. The complex model comprises in total 52,864 discrete blocks, which are necessary to enable the movement in all critical parts of the model, such as the construction ramps and the mortar-basalt filling between the shells.

Regardless which of the presented approaches is applied, a thorough model development process is essential. Either for a reconstruction of the original state or the modeling of the current state an accurate documentation of the archaeological structure is essential, not only as base for the model development but also as reference to evaluate the simulation results. As shown 3D laser scans are an excellent tool for accurately surveying archaeological structures and the resulting 3D point clouds serve both purposes well.

As shown it is important to choose a software solution for the simulation that is able to meet all requirements of the model. During the development process of both models three different software solutions UM, Unity and 3DEC were tested. Each of these is rich in different features and has advantages and disadvantages for archaeoseismological application. While UM and 3DEC have been used in numerous studies before and are known to be capable tools (*e.g.* Psycharis *et al.* 2003, Hinzen 2009a, Hinzen *et al.* 2013b, Cakti *et al.* 2016, Galvez *et al.* 2018), Unity is quite new in this field and is not yet widely used, but has shown that it is a valuable tool for archaeoseismological research (*e.g.* Hinzen and Montabert 2017, Schweppe 2017). Regardless of the software solution used, it is advisable to divide the model development into different logical units and also to constantly check the functionality of the model during the development process, not only to ensure the full functionality but also to avoid errors, which would propagate in the simulations.

## 8 LITERATURE

3DEC Manual (2016). 3DEC 3 Dimensional Distinct Element Code User's Guide, *Itasca Consulting Group Inc.*, Minnesota.

Adams, W. M., and D. C. Allen (1961). Reading Seismograms with Digital Computers, *Bull. Seism. Soc. Am.* **51**, 61-67.

Agamennone, G. (1935). Come e quando rovinò il tempio di Venere Genitrice, *Boll Soc Sism Ital* **33**, 89-91.

Agnon, A., C. Migowski, and S. Marco (2006). Intraclast Breccias in Laminated Sequences: Recorders of Paleo-Earthquakes, *Geol. Soc. Am. Spec. Pap.* **401**, 195-214.

Agnon, A. (2014). Pre-Instrumental Earthquakes Along the Dead Sea Rift, in *The Dead Sea Transform Fault System: Reviews*, Z. Garfunkel, Z. Ben-Avraham, and E. Kagan (Eds.), Springer, Dordrecht, 207-261.

Aki, K. (1966). 4. Generation and Propagation of G Waves from the Niigata Earthquake of June 16, 1964. Part 2. Estimation of Earthquake Moment, Released Energy, and Stress-Strain Drop from the G Wave Spectrum, *Bulletin of the Earthquake Research Institute* **44**, 73-88.

Akyuz, H. S., E. Altunel, V. Karabacak, and C. C. Yalciner (2006). Historical Earthquake Activity of the Northern Part of the Dead Sea Fault Zone, Southern Turkey, *Tectonophysics* **426**, 281-293.

Alexandris, A., E. Protopapa, and I. Psycharis (2004). Collapse Mechanisms of Masonry Buildings Derived by the Distinct Element Method, in *Proceedings of the 13th World Conference on Earthquake Engineering* **59**, No. 548.

Alfonsi, L., F. R. Cinti, D. di Mauro, and S. Marco (2012). Archaeoseismic Evidence of Two Neolithic (7,500-6,000 B.C) Earthquakes at Tell es-Sultan, Ancient Jericho, Dead Sea Fault, *Seismological Research Letters* **83**, 639- 648.

Altunel, E., M. Meghraoui, V. Karabacak, S. H. Akyuz, M. Ferry, C. C. Yalciner, and M. Munschy (2009). Archaeological Sites (Tell and Road) Offset by Dead Sea Fault in the Amik Basin, Southern Turkey, *Geophys. J. Int.* **179**, 1313-1329.

Ambraseys, N. N. (1971). Value of Historical Records of Earthquakes, *Nature* **232**, 375-379.

Ambraseys, N. N., and C. Finkel (1987). Seismicity of Turkey and Neighboring Regions 1899-1915, *Ann. Geophys. Series B* **5**, 701-726.

Ambraseys, N. N., and C. P. Melville (1988). An Analysis of the Eastern Mediterranean Earthquake of 20 May 1202, in *Historical Seismograms and Earthquakes of the World*, W. H. K. Lee, H. Meyers, and K. Shimanzki (Eds.), Academic Press, San Diego, 181-200.

Ambraseys, N. N., and M. Barazangi (1989). The 1759 Earthquake in the Bekaa Valles: Implications for Earthquake Hazard Assessment in the Eastern Mediterranean Region, *J. Geophys. Res.* **94**, 4007-4013.

## Literature

---

Ambraseys, N. N., C. P. Melville, and R. D. Adams (1994). *The Seismicity of Egypt, Arabia and the Red Sea: a Historical Review*, Cambridge University Press, New York, 181 pp.

Ambraseys, N. N. (2005). The Seismic Activity in Syria and Palestine During the Middle of the 8<sup>th</sup> Century; an Amalgamation of Historical Earthquakes, *J. Seismol.* **9**, 115-125.

Amit, R., J. B. J. Harrison, Y. Enzel, and N. Porat (1996). Soils as a Tool for Estimating Ages of Quaternary Fault Scarps in a Hyperarid Environment - The Southern Arava Valley, the Dead Sea Rift, Israel, *Catena* **28**, 21-45.

Amit, R., E. Zilberman, N. Porat, and Y. Enzel (1999). Relief Inversion in the Avrona Playa as Evidence of Large-Magnitude Historical Earthquakes, Southern Arava Valley, Dead Sea Rift, *Quat. Res.* **52**, 76-91.

Amit, R., E. Zilberman, Y. Enzel, and N. Porat (2002). Paleoseismic Evidence for Time Dependency of Seismic Response on a Fault System in the Southern Arava Valley, Dead Sea Rift, *Israel. Geol. Soc. Am. Bull.* **114**, 192-206.

Anooshehpour, A., J. N. Brune, and Y. Zeng (2004). Methodology of Obtaining Constraints on Ground Motion from Precariously Balanced Rocks, *Bull. Seism. Soc. Am.* **94**, 285-303.

Anvi, R., D. Bowman, A. Shapira, and A. Nur (2002). Erroneous Interpretation of Historical Documents Related to the Epicenter of the 1929 Jericho Earthquake in the Holy Land, *J. Seismol.* **6**, 469-476.

Baer, G., D. Sandwell, S. Williams, and Y. Bock (1999). Coseismic Deformation Associated with the November 1995, Mw=7.1 Nuweiba Earthquake, Gulf of Elat (Aqaba), Detected by Synthetic Aperture Radar Interferometry, *J. Geophys. Res.* **104**, 25221-25232.

Bakun, W. H., and T. V. McEvilly (1984). Recurrence Models and Parkfield, California, Earthquakes, *J. Geophys. Res.* **89**, 3051-3058.

Barber, M. (1998). Frontier Warfare in the Latin Kingdom of Jerusalem: The Campaign of Jacob's Ford, 1178-1179, in *The Crusades and Their Sources. Essays Presented to Bernard Hamilton*, J. France, and W. G. Zajac (Eds.), Ashgate, Aldershot, 9-22.

Bartov, Y., G. Steinitz, M. Eyal, and Y. Eyal (1980). Sinistral Movement Along the Gulf of Aqaba - Its Age and Relation to the Opening of the Red Sea, *Nature* **285**, 220-221.

Begin, B. Z., D. M. Steinberg, G. A. Ichinose, and S. Marco (2005). A 40,000 Years Unchanging Seismic Regime in the Dead Sea Rift, *Geology* **33**, 257-260.

Ben-Avram, Z., and G. Schubert (2006). Deep "Drop Down" Basin in the Southern Dead Sea, *Earth Planet Sci. Lett.* **251**, 254-263.

Ben-Menahem, A. (1981). Variation of Slip and Creep Along the Levant Rift over the Past 4500 Years, *Tectonophysics* **80**, 183-197.

Ben-Menahem, A. (1991). Four Thousand Years of Seismicity Along the Dead Sea Rift, *J. Geophys. Res.* **96**, 20195-20216.

## Literature

---

- Bogert, B. P. (1961). Seismic Data Collection, Reduction, and Digitization, *Bull. Seism. Soc. Am.* **51**, 515-525.
- Bourbie, Th., O. Coussy, and B. Zinszner (1987). *Acoustic of Porous Media*, Gulf publishing Co., Houston, 334 pp.
- Bowles, L. E. (1996). *Foundation Analysis and Design*, McGraw-Hill, New York, 123 pp.
- Brune, J. N. (1996). Precariously Balanced Rocks and Ground Motion Maps for Southern California, *Bull. Seism. Soc. Am.* **86**, 43-54.
- Bryan, P. (2004). 3D Laserscanning – New Techniques of Observation, *Conservation Bulletin* **45**, 6-8.
- Bui, T. T., A. Limam, V. Sarhosis, and M. Hjiatj, M. (2017). Discrete Element Modelling of the In-Plane and Out-Of-Plane Behaviour of Dry-Joint Masonry Wall Constructions, *Engineering Structures* **136**, 277-294.
- Cakti, E., Ö. Saygili, J. V. Lemos, and C. S. Oliveira (2016). Discrete Element Modeling of a Scaled Masonry Structure and its Validation, *Engineering Structures* **126**, 224-236.
- Chorowicz, J., D. Dhont, O. Ammar, M. Rukieh, and A. Bilal (2005). Tectonics of the Pliocene Homs, Basalts (Syria) and Implications for the Dead Sea Fault Zone Activity, *J. Geo. Soc.* **162**, 259-271.
- Conder, C. R., and H. H. Kitchner (1882). *The Survey of Western Palestine. Memoirs of the Topography, Orography, Hydrography, and Archaeology.*, Palestine Exploration Fund, London, 226-227.
- Cundall, P. A. (1988). Formulation of a Three-Dimensional Distinct Element Model – Part I: A Scheme to Detect and Represent Contact in a System Composed of Many Polyhedral Blocks, *Int. J. Rock Mech. Min. Sci. & Geomech. Abstr.* **25**, 107-116.
- Cundall, P. A., and R. D. Hart (1992). Numerical Modelling of Discontinua, *Engineering Computations*, **9**, 101-113.
- Cyrus, M., and J. Beck (1978). Generalized Two- and Three-Dimensional Clipping, *Computers & Graphics* **3**, 23-28.
- Daëron, M., L. Benedetti, P. Tapponier, A. Sursock, and R. C. Finkel (2004). Constraints on the Post 25-ka Slip Rate of the Yammouneh Fault (Lebanon) Using in situ Cosmogenic <sup>36</sup>Cl Dating of Offset Limestone-Clast Fans, *Earth Planet Sci. Lett.* **227**, 105-119.
- Daëron, M., Y. Klinger, P. Tapponier, A. Elias, E. Jacques, and A. Sursock (2005). Sources of the Large AD 1202 and 1759 Near East Earthquakes, *Geology* **33**, 529-532.
- Daëron, M., Y. Klinger, P. Tapponier, A. Elias, E. Jacques, and A. Sursock (2007). 12,000-Year-Long Record of 10 to 13 Paleoequakes on the Yammouneh Fault, Levant Fault system, Lebanon, *Bull. Seism. Soc. Am.* **97**, 749-771.
- De Rossi, M. S. (1874). La basilica di Santa Petronilla presso Roma, testé discoperta, caduta per terremoto, *Bull Vul Ital*, **1**, 62-65.

- Dewey, J., and P. Byerly (1969). The Early History of Seismometry (To 1900), *Bull. Seism. Soc. Am.* **59**, 183-227.
- Elias, A., P. Tapponnier, S. C. Singh, G. C. P. King, A. Briais, M. Daëron, H. Carton, A. Sursock, E. Jacques, R. Jomaa, and Y. Klinger (2007). Active Thrusting Offshore Mount Lebanon: Source of the Tsunamigenic A.D. 551 Beirut-Tripoli Earthquake, *Geology* **35**, 755-758.
- Ellenblum, R. (1989). Who Built Qal'at al-Subayba?, *Dumbarton Oaks Papers* **43**, 103-112.
- Ellenblum, R. (1998). *Frankish Rural Settlement in the Latin Kingdom of Jerusalem*, Cambridge University Press, Cambridge, 321 pp.
- Ellenblum, R., S. Marco, A. Agnon, T. Rockwell, and A. Boas (1998). Crusader Castle Torn Apart by Earthquake at Dawn, 20 May 1202, *Geology* **26**, 303-306.
- Ellenblum, R. (2007). The Construction of a Frontier Castle: The Case of Vadum Iacob, in *Crusader Castles Modern Histories*, Cambridge University Press, Cambridge, 258-274.
- Ellenblum, R., S. Marco, R. Kool, U. Davidovitch, R. Porat, and A. Agnon (2015). Archaeological Record of Earthquake Ruptures in Tell Ateret, the Dead Sea Fault, *Tectonics* **34**, 2105–2117.
- Enzel, Y., G. Kadan, and Y. Eyal (2000). Holocene Earthquakes Inferred from a Fan-Delta Sequence in the Dead Sea Graben, *Quat. Res.* **53**, 34-48.
- Evans, A. (1928). *The Palace of Minos, Part II*. London, 844 pp.
- Fenner, F. (1905). In *Obergaliläa*. PJB 1:99-II0.
- Ferry, M., M. Meghraoui, N. Abou Karaki, M. Al-Taj, H. Amoush, and M. Barjous (2007). A 48-kyr-Long Slip Rate History for the Jordan Valley Segment of the Dead Sea Fault, *Earth Planet Sci. Lett.* **260**, 394-406.
- Ferry, M., M. Meghraoui, N. Abou Karaki, M. Al-Taj, and L. Khalil (2011). Episodic Behavior of the Jordan Valley Section of the Dead Sea Fault Inferred from a 14-ka-Long Integrated Catalog of Large Earthquakes, *Bull. Seism. Soc. Am.* **101**, 39-67.
- Fleischer, C., K.-G. Hinzen, and S. Schreiber (2010). Laserscanning eines römischen Brunnens in der Archäologischen Zone Köln, *Allgemeine Vermessungs Nachrichten* **5/2010**, 176-181.
- Fischer, M., A. Ovadia, and I. Roll (1984). The Roman Temple at Kedesh, Upper Galilee, *Tel Aviv* **11**, 146-172.
- Freund, R. (1965). A Model for the Structural Development of Israel and Adjacent Areas Since Upper Cretaceous Times, *Geol. Mag.* **102**, 189-205.
- Freund, R., I. Zak, and Z. Garfunkel (1968). Age and Rate of the Sinistral Movement Along the Dead Sea Rift, *Nature* **220**, 253-255.
- Freund, R., I. Zak, Z. Garfunkel, M. Goldberg, T. Weissbrod, and B. Derin (1970). The Shear Along the Dead Sea Rift, *Phil. Trans. Roy. Soc. Lond. A.* **267**, 107-130.

## Literature

---

- Galadini, F., K.-G. Hinzen, and S. Stiros (2006). Archaeoseismology: Methodological Issues and Procedure, *J. Seismol.* **10**, 395-414.
- Galli, P. (1999). Active Tectonics Along the Wadi Araba-Jordan Valley Transform Fault, *J. Geophys. Res.* **104**, 2777-2796.
- Galvez, F., M. Giaretton, S. Abeling, J. M. Ingham, and D. Dizhur (2018). Discrete Element Modeling of a Two Storey Unreinforced Masonry Scaled Model, in *16<sup>th</sup> European Conference on Earthquake Engineering*, Thessaloniki, 18-21 June 2018.
- Garfunkel, Z. (1981). Internal Structure of the Dead Sea Leaky Transform (Rift) in Relation to Plate Kinematics, *Tectonophysics* **80**, 81-108.
- Garfunkel, Z., and B. Derin (1984). Permian-Early Mesozoic Tectonism and Continental Margin Formation in Israel and its Implications for the History of the Eastern Mediterranean, *Geological Society, London, Special Publications* **17**, 187-201.
- Garfunkel, Z. (1988). Pre-Quaternary Geology of Israel, in *The Zoogeography of Israel*, Y. Yom-Tov, E. Tchernov (Eds.), Springer, Dordrecht, 7-34.
- GII (The Geophysical Institute of Israel) (2013). Seismological Bulletin Earthquakes in and Around Israel During 2009, Perot GII No 030/715/13 January 2013, 13-14.
- Gomez, F., M. Meghraoui, A. N. Darkal, R. Sbeinati, R. Darawcheh, C. Tabet, M. Khawlie, M. Charabe, K. Khair, and M. Barazangi (2001). Coseismic Displacements Along the Serghaya Fault: an Active Branch on the Dead Sea Fault System in Syria and Lebanon, *J. Geol. Soc.* **158**, 405-408.
- Gomez, F., M. Meghraoui, A. N. Darkal, F. Hijazi, M. Mouty, Y. Suleiman, R. Sbeinati, R. Darawcheh, R. Aal-Ghazzi, and M. Barazangi (2003). Holocene Faulting and Earthquake Recurrence Along the Serghaya Branch of the Dead Sea Fault System in Syria and Lebanon, *J. Geol. Soc.* **153**, 658-674.
- Gomez, F., G. Karam, M. Khawlie, S. McClusky, P. Vernnt, R. Reilinger, R. Jaafar, C. Tabet, K. Khair, and M. Barazangi (2007a). Global Positioning System Measurements of Strain Accumulation and Slip Transfer Through the Restraining Bend Along the Dead Sea Fault System in Lebanon, *Geophys. J. Int.* **168**, 1021-1028.
- Gomez, F., T. Nemer, C. Tabet, M. Khawlie, M. Meghraoui, and M. Barazangi (2007b). Strain Partitioning of Active Transpression within the Lebanese Restraining Bend of the Dead Sea Fault (Lebanon and SW Syria), *Geological Society London* **290**, 285-303.
- Gould, R. G. (1959). The LASER, Light Amplification by Stimulated Emission of Radiation, in *The Ann Arbor Conference on Optical Pumping, the University of Michigan*, P. A. Franken, and R. H. Sands (Eds.) **15**, 128 pp.
- Gregory, J. W. (1921). *The Rift Valleys and Geology of East Africa*, Seely, London, 479 pp.
- Grünthal, G. (Ed.) (1998). The European Macroseismic Scale EMS-88, Centre Européen de Géodynamique et de Séismologie (ECGS) **15**, 1-99.

- Guidoboni, E., A. Comastri, and G. Traina (1994). Catalogue of Ancient Earthquakes in the Mediterranean Area up to the 10<sup>th</sup> Century. INGV-SGA, Rome.
- Guidoboni, E. (1996). Archaeology and Historical Seismology: The Need for Collaboration in the Mediterranean Area, in *Archaeoseismology*, S. Stiros, and R. E. Jones (Eds.), British School at Athens, Fitch Laboratory Occasional Paper **7**, 7-13.
- Guidoboni, E., and A. Comastri (2005). Catalogue of Earthquakes and Tsunamis in the Mediterranean Area from the 11<sup>th</sup> to the 15<sup>th</sup> Century. INGV-SGA, Bologna.
- Gutenberg, B., and C. F. Richter (1956). Earthquake Magnitude, Intensity, Energy, and Acceleration, *Bull. Seism. Soc. Am.* **46**, 105–145.
- Hambright, K. D., and T. Zohary (1998). Lakes Hula and Agmon: Destruction and Creation of Wetland Ecosystems in Northern Israel, *Wetlands Ecology and Management* **6**, 83-89.
- Hamiel, Y., O. Piatibratova, and Y. Mizrahi (2016). Creep Along the Northern Jordan Valley Section of the Dead Sea Fault, *Geophys. Res. Lett.* **43**, 2492-2501.
- Hanks, T. C., and H. Kanamori (1979). A Moment Magnitude Scale, *Journal of Geophysical Research: Solid Earth* **84**, 2348-2350.
- Hart, R. D., P. A. Cundall, and J. V. Lemos (1988). Formulation of a Three-Dimensional Distinct Element Method – Part II: Mechanical Calculations for Motion and Interaction of a System Composed of Many Polyhedral Blocks, *Int. J. Rock Mech. Min. Sci. & Geomech. Abstr.* **25**, 117-125.
- Haynes, J. M., T. M. Niemi, and M. Atallah (2006). Evidence for Ground-Rupturing Earthquakes on the Northern Wadi Araba Fault at the Archaeological Site of Qasar Tilah, Dead Sea Transform Fault System, Jordan, *J. Seismol.* **10**, 415-430.
- Heimann, A. and E. Sass (1989). Travertines in Northern Hula Valley, *Sedimentology* **36**, 95-108.
- Hinojossa-Prieto, H. R., and K.-G. Hinzen (2015). Seismic Velocity Model and Near-Surface Geology at Mycenaean Tiryns, Argive Basin, Peloponnese, Greece, *Near Surface Geophysics* **13**, 103-113.
- Hinzen, K.-G. (2005). The Use of Engineering Seismological Models to Interpret Archaeoseismological Findings in Tolbiacum, Germany: A Case Study, *Bull. Seism. Soc. Am.* **95**, 521-539.
- Hinzen, K.-G. (2009a). Simulation of Toppling Columns in Archaeoseismology, *Bull. Seism. Soc. Am.* **99**, 2855–2875.
- Hinzen, K.-G. (2009b). Sensitivity of Earthquake-Toppled Columns to Small Change in Ground Motion and Geometry, *Israel J. Earth Sci.* **58**, 309-326.
- Hinzen, K.-G., C. Fleischer, S. K. Reamer, S. Schreiber, S. Schütte, and B. Yerli (2009). Quantitative Methods in Archaeoseismology, *1st INQUA-IGCP-567 International Workshop on Earthquake Archaeology and Palaeoseismology*, 50-51.

- Hinzen, K.-G., and J. Weiner (2009). What Caused the Damage of the Neolithic Wooden Well of Erkelenz-Kückhoven, Germany?, in *Palaeoseismology: Historical and Prehistorical Records of Earthquake Ground Effects for Seismic Hazard Assessment*, K. Reicherter, A. M. Michetti and P. G. Silva, (Eds.), Geological Society Special Publication, London **316**, 189–205.
- Hinzen, K.-G. (2010). Sensitivity of Earthquake-Topped Columns to Small Changes in Ground Motion and Geometry, *Israel J. Earth Sci.* **58**, 390-326.
- Hinzen, K.-G., S. Schreiber, and B. Yerli (2010). The Lycian Sarcophagus of Arttumpara, Pınara, Turkey: Testing Seismogenic and Anthropogenic Damage Scenarios, *Bull. Seism. Soc. Am.* **100**, 3148-3164.
- Hinzen, K.-G., and R. Kovalev (2010). Hiller's Seismoscope, *Seismological Research Letters* **81**, 804-810.
- Hinzen, K.-G. (2011). Archaeoseismology, in *Encyclopedia of Solid Earth Geophysics. Encyclopedia of Earth Sciences Series*, H. K. Gupta (Eds.), Springer, Dordrecht, 11-15.
- Hinzen, K.-G., C. Fleischer, S. K. Reamer, S. Schreiber, S. Schütte, and B. Yerli (2011). Quantitative Methods in Archaeoseismology, *Quaternary International* **242**, 31-41.
- Hinzen, K.-G., S. Schreiber, S. K. Reamer, and I. Wisona (2012). Archaeoseismic Study of Damage in Roman and Medieval Structures in the Center of Cologne, Germany, *J. Seismol.* **17**, 339-424.
- Hinzen, K.-G., H. Kehmeier, and S. Schreiber (2013a). Quantitative Archaeoseismological Study of the Roman Mausoleum in Pınara (Turkey)- Testing Seismogenic and Rockfall Damage Scenarios, *Bull. Seism. Soc. Am.* **103**, 1008-1021.
- Hinzen, K.-G., S. Schreiber, and S. Rosellen (2013b). A High Resolution Laser Scanning Model of the Roman Theater in Pınara, Turkey - Comparison to Previous Measurements and Search for the Causes of Damage, *Journal of Cultural Heritage*, **14**, 424-430.
- Hinzen, K.-G., M. Veters, T. Kalytta, S. K. Reamer, and U. Damm-Meinhardt (2014a). Testing the Response of Mycenaean Terracotta Figures and Vessels to Earthquake Ground Motions, *Geoarchaeology* **30**, 1-18.
- Hinzen, K.-G., R. Kovalev, S. Marco, and G. Schweppe (2014b). Constraints on Earthquake Slip Velocity Using an Archaeoseismic Model of the Ateret Fortress on the Dead Sea Transform Fault, in *The 8<sup>th</sup> International Symposium on Eastern Mediterranean Geology, 13-17 October 2014*, Muğla Sıtkı Koçman University, Turkey.
- Hinzen, K.-G., I. Schwellenbach, G. Schweppe, and S. Marco (2016a). Quantifying Earthquake Effects on Ancient arches, Example: The Kalat Nimrod Fortress, Dead Sea Fault Zone, *Seismological Research Letters* **87**, 751-764.
- Hinzen, K.-G., H. R. Hinojosa-Prieto, and T. Kalytta (2016b). Site Effects in Archaeoseismic Studies at Mycenaean Tiryns and Midea, *Seismological Research Letters* **87**, 1060-1074.
- Hinzen, K.-G., and A. Montabert (2017). Rectangular Blocks vs Polygonal Walls in Archaeoseismology, *Annals of Geophysics* **60**, S0443.

- Hinzen, K.-G., R. Arav, S. Filin, S. Marco, and G. Schweppe (2017). High Resolution DTM Reveals Tectonic Signal of the Dead Sea Fault at the Ateret Archaeological Site, Poster SSA Annual Meeting, Denver, Colorado.
- Hinzen, K.-G., J. Maran, H. R. Hinojosa-Prieto, U. Damm-Meinhardt, S. K. Reamer, J. Tzislakis, K. Kemna, G. Schweppe, C. Fleischer, and K. Demakopoulou (2018). Reassessing the Mycenaean Earthquake Hypothesis: Results of the HERACLES Project from Tiryns and Midea, Greece, *Bull. Seism. Soc. Am.* **108**, 1046-1070.
- Hofstetter, A., C. Dorbath, and L. Dorbath (2014). Instrumental Data on the Seismic Activity Along the Dead Sea Transform, in *The Dead Sea Transform Fault System: Reviews*, Z. Garfunkel, Z. Ben-Menahem, and E. Kagan (Eds.), Springer, Dordrecht, 263-278.
- Horowitz, A (1973). Development of the Hula Basin, Israel, *Israel J. Earth Sci.* **22**, 107-139.
- Housner, G. W. (1963). The Behavior of Inverted Pendulum Structures During Earthquakes, *Bull. Seism. Soc. Am.* **53**, 403-417.
- Kamai, R., and Y. H. Hatzor (2008). Numerical Analysis of Block Stone Displacements in Ancient Masonry Structures: A New Method to Estimate Historic Ground Motions, *Int. J. Numer. Anal. Meth. Geomech.* **32**, 1321-1340.
- Karabacak, V., E. Altunel, M. Meghraoui, and H. Akyüz (2010). Field Evidences from Northern Dead Sea Fault Zone (South Turkey): New Findings for the Initiation Age and Slip Rate, *Tectonophysics* **141**, 172-182.
- Karcz, I., U. Kafri, and Z. Meshel (1977). Archaeological Evidence for Subrecent Seismic Activity Along the Dead Sea-Jordan Rift, *Nature* **269**, 234-235.
- Karcz, I. and U. Kafri (1978). Evaluation of Supposed Archaeoseismic Damage in Israel, *Journal of Archaeological Science* **5**, 237-253.
- Karcz, I., and U. Kafri (1981). Studies in Archaeoseismicity of Israel: Hisham's Palace Jericho, *Israel J. Earth Sci.* **30**, 12-23.
- Karcz, I. (2004). Implications of Some Early Jewish Sources for Estimates of Earthquake Hazard in the Holy Land, *Ann. Geophys.* **47**, 759-792.
- Ken-Tor, R., M. Stein, Y. Enzel, A. Agnon, S. Marco, and J. F. W. Negendank (2001). Precision of Calibrated Radiocarbon Ages of Historic Earthquakes in the Dead Sea Basin, *Radiocarbon* **44**, 396-397.
- Klinger, Y., L. Rivera, H. Haessler, and J. C. Maurin (1999). Active Faulting in the Gulf of Aqaba: New Knowledge from the Mw 7.3 Earthquake of 22 November 1995, *Bull. Seism. Soc. Am.* **89**, 1025-1036.
- Klinger, Y., J. P. Avouac, N. Abou Karaki, L. Dorbath, and D. Bourles (2000a). Slip Rate on the Dead Sea Transform Fault in Northern Araba Valley (Jordan), *Geophys. J. Int.* **142**, 755-768.
- Klinger, Y., J. P. Avouac, L. Dorbath, N. Abou-Karaki, and N. Tisnerat (2000b). Seismic Behavior of the Dead Sea Fault Along Araba Valley, *Jordan, Geophys. J. Int.* **142**, 769-782.

- Kohl, H., and C. Watzinger (1916). *Antike Synagogen In Galilaea*. J. C. Hinrichs, Leipzig, 250 pp.
- Konietzky, H., L. te Kamp, and H. Hagedorn (2004). The Gotthard-Base-Tunnel: Conceptual Modeling for Tunneling Extremely Weak Zones, in *Numerical Modeling of Discrete Materials in Geotechnical Engineering*, H. Konietzky (Ed.), A. A. Balkema, 21-27.
- Konstandinidis, D., and N. Markis (2005). Seismic Response of Multidrum Classical Columns. Earthquake, *Eng. Struc. Dyn.* **34**, 1243-1270.
- Krausz, K. (2002). Tragverhalten gemauerter Tonnengewölbe mit Stichkappen, Dissertation, Institut für Baustatik der Universität Stuttgart, 42 pp.
- Lanciani, R. (1918). Segni di terremoti negli edifizii di Roma antica, *Bull Comm Archeol Comunale Roma* **45**, 1-28.
- Le Beon, M., Y. Klinger, A. Q. Amrat, A. Agnon, L. Dorbath, G. Baer, J.-C. Ruegg, O. Charade, and O. Mayyas (2008). Slip Rate Locking Depth from GPS Profiles Across the Southern Dead Sea Transform, *Journal of Geophysical Research* **113**, B11403.
- Le Beon, M., Y. Klinger, M. Al-Qaryouti, A. S. Meriaux, R. C. Finkel, A. Elias, O. Mayyas, F. J. Ryerson, and P. Tapponnier (2010). Early Holocene and Late Pleistocene Slip Rates of the Southern Dead Sea Fault Determined from Be-10 Cosmogenic Dating of Offset Alluvial Deposits, *J. Geophys. Res. Solid Earth* **115**, B11414.
- Le Beon, M., Y. Klinger, A. S. Meriaux, M. Al-Qaryouti, R. C. Finkel, O. Mayyas, and P. Tapponnier (2012). Quaternary Morphotectonic Mapping of the Wadi Araba and Implications for the Tectonic Activity of the Southern Dead Sea fault, *Tectonics* **21**, TC5003.
- Lemos, J. V., S. Oliveira, and P. Mendes (2006). Analysis of the Dynamic Behaviour of Cabril Dam Considering the Influence of Contraction Joints, in *7th European Conference on Structural Dynamics (EURODYN 2008)*, Univ. de Southampton, E255.
- Lemos, J. V., C. S. Oliveira, and M. Navarro (2015). 3-D Nonlinear Behavior of an Obelisk Subjected to the Lorca May 11, 2011 Strong Motion Record, *Engineering Failure Analysis*, **58**, 212-228.
- Lourenco, P. B., D. V. Oliveira, P. Roca, and A. Orduna (2005). Dry Joint Stone Masonry Wall Subjected to In-Plane Combined Loading, *Journal of Structural Engineering* **131**, 1665-1673.
- Magness, J. (1990). Some Observations on the Roman Temple at Kedesh, *Israel Exploration Journal* **40**, 173-181.
- Mahmoud, S., R. Reilinger, S. McClusky, P. Vemant, and A. Tealeb (2005). GPS Evidence for Northward Motion of the Siani Block: Implications for E. Mediterranean Tectonics, *Earth and Planetary Science Letters* **238**, 217-224.
- Maiman, T. H. (1960). Stimulated Optical Radiation in Ruby, *Nature* **187**, 493-494.

- Makovsky, Y., A. Wunch, R. Ariely, Y. Shaked, A. Rivilin, A. Shemesh, Z. Ben Avraham, and A. Agnon (2008). Quaternary Transform Kinematics Constrained by Sequence Stratigraphy and Submerged Coastline Features: the Gulf of Aqaba, *Earth Planet. Sci. Lett.* **271**, 109-122.
- Marco, S., and A. Agnon (1995). Prehistoric Earthquake Deformations Near Masada, Dead Sea Graben, *Geology* **23**, 695-698.
- Marco, S., M. Stein, A. Agnon, and H. Ron (1996). Long Term Earthquake Clustering: a 50,000 Year Paleoseismic Record in the Dead Sea Graben, *Journal of Geophysical Research* **101**, 6179-6192.
- Marco, S., A. Agnon, R. Ellenblum, A. Eidelman, U. Basson, and A. Boas (1997). 817-Year-Old Walls Offset Sinistral 2.1 m by the Dead Sea Transform, Israel, *Journal Geodynamics* **24**, 11-20.
- Marco, S., M. Hartal, N. Hazan, L. Lec, and M. Stein (2003). Archaeology, History, and Geology of the A.D. 749 Earthquake, Dead Sea Transform, *Geology* **31**, 665-668.
- Marco, S., and A. Agnon (2005). High-Resolution Stratigraphy Reveals Repeated Earthquake Faulting in the Masada Fault Zone, Dead Sea Transform, *Tectonophysics* **408**, 101-112.
- Marco, S., T. K. Rockwell, A. Heimann, U. Frieslander, and A. Agnon (2005). Late Holocene Activity of the Dead Sea Transform Revealed in 3D Palaeoseismic Trenches on Jordan Gorge Segment, *Earth and Planetary Science Letters* **234**, 189-205.
- Marco, S., and Y. Klinger (2014). Review of On-Fault Palaeoseismic Studies Along the Dead Sea Fault, in *The Dead Sea Transform Fault System: Reviews*, Z. Garfunkel, Z. Ben-Avraham, and E. Kagan (Eds.), Springer, Dordrecht, 183-205.
- Matthews, A., A. P. S. Reymer, D. Avigad, J. Cochon, and S. Marco (1989). Pressures and Temperatures of Pan-African High-Grade Metamorphism in the Elat Association, NE Sinai, *Isr. J. Earth Sci.* **38**, 1-17.
- McCalpin, J. P. (1996). *Paleoseismology*, Academic Press, San Diego, 588 pp.
- McClusky, S., R. Reilinger, S. Mahmoud, D. Ben Sari, and A. Tealeb (2003). GPS Constraints on Africa (Nubia) and Arabia Plate Motions, *Geophys. J. Int.* **155**, 126-138.
- Medvedev, S., W. Sponheuer, and V. Karník (1964). Neue seismische Skala, in *7. Tagung der Europäischen Seismologischen Kommission vom 24.9. bis 30.9.1962 in Jena, DDR*, Deutsche Akademie der Wissenschaften zu Berlin, 69-76.
- Meskouris, K. (1999). *Baudynamik: Modelle, Methoden, Praxisbeispiele*, Ernst und Sohn, Berlin, 379 pp.
- Meskouris, K., K.-G. Hinzen, C. Butenweg, and M. Mistler (2011). *Bauwerke und Erdbeben: Grundlagen – Anwendung – Beispiele*, 3-Auflage, Vieweg+Teubner Verlag, Wiesbaden, 718 pp.
- Meghraoui, M., F. Gomez, R. Sbeinati, J. Van der Woerd, M. Mouty, A. N. Darkal, Y. Radwan, I. Layyous, H. A. Najjar, R. Darawcheh, F. Hijazi, R. Al-Ghazzi, and M. Barazangi (2003). Evidence for 830 Years of Seismic Quiescence from Palaeoseismology, Archaeoseismology and Historical Seismicity Along the Dead Sea Fault in Syria, *Earth Planet Sci. Lett.* **210**, 35-52.

- Michetti, A. M., E. Esposito, L. Guerrieri, S. Porfido, L. Serva, R. Tatevossian, E. Vittori, F. Audemard, T. Azuma, J. Clague, V. Comerci, A. Gurpinar, J. Mc Calpin, B. Mohammadioun, N.A. Morner, Y. Ota, and E. Roghozin (2007). Intensity Scale ESI 2007, *Memorie Descrittive Della Carta Geologica d'Itally* **74**, L. Guerrieri, E. Vittori (Eds.), 41 pp.
- Migowski, C., A. Agnon, R. Bookman, J. F. W. Negendank, and M. Stein (2004). Recurrence Pattern of Holocene Earthquakes Along the Dead Sea Transform Revealed by Varve-Counting and Radiocarbon Dating of Lacustrine Sediments, *Earth Planet. Sci. Lett.* **222**, 301-314.
- Nemer, T., and M. Meghraoui (2006). Evidence of Coseismic Rupture Along the Roum Fault (Lebanon): A Possible Source for the AD 1837 Earthquake, *Journal of Structural Geology* **28**, 1483-1495.
- Nemer, T., M. Meghraoui, and K. Khair (2008). The Rachaya-Serghaya Fault System (Lebanon): Evidence of Coseismic Ruptures, and the AD 1759 Earthquakes Sequence, *Journal of Geophysical Research*, **113**, B05312, 1-12.
- Niemi, T. M., H. Zhang, M. Atallah, and J. B. J. Harrison (2001). Late Pleistocene and Holocene Slip Rate of the Northern Wadi Araba Fault, Dead Sea Transform, Jordan, *J. Seismol.* **5**, 449-474.
- Oliveira, D. V., G. Greechi, A. McCall, J. Noh, E. Speer, and M. Tohidi (2012). Seismic Analysis of the Roman Temple of Evora, Portugal, in *15th World Conference on Earthquake Engineering. Sociedade Portuguesa de Engenharia Sísmica*, 1-10.
- Otter, J. R. H., A. C. Cassell, and R. E. Hobbs (1966). Dynamic Relaxation (Paper No. 6986), *Proc. Inst. Civ. Engrs.* **35**, 633-656.
- Ovadiah, A., I. Roll, and M. Fischer (1993). The Roman Temple at Kedesh in Upper Galilee: A Response. *Israel Exploration Journal* **43**, 60-63.
- Papantonopoulos, C., I. N. Psycharis, D. Y. Papastamatiou, J. V. Lemos, and H. P. Mouzakis (2002). Numerical Prediction of the Earthquake Response of Classical Columns Using the Distinct Element Method, *Earthquake Eng. Struc.* **31**, 1699-1717.
- Papastamatiou, D., and I. Psycharis (1993). Seismic Response of Classical Monuments. A Numerical Perspective Developed at the Temple of Apollo in Bassae, Greece, *Terra Nova*, **5**, 591-601.
- Papastamatiou, D., and I. Psycharis (1996). Numerical Simulation of the Seismic Response of Megalithic Monuments: Preliminary Investigations Related to the Apollo Temple in Vassai, in *Archaeoseismology*, S. Stiros, and R. E. Jones (Eds.), British School at Athens, Fitch Laboratory Occasional Paper **7**, 225-236.
- Peña, F., F. Prieto, P. B. Lourenço, A. Campos Costa, and J. V. Lemos (2007). On the Dynamics of Rocking Motion of Single Rigid-Block Structures, *Earthquake Engineering & Structural Dynamics* **36**, 2383-2399.
- Picard, L. (1939). Outline of the Tectonics of the Earth, *Bull. Geol. Dept. Hebrew Univ. Jerusalem* **2**, 58-84.
- Prieto, F., and P. B. Lourenco (2005). On the Rocking Behavior of Rigid Objects, *Meccanica* **40**, 121-133.

- Psycharis, I. N., D. Y. Papastamatiou, and A. P. Alexandris (2000). Parametric Investigation of the Stability of Classical Columns Under Harmonic and Earthquake Excitations, *Earthquake Engineering and Structural Dynamics* **29**, 1093-1109.
- Psycharis, I. N., J. V. Lemos, D. Y. Papastamatiou, C. Zambas, and C. Papantonopoulos (2003). Numerical Study of the Seismic Behavior of a Part of the Parthenon Pronaos, *Earthquake Engineering and Structural Dynamics* **32**, 2063-2084.
- Quennell, A. M. (1956a). The Structural and Geomorphic Evolution of the Dead Sea Rift, *Quarterly Journal of the Geological Society* **114**, 1-24.
- Quennell, A. M. (1956b). Tectonics of the Dead Sea Rift, in *Asociacion de Servicios Geologicos Africanos, Congreso Geologico Internacional, 20th session, Mexico*, 385-405.
- Quennell, A. M. (1959). Tectonics of the Dead Sea Rift, *Int. Geo. Congr. 20 (Mexico), Assoc. Serv. Geol., Afr.*, 385-405.
- Reches, Z., and D. F. Hoexter (1981). Holocene Seismic and Tectonic Activity in the Dead Sea Area, *Tectonophysics* **80**, 235-254.
- Reid, H. F. (1910). The California Earthquake of April 18, 1906, Mechanics of the Earthquake, in *Report of the State Earthquake Investigation Commission in Two Volumes and Atlas*, Carnegie Institute of Washington, 192 pp.
- Reilinger, R., S. McClusky, P. Vernant, S. Lawrence, S. Ergintav, R. Cakmak, H. Ozener, F. Kadirov, I. Guliev, R. Stephanyan, M. Nadariya, G. Hahubia, S. Mahmoud, K. Sakr, A. ArRajehi, D. Paradissis, A. Al-Aydrus, M. Prilepin, T. Guseva, E. Evren, A. Dmitrotsa, S. V. Filikov, F. Gomez, R. Al-Ghazzi, and G. Karam (2006). GPS Constraints on Continental Deformation in the Africa-Arabia-Eurasia Continental Collision Zone and Implications for the Dynamics of Plate Interactions, *Journal of Geophysical Research* **11**, B05411.
- Renan, E. (1864). *Mission en Phénicie*. Impr. Impériale, Paris, 884 pp.
- Reubeur-Paschwitz, E. (1895). Prof. Milne's Observation of the Argentine Earthquake, October 27, 1894, *Nature* **2**, 55.
- Richter C. F. (1935). An Instrumental Earthquake Magnitude Scale, *Bull. Seism. Soc. Am.* **25**, 1-32.
- Richter C. F. (1956). *Elementary Seismology*, Freeman, San Francisco, 578 pp.
- Rusinkiewicz, S., and M. Levory (2001). Efficient Variants of the ICP Algorithm, in *Proceedings Third International Conference on 3-D Digital Imaging and Modeling*, Quebec City, 145-152.
- Sadeh, M., Y. Hamiel, A. Ziv, Y. Bock, P. Fang, and S. Wdowinski (2012). Crustal Deformation Along the Dead Sea Transform and the Carmel Fault Inferred from 12 Years of GPS Measurements, *J. Geophy. Res. Solid Earth* **117**, B8, B08410.

- Salamon A., T. Rockwell, S. N. Ward, E. Guidoboni, and A. Comastri (2007). Tsunami Hazard Evaluation of the Eastern Mediterranean: Historical Analysis and Selected Modeling, *Bull. Seism. Soc. Am.* **97**, 705-724.
- Sass, E., and A. Bein (1982). The Cretaceous Carbonate Platform in Israel, *Cretaceous Research* **3**, 135-144.
- Sbeinati, M. R., R. Darawcheh, and M. Mouty (2005). The Historical Earthquakes of Syria: an Analysis of Large and Moderate Earthquakes from 1365 B.C. to 1900 A.D., *Ann. Geophys.* **48**, 347-435.
- Sbeinati, M. R., M. Meghraoui, G. Suleyman, F. Gomez, P. Grootes, M.-J. Nadeau, H. Al Najjar, and R. Al-Ghazzi (2010). Timing of Earthquake Ruptures at the Al Harif Roman Aqueduct (Dead Sea Fault, Syria) from Archaeoseismology and Paleoseismology, in *Ancient Earthquakes* M. Sintubin, I. S. Stewart, T. M. Niemi, and E. Altunel (Eds.), *Geological Society of America Special Paper* **471**, 243-267.
- Schreiber, S., K.-G. Hinzen, and C. Fleischer (2009). An Application of 3D Laser Scanning in Archaeology and Archaeoseismology – The Medieval Cesspit in the Archaeological Zone Cologne, Germany, in *1st INQUA-IGCP-567 International Workshop on Earthquake Archaeology and Palaeoseismology*, Baelo Claudia, Spain, 136-138.
- Schreiber, S., and K.-G. Hinzen (2010). Deformation Analysis on Ancient Structures Based on 3D-Laserscanning, *Geophysical Research Abstracts* **12**, EGU2010-4870.
- Schreiber, S., K.-G. Hinzen, and C. Fleischer (2010). Close-Range Laserscanning in the Archaeological Zone Cologne, Germany, Poster Workshop on Remote Sensing Methods for Change Detection and Process Modelling, 18.-19.11.2010, Cologne.
- Schreiber, S., K.-G. Hinzen, C. Fleischer, and S. Schütte (2012). Excavation-Parallel Laser Scanning of a Medieval Cesspit in the Archaeological Zone Cologne, Germany, *ACM J. Comput. Cult. Herit.* **5**, 22 pp.
- Schwellenbach, I. (2015). Reconstruction of Ground Motions from the 1759 Lebanon Earthquake to Facilitate Damage Analysis of the Nimrod Castel, Golan Heights. *Master thesis, Mathematisch-Naturwissenschaftliche Fakultät, Universität zu Köln*, 95 pp.
- Schweppe, G., K.-G. Hinzen, S. Reamer, M. Fischer, and S. Marco (2017). The ruin of the Roman Temple of Kedesh, Israel; Example of a Precariously Balanced Archaeological Structure Used as a Seismoscope, *Annals of Geophysics* **60**, S0444.
- Shaked, Y, A. Agnon, B. Lazar, S. Marco, U. Avner, and M. Stein (2004). Large Earthquakes Kill Coral Reefs at the North-West Gulf of Aqaba, *Terra Nova* **16**, 133-138.
- Shamir, G., G. Baer, and A. Hofstetter (2003). Three-Dimensional Elastic Earthquake Modelling Based on Integrated Seismological and InSAR Data: the  $M_w=7.2$  Nuweiba Earthquake, Gulf of Elat/Aqaba 1995 November, *Geophys. J. Int.* **154**, 731-744.
- Shapira A., and A. Hofstetter (1993). Source Parameters and Scaling Relationships of Earthquakes in Israel, *Tectonophysics* **217**, 217-226.

## Literature

---

- Shebalin, N. V., V. Karnik, and D. Hadzievski (1974). *Catalogue of Earthquakes of the Balkan Region, Part I*, UNDP-UNESCO Survey of the seismicity of the Balkan region, 599 pp.
- Sieberg, A. (1933). *Erdbebenforschung und ihre Verwertung für Technik, Bergbau und Geologie*, G. Fischer, Jena 44 pp.
- Siegman, A. E. (1986). *Lasers*, University Science Books, Mill Valley, CA 37, 13054 pp.
- Sneh A, and R. Weinberger (2006). Geological Map of Israel. Sheet 2-IV Rosh Pinna, scale 1:50000. Geological Survey Israel.
- Steinitz, G., Y. Bartov, and J. C. Hunziker (1978). K-Ar Determinations of Some Miocene-Pliocene Basalts in Israel: Their Significance to the Tectonics of the Rift Valley, *Geol. Mag.* **115**, 329-340.
- Stiros, S. and R. E. Jones (1996). *Archaeoseismology*. Fitch Laboratory Occasional Paper **7**, Athens, British School of Athens, 268 pp.
- Suess, E. (1891). Die Brüche von Africa, *Denkschriften Akademie Wissenschaft, Wien* **58**, 555-584.
- Thomas, R., T. M. Niemi, and S. T. Parker (2007). Structural Damage from Earthquakes in the Second-Ninth Centuries at the Archaeological Site of Aila in Aqaba, Jordan, *Bull. Am. Sch. Orient. Res.* **346**, 59-77.
- Torres, H. E. (2014). Builders in pre-Hispanic Peruvian Andes: Analytical Approaches to Knowledge their Seismic Resistance in *9<sup>th</sup> International Conference on Structural Analysis of Historical Constructions* F. Peña and M. Chávez (Eds.).
- UM Manual (2016). Universal Mechanism User's Manual, Laboratory of Computational Mechanics, Bryansk State Technical University, Bryansk , Russia.
- Unity Manual (2017). Unity User Manual, Unity Technologies Ltd, <https://docs.unity3d.com/Manual/> (last accessed date 05.2017)
- Vigny C., P. Huchon, J.-C. Ruegg, K. Kahnbari, and L.M. Asfaw (2006). Confirmation of Arabian Plate Slow Motion by New GPS Data in Yemen, *Journal of Geophysical Research* **111**, B02402.
- Wald, D. J., V. Quitoriano, T. H. Heaton, and H. Kanamori, (1999). Relationships Between Peak Ground Acceleration, Peak Ground Velocity, and Modified Mercalli Intensity in California, *Earthquake Spectra* **15**, 557-564.
- Wang, R. (1999). A Simple Orthonormalization Method for Stable and Efficient Computation of Green's Functions, *Bull. Seism. Soc. Am.* **89**, 733-741.
- Wdowinski, S., Y. Bock, G. Baer, L. Prawirodirdjo, N. Bechor, S. Naaman, R. Knafo, Y. Forrai, and Y. Melzer (2004). GPS Measurements of Current Crustal Movements Along the Dead Sea Fault *Journal of Geophysical Research*, **109**, B05403.
- Wechsler, N., O. Katz, Y. Dray, I. Gonen, and S. Marco (2009). Estimating Location and Size of Historical Earthquakes by Combining Archaeology and Geology in Umm-El-Quanatir, Dead Sea Transform, *Natural Hazards* **50**, 27-43.

## Literature

---

- Wechsler, N., T. K. Rockwell, Y. Klinger, P. Stepancikova, M. Kanari, S. Marco, and A. Agnon (2014). A Paleoseismic Record of Earthquakes for the Dead Sea Transform Fault Between the First and Seventh Centuries C.E.: Nonperiodic Behaviour of a Plate Boundary Fault, *Bull. Seism. Soc. Am.* **104**, 1329-1347.
- Wechsler, N., S. Shmuel, K.-G. Hinzen, and H. Hinojosa-Prieto (2018). Historical Earthquakes Around the Sea of Galilee in *Hippos-Sussita of the Decapolis. The First Twelve Seasons of Excavations 2000 - 2011 Volume II*. The Zinman Institute of Archaeology, 5-12.
- Wells, D. L., and K. J. Coppersmith (1994). New Empirical Relationships Among Magnitude, Rupture Length, Rupture Width, Rupture Area, and Surface Displacement, *Bull. Seism. Soc. Am.* **84**, 974-1002.
- Wiechert, E. (1926). Untersuchungen der Erdrinde mit Hilfe von Sprengungen, *Geologische Rundschau* **17**, 339-346.
- Willis, B. (1928). Dead Sea Problem: Rift Valley or Ramp Valley? *Bulletin of Geological Society of America* **39**, 490-542.
- Wood, H. O., and R. Neumann (1931). Modified Mercalli Intensity Scale of 1931, *Bull. Seism. Soc. Am.* **21**, 277-283.
- Yerli, B., J. H. ten Veen, M. Sintubin, V. Karabacak, C. Yalçın, and E. Altunel (2010). Assessment of Seismically Induced Damage Using Lidar: The Ancient City of Pınara (SW Turkey) as a Case Study, in *Ancient Earthquakes*, M. Sintubin, I. S. Stewart, T. M. Niemi, E. Altunel (Eds.), *Geological Society of America Special Paper* **471**, 157-170.
- Zhang, B., L. Yuhua, G. Shumin, R. E. Wallace, R.C. Bucknam, and T. C. Hanks (1986). Fault Scarps Related to the 1739 Earthquake and Seismicity of the Yinchuan Graben, Ningxia Huizi Zizhiqu, China, *Bull. Seism. Soc. Am.* **76**, 1253-1287.
- Zhang J., and N. Makris (2001). Rocking Response of Free-Standing Blocks Under Cycloidal Pulses, *J. Eng. Mechanics* **127**, 473-483.
- Zilberman, E., R. Amit, A. Heimann, and N. Porat (2000). Changes in Holocene Paleoseismic Activity in the Hula Pull-Apart Basin, Dead Sea Rift, Northern Israel, *Tectonophysics* **321**, 237-252.
- Zilberman, E., R. Amit, N. Porat, Y. Enzel, and U. Avner (2005). Surface Rupture Induced by the Devastating 1068 AD Earthquake in the Southern Arava Valley, Dead Sea Rift, Israel, *Tectonophysics* **408**, 79-99.
- Zohar, M., and S. Marco (2012). Re-Estimating the Epicenter of the 1927 Jericho Earthquake Using Spatial Distribution of Intensity Data, *Journal of Applied Geophysics* **82**, 19-29.

## 9 DATA AND RESOURCES

Blender - a 3D modelling and rendering package Ver. 2.77a Blender Online Community, Blender Foundation Blender Institute, Amsterdam (<https://www.blender.org/>)

Didger Golden Software, LLC, Colorado, USA.

GIMP - Gnu Image Manipulation Program Ver. 2.10 (<http://www.gimp.org/>)

Grapher Golden Software, LLC, Colorado, USA.

PhysX Engine NVIDIA Corporation.

Universal Mechanism Version 7, Laboratory of Computational Mechanics, Bryansk State Technical University, Bryansk , Russia.

Unity3D Unity Technologies Ver. 5.3.5f 20 May, 2016

Itasca Consulting Group, Inc. (2013) 3DEC - Three-Dimensional Distinct Element Code, Ver. 5.0. Minneapolis: Itasca.

Itasca Consulting Group, Inc. (2016) 3DEC - Three-Dimensional Distinct Element Code, Ver. 5.2. Minneapolis: Itasca.

Surfer Golden Software, LLC, Colorado, USA.

Python Software Foundation. Python Language Reference, Ver. 3.6

## A. APPENDIX CRUSADER FORTRESS ATERET

### a. First Scenario

Offset	1.75 m
PGV	0.1 m/s
Direction	north

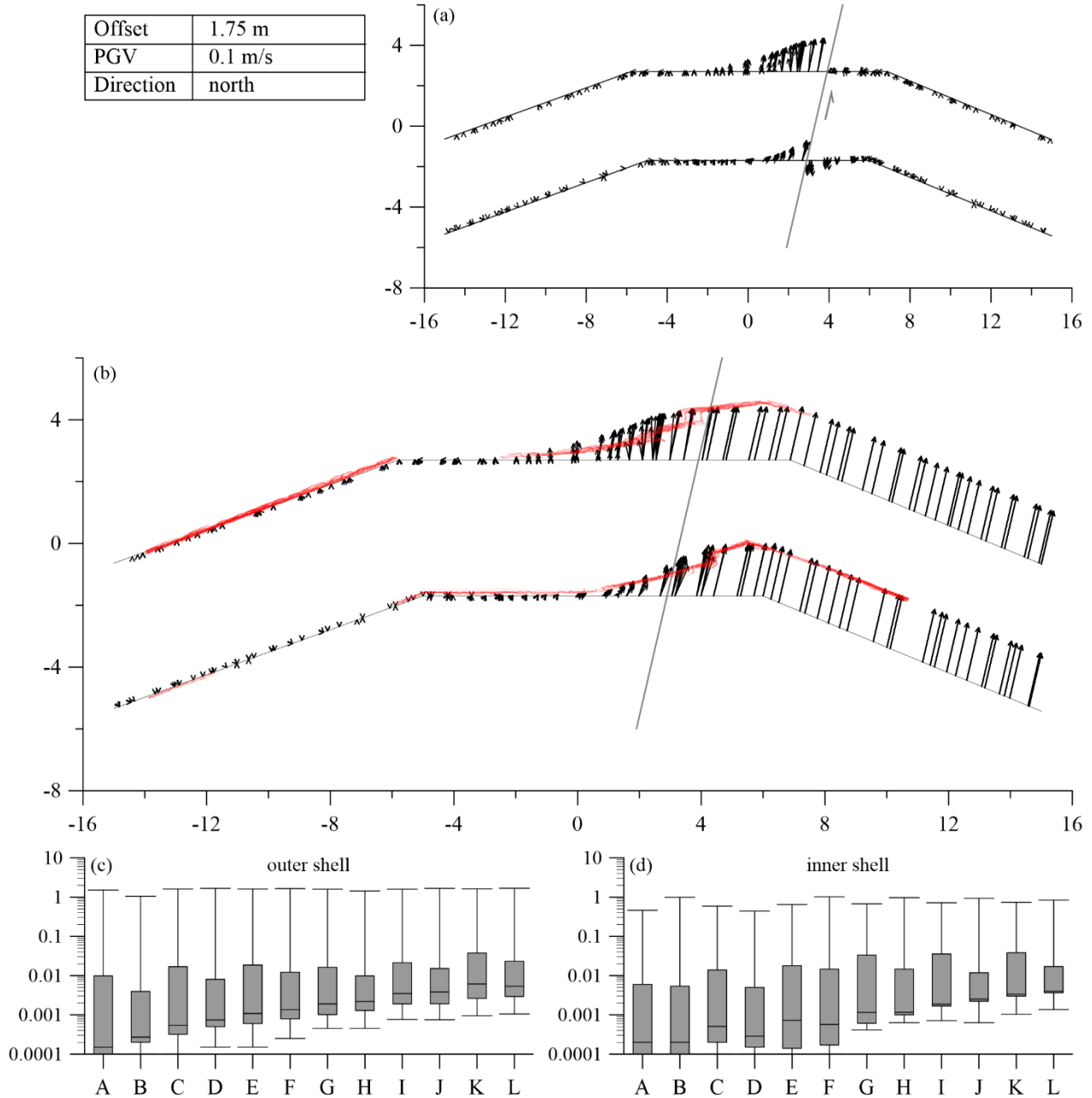


Figure A.1: Results of the simulation with a cycloidal pulse for a displacement of 1.75 m and a PGV of 0.1 m/s. (a) Displacement vectors of the blocks relative to the displacement of the baseplate beneath the blocks from a top view perspective. The light grey line marks the course of the fault line in the model. The light grey arrows point in direction of the ground motion. The dark grey lines mark the course of the initial wall line. (b) Vector plot of the absolute displacement (m) of all blocks from a top view perspective. The grey line marks the course of the fault line in the model and strikes in north-south direction. The superposed red points are the measured points from the 3D laser scanning survey. (c) Boxplot of the vector length relative to the displacement of the baseplate for all blocks in individual rows with row A: bottom and row L: top of the outer shell. (d) the same as (c) for the inner shell.

## Appendix Crusader Fortress Ateret

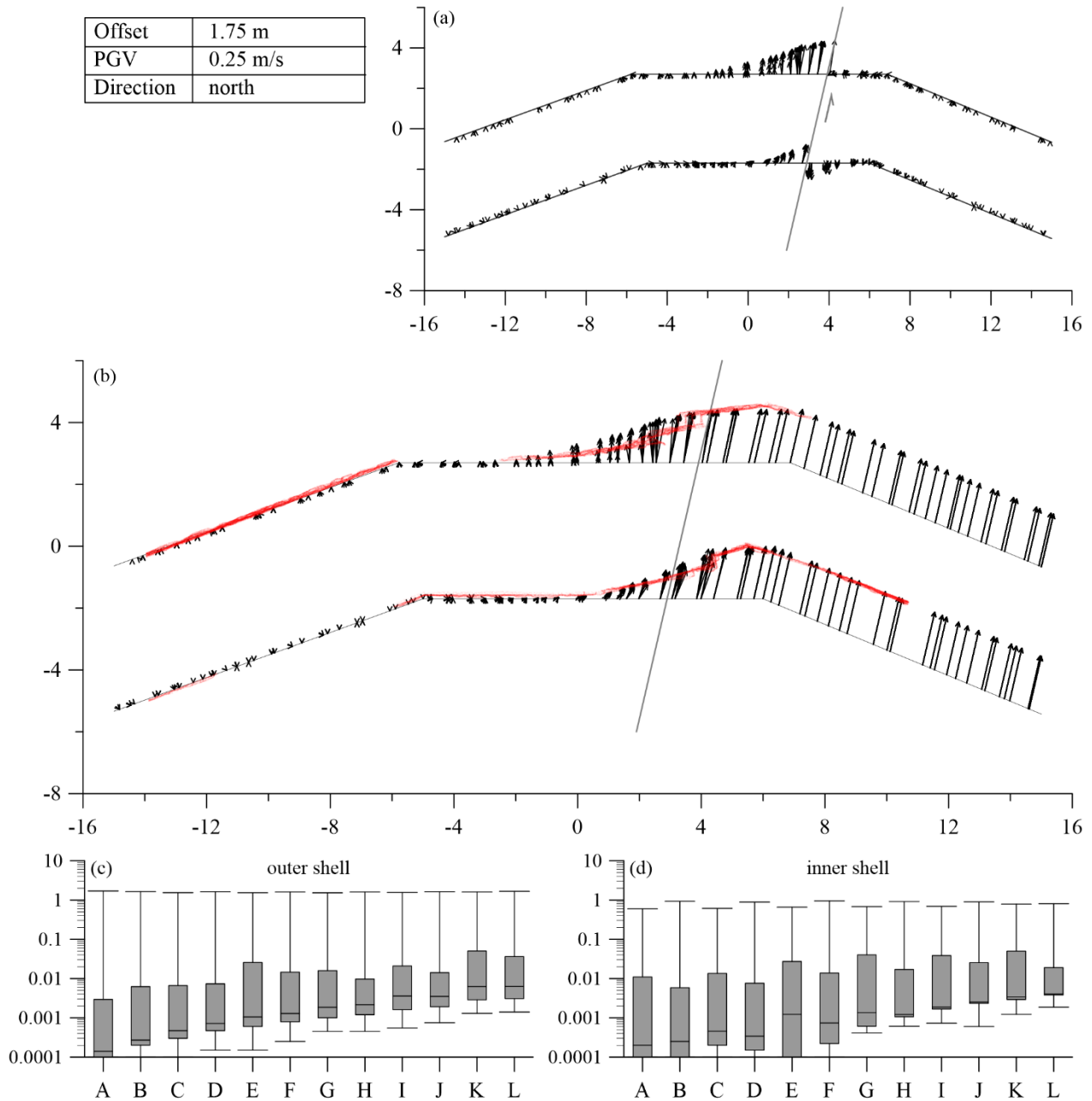


Figure A.2: Results of the simulation with a cycloidal pulse for a displacement of 1.75 m and a PGV of 0.25 m/s. (a) Displacement vectors of the blocks relative to the displacement of the baseplate beneath the blocks from a top view perspective. The light grey line marks the course of the fault line in the model. The light grey arrows point in direction of the ground motion. The dark grey lines mark the course of the initial wall line. (b) Vector plot of the absolute displacement (m) of all blocks from a top view perspective. The grey line marks the course of the fault line in the model and strikes in north-south direction. The superposed red points are the measured points from the 3D laser scanning survey. (c) Boxplot of the vector length relative to the displacement of the baseplate for all blocks in individual rows with row A: bottom and row L: top of the outer shell. (d) the same as (c) for the inner shell.

## Appendix Crusader Fortress Ateret

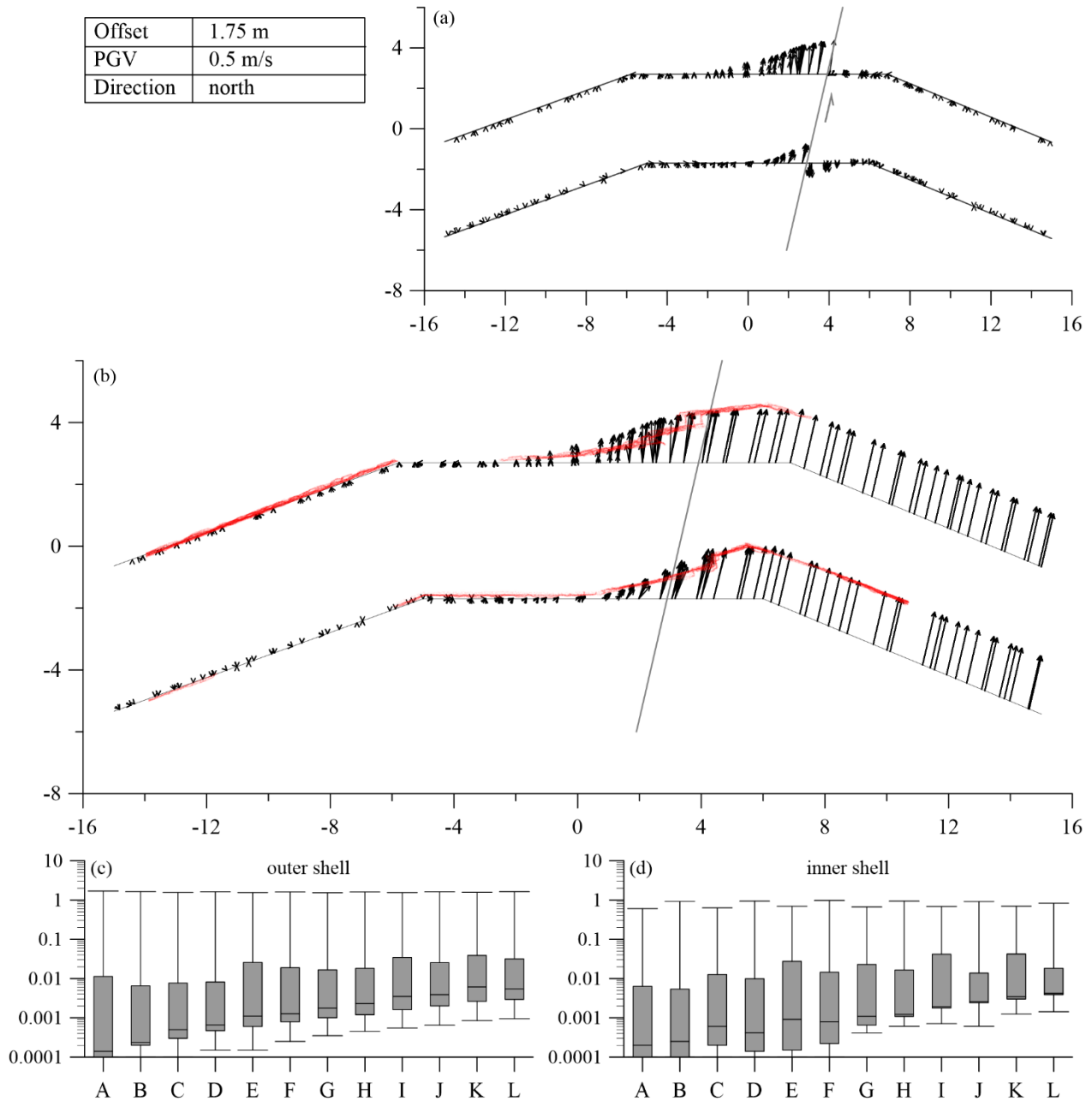


Figure A.3: Results of the simulation with a cycloidal pulse for a displacement of 1.75 m and a PGV of 0.5 m/s. (a) Displacement vectors of the blocks relative to the displacement of the baseplate beneath the blocks from a top view perspective. The light grey line marks the course of the fault line in the model. The light grey arrows point in direction of the ground motion. The dark grey lines mark the course of the initial wall line. (b) Vector plot of the absolute displacement (m) of all blocks from a top view perspective. The grey line marks the course of the fault line in the model and strikes in north-south direction. The superposed red points are the measured points from the 3D laser scanning survey. (c) Boxplot of the vector length relative to the displacement of the baseplate for all blocks in individual rows with row A: bottom and row L: top of the outer shell. (d) the same as (c) for the inner shell.

## Appendix Crusader Fortress Ateret

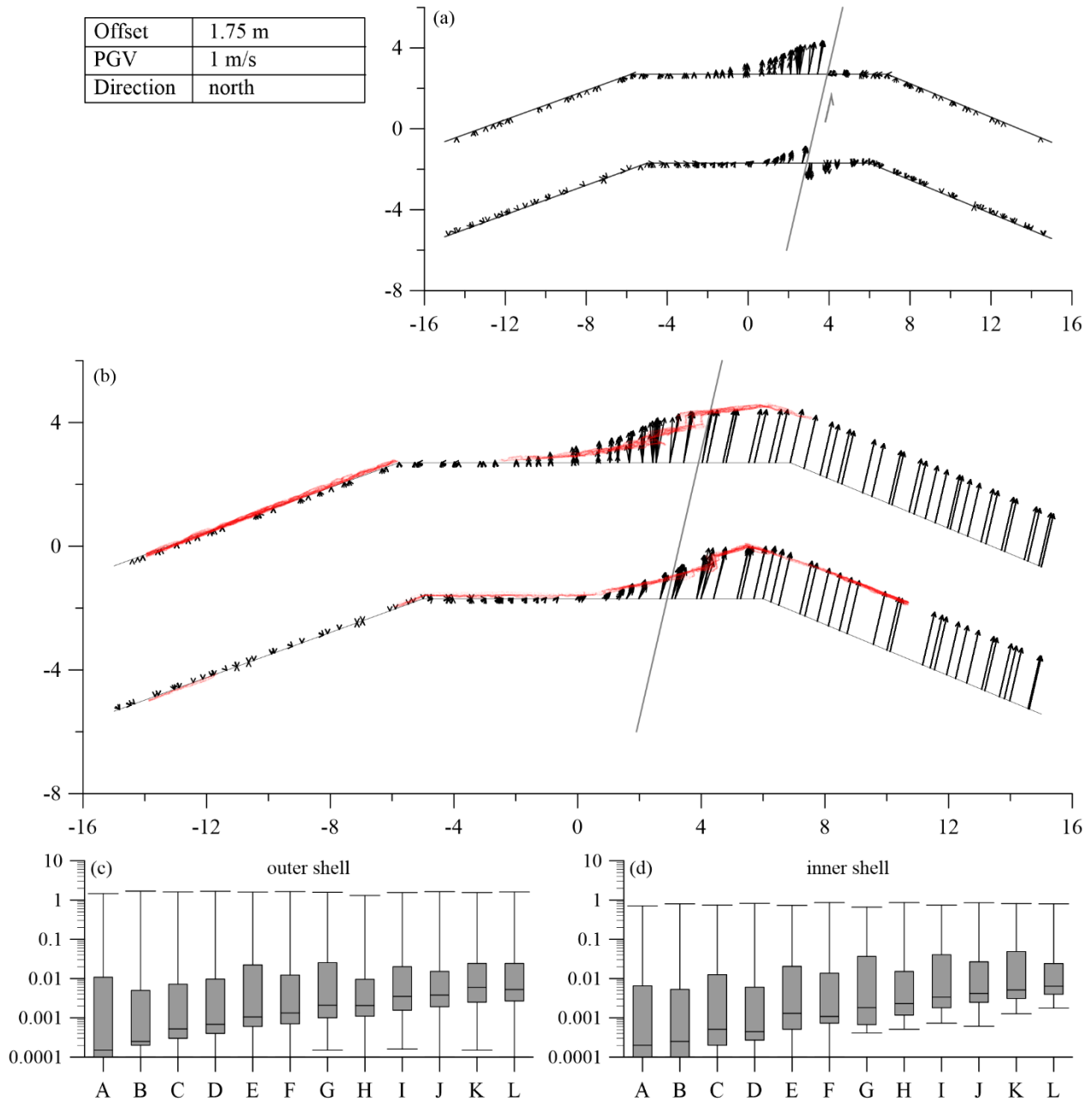


Figure A.4: Results of the simulation with a cycloidal pulse for a displacement of 1.75 m and a PGV of 1 m/s. (a) Displacement vectors of the blocks relative to the displacement of the baseplate beneath the blocks from a top view perspective. The light grey line marks the course of the fault line in the model. The light grey arrows point in direction of the ground motion. The dark grey lines mark the course of the initial wall line. (b) Vector plot of the absolute displacement (m) of all blocks from a top view perspective. The grey line marks the course of the fault line in the model and strikes in north-south direction. The superposed red points are the measured points from the 3D laser scanning survey. (c) Boxplot of the vector length relative to the displacement of the baseplate for all blocks in individual rows with row A: bottom and row L: top of the outer shell. (d) the same as (c) for the inner shell.

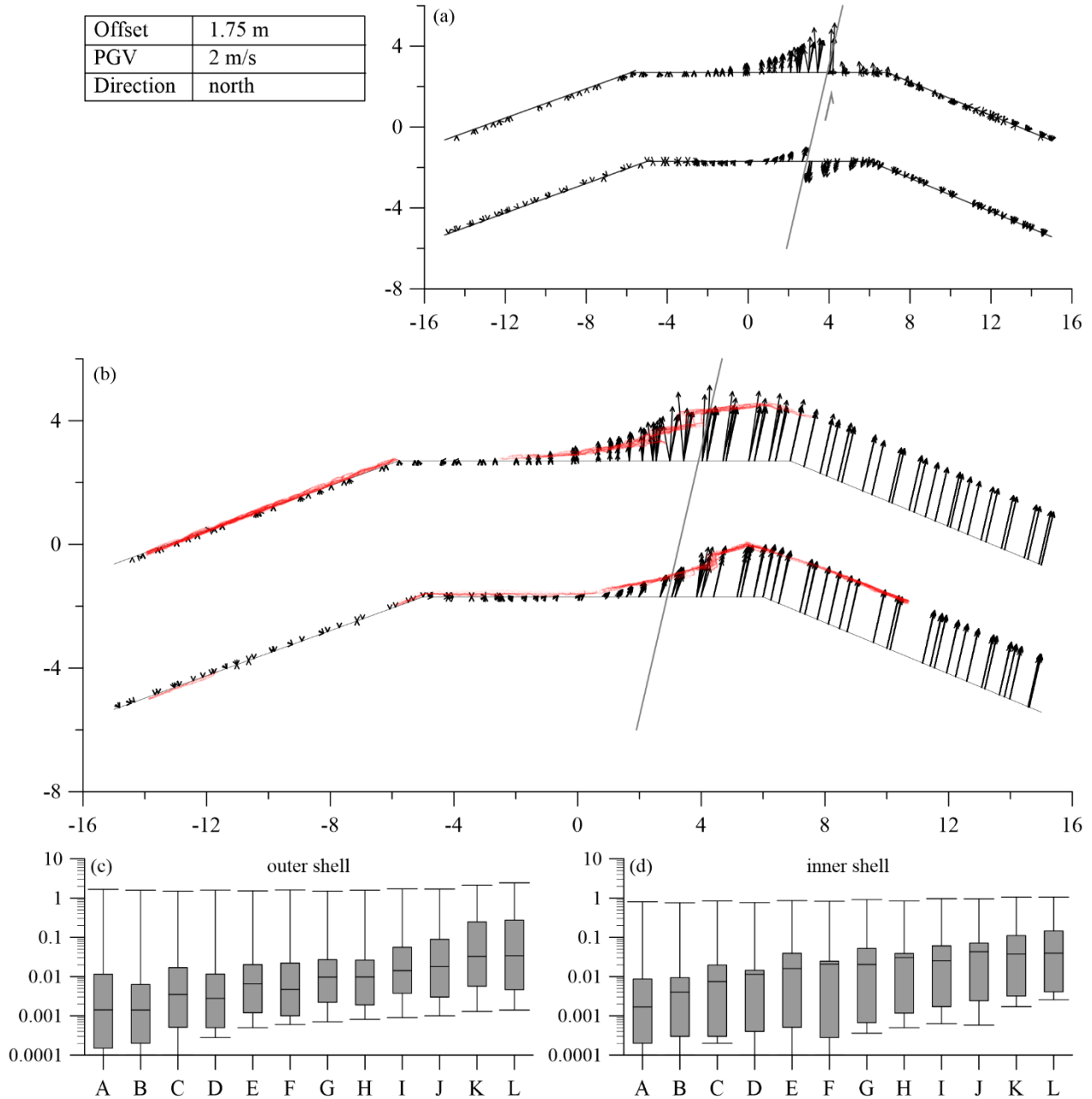


Figure A.5: Results of the simulation with a cycloidal pulse for a displacement of 1.75 m and a PGV of 2 m/s. (a) Displacement vectors of the blocks relative to the displacement of the baseplate beneath the blocks from a top view perspective. The light grey line marks the course of the fault line in the model. The light grey arrows point in direction of the ground motion. The dark grey lines mark the course of the initial wall line. (b) Vector plot of the absolute displacement (m) of all blocks from a top view perspective. The grey line marks the course of the fault line in the model and strikes in north-south direction. The superposed red points are the measured points from the 3D laser scanning survey. (c) Boxplot of the vector length relative to the displacement of the baseplate for all blocks in individual rows with row A: bottom and row L: top of the outer shell. (d) the same as (c) for the inner shell.

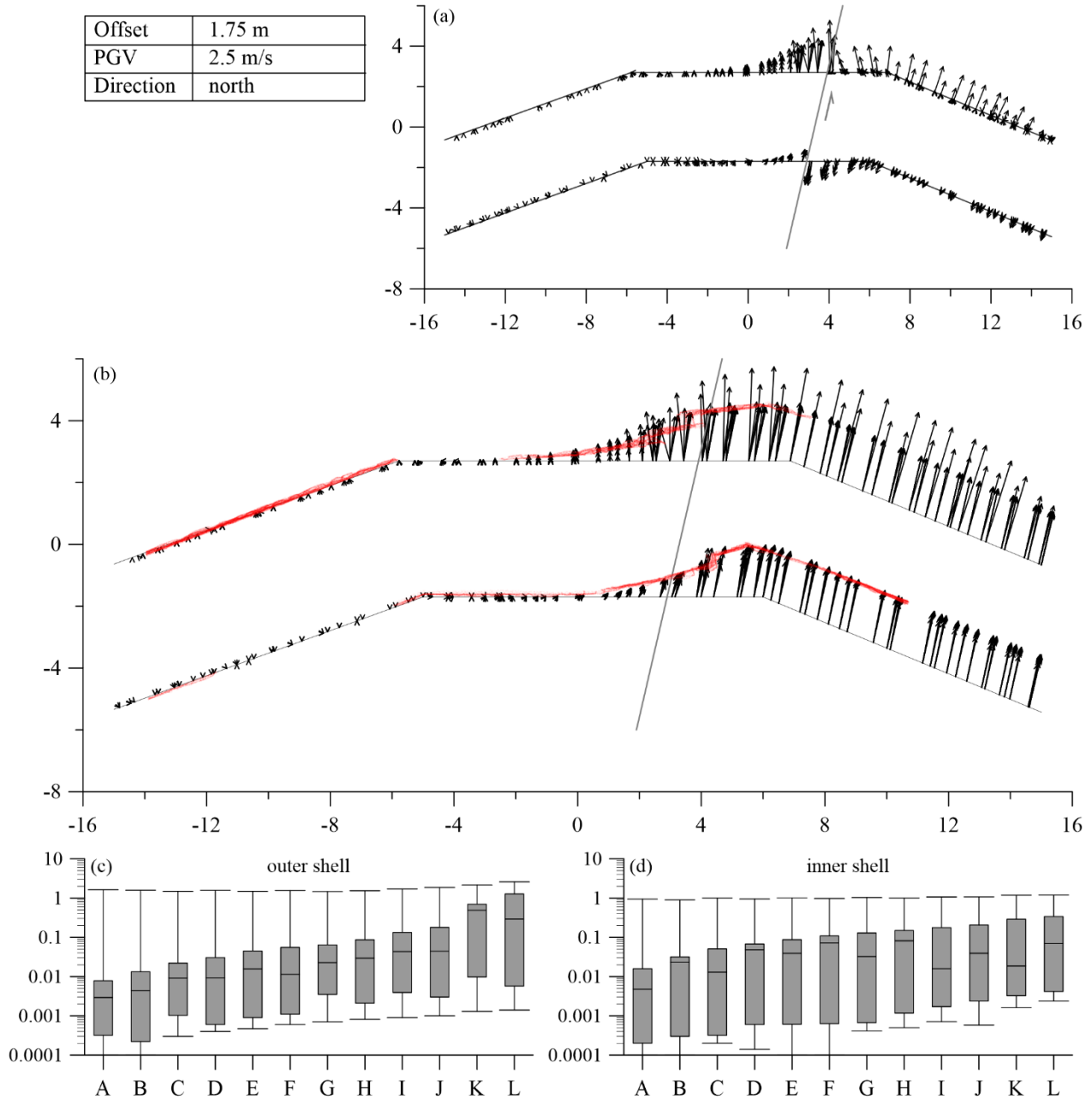


Figure A.6: Results of the simulation with a cycloidal pulse for a displacement of 1.75 m and a PGV of 2.5 m/s. (a) Displacement vectors of the blocks relative to the displacement of the baseplate beneath the blocks from a top view perspective. The light grey line marks the course of the fault line in the model. The light grey arrows point in direction of the ground motion. The dark grey lines mark the course of the initial wall line. (b) Vector plot of the absolute displacement (m) of all blocks from a top view perspective. The grey line marks the course of the fault line in the model and strikes in north-south direction. The superposed red points are the measured points from the 3D laser scanning survey. (c) Boxplot of the vector length relative to the displacement of the baseplate for all blocks in individual rows with row A: bottom and row L: top of the outer shell. (d) the same as (c) for the inner shell.

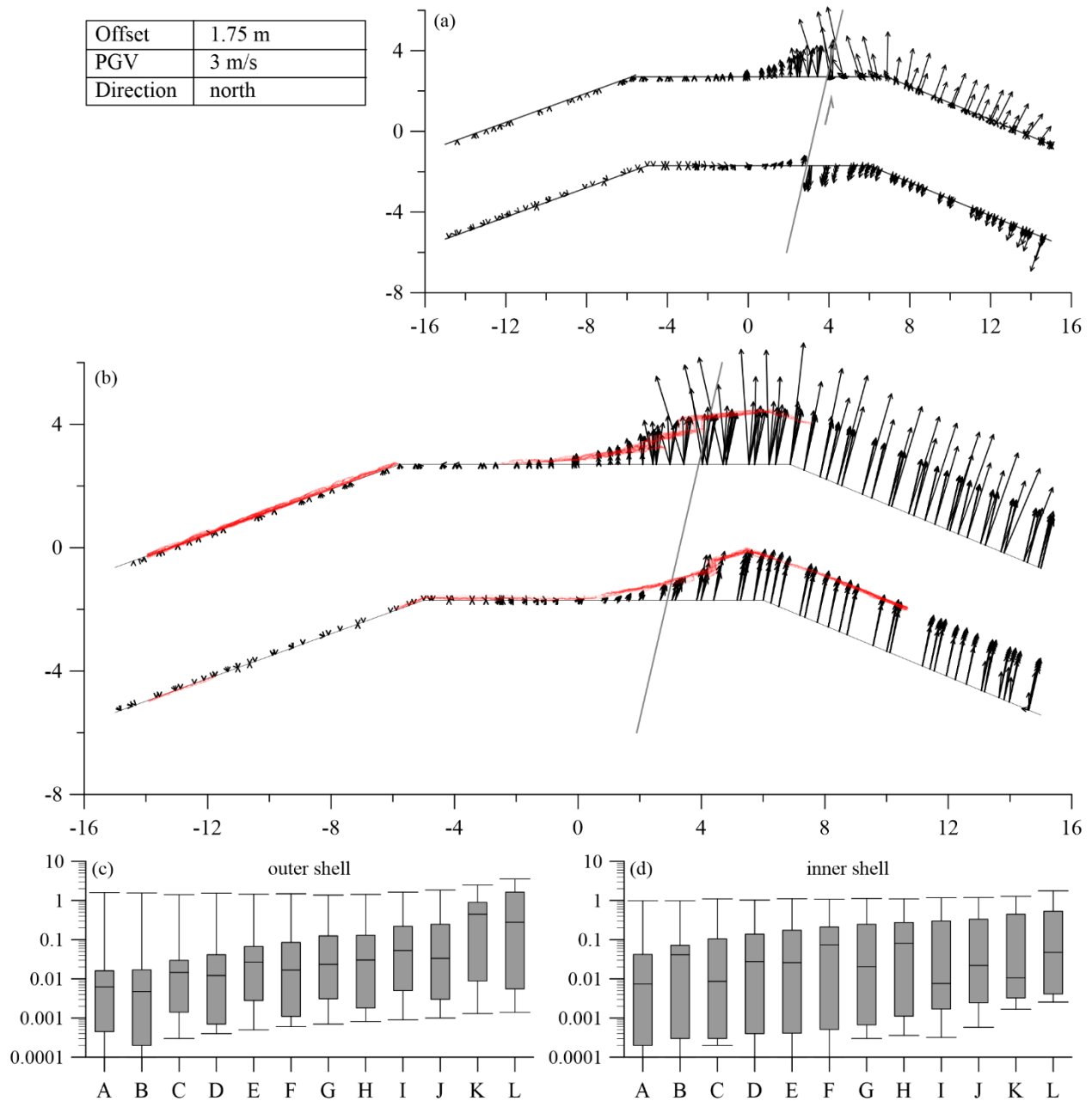


Figure A.7: Results of the simulation with a cycloidal pulse for a displacement of 1.75 m and a PGV of 3 m/s. (a) Displacement vectors of the blocks relative to the displacement of the baseplate beneath the blocks from a top view perspective. The light grey line marks the course of the fault line in the model. The light grey arrows point in direction of the ground motion. The dark grey lines mark the course of the initial wall line. (b) Vector plot of the absolute displacement (m) of all blocks from a top view perspective. The grey line marks the course of the fault line in the model and strikes in north-south direction. The superposed red points are the measured points from the 3D laser scanning survey. (c) Boxplot of the vector length relative to the displacement of the baseplate for all blocks in individual rows with row A: bottom and row L: top of the outer shell. (d) the same as (c) for the inner shell.

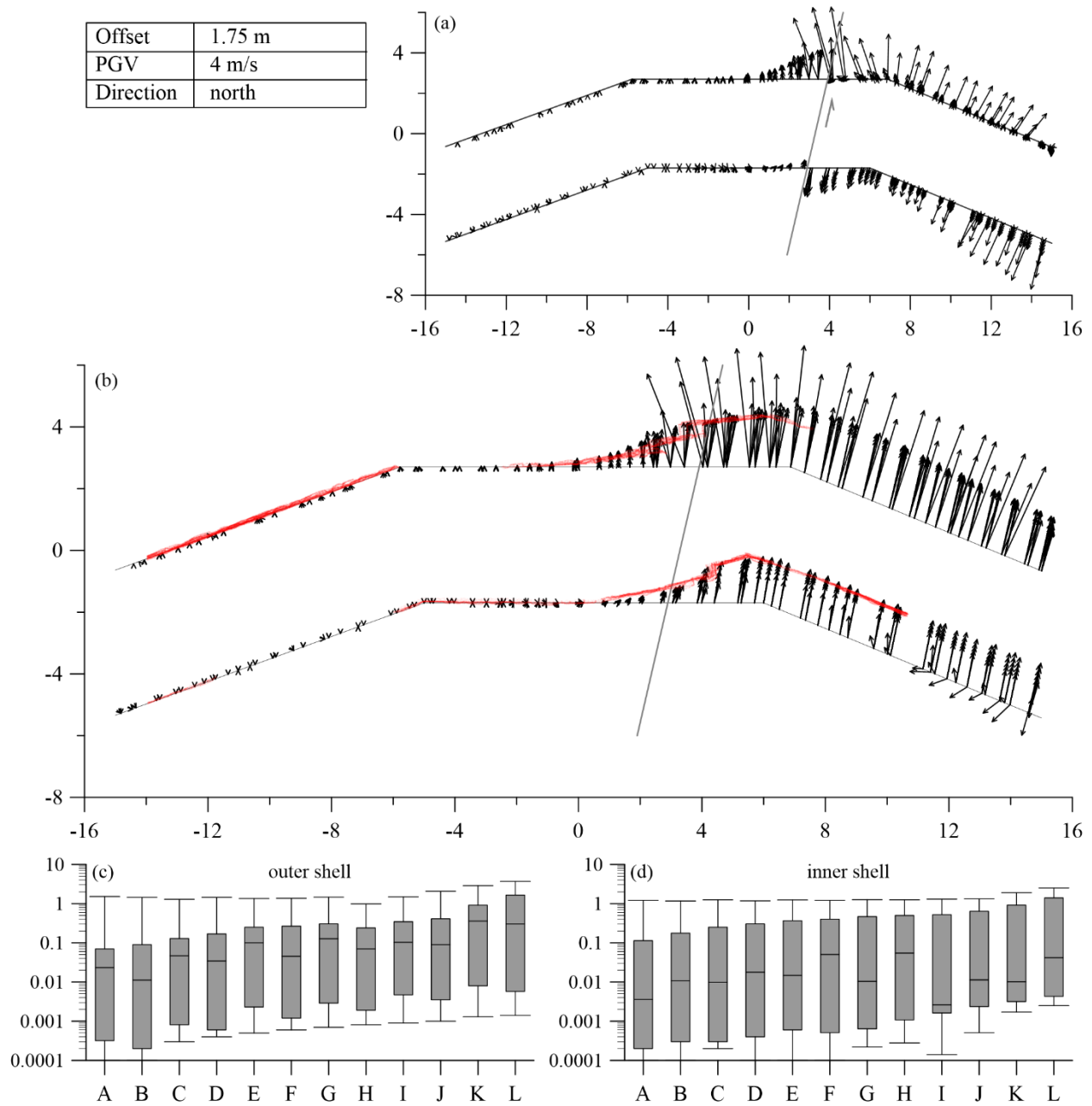


Figure A.8: Results of the simulation with a cycloidal pulse for a displacement of 1.75 m and a PGV of 4 m/s. (a) Displacement vectors of the blocks relative to the displacement of the baseplate beneath the blocks from a top view perspective. The light grey line marks the course of the fault line in the model. The light grey arrows point in direction of the ground motion. The dark grey lines mark the course of the initial wall line. (b) Vector plot of the absolute displacement (m) of all blocks from a top view perspective. The grey line marks the course of the fault line in the model and strikes in north-south direction. The superposed red points are the measured points from the 3D laser scanning survey. (c) Boxplot of the vector length relative to the displacement of the baseplate for all blocks in individual rows with row A: bottom and row L: top of the outer shell. (d) the same as (c) for the inner shell.

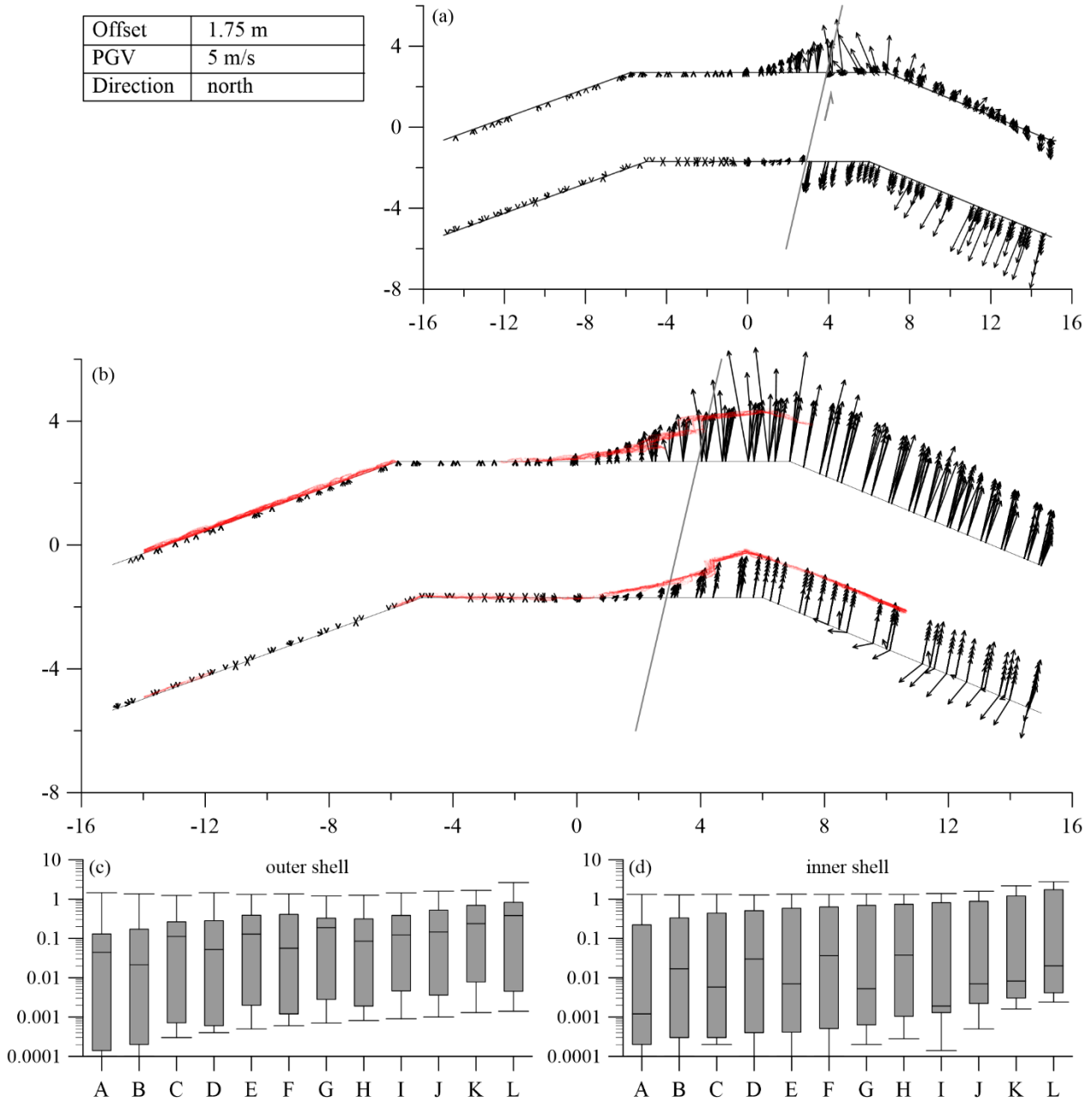


Figure A.9: Results of the simulation with a cycloidal pulse for a displacement of 1.75 m and a PGV of 5 m/s. (a) Displacement vectors of the blocks relative to the displacement of the baseplate beneath the blocks from a top view perspective. The light grey line marks the course of the fault line in the model. The light grey arrows point in direction of the ground motion. The dark grey lines mark the course of the initial wall line. (b) Vector plot of the absolute displacement (m) of all blocks from a top view perspective. The grey line marks the course of the fault line in the model and strikes in north-south direction. The superposed red points are the measured points from the 3D laser scanning survey. (c) Boxplot of the vector length relative to the displacement of the baseplate for all blocks in individual rows with row A: bottom and row L: top of the outer shell. (d) the same as (c) for the inner shell.

## Appendix Crusader Fortress Ateret

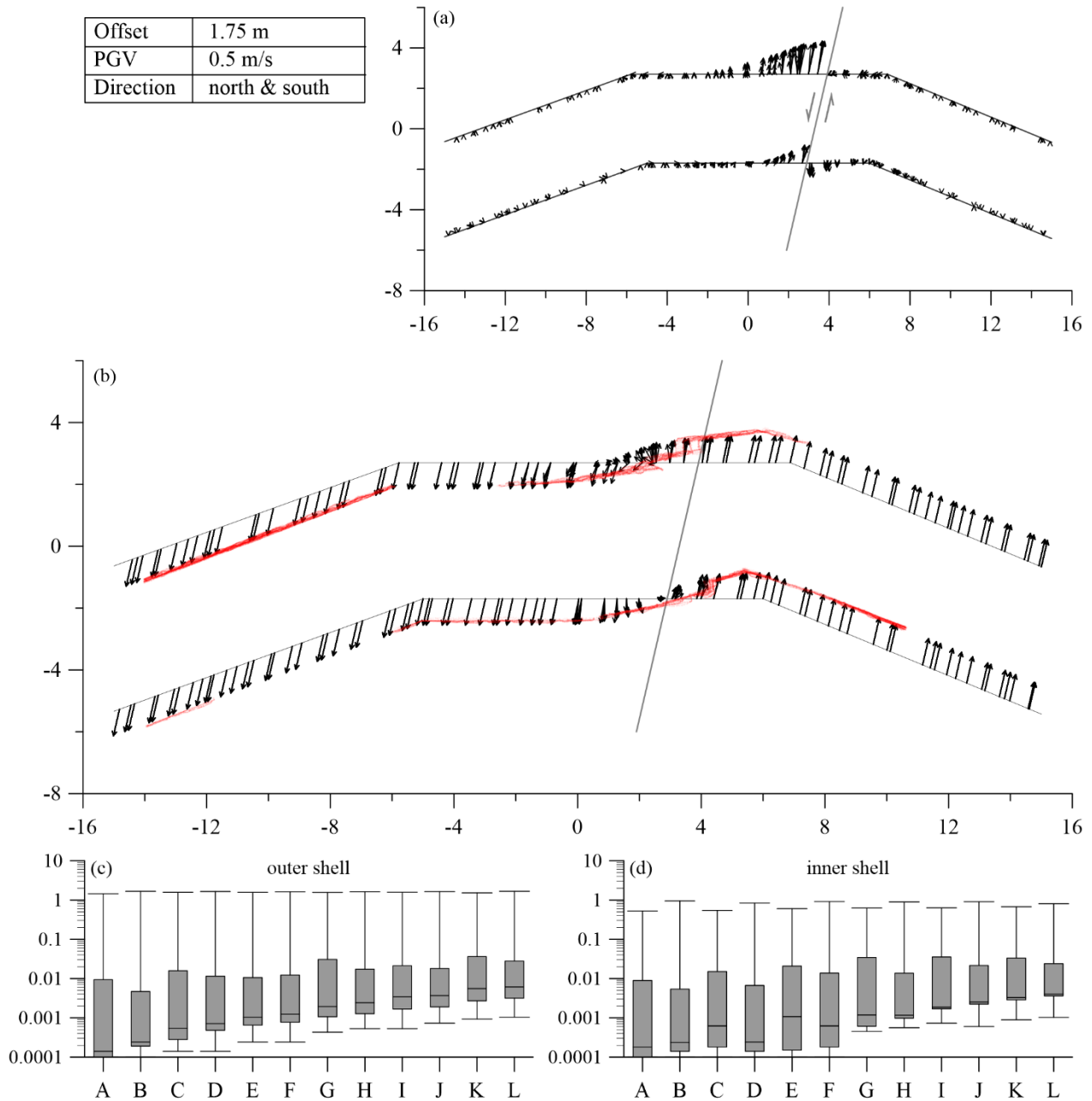


Figure A.10: Results of the simulation with a cycloidal pulse for a displacement of 1.75 m and a PGV of 0.5 m/s. (a) Displacement vectors of the blocks relative to the displacement of the baseplate beneath the blocks from a top view perspective. The light grey line marks the course of the fault line in the model. The light grey arrows point in direction of the ground motion. The dark grey lines mark the course of the initial wall line. (b) Vector plot of the absolute displacement (m) of all blocks from a top view perspective. The grey line marks the course of the fault line in the model and strikes in north-south direction. The superposed red points are the measured points from the 3D laser scanning survey. (c) Boxplot of the vector length relative to the displacement of the baseplate for all blocks in individual rows with row A: bottom and row L: top of the outer shell. (d) the same as (c) for the inner shell.

## Appendix Crusader Fortress Ateret

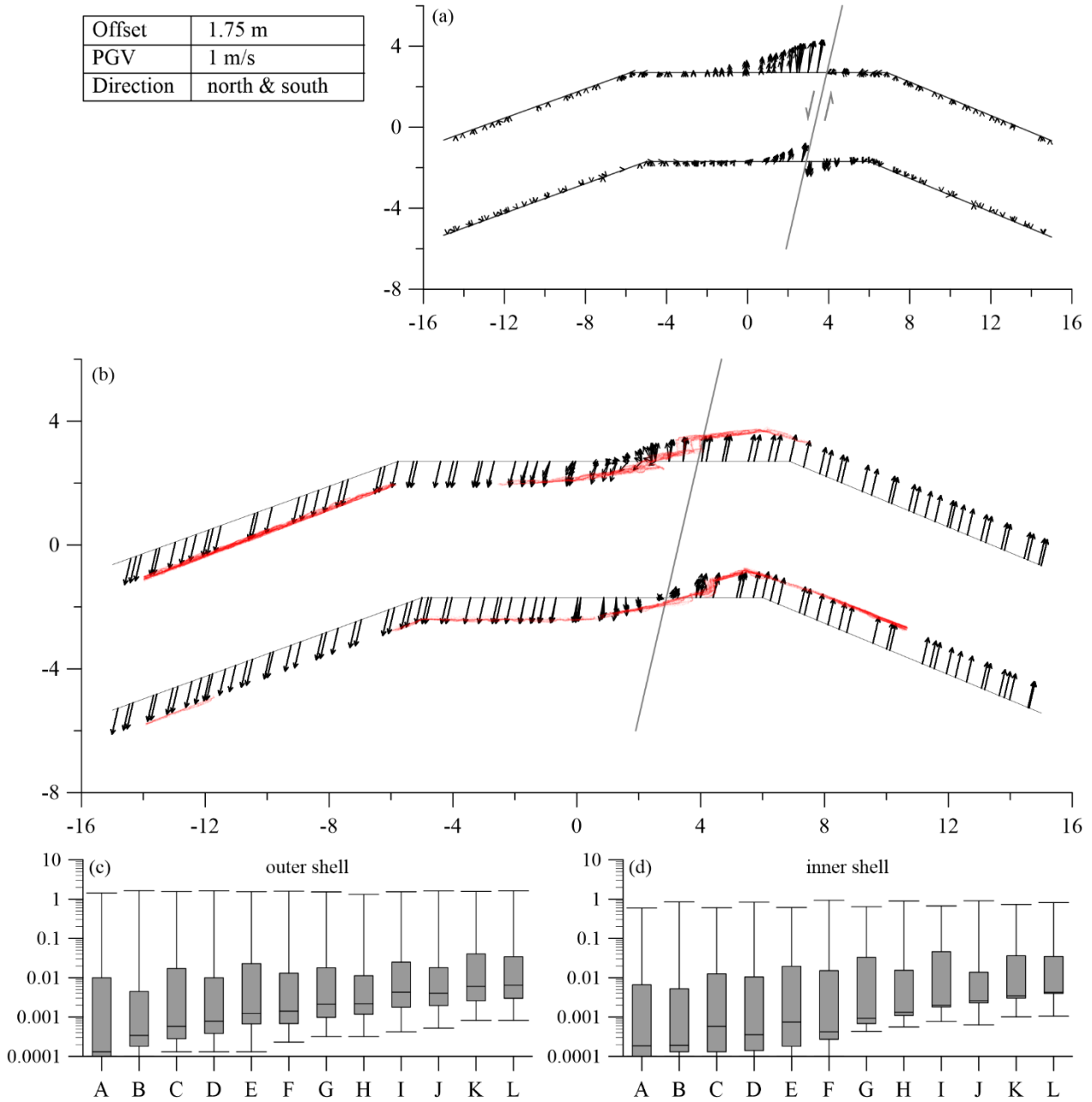


Figure A.11: Results of the simulation with a cycloidal pulse for a displacement of 1.75 m and a PGV of 1 m/s. (a) Displacement vectors of the blocks relative to the displacement of the baseplate beneath the blocks from a top view perspective. The light grey line marks the course of the fault line in the model. The light grey arrows point in direction of the ground motion. The dark grey lines mark the course of the initial wall line. (b) Vector plot of the absolute displacement (m) of all blocks from a top view perspective. The grey line marks the course of the fault line in the model and strikes in north-south direction. The superposed red points are the measured points from the 3D laser scanning survey. (c) Boxplot of the vector length relative to the displacement of the baseplate for all blocks in individual rows with row A: bottom and row L: top of the outer shell. (d) the same as (c) for the inner shell.

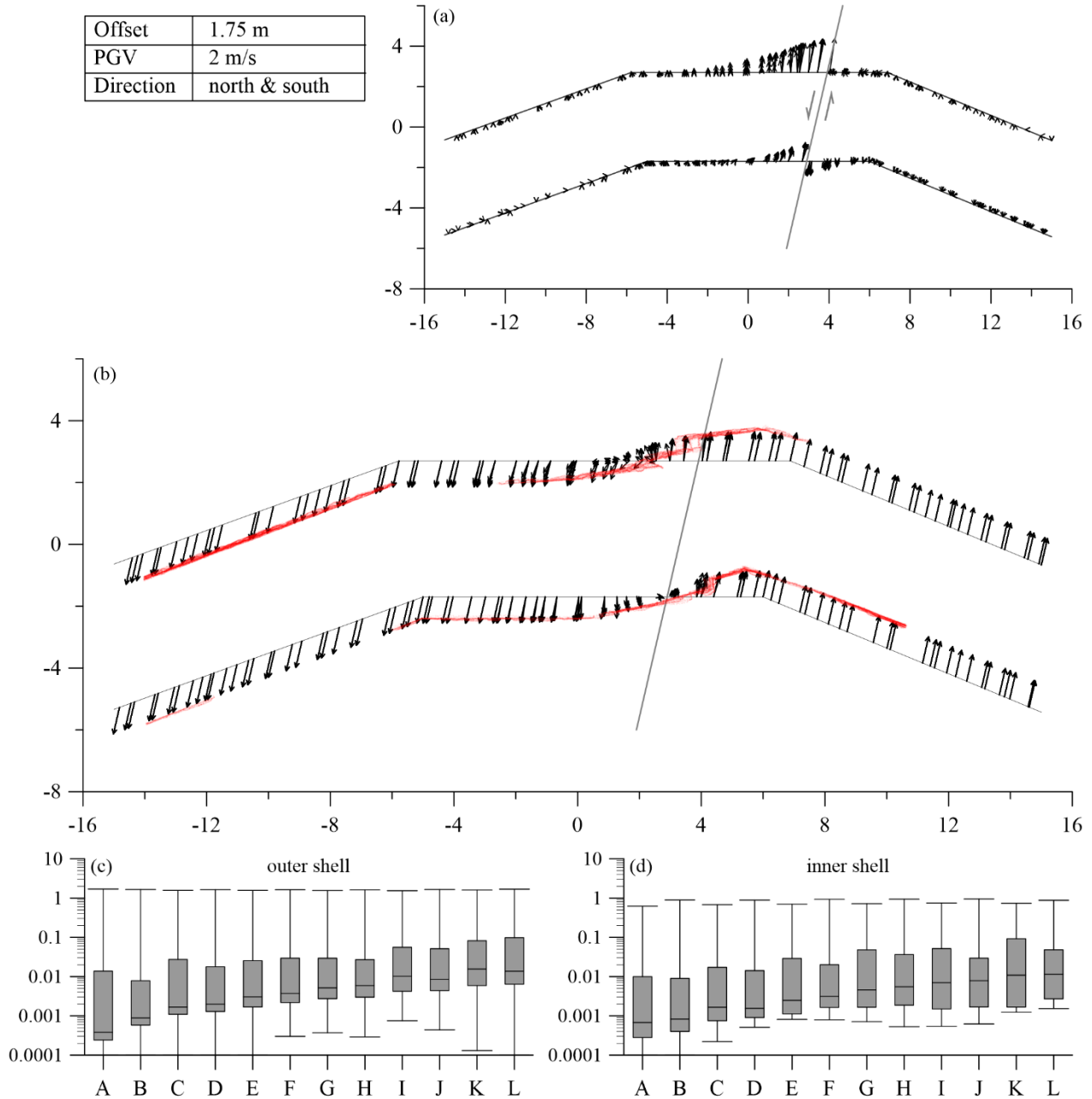


Figure A.12: Results of the simulation with a cycloidal pulse for a displacement of 1.75 m and a PGV of 2 m/s. (a) Displacement vectors of the blocks relative to the displacement of the baseplate beneath the blocks from a top view perspective. The light grey line marks the course of the fault line in the model. The light grey arrows point in direction of the ground motion. The dark grey lines mark the course of the initial wall line. (b) Vector plot of the absolute displacement (m) of all blocks from a top view perspective. The grey line marks the course of the fault line in the model and strikes in north-south direction. The superposed red points are the measured points from the 3D laser scanning survey. (c) Boxplot of the vector length relative to the displacement of the baseplate for all blocks in individual rows with row A: bottom and row L: top of the outer shell. (d) the same as (c) for the inner shell.

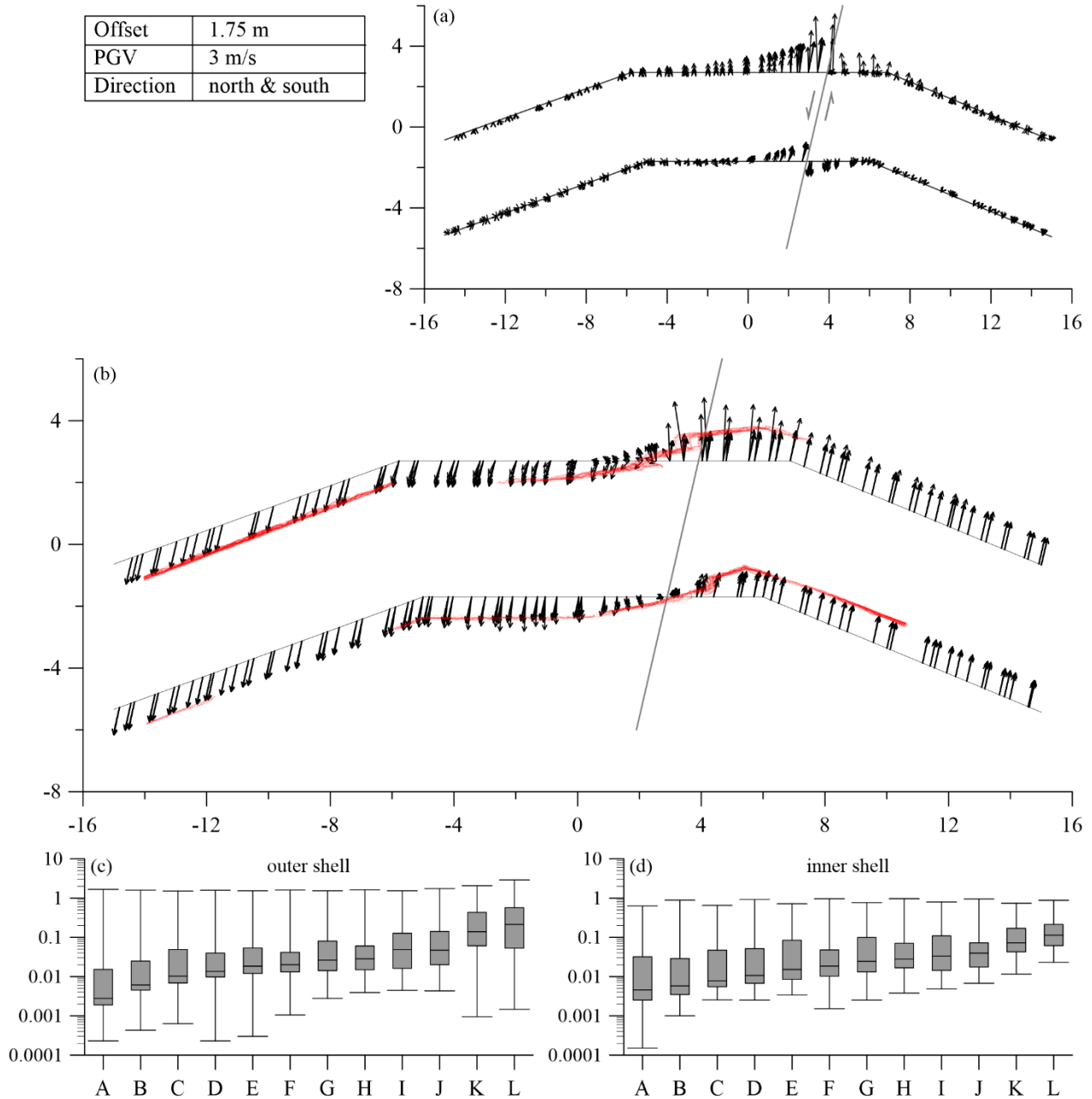


Figure A.13: Results of the simulation with a cycloidal pulse for a displacement of 1.75 m and a PGV of 3 m/s. (a) Displacement vectors of the blocks relative to the displacement of the baseplate beneath the blocks from a top view perspective. The light grey line marks the course of the fault line in the model. The light grey arrows point in direction of the ground motion. The dark grey lines mark the course of the initial wall line. (b) Vector plot of the absolute displacement (m) of all blocks from a top view perspective. The grey line marks the course of the fault line in the model and strikes in north-south direction. The superposed red points are the measured points from the 3D laser scanning survey. (c) Boxplot of the vector length relative to the displacement of the baseplate for all blocks in individual rows with row A: bottom and row L: top of the outer shell. (d) the same as (c) for the inner shell.

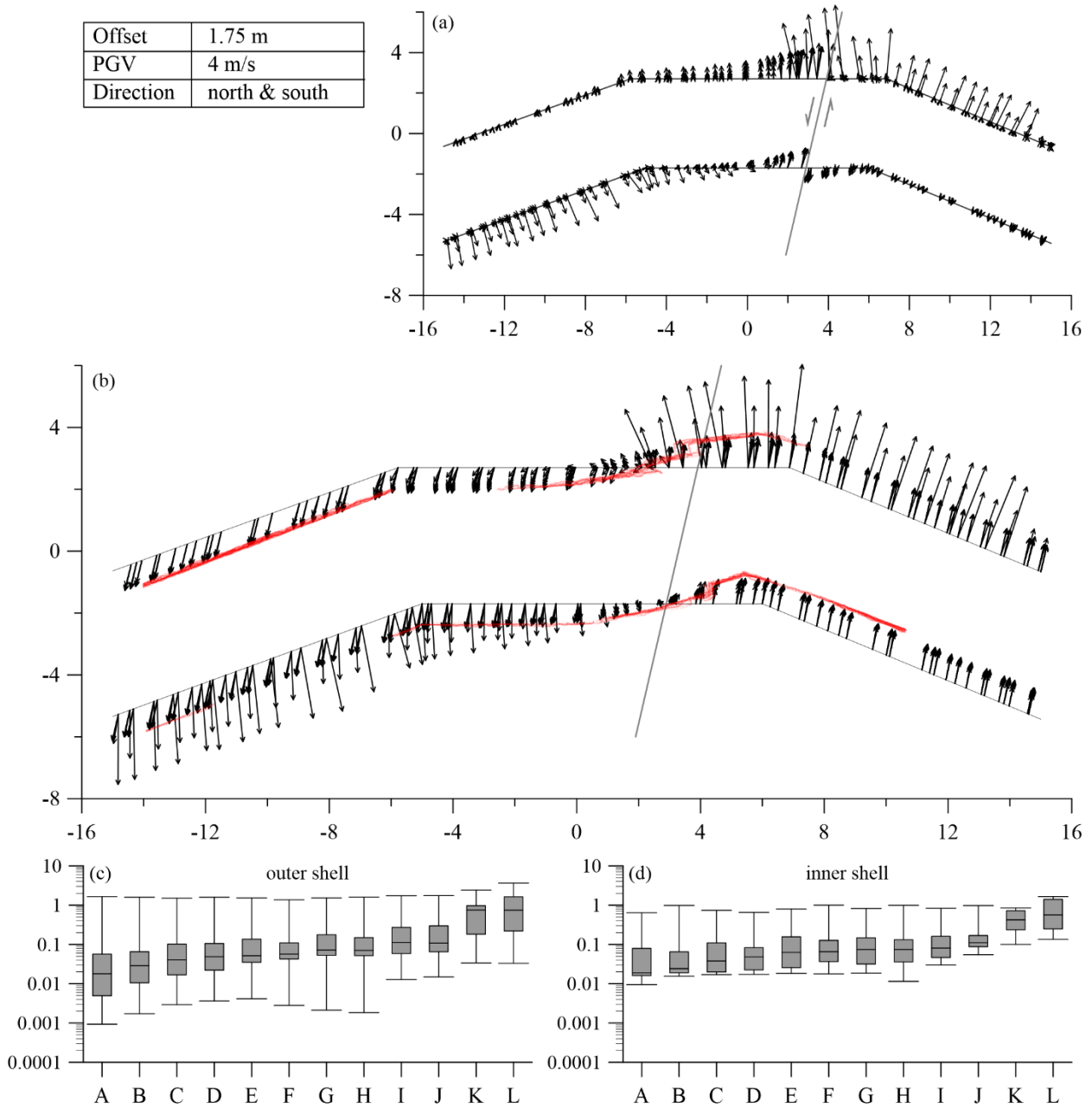


Figure A.14: Results of the simulation with a cycloidal pulse for a displacement of 1.75 m and a PGV of 4 m/s. (a) Displacement vectors of the blocks relative to the displacement of the baseplate beneath the blocks from a top view perspective. The light grey line marks the course of the fault line in the model. The light grey arrows point in direction of the ground motion. The dark grey lines mark the course of the initial wall line. (b) Vector plot of the absolute displacement (m) of all blocks from a top view perspective. The grey line marks the course of the fault line in the model and strikes in north-south direction. The superposed red points are the measured points from the 3D laser scanning survey. (c) Boxplot of the vector length relative to the displacement of the baseplate for all blocks in individual rows with row A: bottom and row L: top of the outer shell. (d) the same as (c) for the inner shell.

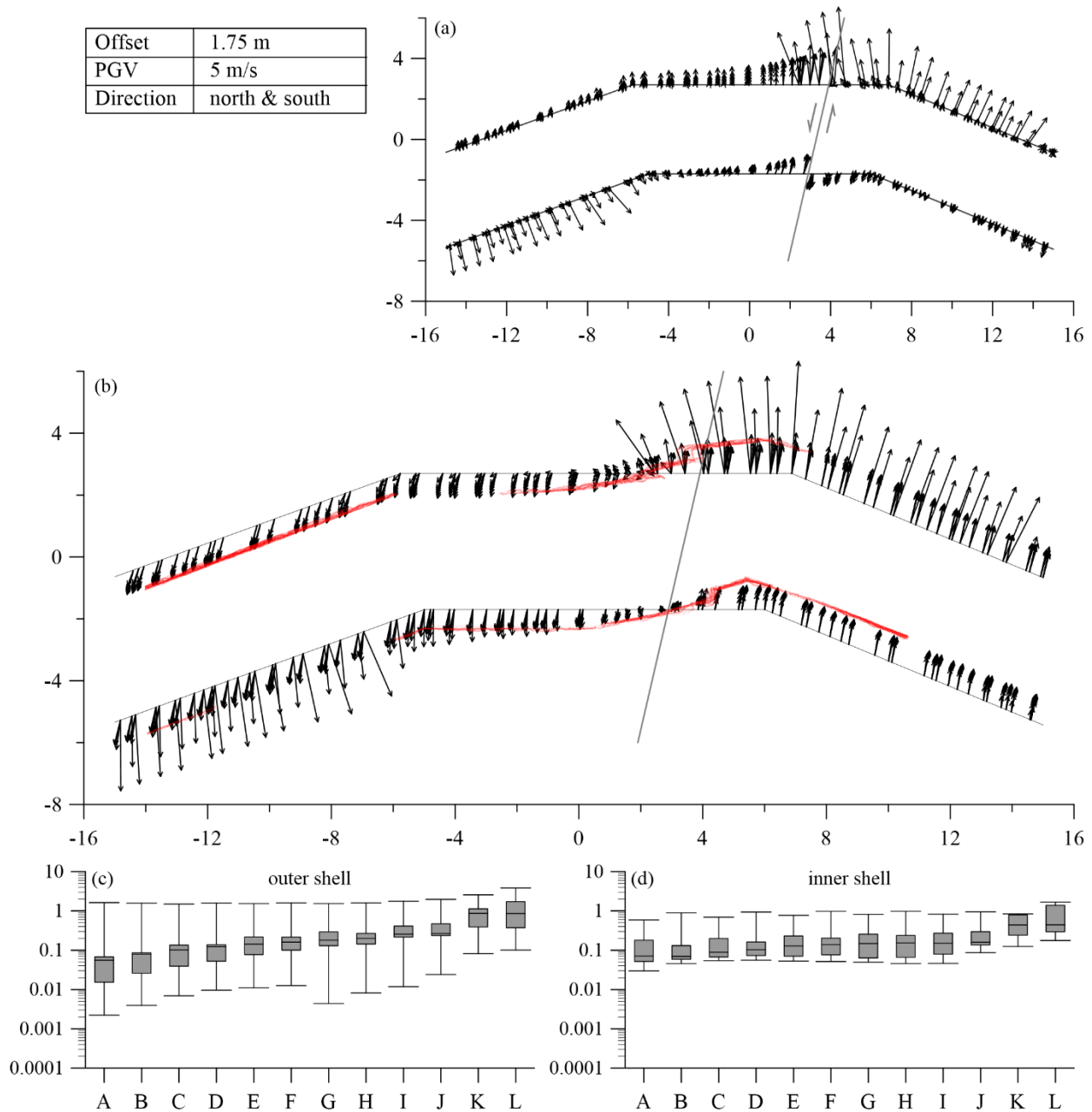


Figure A.15: Results of the simulation with a cycloidal pulse for a displacement of 1.75 m and a PGV of 5 m/s. (a) Displacement vectors of the blocks relative to the displacement of the baseplate beneath the blocks from a top view perspective. The light grey line marks the course of the fault line in the model. The light grey arrows point in direction of the ground motion. The dark grey lines mark the course of the initial wall line. (b) Vector plot of the absolute displacement (m) of all blocks from a top view perspective. The grey line marks the course of the fault line in the model and strikes in north-south direction. The superposed red points are the measured points from the 3D laser scanning survey. (c) Boxplot of the vector length relative to the displacement of the baseplate for all blocks in individual rows with row A: bottom and row L: top of the outer shell. (d) the same as (c) for the inner shell.

## Appendix Crusader Fortress Ateret

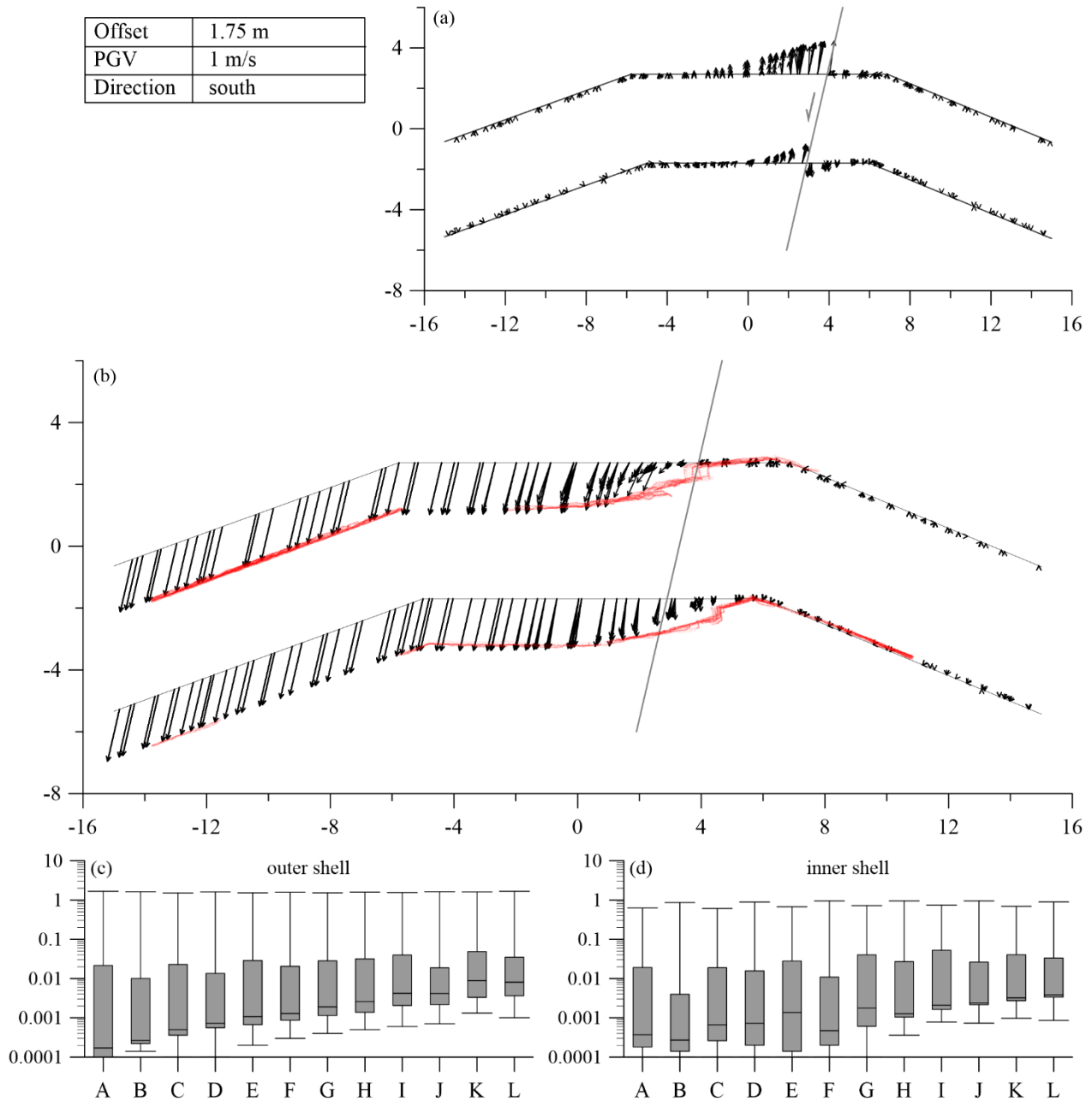


Figure A.16: Results of the simulation with a cycloidal pulse for a displacement of 1.75 m and a PGV of 1 m/s. (a) Displacement vectors of the blocks relative to the displacement of the baseplate beneath the blocks from a top view perspective. The light grey line marks the course of the fault line in the model. The light grey arrows point in direction of the ground motion. The dark grey lines mark the course of the initial wall line. (b) Vector plot of the absolute displacement (m) of all blocks from a top view perspective. The grey line marks the course of the fault line in the model and strikes in north-south direction. The superposed red points are the measured points from the 3D laser scanning survey. (c) Boxplot of the vector length relative to the displacement of the baseplate for all blocks in individual rows with row A: bottom and row L: top of the outer shell. (d) the same as (c) for the inner shell.

## Appendix Crusader Fortress Ateret

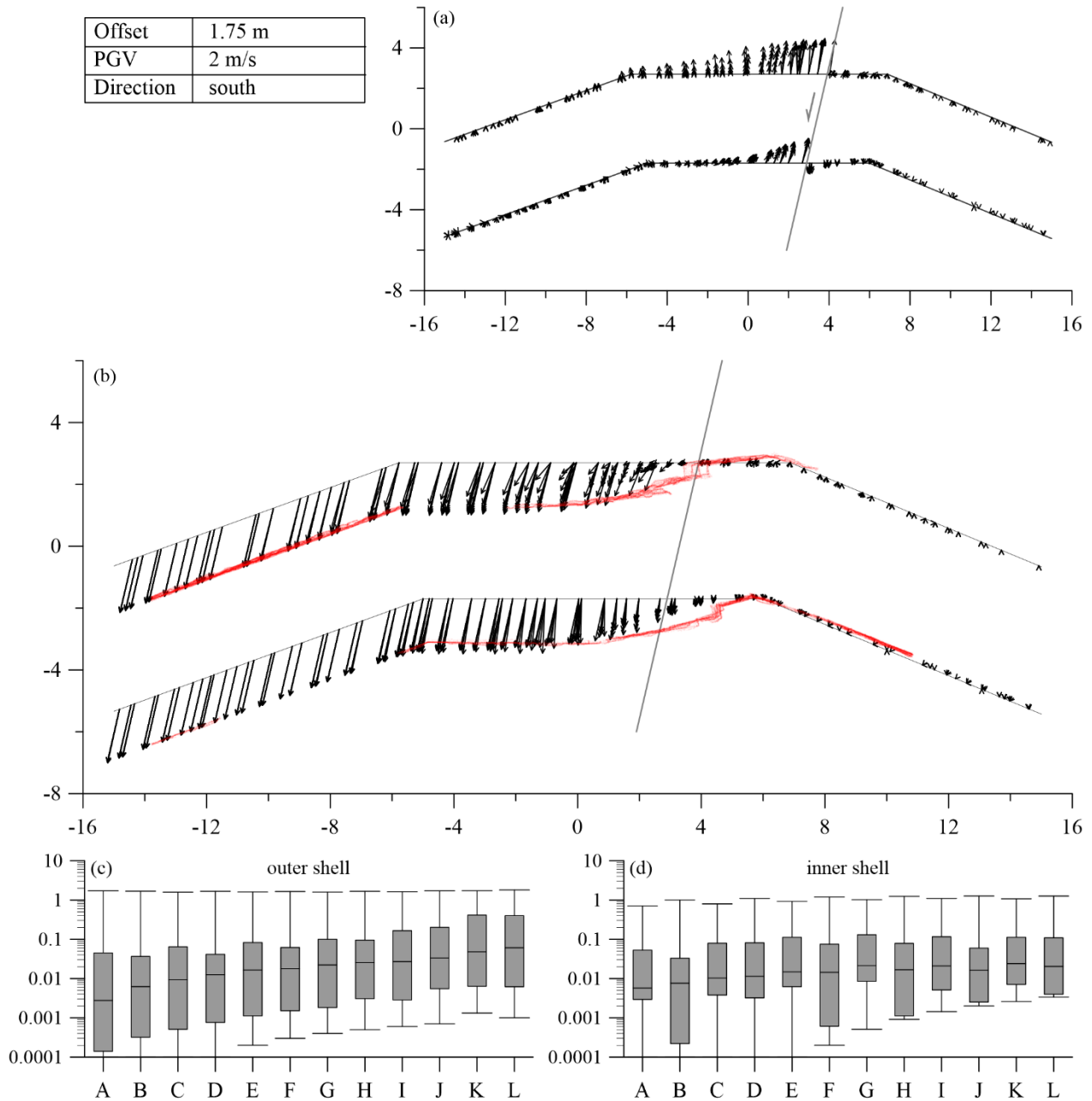


Figure A.17: Results of the simulation with a cycloidal pulse for a displacement of 1.75 m and a PGV of 2 m/s. (a) Displacement vectors of the blocks relative to the displacement of the baseplate beneath the blocks from a top view perspective. The light grey line marks the course of the fault line in the model. The light grey arrows point in direction of the ground motion. The dark grey lines mark the course of the initial wall line. (b) Vector plot of the absolute displacement (m) of all blocks from a top view perspective. The grey line marks the course of the fault line in the model and strikes in north-south direction. The superposed red points are the measured points from the 3D laser scanning survey. (c) Boxplot of the vector length relative to the displacement of the baseplate for all blocks in individual rows with row A: bottom and row L: top of the outer shell. (d) the same as (c) for the inner shell.

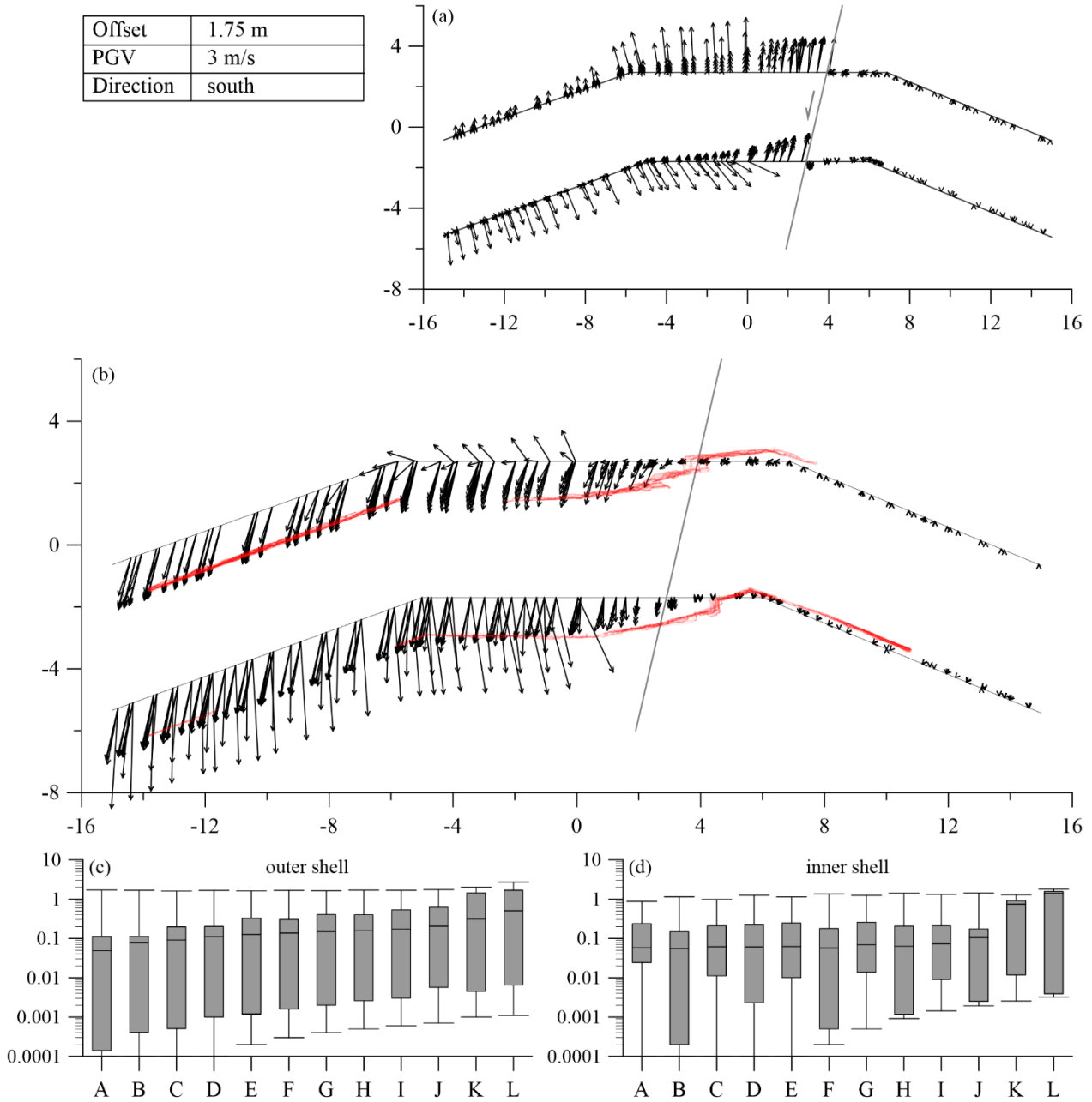


Figure A.18: Results of the simulation with a cycloidal pulse for a displacement of 1.75 m and a PGV of 3 m/s. (a) Displacement vectors of the blocks relative to the displacement of the baseplate beneath the blocks from a top view perspective. The light grey line marks the course of the fault line in the model. The light grey arrows point in direction of the ground motion. The dark grey lines mark the course of the initial wall line. (b) Vector plot of the absolute displacement (m) of all blocks from a top view perspective. The grey line marks the course of the fault line in the model and strikes in north-south direction. The superposed red points are the measured points from the 3D laser scanning survey. (c) Boxplot of the vector length relative to the displacement of the baseplate for all blocks in individual rows with row A: bottom and row L: top of the outer shell. (d) the same as (c) for the inner shell.

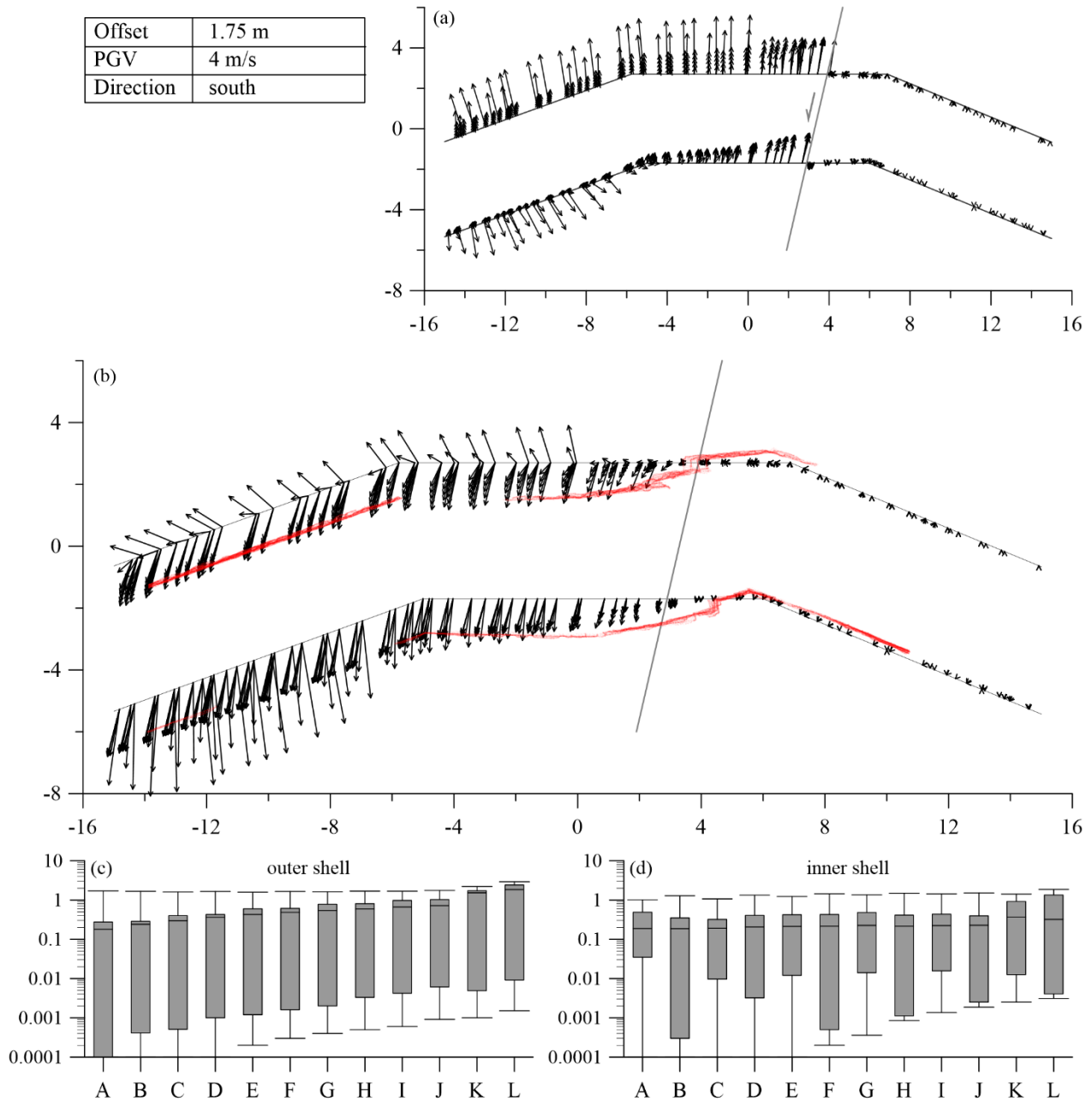


Figure A.19: Results of the simulation with a cycloidal pulse for a displacement of 1.75 m and a PGV of 4 m/s. (a) Displacement vectors of the blocks relative to the displacement of the baseplate beneath the blocks from a top view perspective. The light grey line marks the course of the fault line in the model. The light grey arrows point in direction of the ground motion. The dark grey lines mark the course of the initial wall line. (b) Vector plot of the absolute displacement (m) of all blocks from a top view perspective. The grey line marks the course of the fault line in the model and strikes in north-south direction. The superposed red points are the measured points from the 3D laser scanning survey. (c) Boxplot of the vector length relative to the displacement of the baseplate for all blocks in individual rows with row A: bottom and row L: top of the outer shell. (d) the same as (c) for the inner shell.

## Appendix Crusader Fortress Ateret

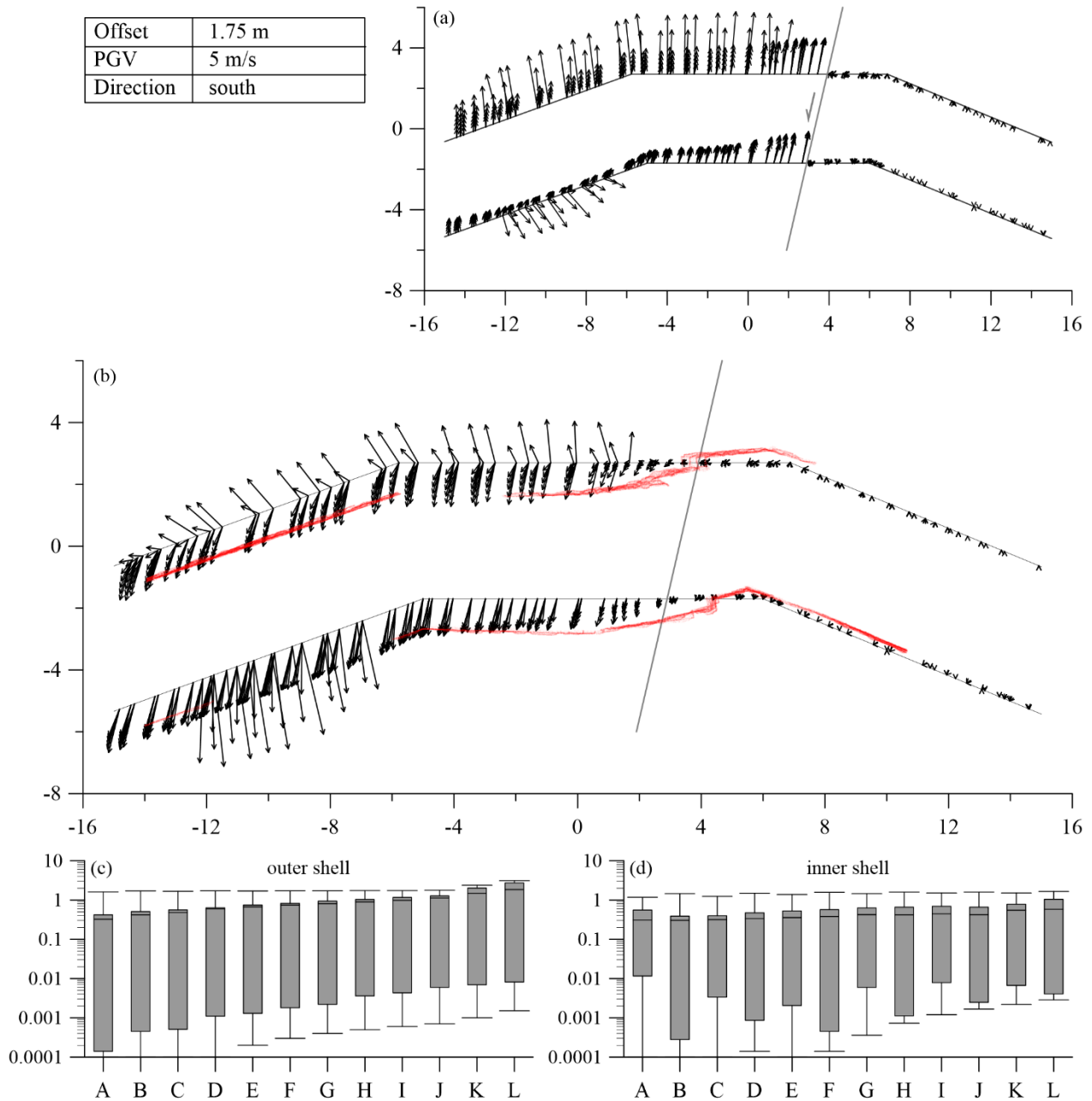


Figure A.20: Results of the simulation with a cycloidal pulse for a displacement of 1.75 m and a PGV of 5 m/s. (a) Displacement vectors of the blocks relative to the displacement of the baseplate beneath the blocks from a top view perspective. The light grey line marks the course of the fault line in the model. The light grey arrows point in direction of the ground motion. The dark grey lines mark the course of the initial wall line. (b) Vector plot of the absolute displacement (m) of all blocks from a top view perspective. The grey line marks the course of the fault line in the model and strikes in north-south direction. The superposed red points are the measured points from the 3D laser scanning survey. (c) Boxplot of the vector length relative to the displacement of the baseplate for all blocks in individual rows with row A: bottom and row L: top of the outer shell. (d) the same as (c) for the inner shell.

## Appendix Crusader Fortress Ateret

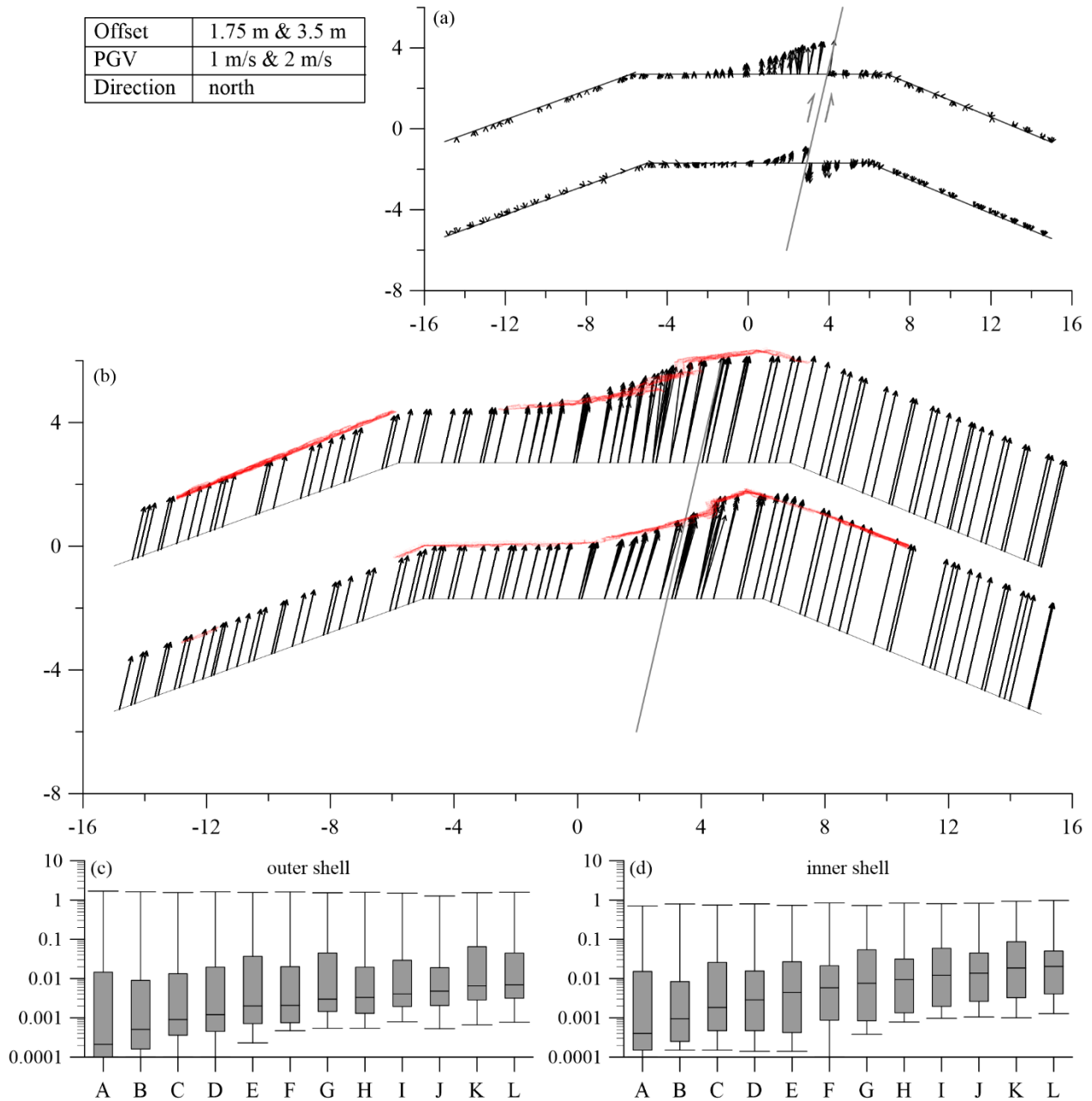


Figure A.21: Results of the simulation with a cycloidal pulse for displacements of 1.75 m and 3.5 m and PGVs of 1 m/s and 2 m/s respectively. (a) Displacement vectors of the blocks relative to the displacement of the baseplate beneath the blocks from a top view perspective. The light grey line marks the course of the fault line in the model. The light grey arrows point in direction of the ground motion. The dark grey lines mark the course of the initial wall line. (b) Vector plot of the absolute displacement (m) of all blocks from a top view perspective. The grey line marks the course of the fault line in the model and strikes in north-south direction. The superposed red points are the measured points from the 3D laser scanning survey. (c) Boxplot of the vector length relative to the displacement of the baseplate for all blocks in individual rows with row A: bottom and row L: top of the outer shell. (d) the same as (c) for the inner shell.

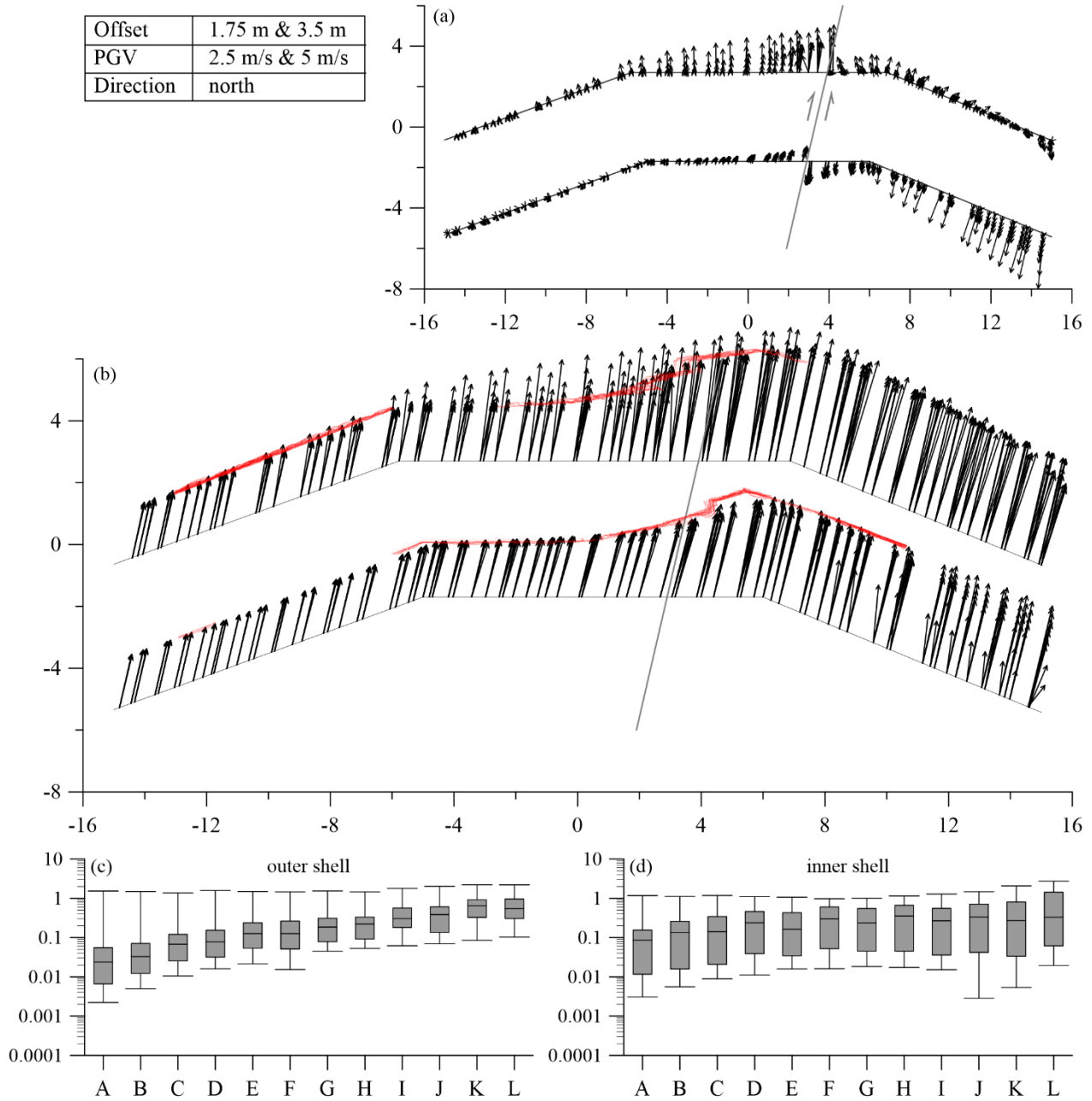


Figure A.22: Results of the simulation with a cycloidal pulse for displacements of 1.75 m and 3.5 m and PGVs of 2.5 m/s and 5 m/s respectively. (a) Displacement vectors of the blocks relative to the displacement of the baseplate beneath the blocks from a top view perspective. The light grey line marks the course of the fault line in the model. The light grey arrows point in direction of the ground motion. The dark grey lines mark the course of the initial wall line. (b) Vector plot of the absolute displacement (m) of all blocks from a top view perspective. The grey line marks the course of the fault line in the model and strikes in north-south direction. The superposed red points are the measured points from the 3D laser scanning survey. (c) Boxplot of the vector length relative to the displacement of the baseplate for all blocks in individual rows with row A: bottom and row L: top of the outer shell. (d) the same as (c) for the inner shell.

*b. Second Scenario*  
**First Stage**

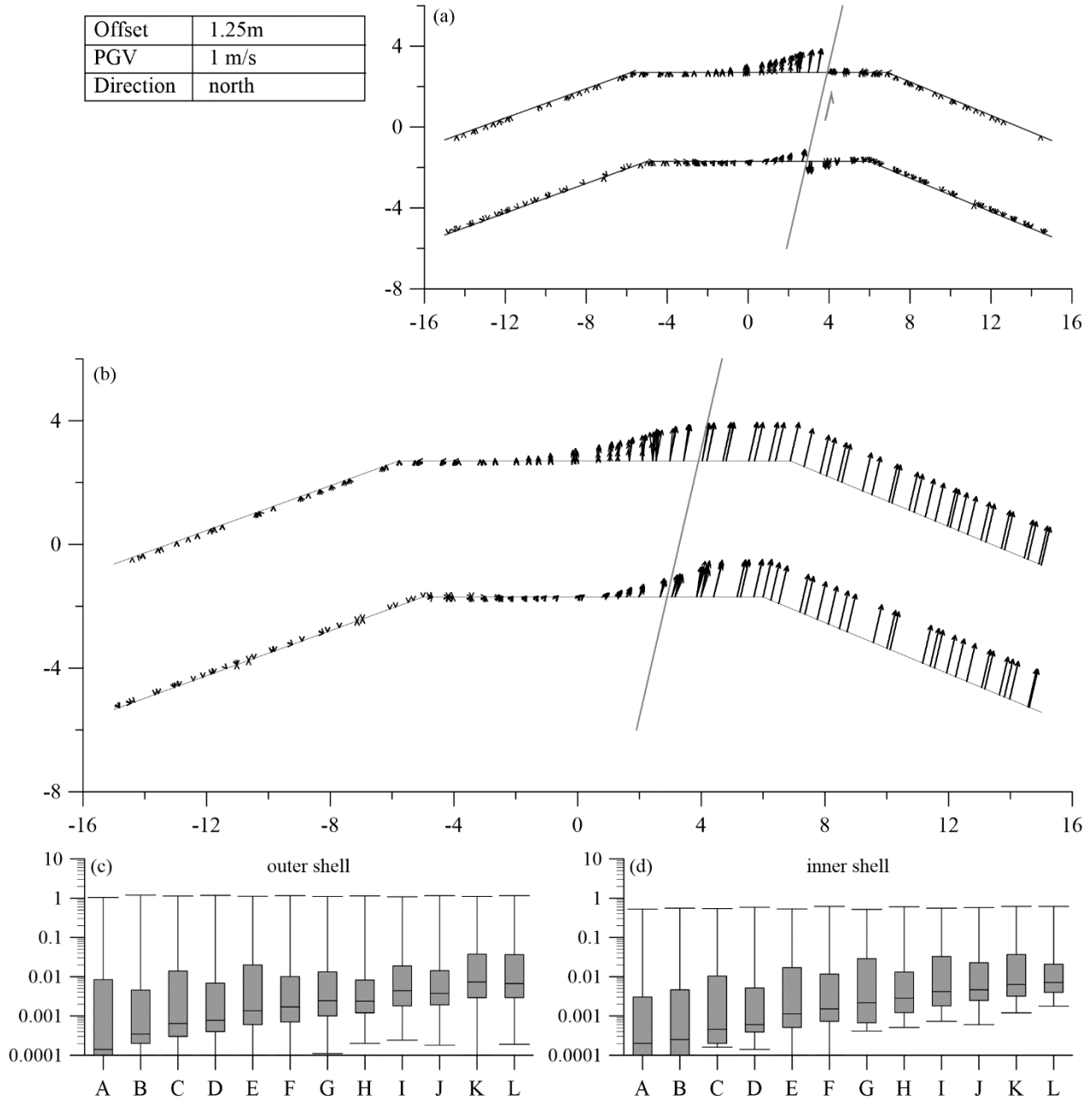


Figure A.23: Results of the simulation with a cycloidal pulse for a displacement of 1.25 m and a PGV of 1 m/s. (a) Displacement vectors of the blocks relative to the displacement of the baseplate beneath the blocks from a top view perspective. The light grey line marks the course of the fault line in the model. The light grey arrows point in direction of the ground motion. The dark grey lines mark the course of the initial wall line. (b) Vector plot of the absolute displacement (m) of all blocks from a top view perspective. The grey line marks the course of the fault line in the model and strikes in north-south direction. (c) Boxplot of the vector length relative to the displacement of the baseplate for all blocks in individual rows with row A: bottom and row L: top of the outer shell. (d) the same as (c) for the inner shell.

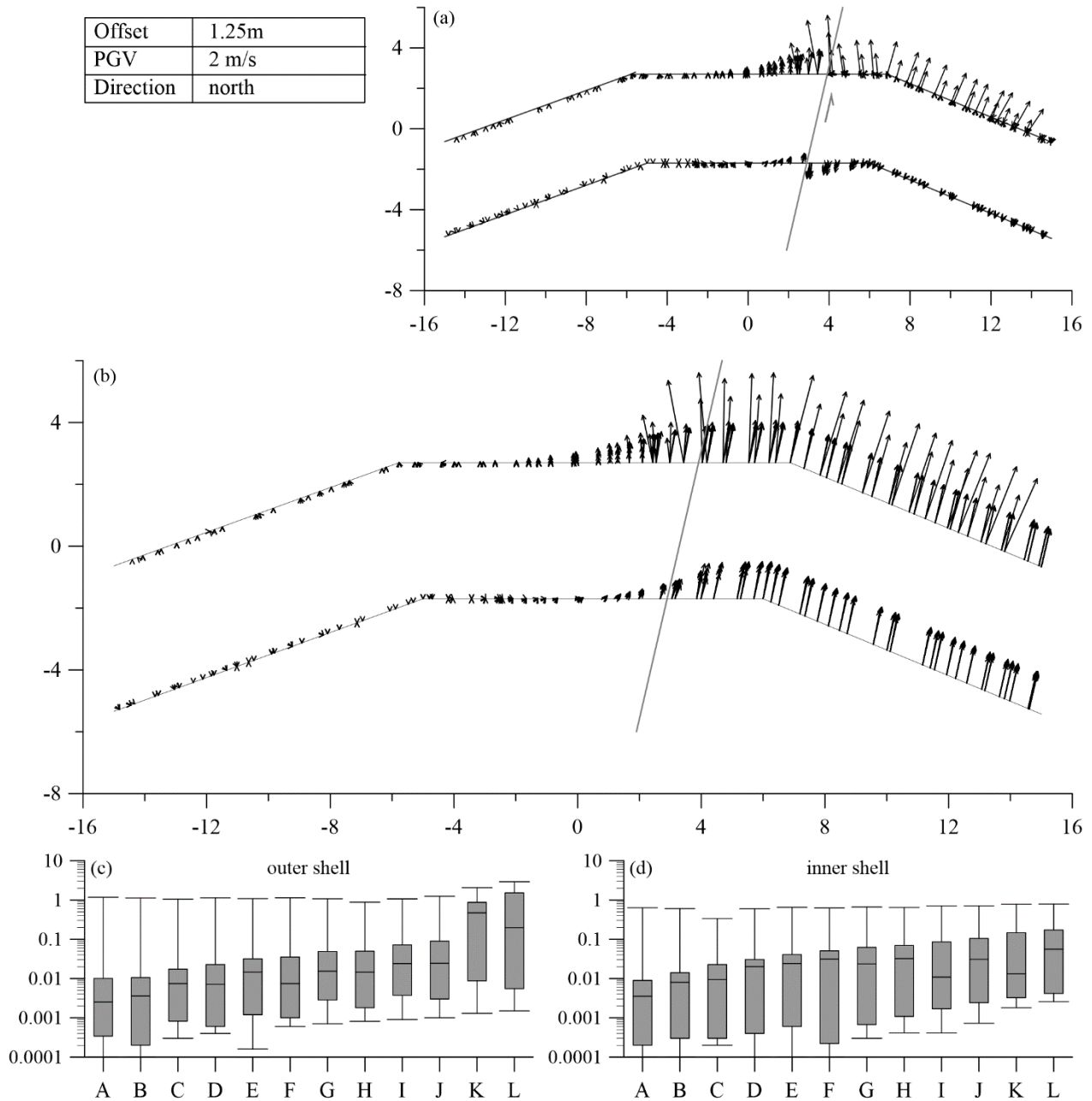


Figure A.24: Results of the simulation with a cycloidal pulse for a displacement of 1.25 m and a PGV of 2 m/s. (a) Displacement vectors of the blocks relative to the displacement of the baseplate beneath the blocks from a top view perspective. The light grey line marks the course of the fault line in the model. The light grey arrows point in direction of the ground motion. The dark grey lines mark the course of the initial wall line. (b) Vector plot of the absolute displacement (m) of all blocks from a top view perspective. The grey line marks the course of the fault line in the model and strikes in north-south direction. (c) Boxplot of the vector length relative to the displacement of the baseplate for all blocks in individual rows with row A: bottom and row L: top of the outer shell. (d) the same as (c) for the inner shell.

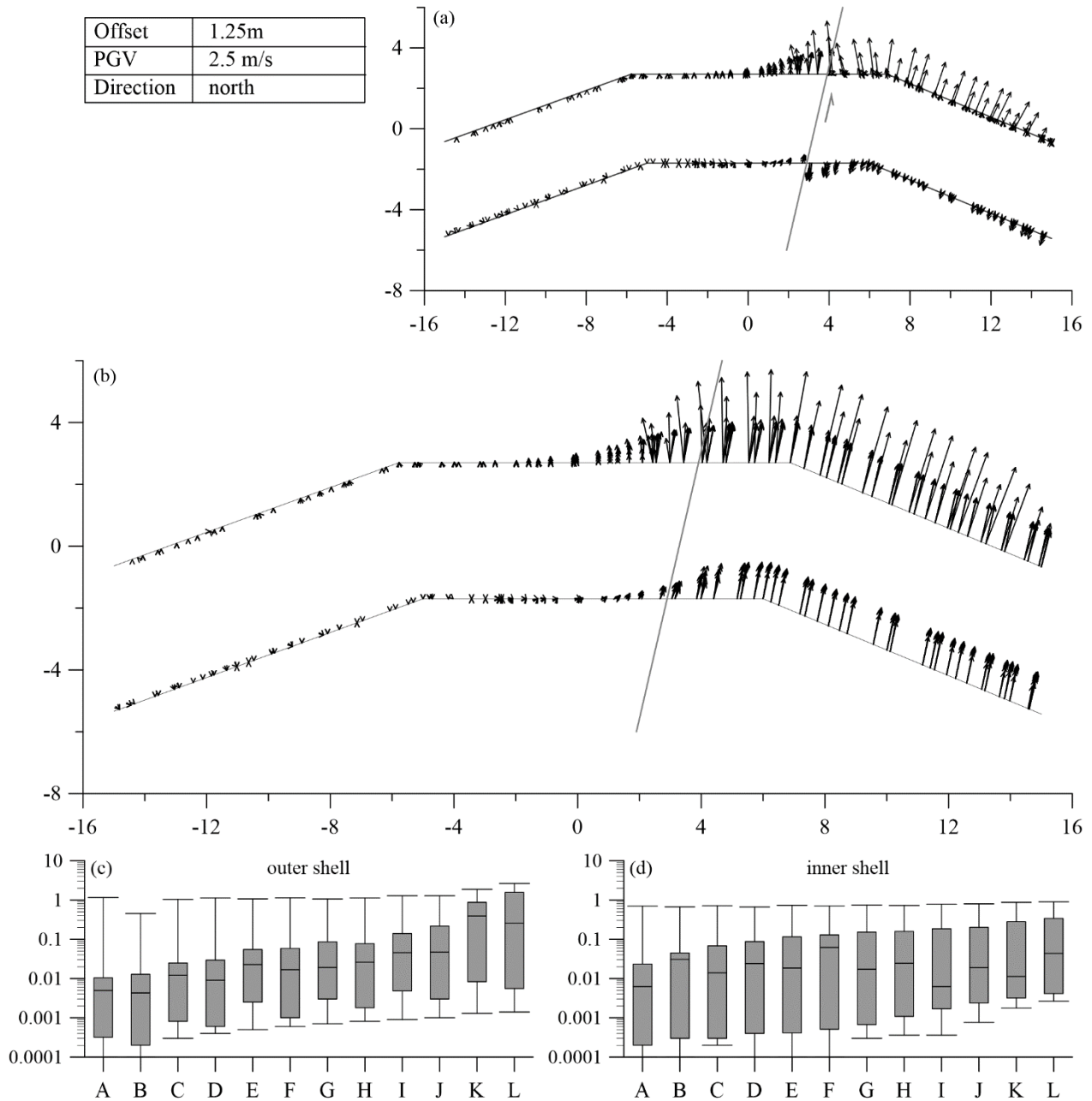


Figure A.25: Results of the simulation with a cycloidal pulse for a displacement of 1.25 m and a PGV of 2.5 m/s. (a) Displacement vectors of the blocks relative to the displacement of the baseplate beneath the blocks from a top view perspective. The light grey line marks the course of the fault line in the model. The light grey arrows point in direction of the ground motion. The dark grey lines mark the course of the initial wall line. (b) Vector plot of the absolute displacement (m) of all blocks from a top view perspective. The grey line marks the course of the fault line in the model and strikes in north-south direction. (c) Boxplot of the vector length relative to the displacement of the baseplate for all blocks in individual rows with row A: bottom and row L: top of the outer shell. (d) the same as (c) for the inner shell.

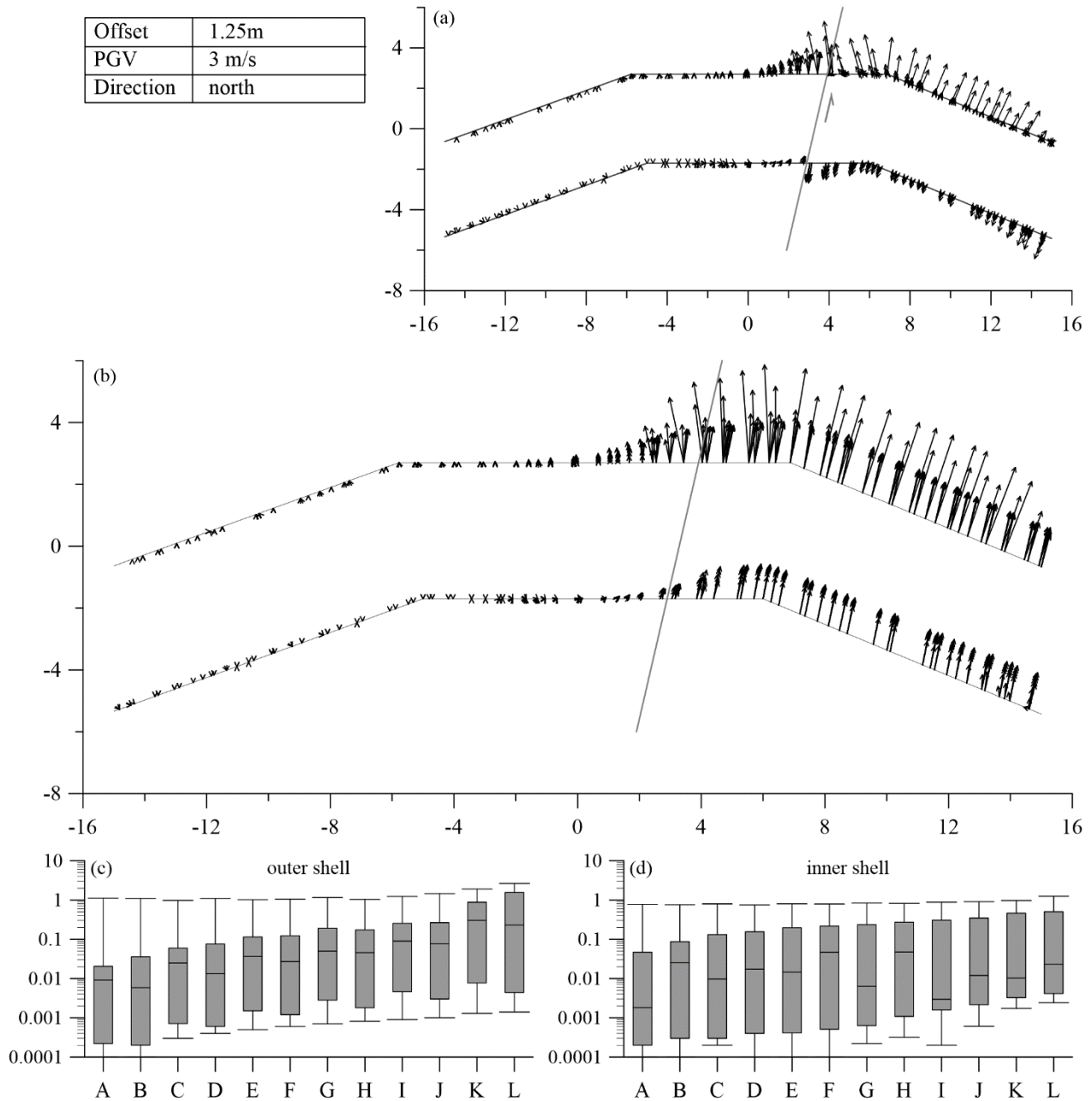


Figure A.26: Results of the simulation with a cycloidal pulse for a displacement of 1.25 m and a PGV of 3 m/s. (a) Displacement vectors of the blocks relative to the displacement of the baseplate beneath the blocks from a top view perspective. The light grey line marks the course of the fault line in the model. The light grey arrows point in direction of the ground motion. The dark grey lines mark the course of the initial wall line. (b) Vector plot of the absolute displacement (m) of all blocks from a top view perspective. The grey line marks the course of the fault line in the model and strikes in north-south direction. (c) Boxplot of the vector length relative to the displacement of the baseplate for all blocks in individual rows with row A: bottom and row L: top of the outer shell. (d) the same as (c) for the inner shell.

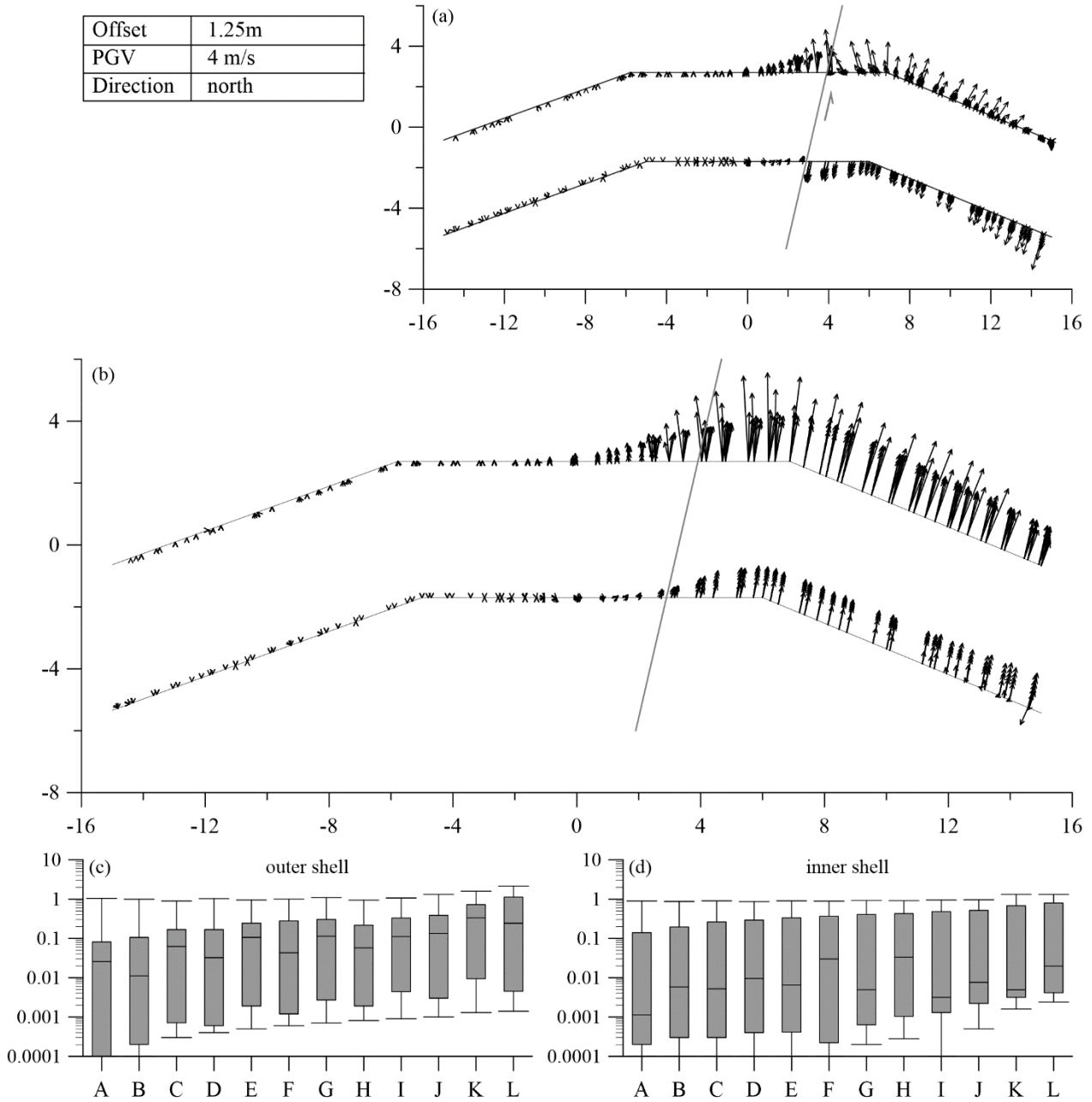


Figure A.27: Results of the simulation with a cycloidal pulse for a displacement of 1.25 m and a PGV of 4 m/s. (a) Displacement vectors of the blocks relative to the displacement of the baseplate beneath the blocks from a top view perspective. The light grey line marks the course of the fault line in the model. The light grey arrows point in direction of the ground motion. The dark grey lines mark the course of the initial wall line. (b) Vector plot of the absolute displacement (m) of all blocks from a top view perspective. The grey line marks the course of the fault line in the model and strikes in north-south direction. (c) Boxplot of the vector length relative to the displacement of the baseplate for all blocks in individual rows with row A: bottom and row L: top of the outer shell. (d) the same as (c) for the inner shell.

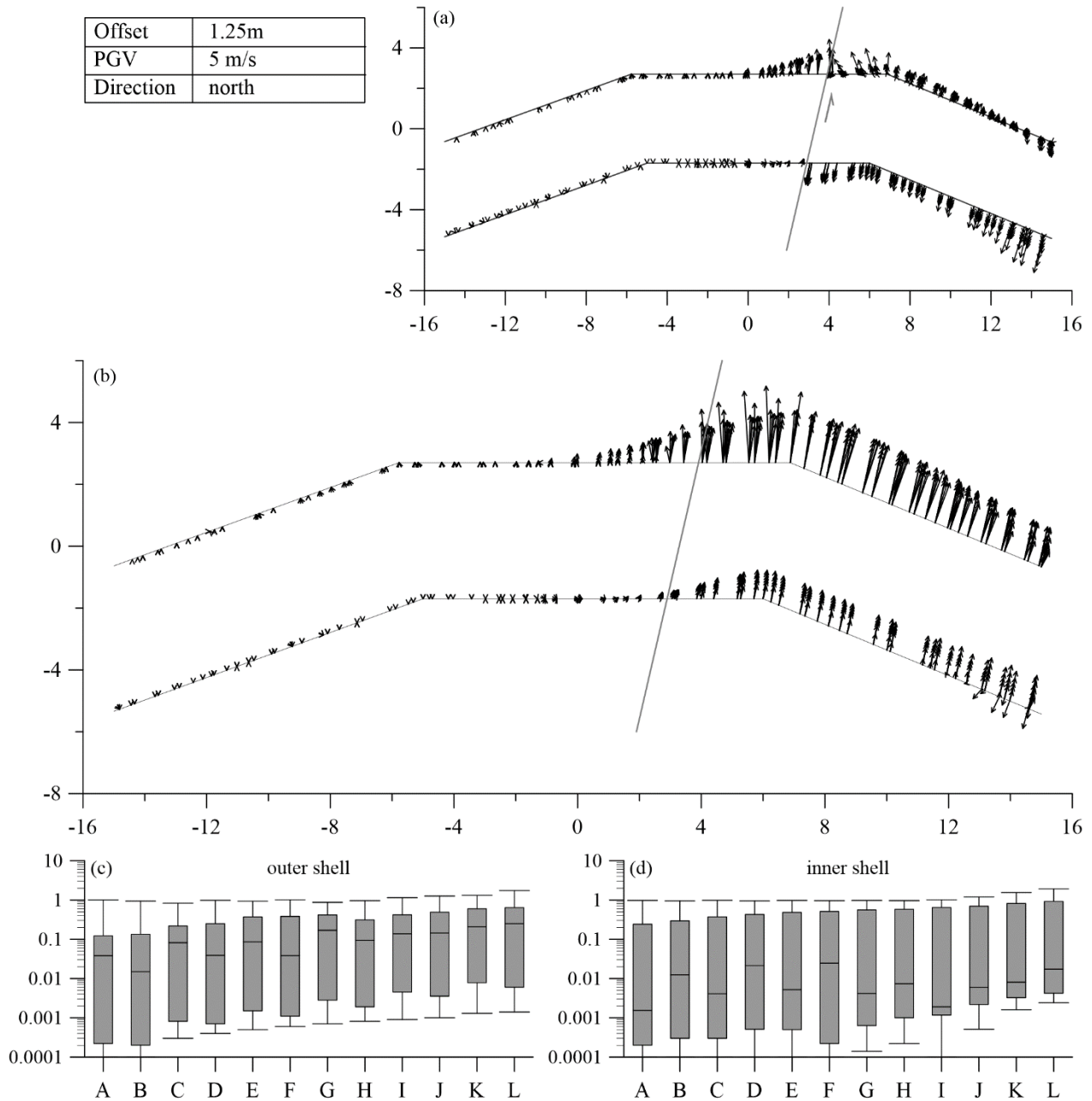


Figure A.28: Results of the simulation with a cycloidal pulse for a displacement of 1.25 m and a PGV of 5 m/s. (a) Displacement vectors of the blocks relative to the displacement of the baseplate beneath the blocks from a top view perspective. The light grey line marks the course of the fault line in the model. The light grey arrows point in direction of the ground motion. The dark grey lines mark the course of the initial wall line. (b) Vector plot of the absolute displacement (m) of all blocks from a top view perspective. The grey line marks the course of the fault line in the model and strikes in north-south direction. (c) Boxplot of the vector length relative to the displacement of the baseplate for all blocks in individual rows with row A: bottom and row L: top of the outer shell. (d) the same as (c) for the inner shell.

Second Stage

Offset	1.25m & 0.5m
PGV	1 m/s & 1 m/s
Direction	north

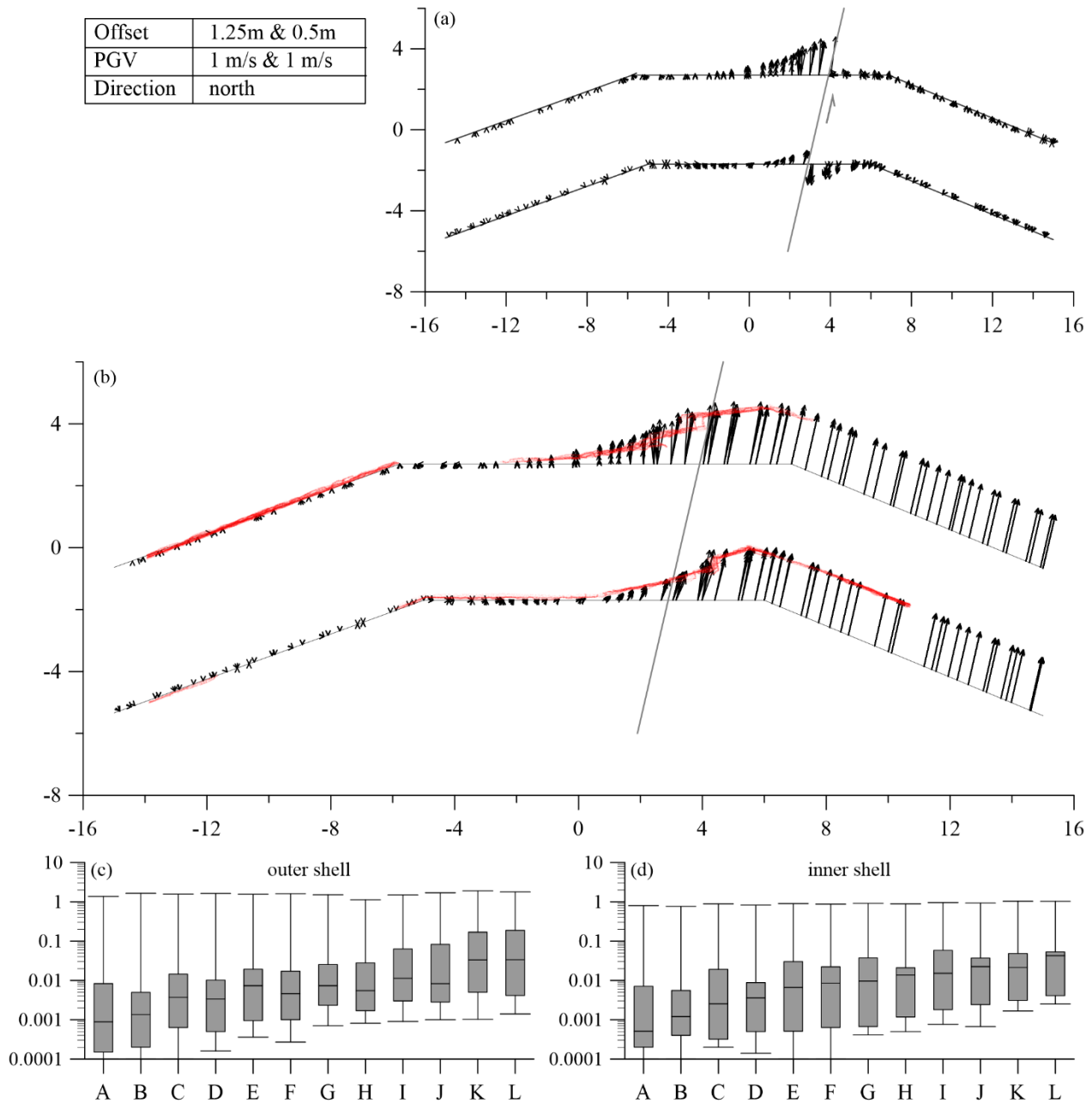


Figure A.29: Results of the simulation with a cycloidal pulse for a displacement of 1.25 m @ 1 m/s and 0.5 m @ 1 m/s. (a) Displacement vectors of the blocks relative to the displacement of the baseplate beneath the blocks from a top view perspective. The light grey line marks the course of the fault line in the model. The light grey arrows point in direction of the ground motion. The dark grey lines mark the course of the initial wall line. (b) Vector plot of the absolute displacement (m) of all blocks from a top view perspective. The grey line marks the course of the fault line in the model and strikes in north-south direction. The superposed red points are the measured points from the 3D laser scanning survey. (c) Boxplot of the vector length relative to the displacement of the baseplate for all blocks in individual rows with row A: bottom and row L: top of the outer shell. (d) the same as (c) for the inner shell.

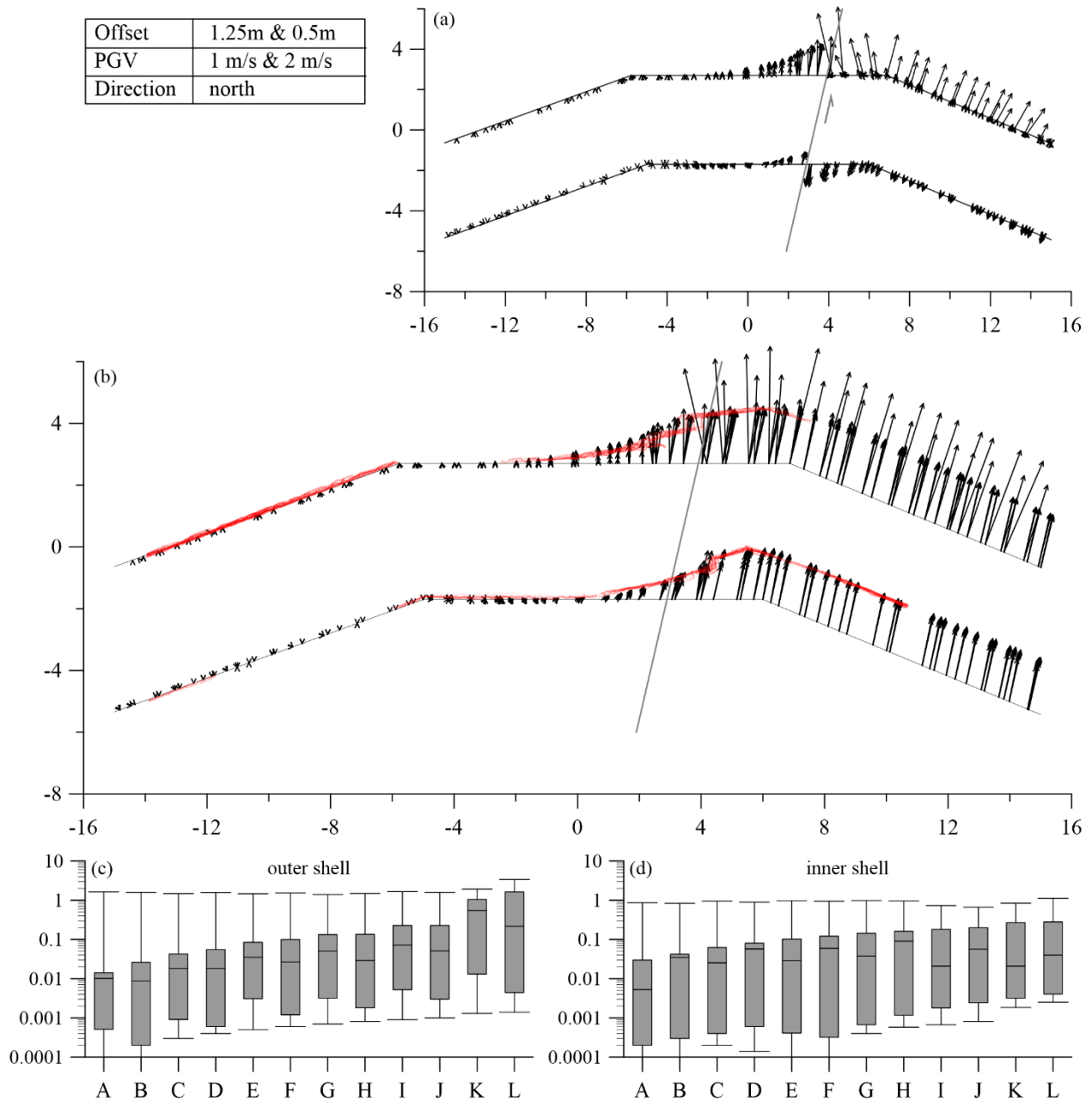


Figure A.30: Results of the simulation with a cycloidal pulse for a displacement of 1.25 m @ 2 m/s and 0.5 m @ 1 m/s. (a) Displacement vectors of the blocks relative to the displacement of the baseplate beneath the blocks from a top view perspective. The light grey line marks the course of the fault line in the model. The light grey arrows point in direction of the ground motion. The dark grey lines mark the course of the initial wall line. (b) Vector plot of the absolute displacement (m) of all blocks from a top view perspective. The grey line marks the course of the fault line in the model and strikes in north-south direction. The superposed red points are the measured points from the 3D laser scanning survey. (c) Boxplot of the vector length relative to the displacement of the baseplate for all blocks in individual rows with row A: bottom and row L: top of the outer shell. (d) the same as (c) for the inner shell.

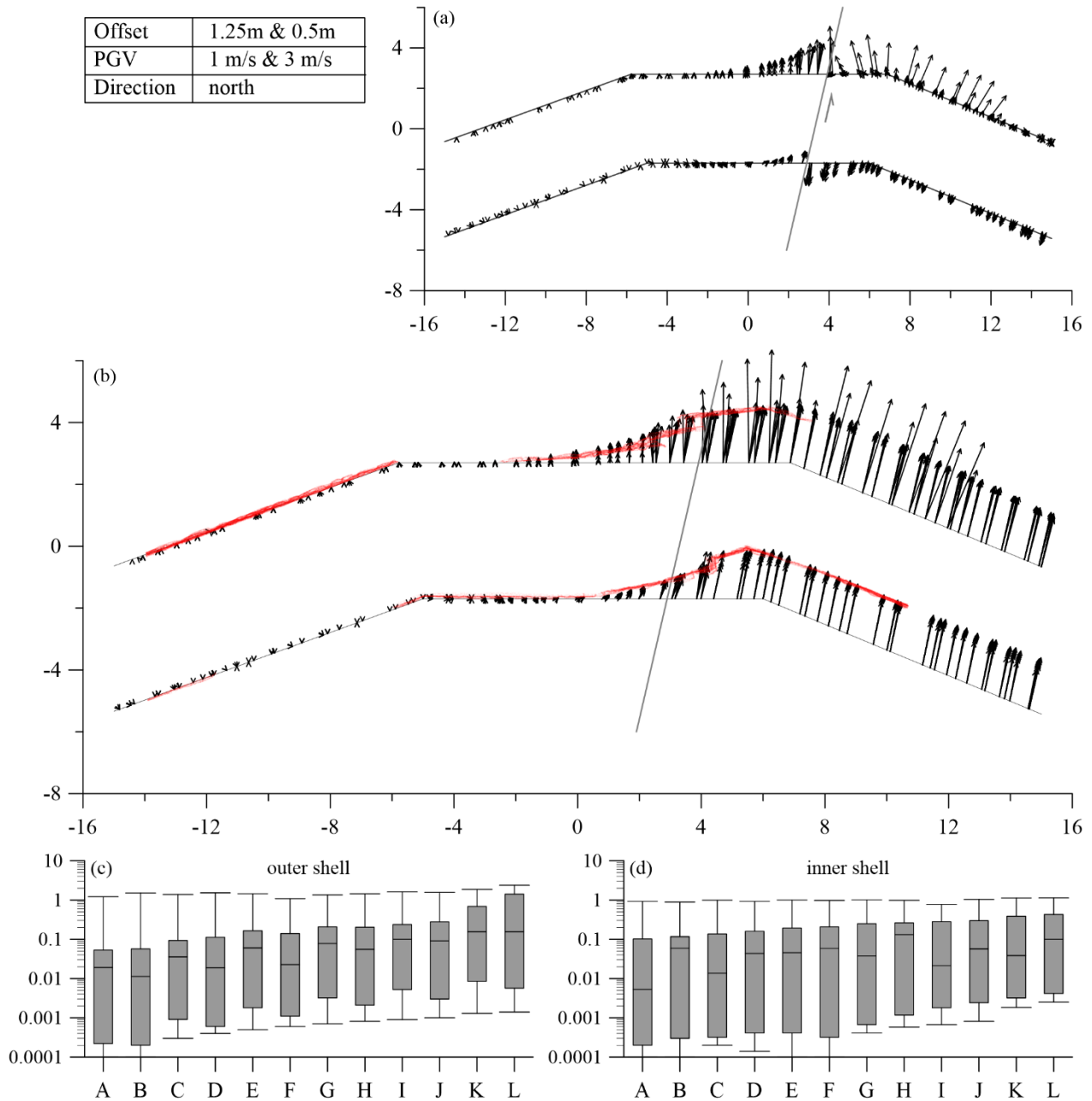


Figure A.31: Results of the simulation with a cycloidal pulse for a displacement of 1.25 m @ 1 m/s and 0.5 m @ 3 m/s. (a) Displacement vectors of the blocks relative to the displacement of the baseplate beneath the blocks from a top view perspective. The light grey line marks the course of the fault line in the model. The light grey arrows point in direction of the ground motion. The dark grey lines mark the course of the initial wall line. (b) Vector plot of the absolute displacement (m) of all blocks from a top view perspective. The grey line marks the course of the fault line in the model and strikes in north-south direction. The superposed red points are the measured points from the 3D laser scanning survey. (c) Boxplot of the vector length relative to the displacement of the baseplate for all blocks in individual rows with row A: bottom and row L: top of the outer shell. (d) the same as (c) for the inner shell.

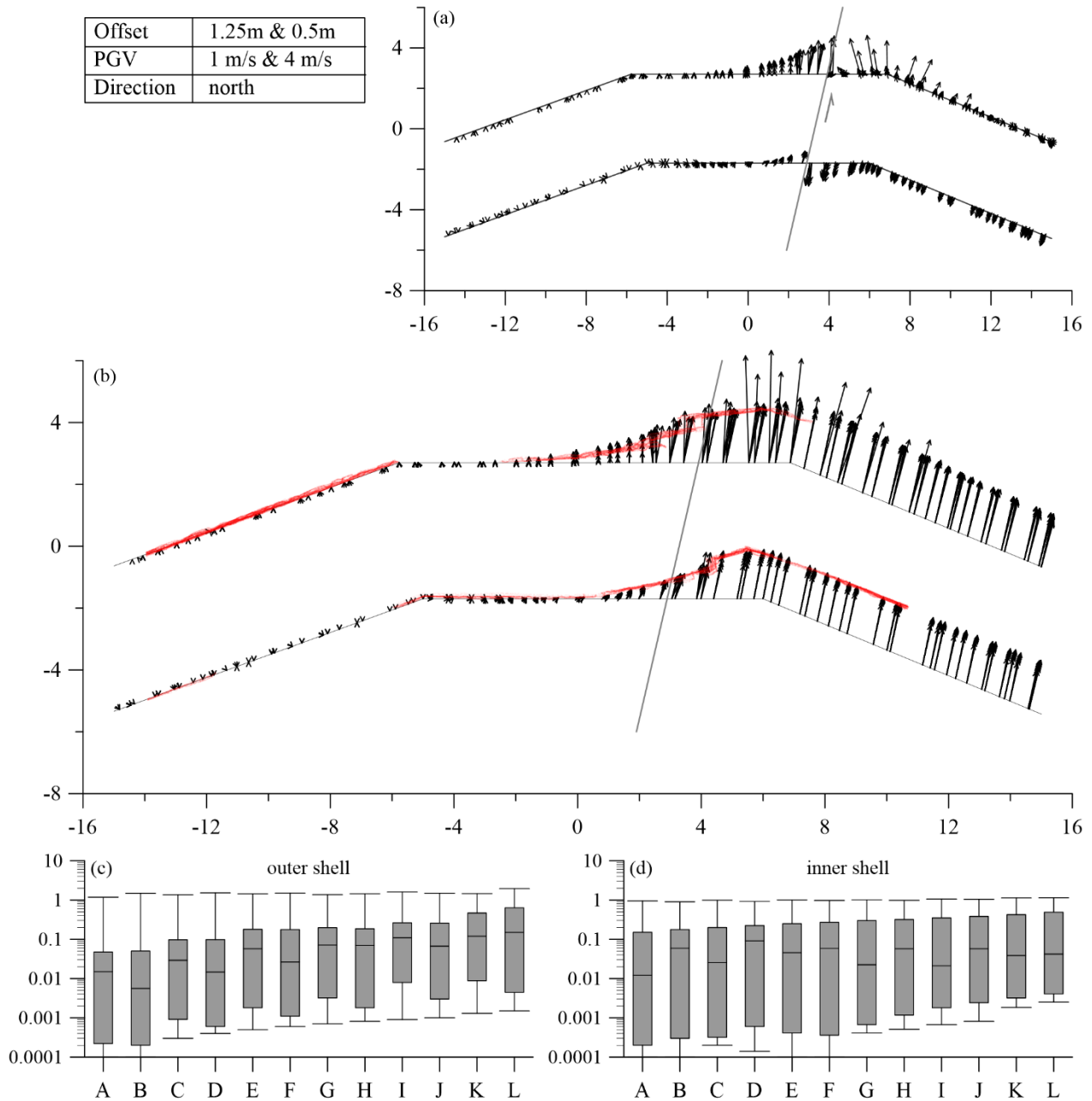


Figure A.32: Results of the simulation with a cycloidal pulse for a displacement of 1.25 m @ 1 m/s and 0.5 m @ 4 m/s. (a) Displacement vectors of the blocks relative to the displacement of the baseplate beneath the blocks from a top view perspective. The light grey line marks the course of the fault line in the model. The light grey arrows point in direction of the ground motion. The dark grey lines mark the course of the initial wall line. (b) Vector plot of the absolute displacement (m) of all blocks from a top view perspective. The grey line marks the course of the fault line in the model and strikes in north-south direction. The superposed red points are the measured points from the 3D laser scanning survey. (c) Boxplot of the vector length relative to the displacement of the baseplate for all blocks in individual rows with row A: bottom and row L: top of the outer shell. (d) the same as (c) for the inner shell.

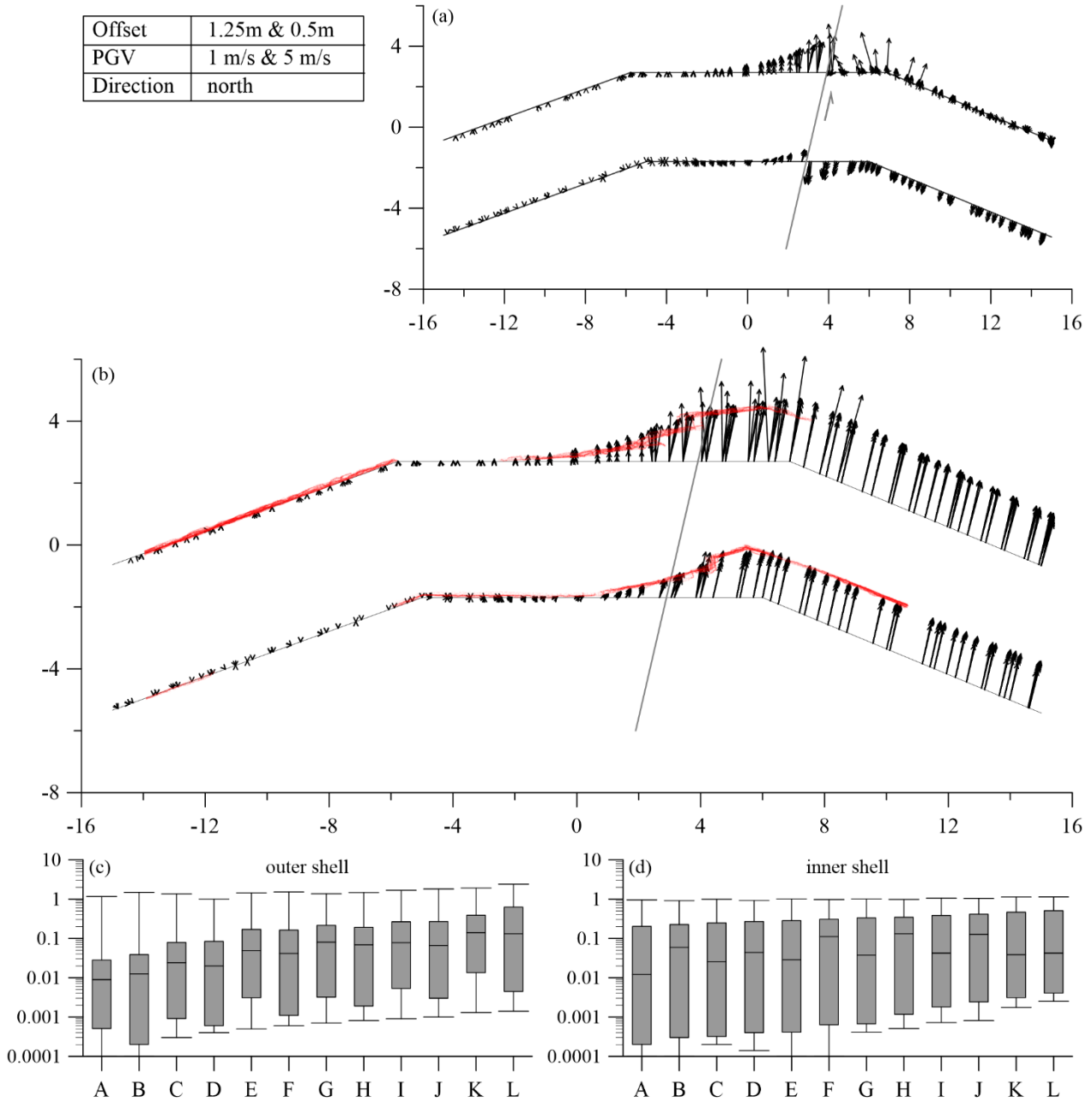


Figure A.33: Results of the simulation with a cycloidal pulse for a displacement of 1.25 m @ 1 m/s and 0.5 m @ 5 m/s. (a) Displacement vectors of the blocks relative to the displacement of the baseplate beneath the blocks from a top view perspective. The light grey line marks the course of the fault line in the model. The light grey arrows point in direction of the ground motion. The dark grey lines mark the course of the initial wall line. (b) Vector plot of the absolute displacement (m) of all blocks from a top view perspective. The grey line marks the course of the fault line in the model and strikes in north-south direction. The superposed red points are the measured points from the 3D laser scanning survey. (c) Boxplot of the vector length relative to the displacement of the baseplate for all blocks in individual rows with row A: bottom and row L: top of the outer shell. (d) the same as (c) for the inner shell.

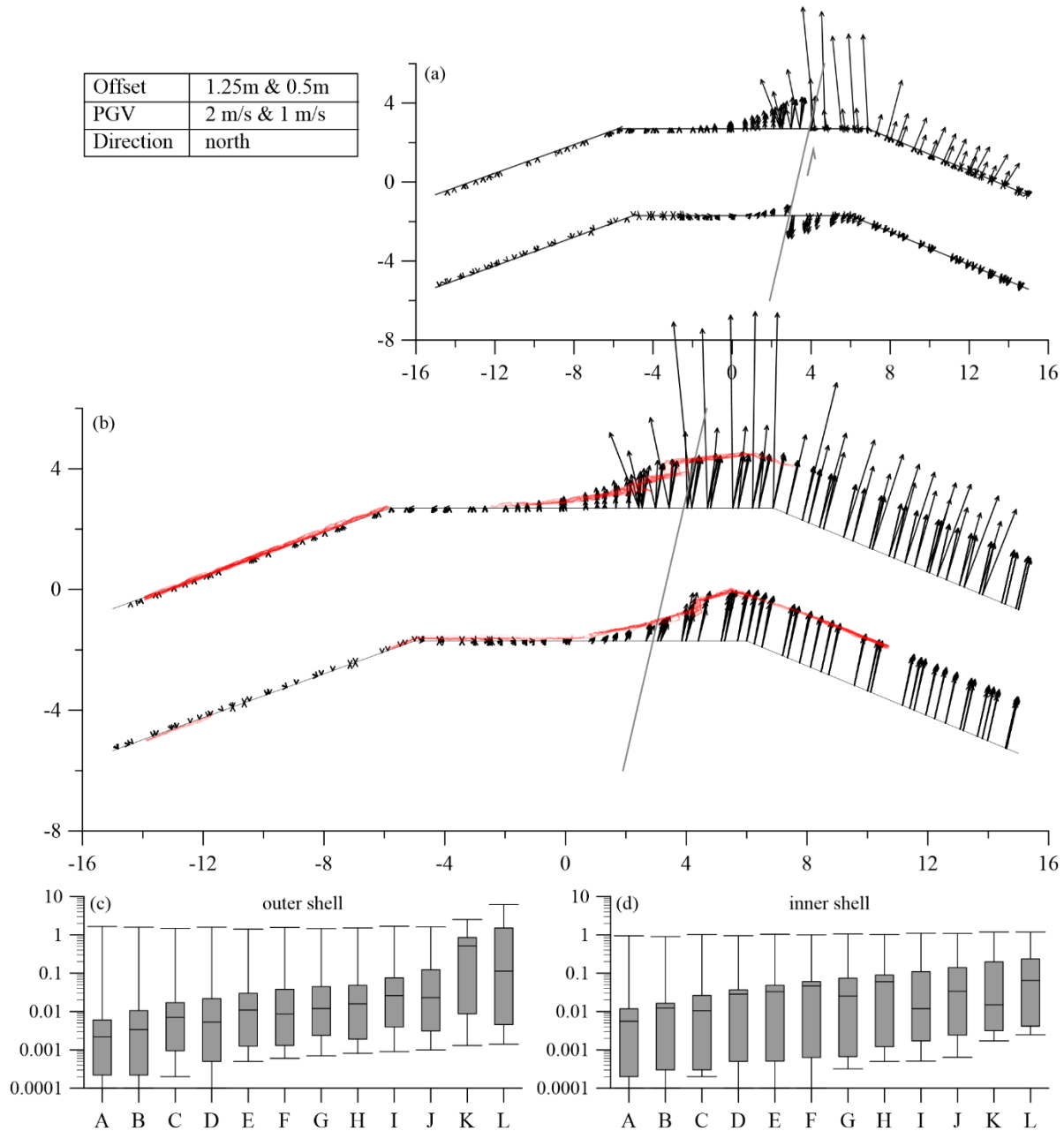


Figure A.34: Results of the simulation with a cycloidal pulse for a displacement of 1.25 m @ 2 m/s and 0.5 m @ 1 m/s. (a) Displacement vectors of the blocks relative to the displacement of the baseplate beneath the blocks from a top view perspective. The light grey line marks the course of the fault line in the model. The light grey arrows point in direction of the ground motion. The dark grey lines mark the course of the initial wall line. (b) Vector plot of the absolute displacement (m) of all blocks from a top view perspective. The grey line marks the course of the fault line in the model and strikes in north-south direction. The superposed red points are the measured points from the 3D laser scanning survey. (c) Boxplot of the vector length relative to the displacement of the baseplate for all blocks in individual rows with row A: bottom and row L: top of the outer shell. (d) the same as (c) for the inner shell.

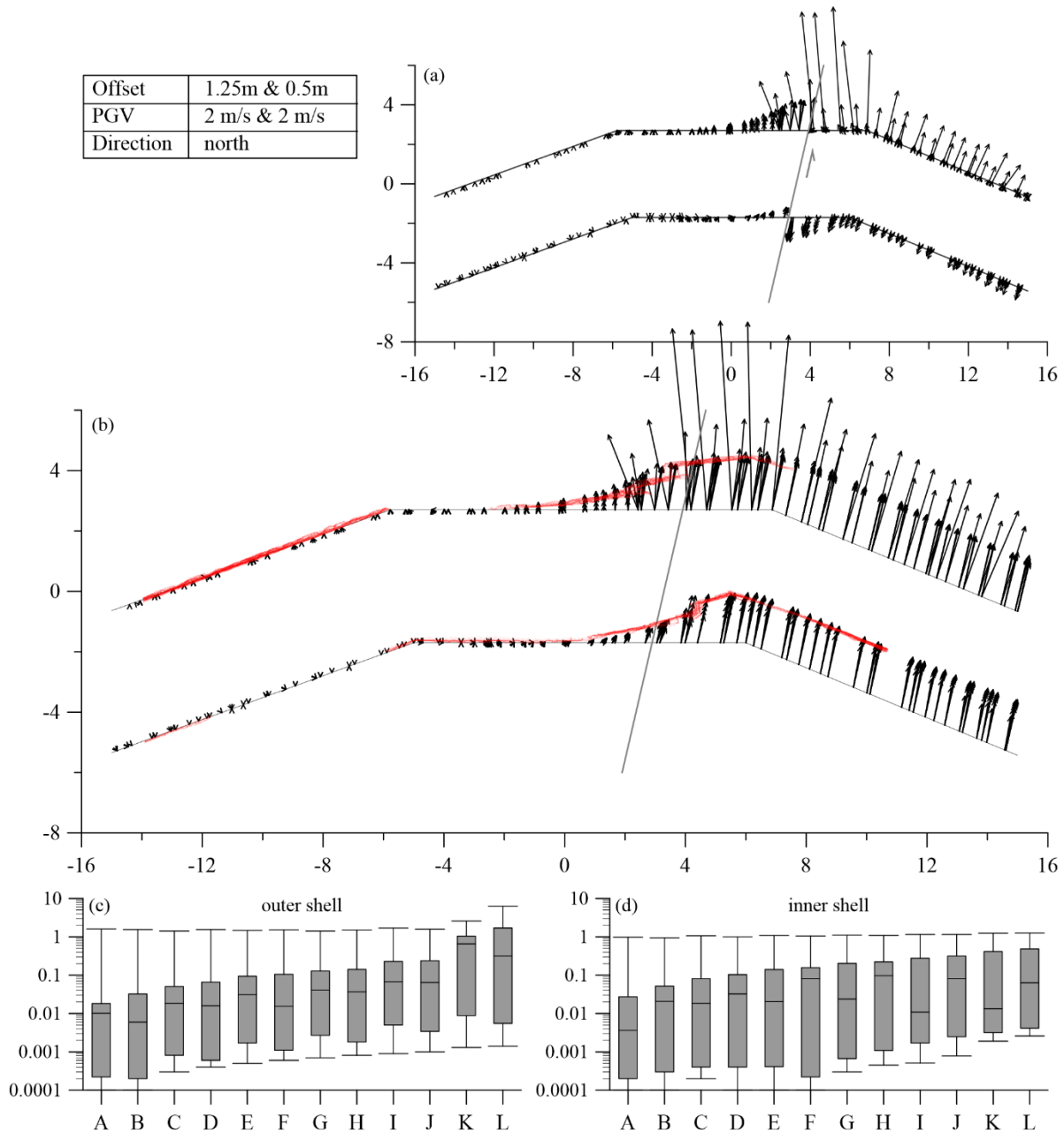


Figure A.35: Results of the simulation with a cycloidal pulse for a displacement of 1.25 m @ 2 m/s and 0.5 m @ 2 m/s. (a) Displacement vectors of the blocks relative to the displacement of the baseplate beneath the blocks from a top view perspective. The light grey line marks the course of the fault line in the model. The light grey arrows point in direction of the ground motion. The dark grey lines mark the course of the initial wall line. (b) Vector plot of the absolute displacement (m) of all blocks from a top view perspective. The grey line marks the course of the fault line in the model and strikes in north-south direction. The superposed red points are the measured points from the 3D laser scanning survey. (c) Boxplot of the vector length relative to the displacement of the baseplate for all blocks in individual rows with row A: bottom and row L: top of the outer shell. (d) the same as (c) for the inner shell.

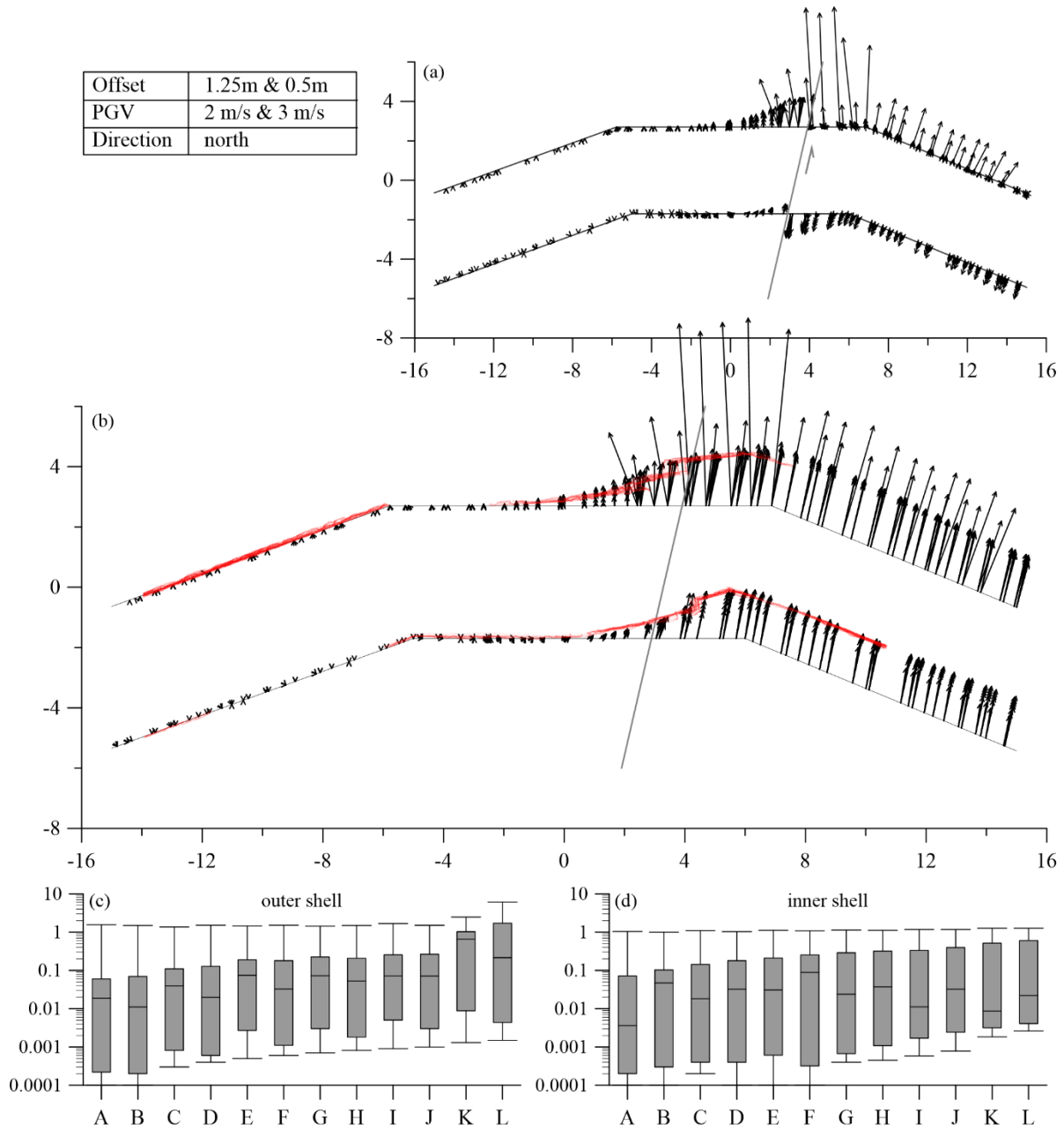


Figure A.36: Results of the simulation with a cycloidal pulse for a displacement of 1.25 m @ 2 m/s and 0.5 m @ 3 m/s. (a) Displacement vectors of the blocks relative to the displacement of the baseplate beneath the blocks from a top view perspective. The light grey line marks the course of the fault line in the model. The light grey arrows point in direction of the ground motion. The dark grey lines mark the course of the initial wall line. (b) Vector plot of the absolute displacement (m) of all blocks from a top view perspective. The grey line marks the course of the fault line in the model and strikes in north-south direction. The superposed red points are the measured points from the 3D laser scanning survey. (c) Boxplot of the vector length relative to the displacement of the baseplate for all blocks in individual rows with row A: bottom and row L: top of the outer shell. (d) the same as (c) for the inner shell.

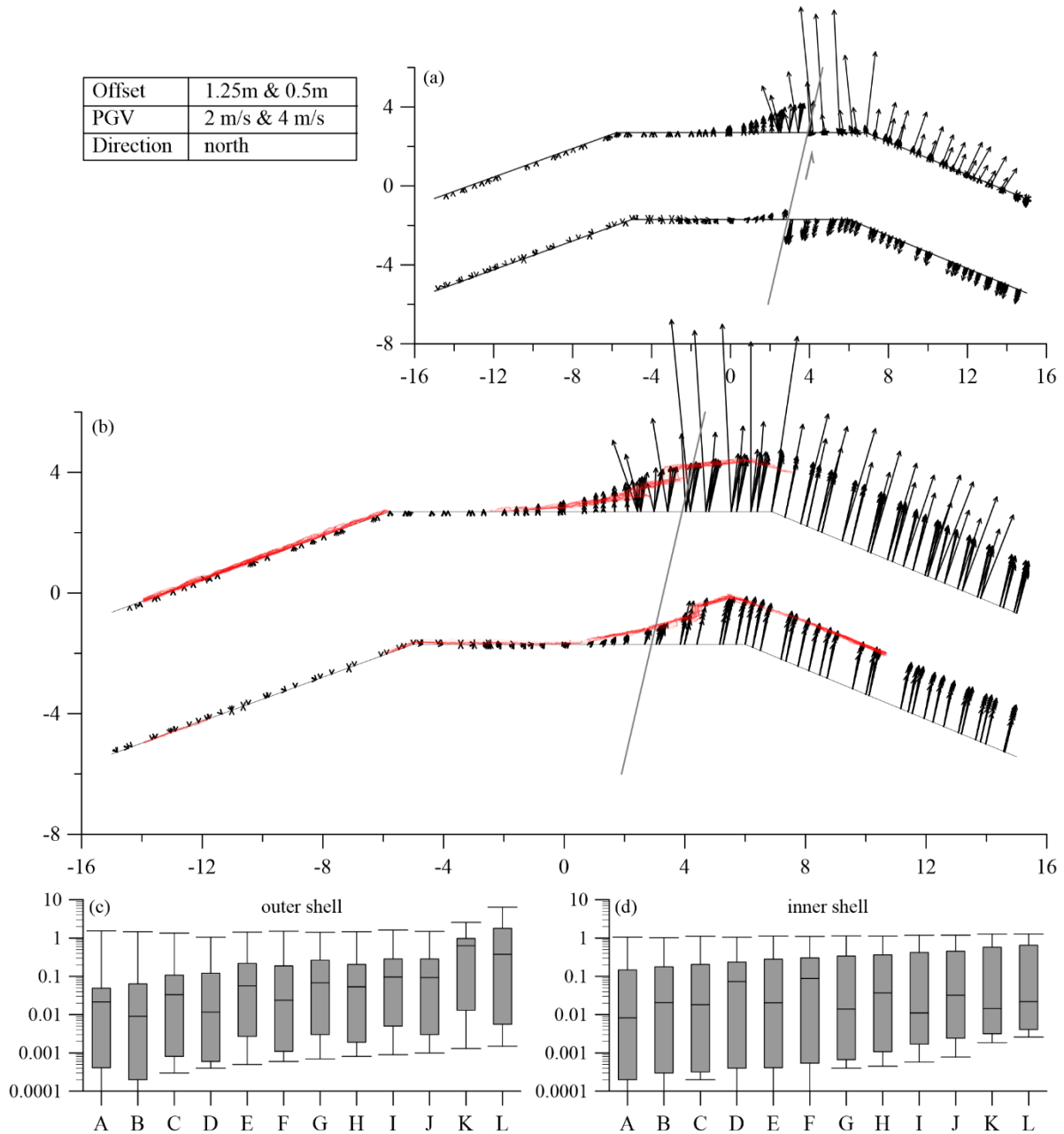


Figure A.37: Results of the simulation with a cycloidal pulse for a displacement of 1.25 m @ 2 m/s and 0.5 m @ 4 m/s. (a) Displacement vectors of the blocks relative to the displacement of the baseplate beneath the blocks from a top view perspective. The light grey line marks the course of the fault line in the model. The light grey arrows point in direction of the ground motion. The dark grey lines mark the course of the initial wall line. (b) Vector plot of the absolute displacement (m) of all blocks from a top view perspective. The grey line marks the course of the fault line in the model and strikes in north-south direction. The superposed red points are the measured points from the 3D laser scanning survey. (c) Boxplot of the vector length relative to the displacement of the baseplate for all blocks in individual rows with row A: bottom and row L: top of the outer shell. (d) the same as (c) for the inner shell.

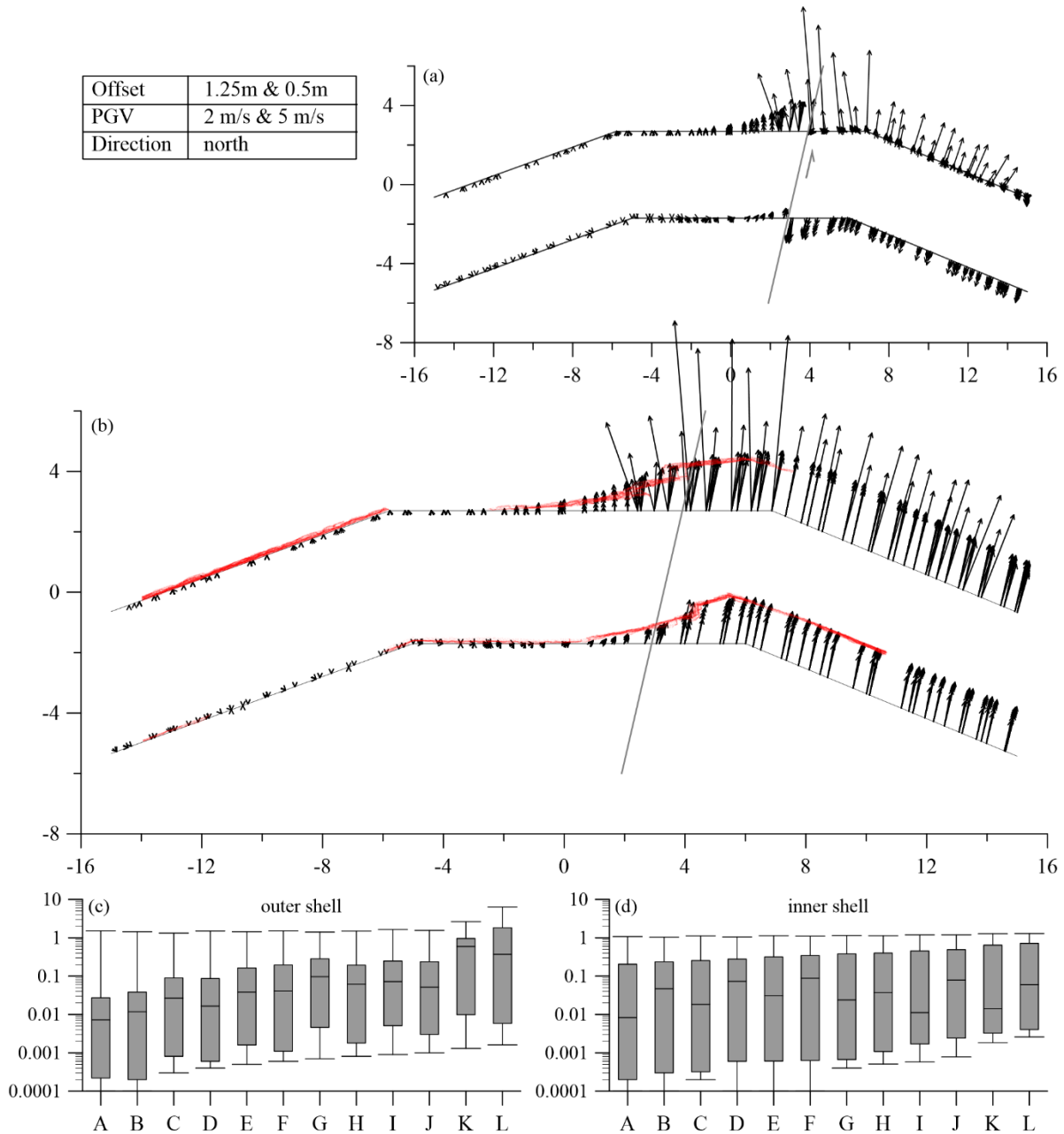


Figure A.38: Results of the simulation with a cycloidal pulse for a displacement of 1.25 m @ 2 m/s and 0.5 m @ 5 m/s. (a) Displacement vectors of the blocks relative to the displacement of the baseplate beneath the blocks from a top view perspective. The light grey line marks the course of the fault line in the model. The light grey arrows point in direction of the ground motion. The dark grey lines mark the course of the initial wall line. (b) Vector plot of the absolute displacement (m) of all blocks from a top view perspective. The grey line marks the course of the fault line in the model and strikes in north-south direction. The superposed red points are the measured points from the 3D laser scanning survey. (c) Boxplot of the vector length relative to the displacement of the baseplate for all blocks in individual rows with row A: bottom and row L: top of the outer shell. (d) the same as (c) for the inner shell.

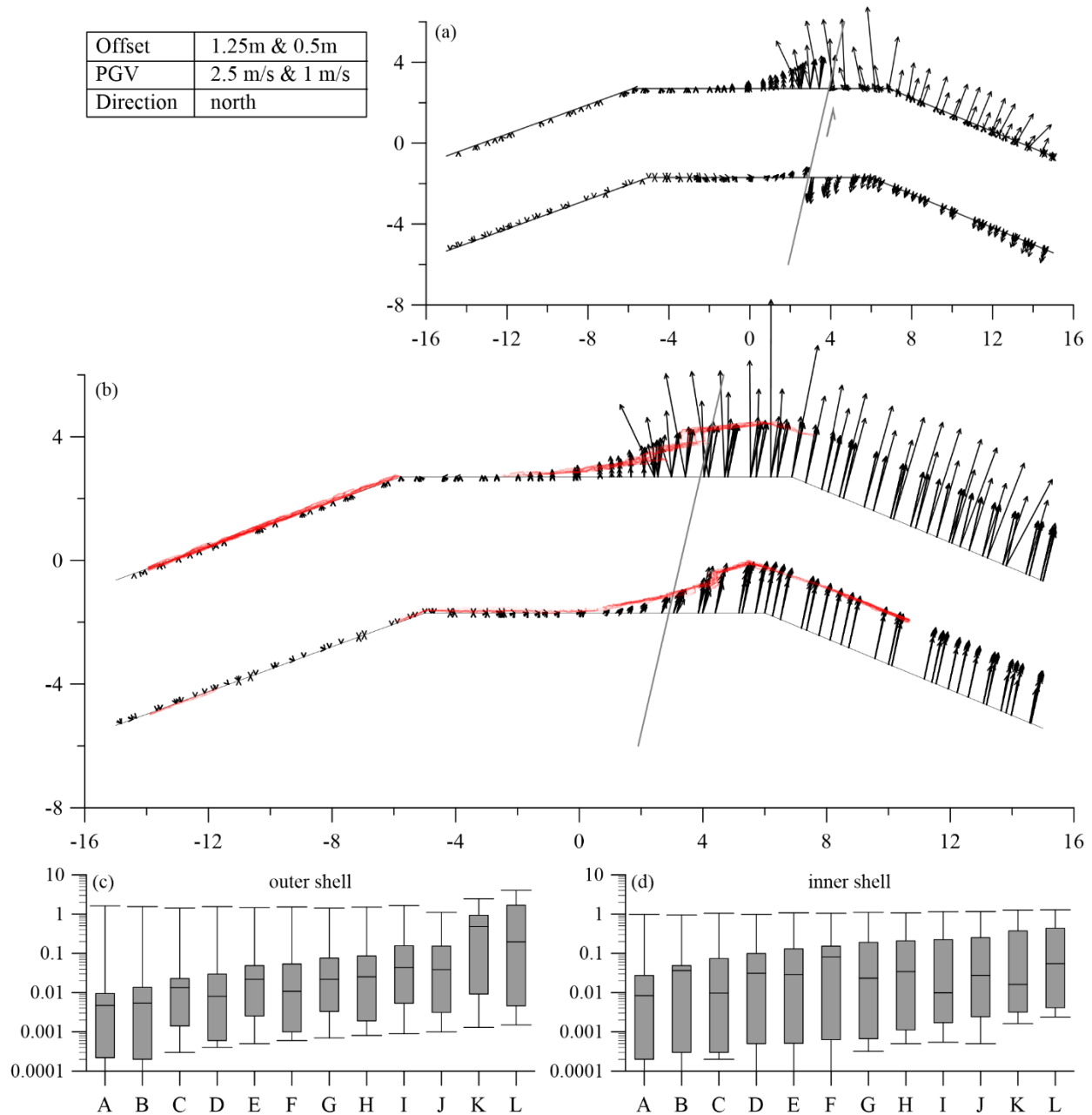


Figure A.39: Results of the simulation with a cycloidal pulse for a displacement of 1.25 m @ 2.5 m/s and 0.5 m @ 1 m/s. (a) Displacement vectors of the blocks relative to the displacement of the baseplate beneath the blocks from a top view perspective. The light grey line marks the course of the fault line in the model. The light grey arrows point in direction of the ground motion. The dark grey lines mark the course of the initial wall line. (b) Vector plot of the absolute displacement (m) of all blocks from a top view perspective. The grey line marks the course of the fault line in the model and strikes in north-south direction. The superposed red points are the measured points from the 3D laser scanning survey. (c) Boxplot of the vector length relative to the displacement of the baseplate for all blocks in individual rows with row A: bottom and row L: top of the outer shell. (d) the same as (c) for the inner shell.

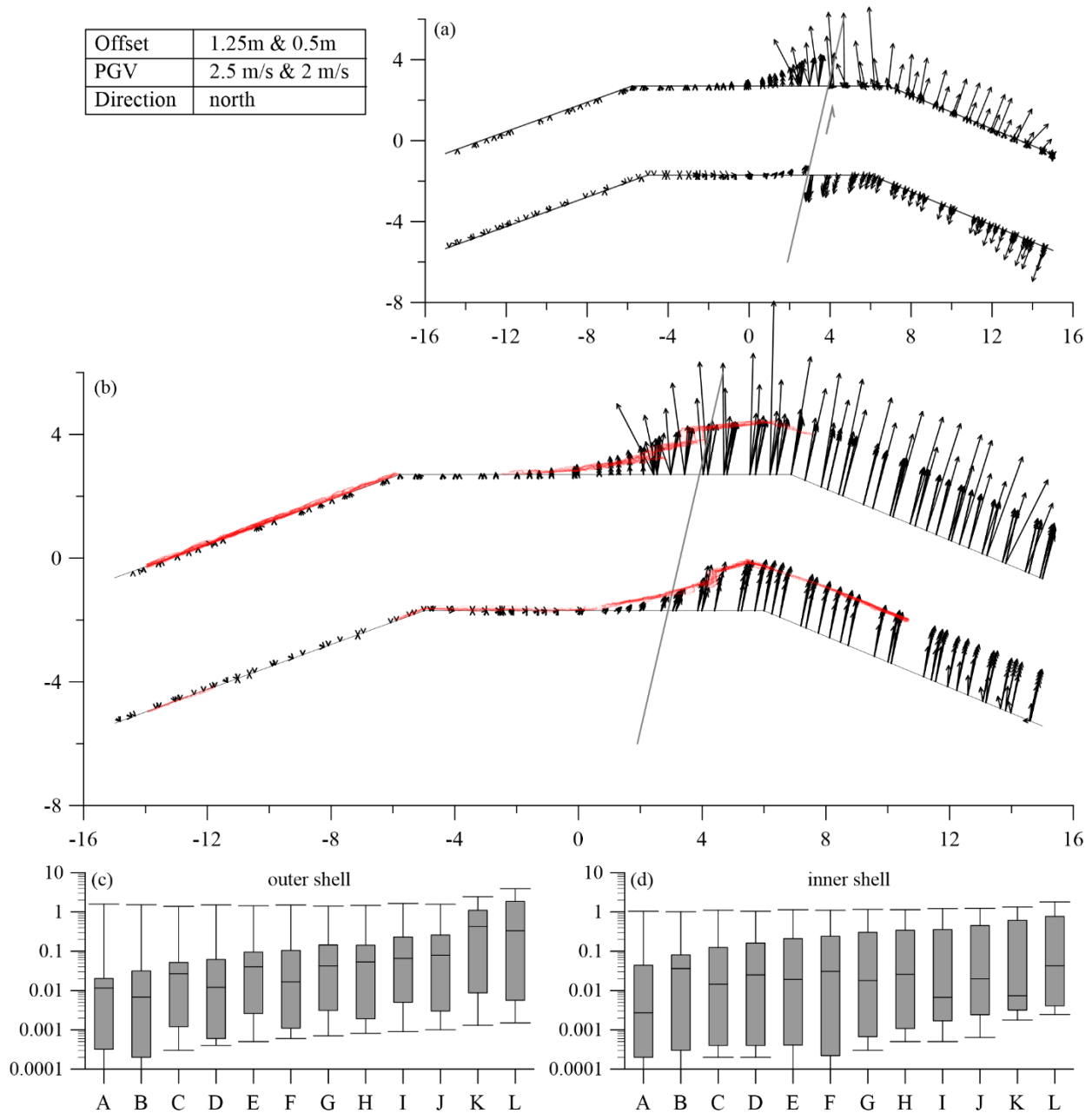


Figure A.40: Results of the simulation with a cycloidal pulse for a displacement of 1.25 m @ 2.5 m/s and 0.5 m @ 2 m/s. (a) Displacement vectors of the blocks relative to the displacement of the baseplate beneath the blocks from a top view perspective. The light grey line marks the course of the fault line in the model. The light grey arrows point in direction of the ground motion. The dark grey lines mark the course of the initial wall line. (b) Vector plot of the absolute displacement (m) of all blocks from a top view perspective. The grey line marks the course of the fault line in the model and strikes in north-south direction. The superposed red points are the measured points from the 3D laser scanning survey. (c) Boxplot of the vector length relative to the displacement of the baseplate for all blocks in individual rows with row A: bottom and row L: top of the outer shell. (d) the same as (c) for the inner shell.

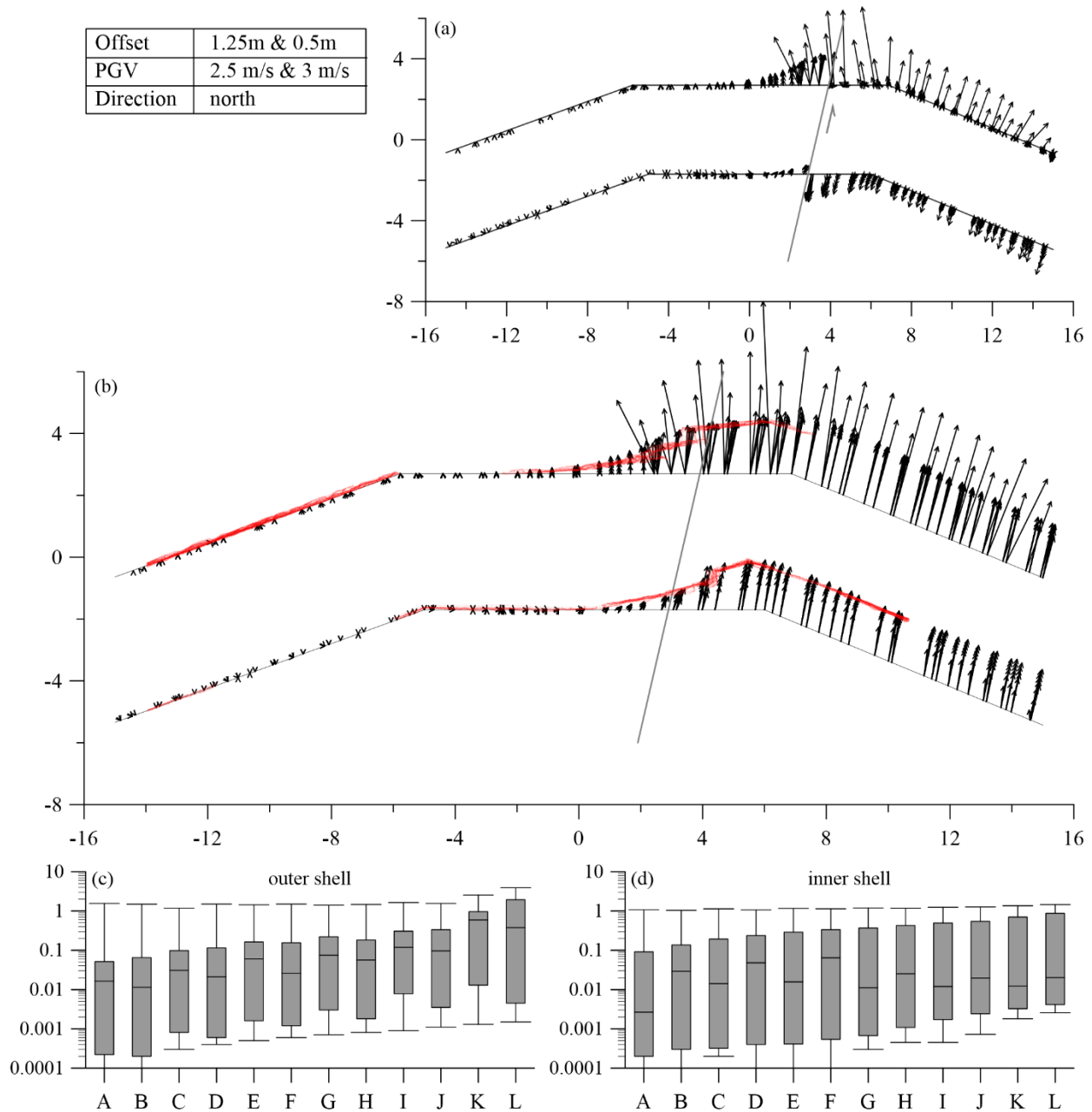


Figure A.41: Results of the simulation with a cycloidal pulse for a displacement of 1.25 m @ 2.5 m/s and 0.5 m @ 3 m/s. (a) Displacement vectors of the blocks relative to the displacement of the baseplate beneath the blocks from a top view perspective. The light grey line marks the course of the fault line in the model. The light grey arrows point in direction of the ground motion. The dark grey lines mark the course of the initial wall line. (b) Vector plot of the absolute displacement (m) of all blocks from a top view perspective. The grey line marks the course of the fault line in the model and strikes in north-south direction. The superposed red points are the measured points from the 3D laser scanning survey. (c) Boxplot of the vector length relative to the displacement of the baseplate for all blocks in individual rows with row A: bottom and row L: top of the outer shell. (d) the same as (c) for the inner shell.

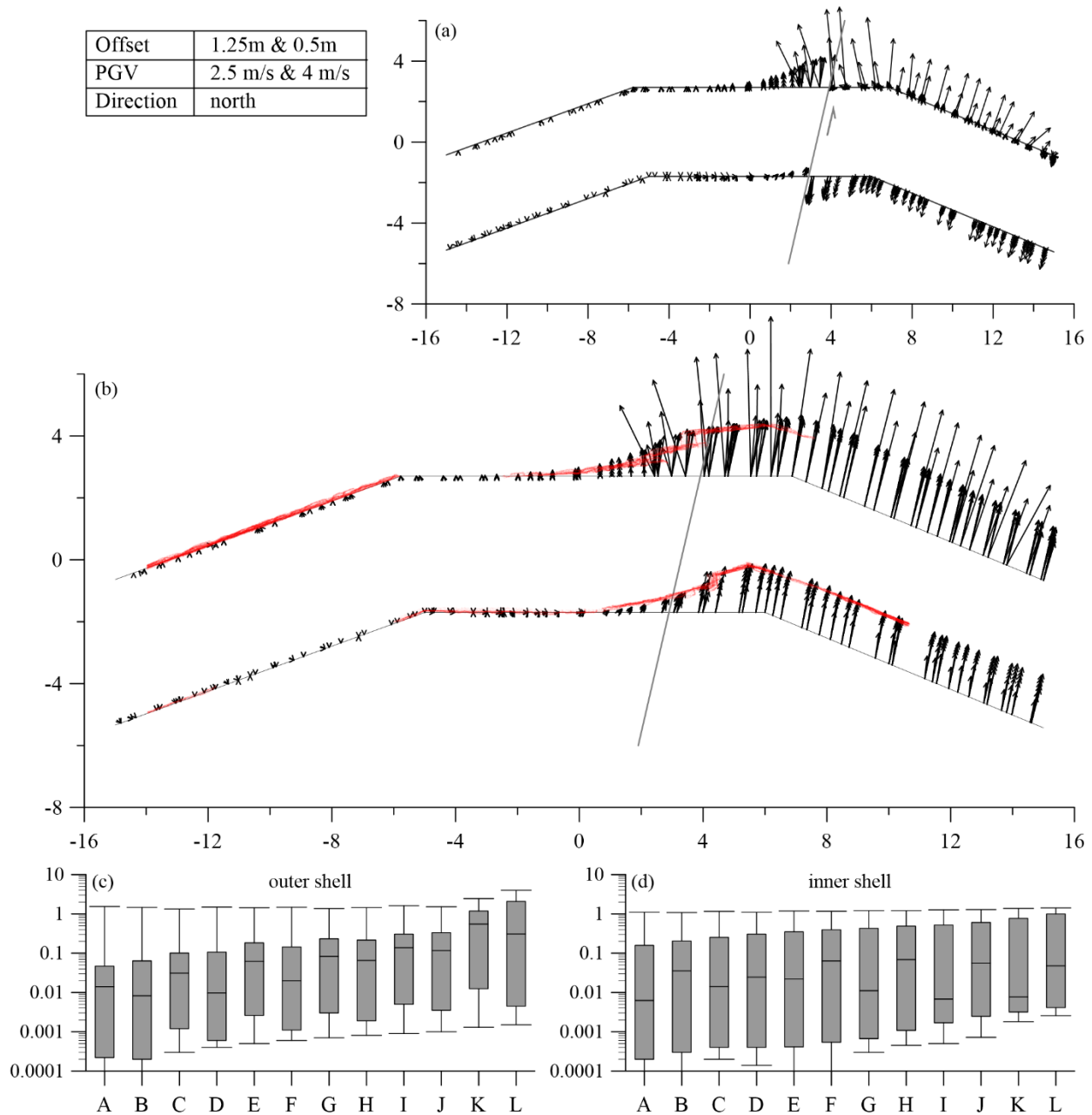


Figure A.42: Results of the simulation with a cycloidal pulse for a displacement of 1.25 m @ 2.5 m/s and 0.5 m @ 4 m/s. (a) Displacement vectors of the blocks relative to the displacement of the baseplate beneath the blocks from a top view perspective. The light grey line marks the course of the fault line in the model. The light grey arrows point in direction of the ground motion. The dark grey lines mark the course of the initial wall line. (b) Vector plot of the absolute displacement (m) of all blocks from a top view perspective. The grey line marks the course of the fault line in the model and strikes in north-south direction. The superposed red points are the measured points from the 3D laser scanning survey. (c) Boxplot of the vector length relative to the displacement of the baseplate for all blocks in individual rows with row A: bottom and row L: top of the outer shell. (d) the same as (c) for the inner shell.

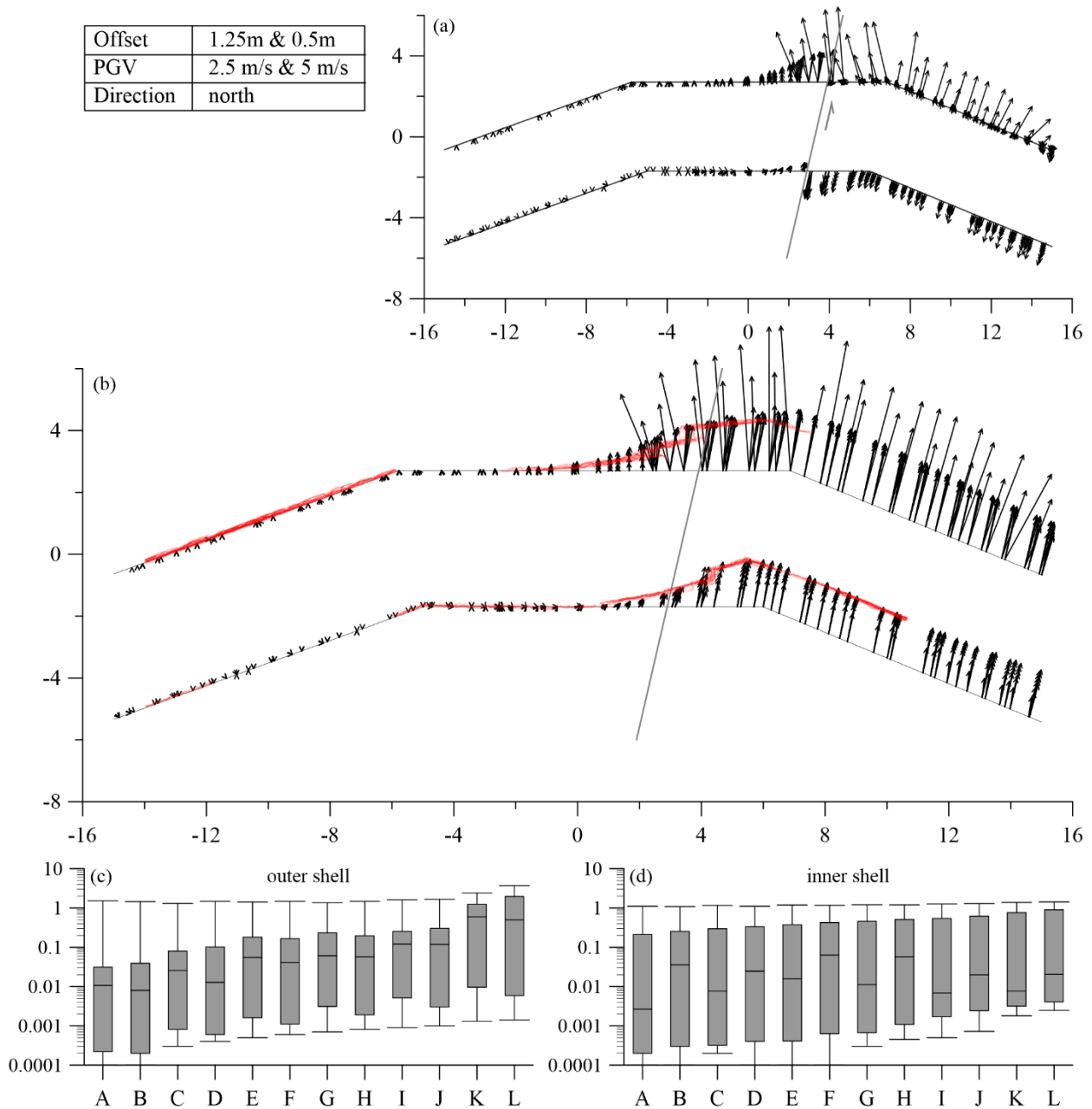


Figure A.43: Results of the simulation with a cycloidal pulse for a displacement of 1.25 m @ 2.5 m/s and 0.5 m @ 5 m/s. (a) Displacement vectors of the blocks relative to the displacement of the baseplate beneath the blocks from a top view perspective. The light grey line marks the course of the fault line in the model. The light grey arrows point in direction of the ground motion. The dark grey lines mark the course of the initial wall line. (b) Vector plot of the absolute displacement (m) of all blocks from a top view perspective. The grey line marks the course of the fault line in the model and strikes in north-south direction. The superposed red points are the measured points from the 3D laser scanning survey. (c) Boxplot of the vector length relative to the displacement of the baseplate for all blocks in individual rows with row A: bottom and row L: top of the outer shell. (d) the same as (c) for the inner shell.

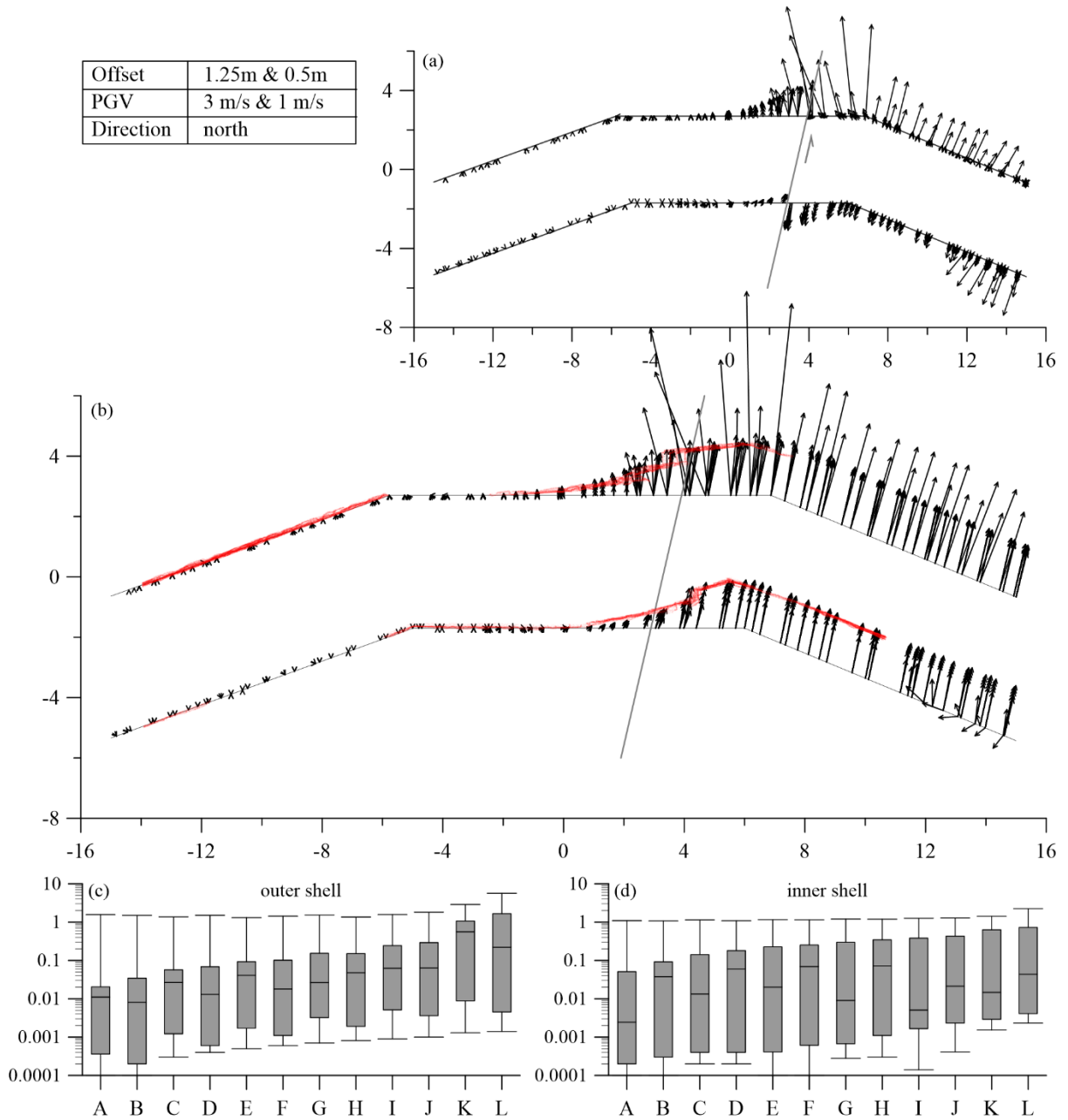


Figure A.44: Results of the simulation with a cycloidal pulse for a displacement of 1.25 m @ 3 m/s and 0.5 m @ 1 m/s. (a) Displacement vectors of the blocks relative to the displacement of the baseplate beneath the blocks from a top view perspective. The light grey line marks the course of the fault line in the model. The light grey arrows point in direction of the ground motion. The dark grey lines mark the course of the initial wall line. (b) Vector plot of the absolute displacement (m) of all blocks from a top view perspective. The grey line marks the course of the fault line in the model and strikes in north-south direction. The superposed red points are the measured points from the 3D laser scanning survey. (c) Boxplot of the vector length relative to the displacement of the baseplate for all blocks in individual rows with row A: bottom and row L: top of the outer shell. (d) the same as (c) for the inner shell.

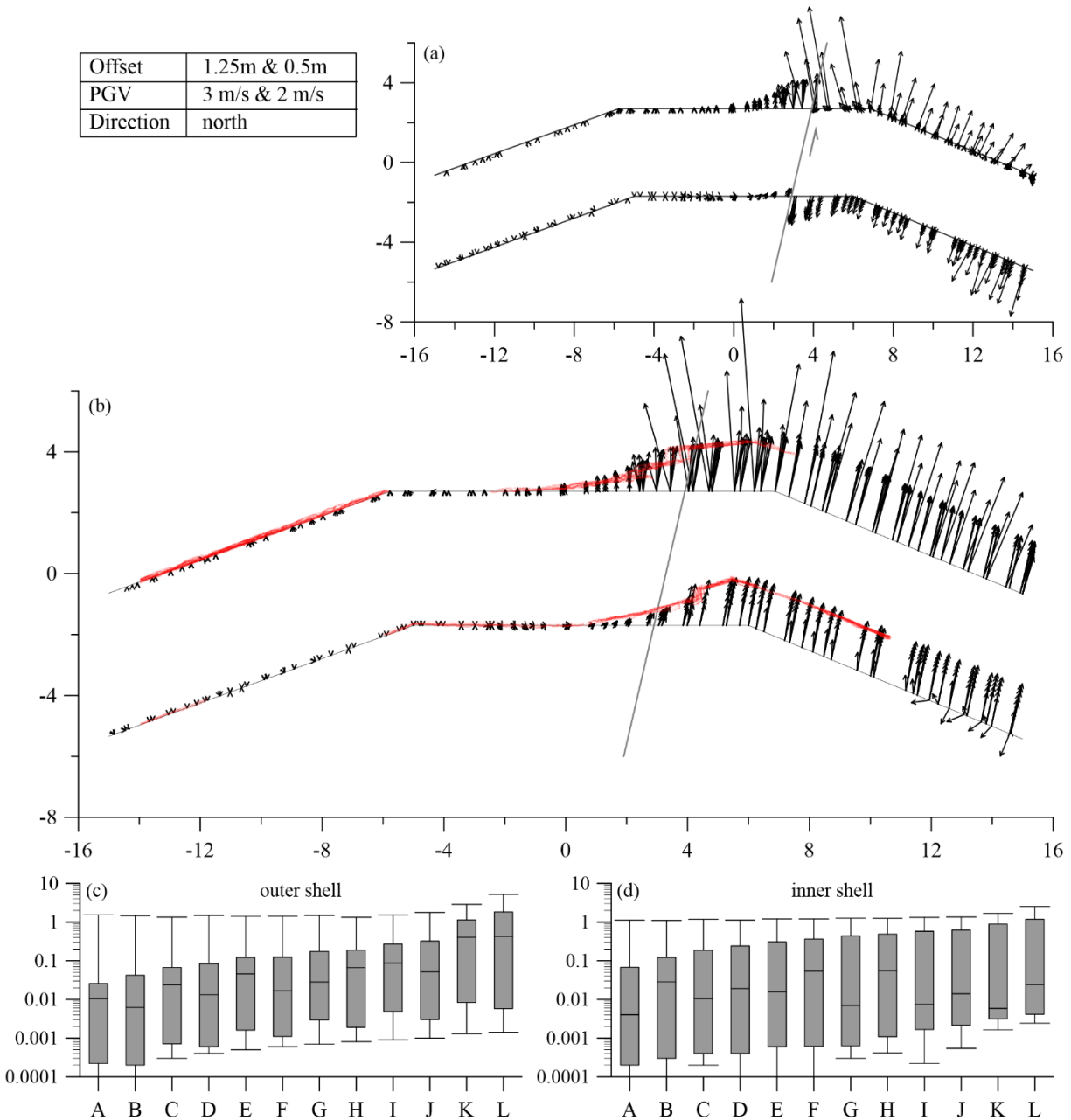


Figure A.45: Results of the simulation with a cycloidal pulse for a displacement of 1.25 m @ 3 m/s and 0.5 m @ 2 m/s. (a) Displacement vectors of the blocks relative to the displacement of the baseplate beneath the blocks from a top view perspective. The light grey line marks the course of the fault line in the model. The light grey arrows point in direction of the ground motion. The dark grey lines mark the course of the initial wall line. (b) Vector plot of the absolute displacement (m) of all blocks from a top view perspective. The grey line marks the course of the fault line in the model and strikes in north-south direction. The superposed red points are the measured points from the 3D laser scanning survey. (c) Boxplot of the vector length relative to the displacement of the baseplate for all blocks in individual rows with row A: bottom and row L: top of the outer shell. (d) the same as (c) for the inner shell.

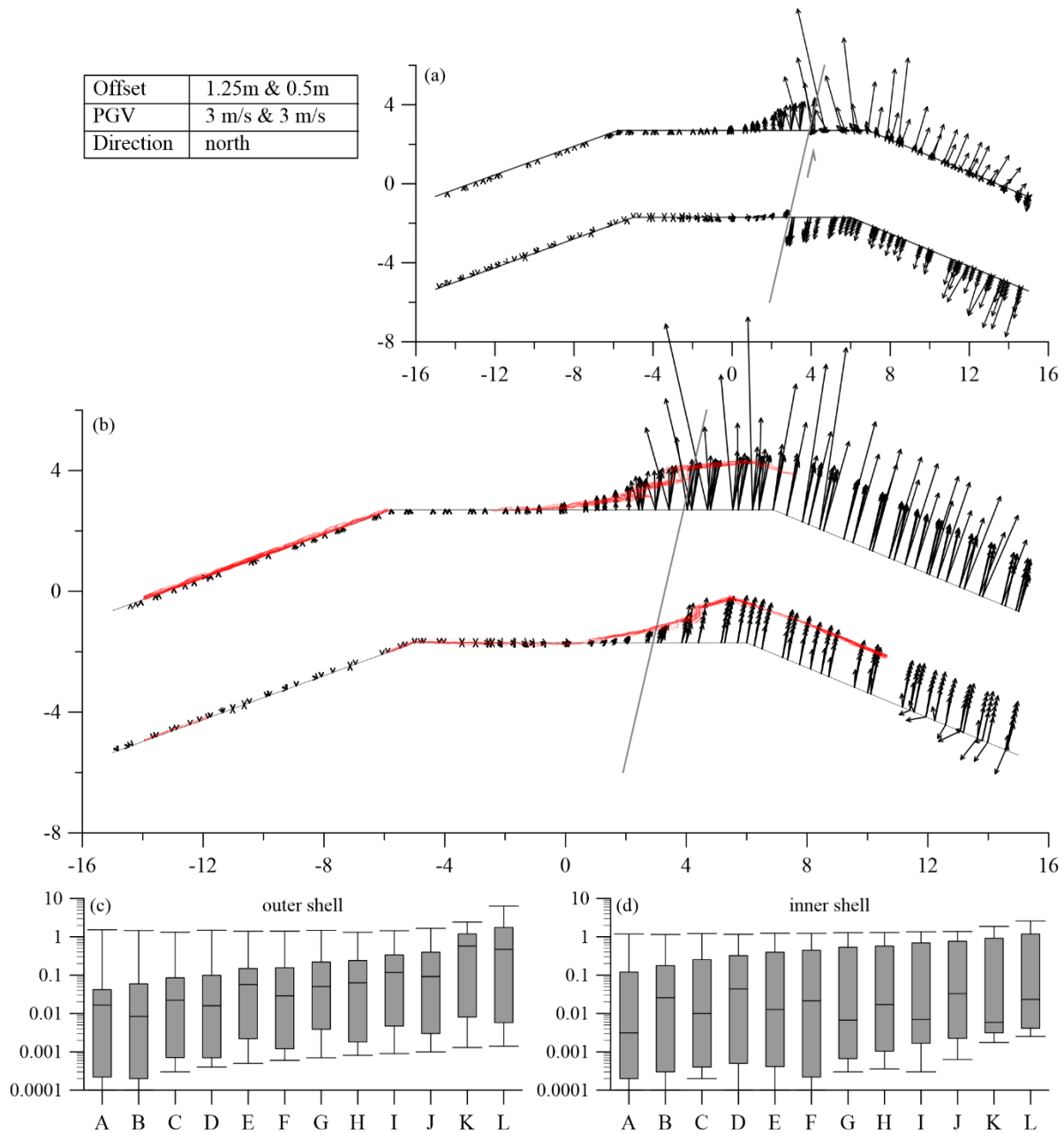


Figure A.46: Results of the simulation with a cycloidal pulse for a displacement of 1.25 m @ 3 m/s and 0.5 m @ 3 m/s. (a) Displacement vectors of the blocks relative to the displacement of the baseplate beneath the blocks from a top view perspective. The light grey line marks the course of the fault line in the model. The light grey arrows point in direction of the ground motion. The dark grey lines mark the course of the initial wall line. (b) Vector plot of the absolute displacement (m) of all blocks from a top view perspective. The grey line marks the course of the fault line in the model and strikes in north-south direction. The superposed red points are the measured points from the 3D laser scanning survey. (c) Boxplot of the vector length relative to the displacement of the baseplate for all blocks in individual rows with row A: bottom and row L: top of the outer shell. (d) the same as (c) for the inner shell.

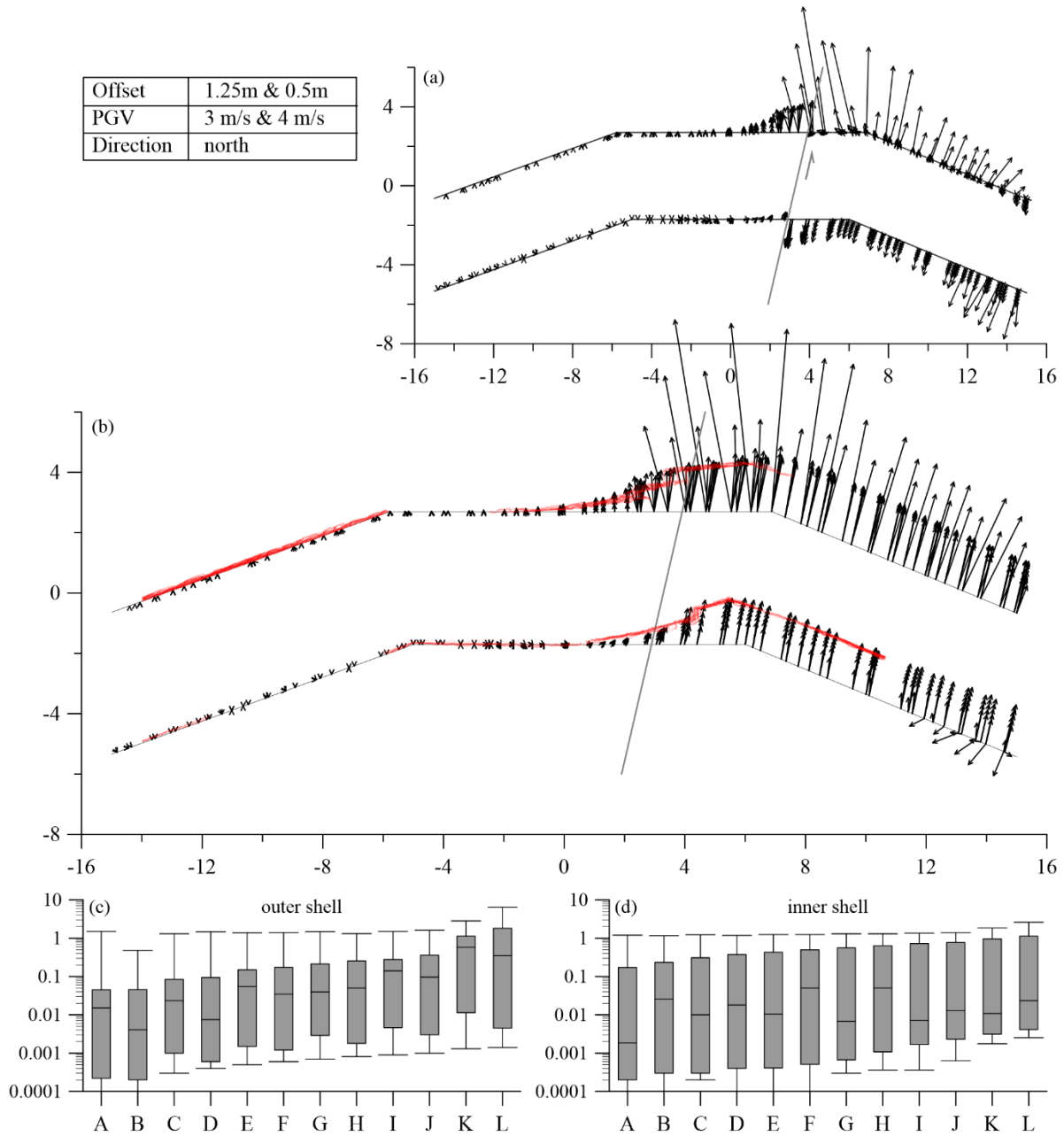


Figure A.47: Results of the simulation with a cycloidal pulse for a displacement of 1.25 m @ 3 m/s and 0.5 m @ 4 m/s. (a) Displacement vectors of the blocks relative to the displacement of the baseplate beneath the blocks from a top view perspective. The light grey line marks the course of the fault line in the model. The light grey arrows point in direction of the ground motion. The dark grey lines mark the course of the initial wall line. (b) Vector plot of the absolute displacement (m) of all blocks from a top view perspective. The grey line marks the course of the fault line in the model and strikes in north-south direction. The superposed red points are the measured points from the 3D laser scanning survey. (c) Boxplot of the vector length relative to the displacement of the baseplate for all blocks in individual rows with row A: bottom and row L: top of the outer shell. (d) the same as (c) for the inner shell.

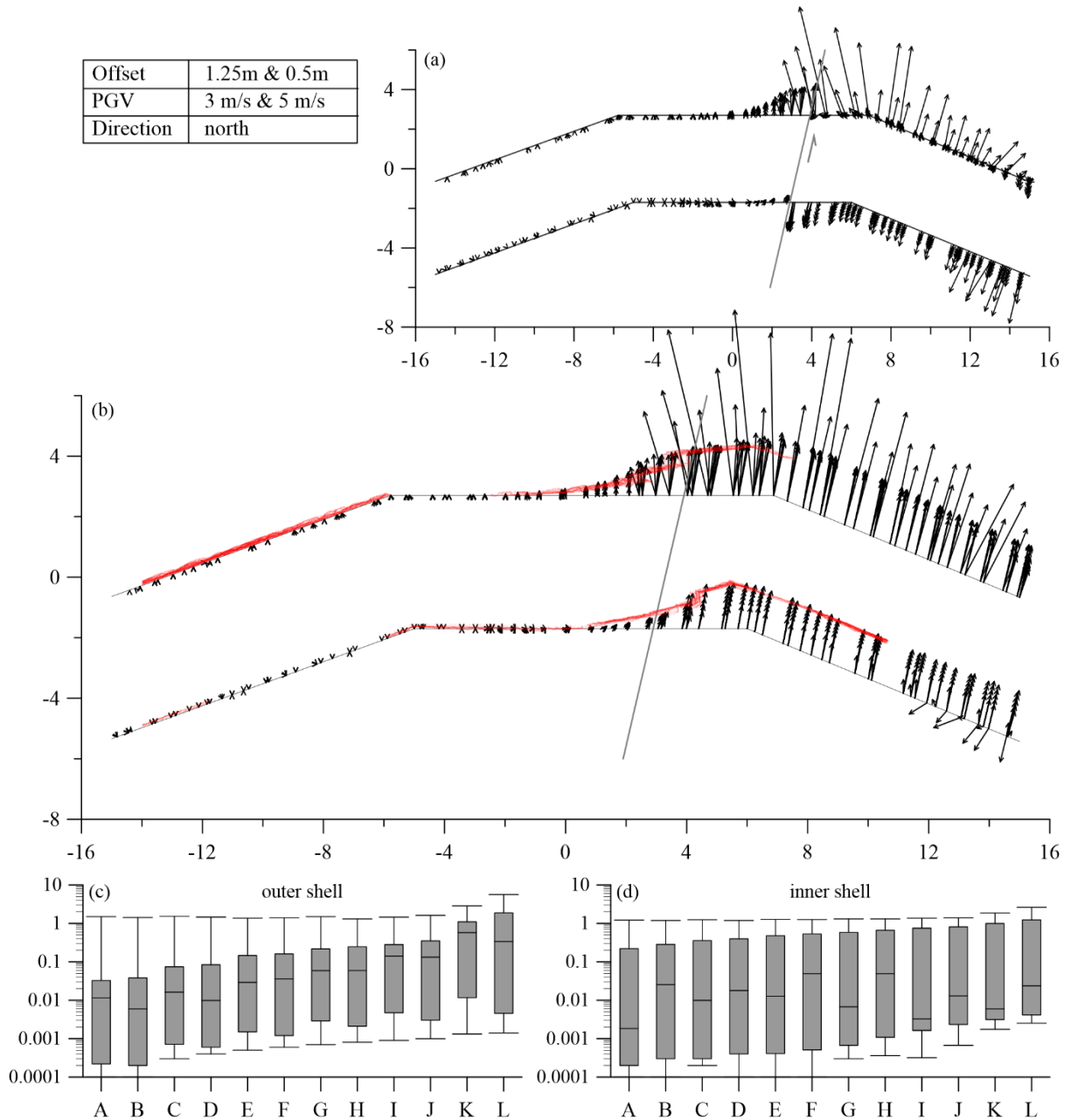


Figure A.48: Results of the simulation with a cycloidal pulse for a displacement of 1.25 m @ 3 m/s and 0.5 m @ 5 m/s. (a) Displacement vectors of the blocks relative to the displacement of the baseplate beneath the blocks from a top view perspective. The light grey line marks the course of the fault line in the model. The light grey arrows point in direction of the ground motion. The dark grey lines mark the course of the initial wall line. (b) Vector plot of the absolute displacement (m) of all blocks from a top view perspective. The grey line marks the course of the fault line in the model and strikes in north-south direction. The superposed red points are the measured points from the 3D laser scanning survey. (c) Boxplot of the vector length relative to the displacement of the baseplate for all blocks in individual rows with row A: bottom and row L: top of the outer shell. (d) the same as (c) for the inner shell.

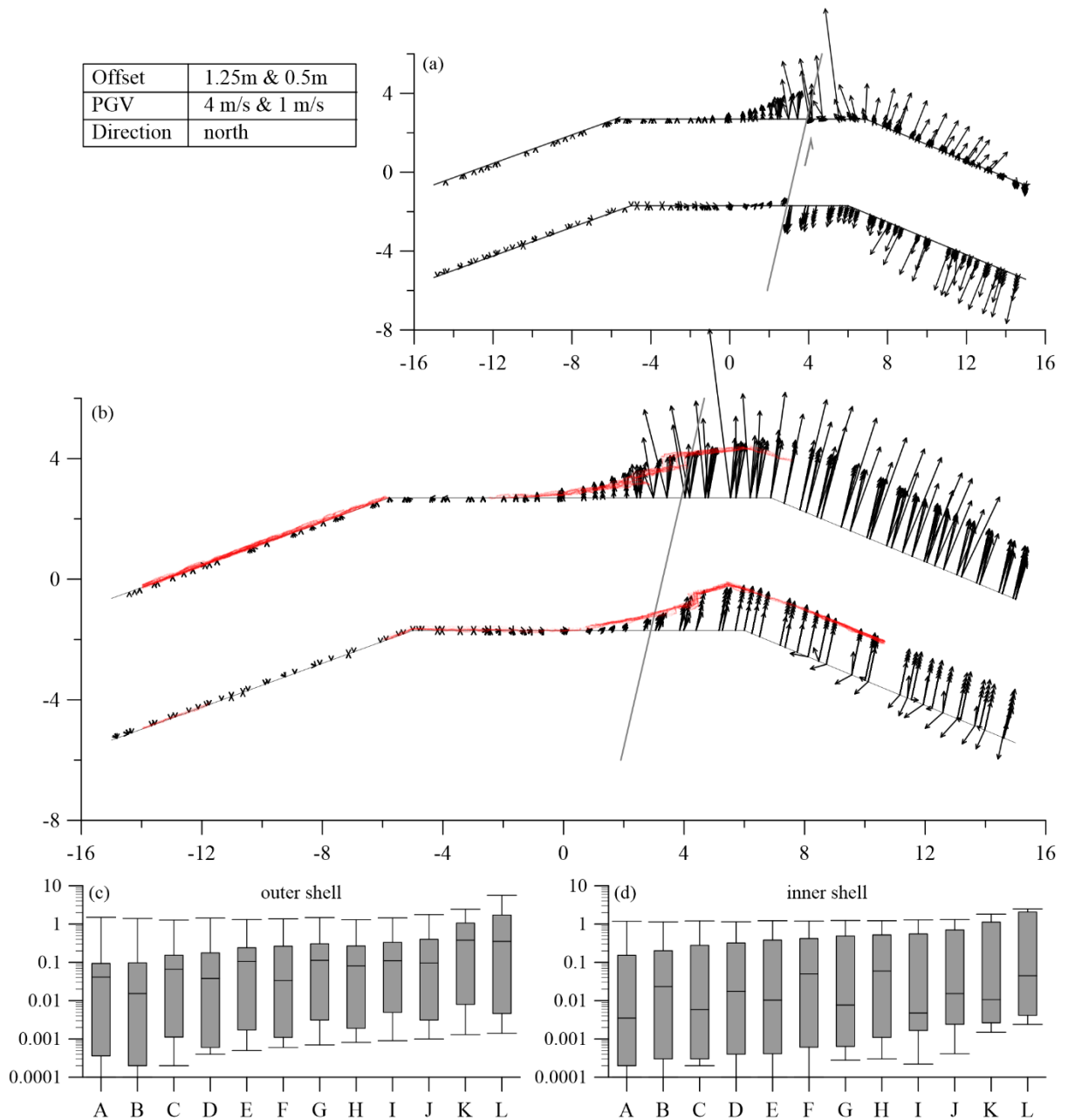


Figure A.49: Results of the simulation with a cycloidal pulse for a displacement of 1.25 m @ 4 m/s and 0.5 m @ 1 m/s. (a) Displacement vectors of the blocks relative to the displacement of the baseplate beneath the blocks from a top view perspective. The light grey line marks the course of the fault line in the model. The light grey arrows point in direction of the ground motion. The dark grey lines mark the course of the initial wall line. (b) Vector plot of the absolute displacement (m) of all blocks from a top view perspective. The grey line marks the course of the fault line in the model and strikes in north-south direction. The superposed red points are the measured points from the 3D laser scanning survey. (c) Boxplot of the vector length relative to the displacement of the baseplate for all blocks in individual rows with row A: bottom and row L: top of the outer shell. (d) the same as (c) for the inner shell.

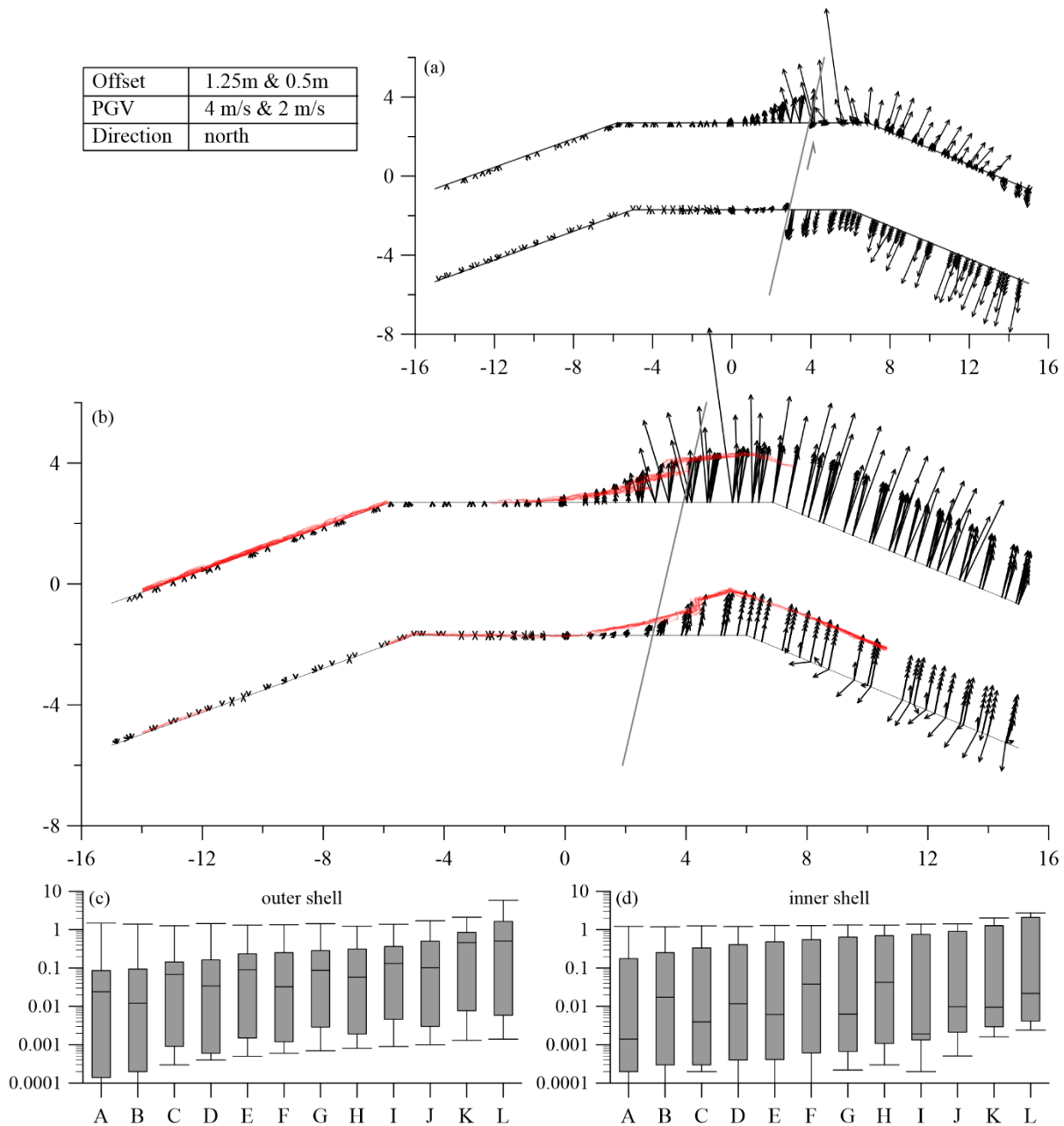


Figure A.50: Results of the simulation with a cycloidal pulse for a displacement of 1.25 m @ 4 m/s and 0.5 m @ 2 m/s. (a) Displacement vectors of the blocks relative to the displacement of the baseplate beneath the blocks from a top view perspective. The light grey line marks the course of the fault line in the model. The light grey arrows point in direction of the ground motion. The dark grey lines mark the course of the initial wall line. (b) Vector plot of the absolute displacement (m) of all blocks from a top view perspective. The grey line marks the course of the fault line in the model and strikes in north-south direction. The superposed red points are the measured points from the 3D laser scanning survey. (c) Boxplot of the vector length relative to the displacement of the baseplate for all blocks in individual rows with row A: bottom and row L: top of the outer shell. (d) the same as (c) for the inner shell.

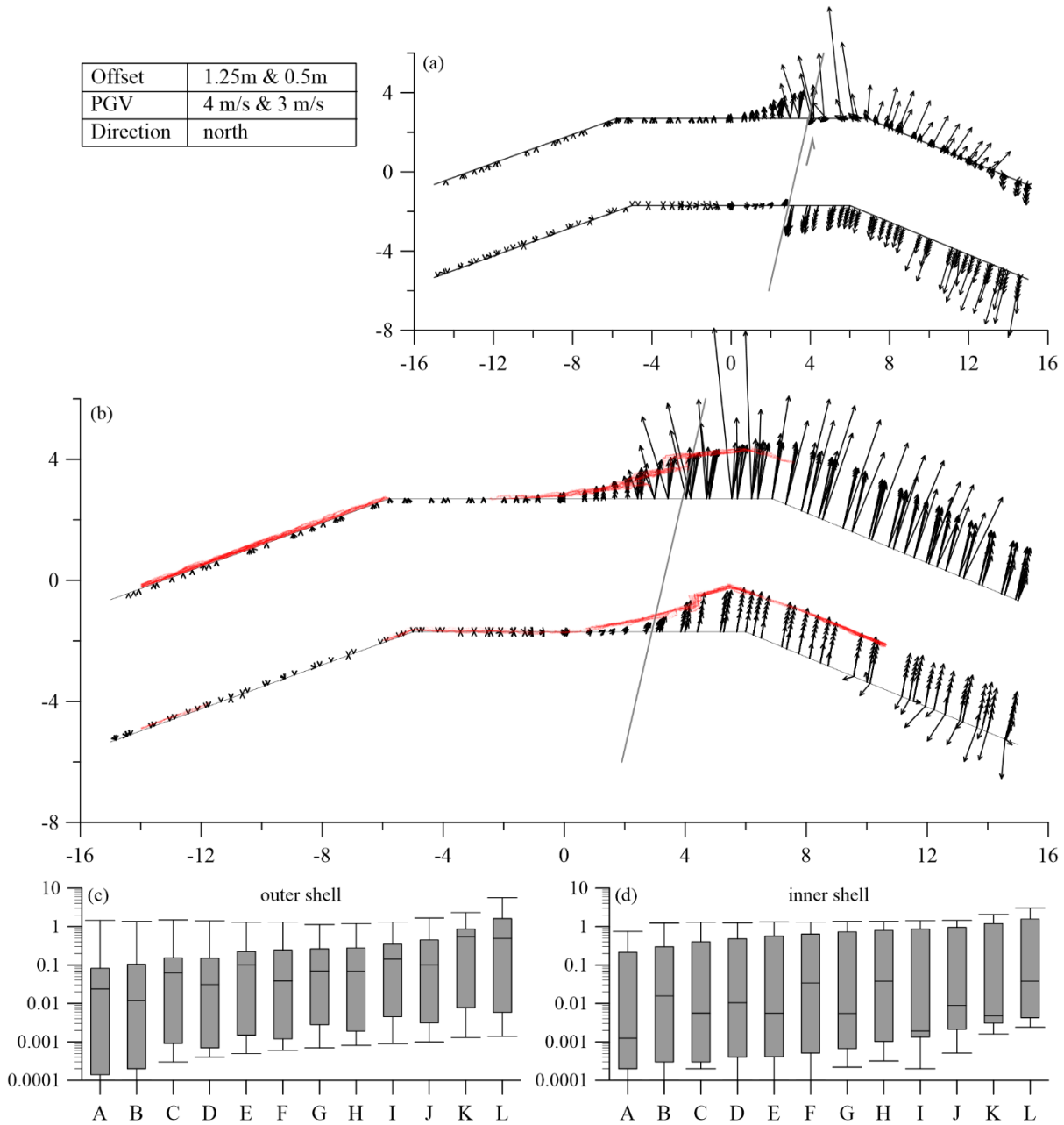


Figure A.51: Results of the simulation with a cycloidal pulse for a displacement of 1.25 m @ 4 m/s and 0.5 m @ 3 m/s. (a) Displacement vectors of the blocks relative to the displacement of the baseplate beneath the blocks from a top view perspective. The light grey line marks the course of the fault line in the model. The light grey arrows point in direction of the ground motion. The dark grey lines mark the course of the initial wall line. (b) Vector plot of the absolute displacement (m) of all blocks from a top view perspective. The grey line marks the course of the fault line in the model and strikes in north-south direction. The superposed red points are the measured points from the 3D laser scanning survey. (c) Boxplot of the vector length relative to the displacement of the baseplate for all blocks in individual rows with row A: bottom and row L: top of the outer shell. (d) the same as (c) for the inner shell.

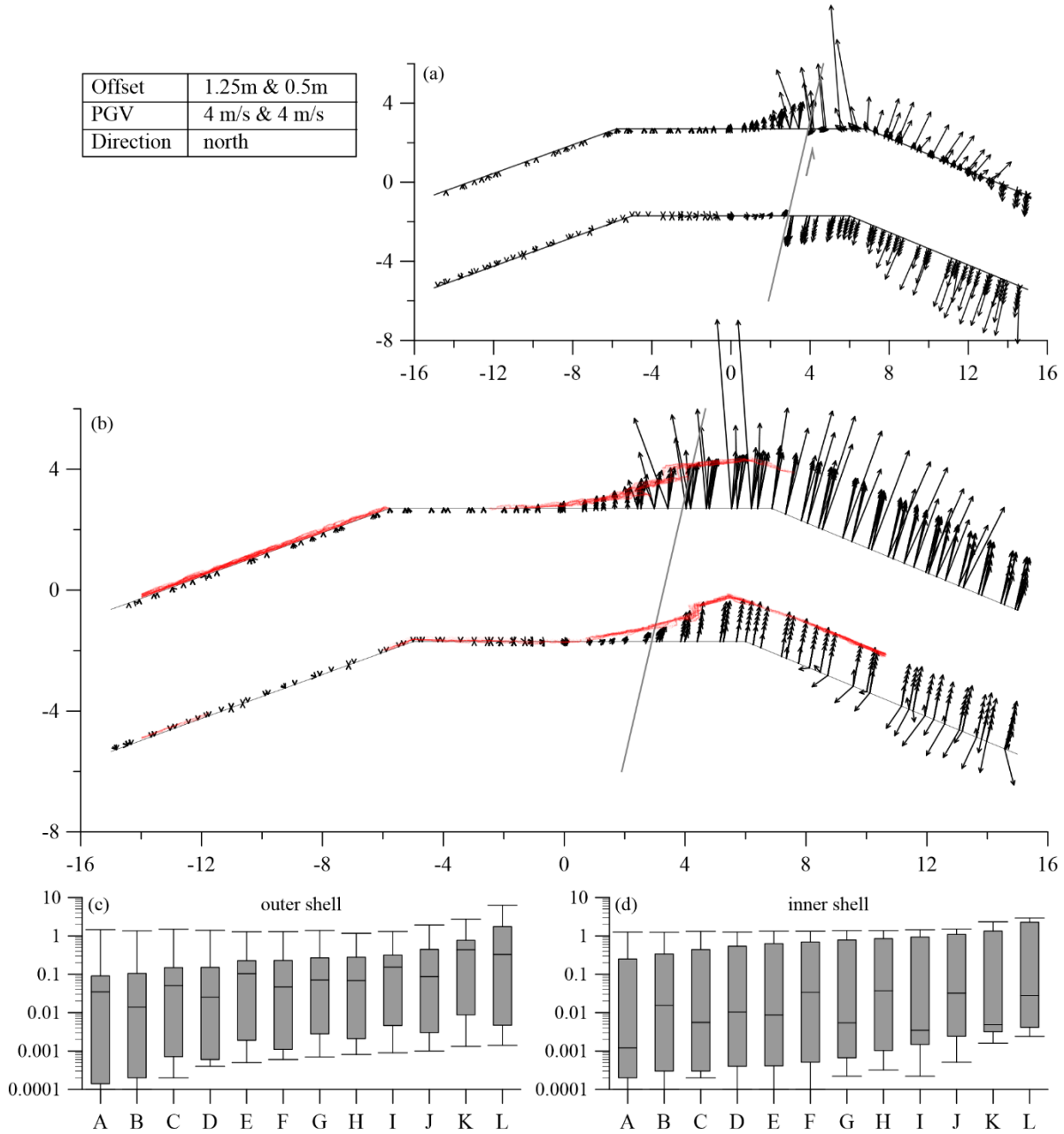


Figure A.52: Results of the simulation with a cycloidal pulse for a displacement of 1.25 m @ 4 m/s and 0.5 m @ 4 m/s. (a) Displacement vectors of the blocks relative to the displacement of the baseplate beneath the blocks from a top view perspective. The light grey line marks the course of the fault line in the model. The light grey arrows point in direction of the ground motion. The dark grey lines mark the course of the initial wall line. (b) Vector plot of the absolute displacement (m) of all blocks from a top view perspective. The grey line marks the course of the fault line in the model and strikes in north-south direction. The superposed red points are the measured points from the 3D laser scanning survey. (c) Boxplot of the vector length relative to the displacement of the baseplate for all blocks in individual rows with row A: bottom and row L: top of the outer shell. (d) the same as (c) for the inner shell.

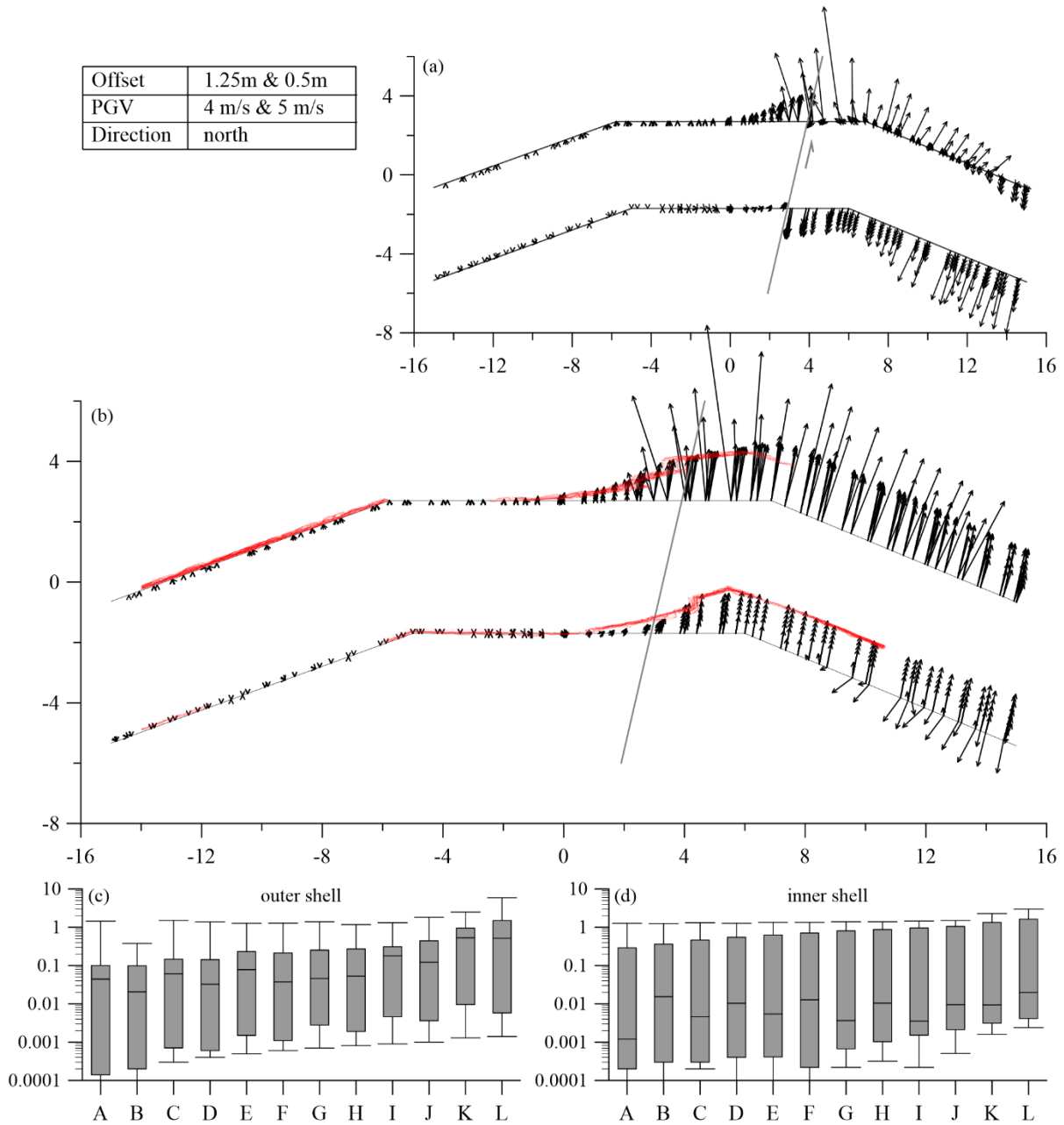


Figure A.53: Results of the simulation with a cycloidal pulse for a displacement of 1.25 m @ 4 m/s and 0.5 m @ 5 m/s. (a) Displacement vectors of the blocks relative to the displacement of the baseplate beneath the blocks from a top view perspective. The light grey line marks the course of the fault line in the model. The light grey arrows point in direction of the ground motion. The dark grey lines mark the course of the initial wall line. (b) Vector plot of the absolute displacement (m) of all blocks from a top view perspective. The grey line marks the course of the fault line in the model and strikes in north-south direction. The superposed red points are the measured points from the 3D laser scanning survey. (c) Boxplot of the vector length relative to the displacement of the baseplate for all blocks in individual rows with row A: bottom and row L: top of the outer shell. (d) the same as (c) for the inner shell.

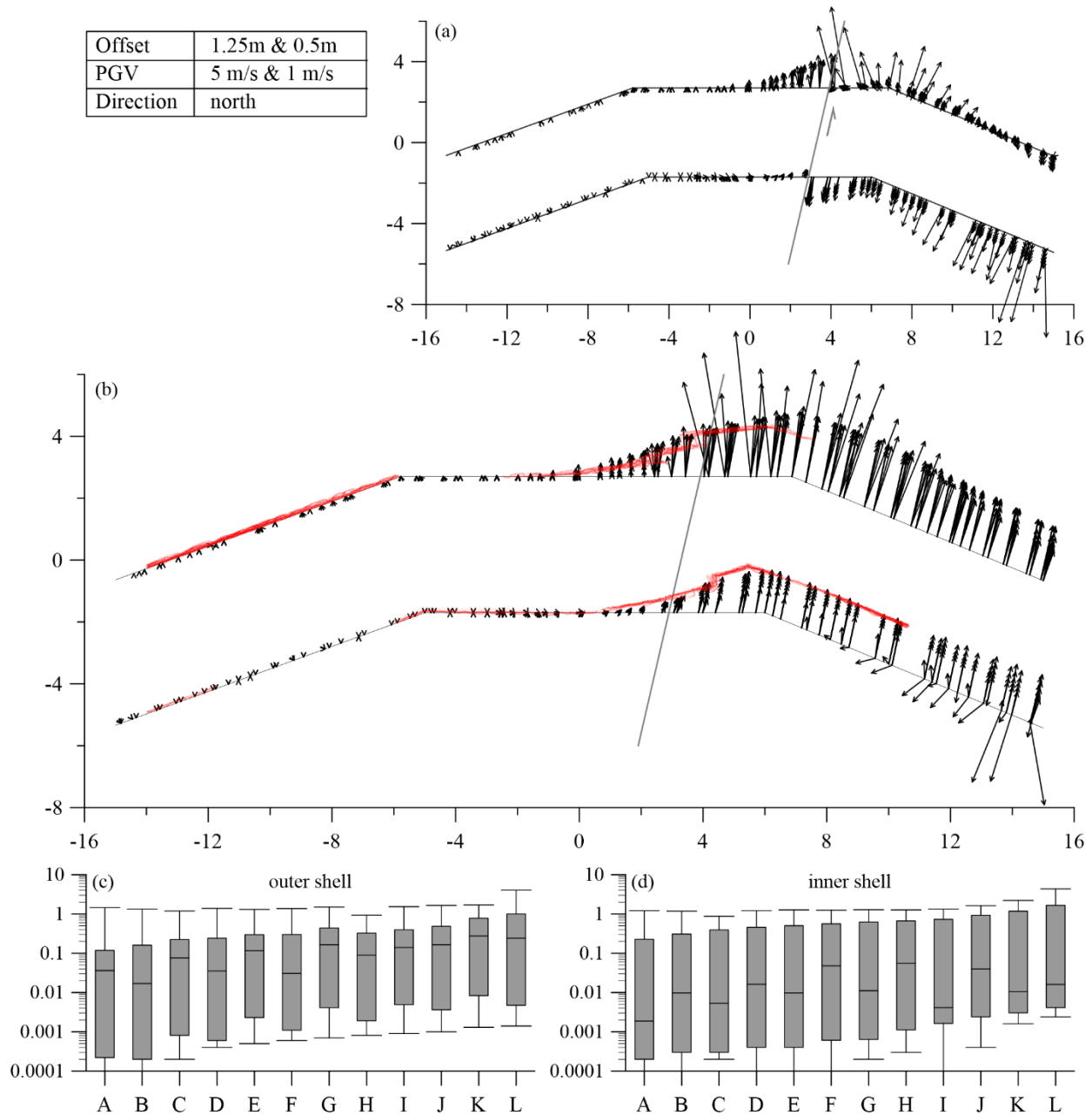


Figure A.54: Results of the simulation with a cycloidal pulse for a displacement of 1.25 m @ 5 m/s and 0.5 m @ 1 m/s. (a) Displacement vectors of the blocks relative to the displacement of the baseplate beneath the blocks from a top view perspective. The light grey line marks the course of the fault line in the model. The light grey arrows point in direction of the ground motion. The dark grey lines mark the course of the initial wall line. (b) Vector plot of the absolute displacement (m) of all blocks from a top view perspective. The grey line marks the course of the fault line in the model and strikes in north-south direction. The superposed red points are the measured points from the 3D laser scanning survey. (c) Boxplot of the vector length relative to the displacement of the baseplate for all blocks in individual rows with row A: bottom and row L: top of the outer shell. (d) the same as (c) for the inner shell.

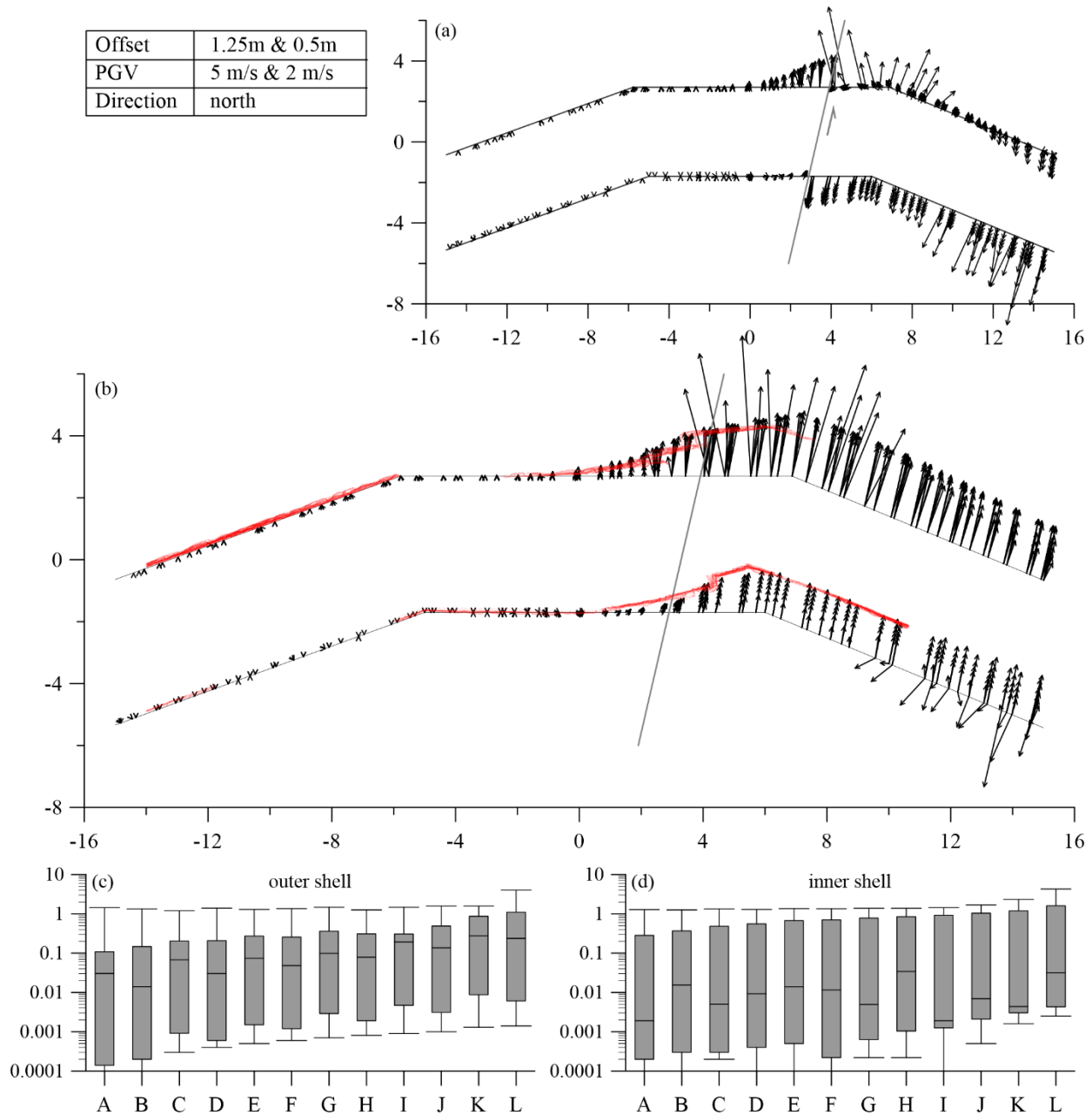


Figure A.55: Results of the simulation with a cycloidal pulse for a displacement of 1.25 m @ 5 m/s and 0.5 m @ 2 m/s. (a) Displacement vectors of the blocks relative to the displacement of the baseplate beneath the blocks from a top view perspective. The light grey line marks the course of the fault line in the model. The light grey arrows point in direction of the ground motion. The dark grey lines mark the course of the initial wall line. (b) Vector plot of the absolute displacement (m) of all blocks from a top view perspective. The grey line marks the course of the fault line in the model and strikes in north-south direction. The superposed red points are the measured points from the 3D laser scanning survey. (c) Boxplot of the vector length relative to the displacement of the baseplate for all blocks in individual rows with row A: bottom and row L: top of the outer shell. (d) the same as (c) for the inner shell.

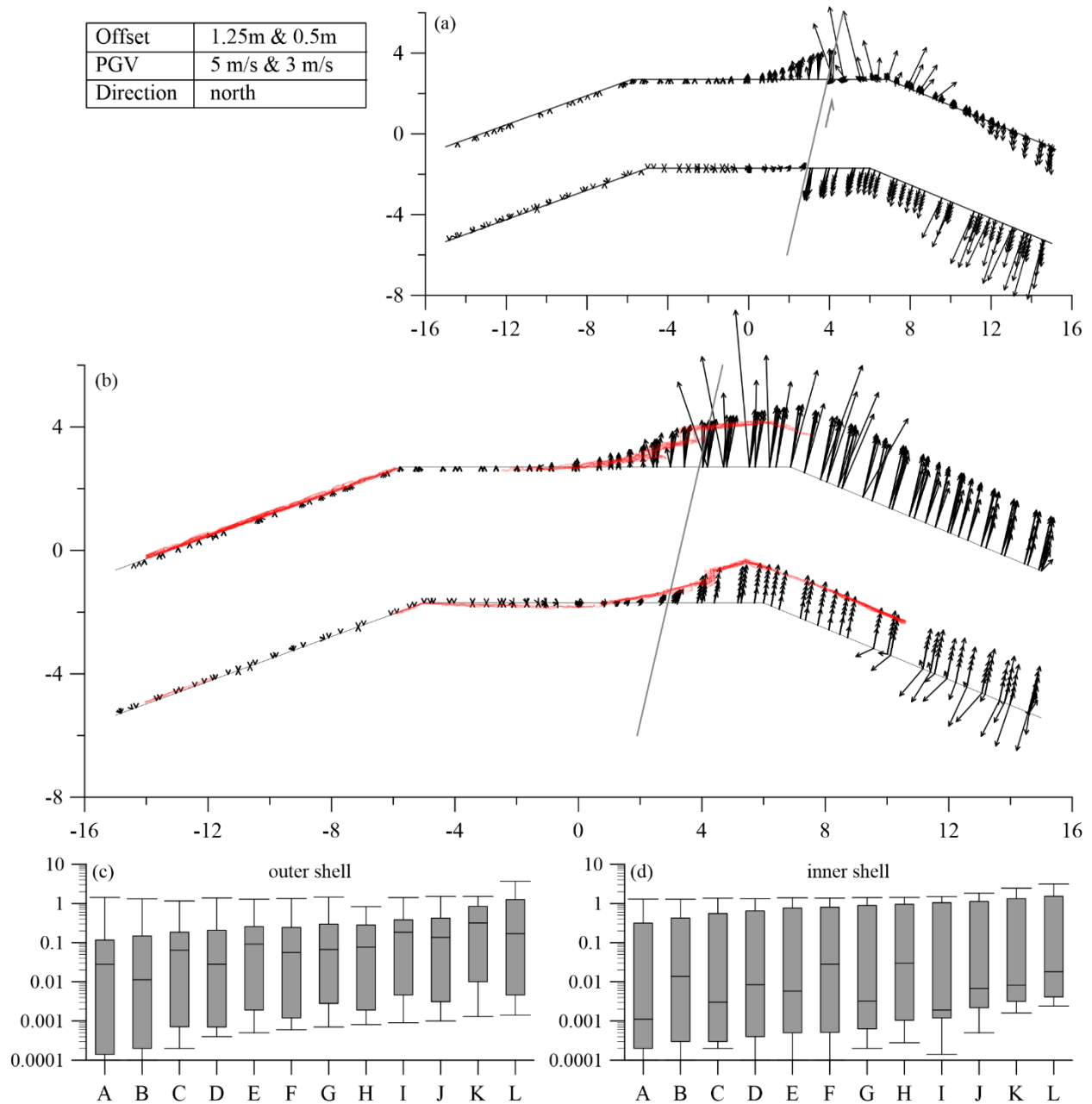


Figure A.56: Results of the simulation with a cycloidal pulse for a displacement of 1.25 m @ 5 m/s and 0.5 m @ 3 m/s. (a) Displacement vectors of the blocks relative to the displacement of the baseplate beneath the blocks from a top view perspective. The light grey line marks the course of the fault line in the model. The light grey arrows point in direction of the ground motion. The dark grey lines mark the course of the initial wall line. (b) Vector plot of the absolute displacement (m) of all blocks from a top view perspective. The grey line marks the course of the fault line in the model and strikes in north-south direction. The superposed red points are the measured points from the 3D laser scanning survey. (c) Boxplot of the vector length relative to the displacement of the baseplate for all blocks in individual rows with row A: bottom and row L: top of the outer shell. (d) the same as (c) for the inner shell.

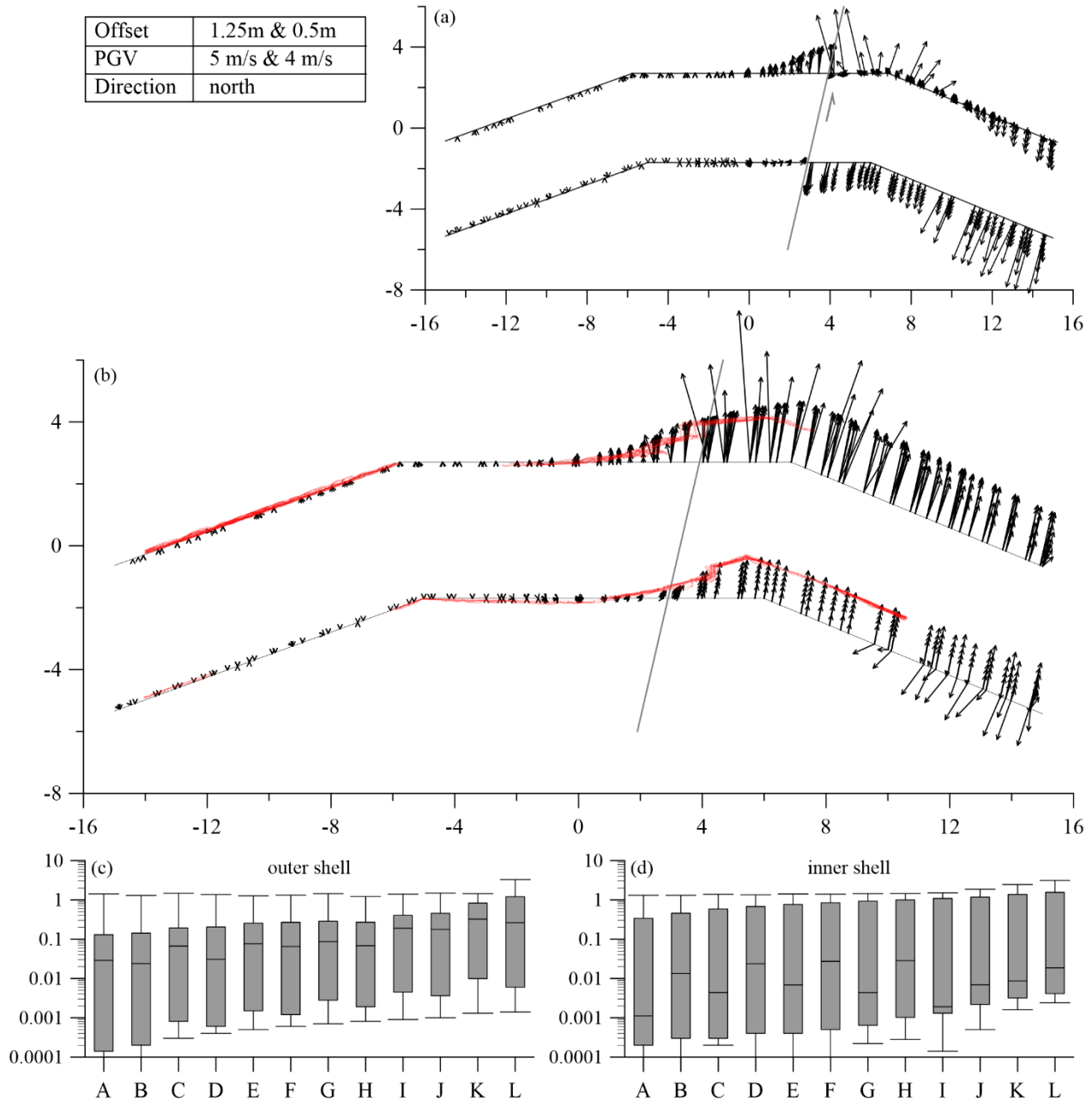


Figure A.57: Results of the simulation with a cycloidal pulse for a displacement of 1.25 m @ 5 m/s and 0.5 m @ 4 m/s. (a) Displacement vectors of the blocks relative to the displacement of the baseplate beneath the blocks from a top view perspective. The light grey line marks the course of the fault line in the model. The light grey arrows point in direction of the ground motion. The dark grey lines mark the course of the initial wall line. (b) Vector plot of the absolute displacement (m) of all blocks from a top view perspective. The grey line marks the course of the fault line in the model and strikes in north-south direction. The superposed red points are the measured points from the 3D laser scanning survey. (c) Boxplot of the vector length relative to the displacement of the baseplate for all blocks in individual rows with row A: bottom and row L: top of the outer shell. (d) the same as (c) for the inner shell.

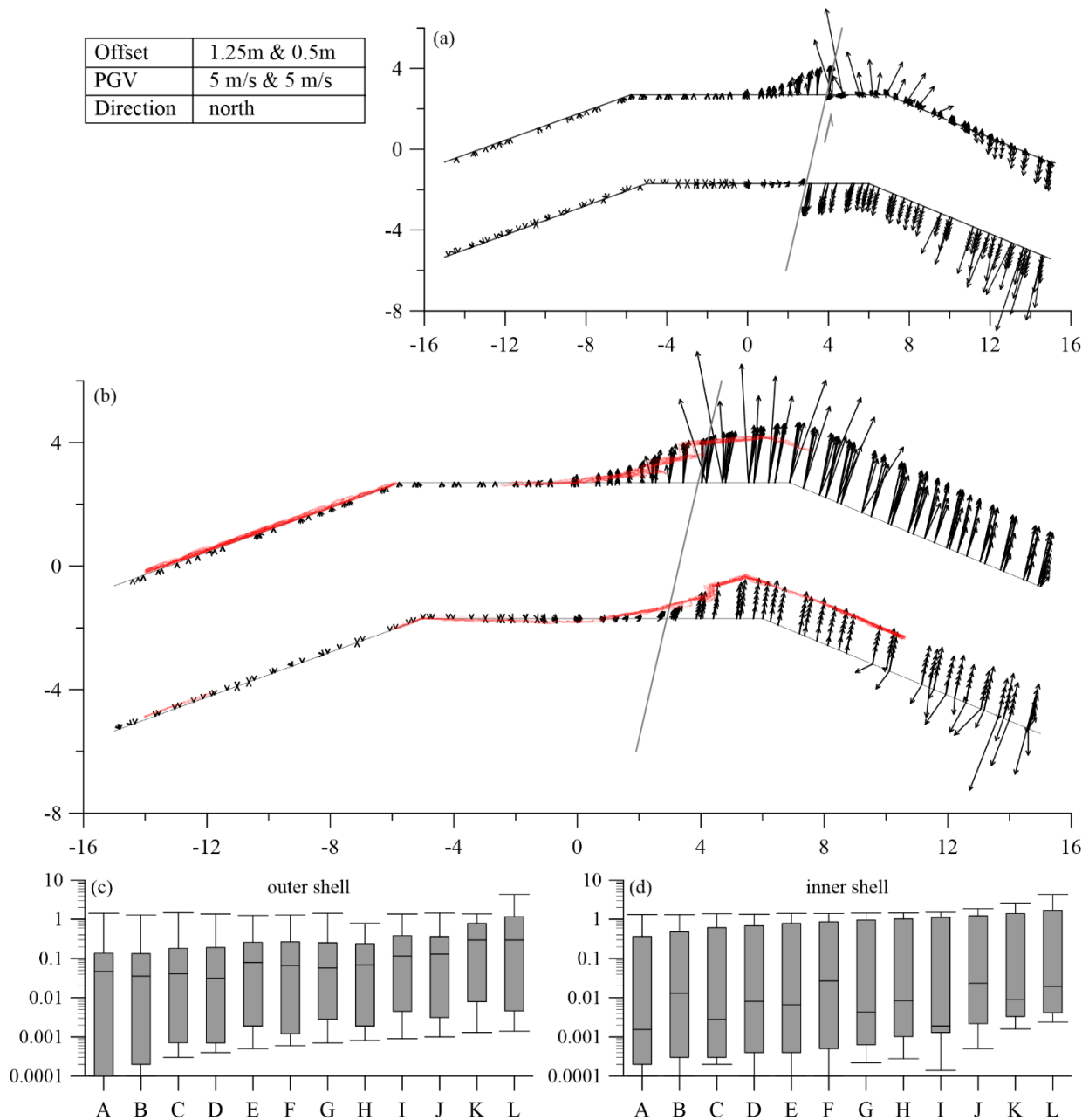


Figure A.58: Results of the simulation with a cycloidal pulse for a displacement of 1.25 m @ 5 m/s and 0.5 m @ 5 m/s. (a) Displacement vectors of the blocks relative to the displacement of the baseplate beneath the blocks from a top view perspective. The light grey line marks the course of the fault line in the model. The light grey arrows point in direction of the ground motion. The dark grey lines mark the course of the initial wall line. (b) Vector plot of the absolute displacement (m) of all blocks from a top view perspective. The grey line marks the course of the fault line in the model and strikes in north-south direction. The superposed red points are the measured points from the 3D laser scanning survey. (c) Boxplot of the vector length relative to the displacement of the baseplate for all blocks in individual rows with row A: bottom and row L: top of the outer shell. (d) the same as (c) for the inner shell.

## ERKLÄRUNG

Ich versichere, dass ich die von mir vorgelegte Dissertation selbständig angefertigt, die benutzten Quellen und Hilfsmittel vollständig angegeben und die Stellen der Arbeit – einschließlich Tabellen, Karten und Abbildungen –, die anderen Werken im Wortlaut oder dem Sinn nach entnommen sind, in jedem Einzelfall als Entlehnung kenntlich gemacht habe; dass diese Dissertation noch keiner anderen Fakultät oder Universität zur Prüfung vorgelegen hat; dass sie – abgesehen von unten angegebenen Teilpublikationen – noch nicht veröffentlicht worden ist, sowie, dass ich eine solche Veröffentlichung vor Abschluss des Promotionsverfahrens nicht vornehmen werde. Die Bestimmungen der Promotionsordnung sind mir bekannt. Die von mir vorgelegte Dissertation ist von Prof. Dr. K.-G. Hinzen betreut worden.

Köln, den 08.04.2019

\_\_\_\_\_  
Gregor Schweppe

### **Folgende Teilpublikationen liegen vor:**

Schweppe, G., K.-G., Hinzen, S., Reamer, M., Fischer, and S., Marco (2017). The ruin of the roman temple of Kedesh, Israel; Example of a precariously balanced archaeological structure used as a Seismoscope, *Annals of Geophysics* **60**, S0444.